Commissariat à l'énergie atomique et aux énergies alternatives

e-den

A Nuclear Energy Division
Monograph

Corrosion and Alteration of Nuclear Materials

EDITIONS LE MONITEUR

energie atomique • energies alternatives

DEN Monographs

A Nuclear Energy Division Monograph
Commissariat à l'énergie atomique,
91191 Gif-sur-Yvette Cedex (France)
Tel: +33 (0)1 64 50 10 00

English translation by Catherine Andrieux.

Administrator: Fanny Bazile.

Editor: Jean-François Parisot.
Graphic concept: Pierre Finot.

Correspondence: all correspondence should be addressed to the Editor or to CEA/DEN Direction scientifique, CEA Saclay
91191 Gif-sur-Yvette Cedex (France)
Tel: +33 (0)1 69 08 16 75

ISBN 978-2-281-11369-3
ISSN pending

Front cover: Stained glass in Notre-Dame des Passes Church, Le Moulleau (Gironde, France).

Commissariat à l'énergie atomique et aux énergies alternatives

e-den

A Nuclear Energy Division
Monograph

Corrosion and Alteration of Nuclear Materials

EDITIONS LE MONITEUR

energie atomique • energies alternatives

Foreword

After a dazzling start in the 1950's as a promising, inexhaustible, cost-effective energy source, nuclear energy was rejected by majority opinion in several Western countries three to four decades later, which suddenly brought its development to a halt.

Although the 1973 and 1979 oil crises marked the beginning of massive construction programs in some countries most heavily penalized by oil imports, France and Japan in particular, they were paradoxically followed by a gap in nuclear spending, first in the United States and then in Western Europe. However, repeated oil market tensions and emerging concerns over non-renewable natural resources should have increased such spending.

There are surely many reasons for this pause, which can in part be explained by the accidents in Three Mile Island in 1979 and Chernobyl in 1986, which deeply impacted public opinion. On top of this, ecological movements and Green parties made their (highly publicized) fight against nuclear energy a key part of their platform.

In France, whose population, with the exception of one case, had never disputed nuclear plant construction, negative attitudes began to surface in the late 1980's concerning the nuclear waste issue. Given Andra's growing difficulties in finding an underground laboratory site, the Government decided to suspend work in favor of a one-year moratorium and submitted the issue to the OPECST (French parliamentary evaluation office for scientific and technological choices).

The French Act of 30 December 1991 on nuclear waste management implemented the essence of the OPECST's recommendations, in particular its definition of a diversified research program and the basis for democratic discussion, thus helping calm the debate. It paved the way for a fifteen-year research period in which various options for long-term radioactive waste management were investigated. This led to the Act of 28 June 2006, which set out the basic framework for this management, to be recognized as a necessity from now on.

In addition, the starting century is marked by renewed collective awareness that our generation's energy needs cannot be met without concern for the environment and without preserving future generations' rights to satisfy these same needs. This concept of sustainable development is an inevitable challenge to our society.

Today, it goes unquestioned that global warming due to increasing greenhouse gas emissions is a human-caused problem. The only remaining debate concerns the extent and consequences of this climate change. Industrialized countries, which are for the most part responsible for the current situation, should feel particularly obliged to voluntarily take steps towards reducing emissions of theses gases. Nuclear energy can but gain considerable ground since, by nature, it does not produce this type of emissions and yet is a relatively abundant, reliable and cost-effective energy source.

Even if the situation still varies from country to country, more especially in Europe, several countries (China, South Korea, Finland, India, South Africa…) have already decided to make huge investments in developing nuclear energy. Others are very close to taking this step, in particular Great Britain and the United States who seem to be determined to launch programs for the construction of new nuclear power plants by the end of the decade, picking up a process that had been on hold for over a quarter-century.

Following France's national energy debate that took place in the first half of 2003, the Energy Act on energy passed in June 2005 established the decision to build an EPR demonstrator in preparation for the replacement of currently operating power plants.

A number of signs lead us to believe that a worldwide boost of nuclear energy is taking place. Nevertheless, the future of nuclear energy in our country, as in many others, will depend largely on its capacity to properly address the following two concerns:

- First, its social acceptability: nuclear energy must be deployed under stringent safety and security conditions, generating as little ultimate waste as possible, with perfect control of the waste that is produced in terms of its possible impact on human health and the environment.

- Secondly, the availability of nuclear resources: it is important to guarantee a long-term supply of fuel, by preparing to resort to systems which are more economical in terms of natural fissile materials and, above all, less dependent on market fluctuations.

These topics are a key part of the CEA Nuclear Energy Division's work. Indeed, this Division is a major player in the research aimed at supporting the nuclear industry's efforts to improve reactor safety and competitiveness, providing the Public Authorities with the elements necessary for making decisions on long-term nuclear waste management, and, finally, developing the nuclear reactor systems of the future. These systems, essentially fast neutron reactors, afford highly promising innovations in waste management and raw material use.

As a fervent partisan of the broadest possible dissemination of scientific and technical knowledge, I believe that this research work, which calls upon a wide range of scientific disciplines often at top worldwide level, should be presented and explained in priority to all those who would like to form their own opinion on nuclear energy. This is the reason why I welcome the publication of these DEN monographs with deep satisfaction, indeed. No doubt that close reading of these works will afford an invaluable source of information to the, I hope, many readers.

I would like to thank all the researchers and engineers who, by contributing to this project, willingly shared their experience and knowledge.

Bernard Bigot,
Chairman of the CEA

Introduction

The context, stakes, and goals

With the purpose of maintaining its economic competitiveness while meeting safety requirements, the nuclear industry works on how to improve and optimize the performance and durability of its facilities (limiting maintenance, extending service life of facilities, maintaining properties over time…).

Whatever the materials used in the nuclear industry may be – metallic alloys, concretes, glasses, or bitumens –, they are altered more or less rapidly on contact with the environment in which they are used.

The modalities of the corrosion process are determined by the physicochemical environment. Consequently, the stresses involved may be precursors, catalyzers, or amplifiers of a material's damage, likely to lead to degraded properties, or lower strength or integrity in the component, structure or works.

So, accurate and reliable knowledge of the behavior, strength, and properties of the materials constituting these facilities in their environment shall be acquired prior to any study of work/structure/object behavior, and shall be taken into account as early as the design step.

Investigations conducted at the CEA on ***nuclear materials corrosion and alteration*** are oriented to operational goals that mean providing information in terms of lifetime prediction, design aid for structures/works, support for safety calculations and demonstration, expert advice and recommendations on materials (formulation, fabrication, conditions of use or preparation…), as a help for nuclear facility design basis, operation, maintenance, and safety.

The systems investigated are extremely varied, complex, and evolutive over time, given the broad range of issues to be considered:

- Homogeneous or heterogeneous, composite,… and potentially reactive materials;
- Environments, and related stresses, that may result in simultaneous, chained, and/or strongly coupled (multi-physics) phenomena, sometimes under extreme conditions (high temperature, high pressure, **irradiations***, chemical concentration, mechanical stresses…);
- As well as broad spatial scales (multi-scale approach), from the materials (nano-, micro-, meso-) scale to the structure (macro-) scale.

In addition, complementary and more specifically nuclear constraints are to be taken into account:

- The long-term issue, to be addressed with robust, reliable, and predictive approaches: up to several thousands of years (e.g. in the case of radioactive waste geological disposal), i.e. beyond usual timescales in the industry (a few decades);
- The (radionuclide and pollutant) containment issue, which makes it necessary to comply with strict margins and constraints.

What is corrosion? A few definitions

Before further proceeding in presenting the Nuclear Energy Division (DEN) studies conducted on materials corrosion and alteration, it is worth noting that there is quite a broad range of definitions available for the terms "corrosion" or "alteration".

Etymologically, the word "corrosion" comes from the Latin corrodere, which means to *gnaw away, to gnaw to pieces*. In addition, generally speaking, corrosion is often defined as the alteration of a material or structure through a chemical or physicochemical reaction with the environment.

This term may either refer to the process, or to the resulting damage. Thus, in the 9th edition of the *Dictionary of the French Academy of Letters*, corrosion is *"the action of corroding or the result of such an action"*.

More scientifically, in the International Union of Pure and Applied Chemistry booklet of chemical definitions (IUPAC *Compendium of Chemical Terminology*, Second Edition, 1997), it is mentioned that *corrosion is an interfacial, irreversible reaction between a material and its environment, which leads to material degradation*.

Concerning metallic materials, the international Standard ISO 8044 [1] defines corrosion as *"(the) physicochemical interaction between a metal and its environment that results in changes in the properties of the metal, and which may lead to significant impairment of the function of the metal, the environment, or the technical system, of which these form a part"*.

This standard clearly presents corrosion as being *"at the interface between the material and the environment"*: it is neither a property of the material alone, nor a property of the environment alone, but it results from an interaction between these two phases. Consequently, corrosion science first requires an *accurate basic knowledge of the material and the environment* in which it is located. That implies many developments, e.g. in cementitious chemistry, mineralogy, metallurgy, interface transport, and solution chemistry.

This material/environment interaction is of a physicochemical type, which excludes from the above definition purely mechanical impairment processes, such as fatigue or wear, even though mechanical loads coupled with physico-chemical processes are likely, indeed, to affect, or even initiate corrosion and alteration phenomena. The words "corrosion", or "alteration", or even "damaging" will thus be used with this restricted meaning in this monograph.

A complex science

The multiphysics, multiscale, and highly coupled aspects of corrosion phenomena may lead to wrong identifying of the "corrosion science" nature, which appears to be similar to a mosaic. Its constitutive disciplines alone can be perceived when observing it too closely: thermodynamics, chemical kinetics, chemistry, electrochemistry, metallurgy, mineralogy, and so many others, up to mechanics, and even biology.

Improving the reliability of behavior predictions can be achieved only through developing robust, validated quantitative mechanistic models. Such an approach is named "mechanistic modelling", an English phrase commonly used in this field: corrosion processes, that may be fairly complex, must be described as more simple physico-chemical steps.

More precisely, mechanistic modelling consists in expressing the various steps as equations displaying the relevant local physico-chemical parameters, e.g. concentrations or potentials, and coupling them with the required equations (such as equilibrium equations for fast reactions, balance equations, Poisson equations, electroneutrality equations, etc.), in order to reach a comprehensive system. Integrating this system for given initial conditions and boundary conditions - a resolution that may require using numerical techniques -, gives access to physical, chemical, kinetic, thermodynamic data…, characteristic of the corrosion phenomenon at any moment.

The physico-chemical "bricks" used for building the modelling hereabove mentioned are chiefly chemical, electrochemical, and quasi-chemical reactions (those involving point defects), as well as volume and intergranular transport by diffusion and electric migration, and, possibly, convection transport through all the system's phases. Diffusion is usually assumed to obey Fick's law. Charge transfers are modelled with the local Ohm's law, and convection, with a flow proportional to a concentration and to a flow velocity.

As in other sciences related to complex systems, the process of modelling corrosion or alteration phenomena is in very close interaction with experimentation and simulation. Indeed, conceptualization of mechanistic (or "physic") modelling requires knowledge of the steps involved, likely to be reached through experimentation or simulation, used as a parametric study tool. This approach makes it possible to identify the prevailing phenomena. Symmetrically, models shall be validated by confronting them with dedicated experimental tests. The whole system's components can thus be fed mutually and iteratively so as to build a quantitative, validated set.

When passing to higher spatial scales, e.g. to investigate structure or object behavior, or corrosion influence upon materials usual properties, such as their mechanical resistance or their radionuclide or chemical toxic containment power, it may be necessary to simplify models (these simplified versions are sometimes called "operational models"), which only retain the prevailing phenomena sufficient to describe alteration under the investigated conditions.

In addition, validating corrosion models is often hindered by the slowness of alteration phenomena, which may imply sometimes prohibitive test periods. A way to escape this difficulty may lie in increasing chemical reaction and transport mechanism kinetics. This can often be achieved with temperatures higher than those of the real phenomenon investigated. Such a method requires the mechanism to be the same at both temperatures. Another way to escape the difficulty is carrying out observations of ancient natural (e.g. archaeological) or synthetic analogs. Yet, another problem may then emerge due to an often incomplete knowledge of how the analog's corrosion process under study has evolved.

Corrosion in the nuclear field

First of all, corrosion is an applied science. Accordingly, in this monograph, the investigations conducted on materials corrosion and alteration are put forward in chapters dealing with the major sectors of the nuclear field, and are classified according to phenomenology, the type of environment, and the type of alteration which materials undergo, still including a few specific nuclear-related features, such as the presence of radiation.

Corrosion in water-cooled reactors (Section 1)

In pressurized water reactors, **general corrosion*** can be found in fuel rod clads: in this case, investigations are focused on assessing the behavior of zirconium alloys used under increasingly stringent operational conditions. They are also aimed at contributing to develop new alloys of higher resistance.

Another important case of general corrosion is that of materials, stainless steels and nickel alloys used in reactor coolant systems: in this case, the industrial issue is not really the material's corrosion-induced damage, but rather the release and transport of corrosion products, vectors of **radioactive contamination***.

In addition to general corrosion, **stress corrosion cracking*** is a critical industrial issue that especially affects a large number of **alloy-600*** steam generator tubes, as well as several other components in presence of coolants. In this field, studies are mainly aimed at developing models able to predict crack initiation and propagation in order to optimize the frequency of monitoring and replacement actions.

In all these cases, studies carried out on mechanisms corroborate the models used, and make it possible to discriminate the relevant parameters involved.

Corrosion in the nuclear reactors of the future (Section 2)

The reactors of the future are likely to use extreme, varied, or little known environments, such as liquid metals, molten salts, or very high-temperature helium containing reactive impurities. For most of these systems, the choice and development of corrosion-resisting materials stand as a key step. In such a context, the aim of the studies conducted at the Nuclear Energy Division (DEN), as part of national and international collaborations, is characterizing corrosion behavior of the best potential materials under representative conditions, and optimizing them as early as the design stage. This characterization is based on mechanism studies and modelling.

Corrosion at the back-end of fuel cycle (Section 3)

In spent fuel treatment, employing nitric acid concentrated solutions leads to use special materials optimized and qualified prior to the facility building. Thus, as regards ongoing investigations, the main operational goals include improved knowledge of the existing materials limits, improved capabilities for predicting equipment lifetime, and qualification of new materials likely to be used for failed component replacement or for plants of the future. The major corrosion forms to be encountered are general corrosion and **intergranular corrosion***. In this case again, investigating related mechanisms enhances the reliability of the models used for behavior predictions.

For surface or subsurface storage and deep geological disposal of radioactive waste, a large number of materials will be considered as package or infrastructure materials, such as concrete, glass, clay, metals and alloys. Their behavior will have to be known over very long periods of time (thousands of years). The requirement to predict over so long timescales stands as the main characteristic for all the studies conducted in this sector: this raises a new, crucial issue for materials science. Ensuring reliable prediction of container corrosion rate, conditioning matrix behavior, and engineered barrier integrity over so long periods of time is, indeed, a paramount scientific and technological challenge. In such a context, investigations carried out on mechanisms cannot be eluded. As part of this

Partnership, a feature of research on corrosion

The stakes involved in corrosion research have been recognized as of prime importance by nuclear industrialists and the organization in charge of nuclear safety expertise, who have joined to the research conducted at the CEA through cofinancing or program follow-up.

Thus, the results highlighted in this monograph are issued from this joint research carried out with AREVA, EDF, the French National Radioactive Waste Management Agency (ANDRA: *Agence Nationale pour la gestion des Déchets RAdioactifs*), and the French Institute for Radiation protection and Nuclear Safety (IRSN: *Institut de Radioprotection et de Sûreté nucléaire*). Broadly speaking, research on water-cooled reactor corrosion has been mainly followed by EDF; that relating to fuel and fuel cycle, by AREVA and EDF; and that focused on waste management, by ANDRA. The IRSN has also taken part in developing innovating experimental techniques.

The industrialists EDF and AREVA have also supported some topics posing longer-term stakes, such as corrosion by molten fluorides, or corrosion by helium impurities, in relation to gas-cooled reactors.

Obviously, industrialists' support and an efficient research-industry partnership are an indispensable requirement for this research to prove successful.

Just as beneficial and fruitful, although of a different nature, is the collaboration with the CNRS (*Centre National de la Recherche Scientifique*: French National Center for Scientific Research), and French or foreign universities within the framework of European-funded programs. Collaboration topics are too numerous to be all mentioned here, but will be highlighted in the following pages.

approach, some of the mechanistic models developed by DEN are fully original. Let us quote, for instance, some models dealing with atmospheric corrosion, or again glass and concrete alteration, which combine chemical and/or electrochemical reactions and diffusion transport under complex physico-chemical and morphological conditions.

Reference

[1] ISO 8044, *"Corrosion des métaux et alliages. Termes principaux et définitions/Corrosion of metals and alloys – Basic terms and definitions"*, International Standard, Reference Number ISO 8044 2000, Geneva, Switzerland.

Gérard Santarini,
High-Commissioner's Cabinet
Damien Féron and Cécile Richet,
Physico-Chemistry Department
Bernard Bonin,
Scientific Division

Corrosion in Water-Cooled Reactors: Phenomenology, Mechanisms, and Remedies

Metallic materials good behavior in pressurized water reactors (PWRs) is one of the key factors to ensure a high safety level while maintaining a competitive operating cost. The basic requirement in safety is that structural materials integrity can be ensured all along reactor lifetime by limiting alterations and aging effects due to temperature, radiation, and chemical environment. For safety is based upon the principle of a threefold barrier surrounding nuclear fuel: the **clad***, the **primary coolant system*** wall, and the **containment building***. Reactor operation is also directly dependent upon materials good behavior, which makes it possible to reach a maximum energy availability factor, and reduce maintainance costs related to in-service inspections and remedial action for any damage repair.

Traditionally, corrosion phenomena are subdivided into two groups: **general corrosion***, and **localized corrosion***.

In pressurized water reactors, general corrosion can be seen on fuel element clads: studies are aimed at assessing the behavior of the zirconium alloys used under increasingly stringent operating conditions, and contributing to the development of new, more corrosion-resistant alloys. Another important case of general corrosion is that of materials used for reactor coolant systems, such as nickel alloys: here, the industrial concern is not really the material's corrosion-induced damage, but rather the release and transport of corrosion products, vectors of **radioactive contamination***. Computational codes used for predicting such phenomena are steadily improved.

The main local corrosion phenomenon to be found in primary and secondary environments is **stress corrosion cracking***, a critical industrial concern that not only affects fuel element clads, but also nickel base alloys and stainless steels, and is so likely to affect most of the nuclear island components (**internals***, vessel heads, piping, steam generator…). Investigations in this field are mainly aimed at developing models able to predict crack initiation and propagation in order to optimize the frequency of monitoring and replacement actions. In all these cases, studies carried out on mechanisms corroborate the models used, and enable the relevant parameters involved to be discriminated.

Uniform Corrosion

Uniform corrosion mechanisms

According to the International Standard ISO 8044, uniform corrosion of metallic materials is defined as a *"general corrosion proceeding at almost the same rate over the whole surface"* [1].

In an aqueous environment, such as water-cooled reactors, metallic materials corrosion is of an electrochemical nature, i.e. it takes the form of at least one anodic reaction, which is metal oxidation:

$$(M^{x+}, xe^-) \rightarrow (M^{x+}) + x(e^-)$$

This anodic reaction has to be coupled with at least one reduction or cathodic reaction, as follows:

$$(Ox^{q+}) + x(e^-) \rightarrow (Red(q-x)+)$$

This cathodic reaction corresponds with the reduction of dissolved oxygen (if any):

$$O_2 + 2H_2O + 4e^- \rightarrow 4OH^-$$

or, in a deoxygenated environment, with the reduction of water itself according to the following reaction:

$$H_2O + e^- \rightarrow 1/2\ H_2 + OH^-$$

Aqueous corrosion is characterized by these basic electrochemical reactions that take place uniformously over the whole surface considered. If corrosion products are soluble, uniform corrosion is evidenced either by a decrease in metal thickness over time (or by a mass loss per unit surface area per unit time), or by the formation of a uniform layer of corrosion products, if the latter are not soluble. So, when considering corrosion mechanisms, two types of uniform corrosion can be distinguished traditionally: active corrosion and passive corrosion.

Active corrosion is characterized by a metal ion transfer from the metal or alloy to the neighbouring aggressive environment, with several steps possibly involved in this transfer. Thus, the processes involved are always of two natures, charge transfer processes and material transport processes. Now, modelling the corrosion rate of a metal in an environment requires to determine which of the processes involved in the corrosion mechanism is the kinetically limiting step. A schematic representation of active corrosion can be seen on Figure 1:

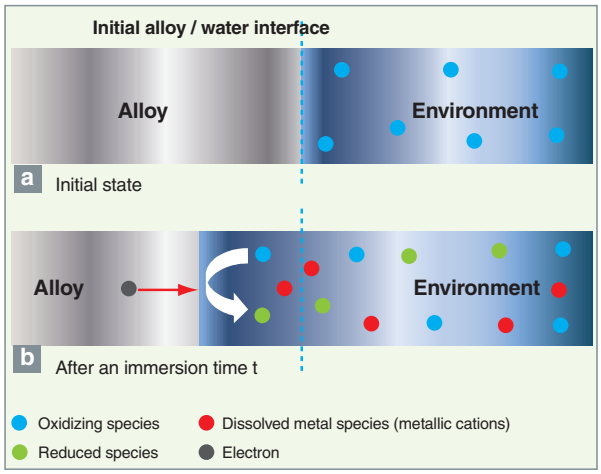

Fig. 1. Schematic representation of the uniform corrosion phenomenon in the active state in an aqueous environment:
a) the initial metallic material / water interface,
b) and the recession of this interface after a given immersion time.

Passive corrosion is characterized by the occurrence of a thin, adhering and protective layer formed at the surface of a metal by reaction between the metal and the environment: this is the passive (or passivation) film. So this corrosion mode induces either the growth of a passive film at the metal / oxide interface, or a metallic cation transfer through the film towards the aggressive environment, or again the coupling of both phenomena. Similarly to uniform corrosion in the active state, it displays charge transfer and material transport processes.

The charge transfer process always appears at the passive layer/aggressive environment interface, and allows the electrons released during metal oxidation to move to the oxidizing species responsible for corrosion in the aggressive environment. The electron is generated at the metallic material/passive film interface during oxidation. It reduces the oxidant either at this internal interface, if the oxidant can diffuse through the corrosion products layer, or at the outer interface between the passive film and the aggressive environment after diffusing through the oxide layer. Material transport processes describe the motion of the metallic cations and reduced species induced by the corrosion reaction, from the metallic material/passive film interface to the aggressive environment volume. They may involve several steps, such as metallic cation and reduced species diffusion through the aggressive environment, steps of **sorption*** / desorption of the same

species at the oxide layer surface, together with possible **complexing*** phenomena, as well as diffusion of metallic or oxidizing species through the passive film.

In addition to the phenomena hereabove mentioned, it is worth noting the oxide layer growth processes.

The corrosion mechanism in the passive state is the sum of these different processes. Assessing the corrosion rate requires to know which of these processes is kinetically limiting. A schematic representation of passive corrosion is shown on Figure 2.

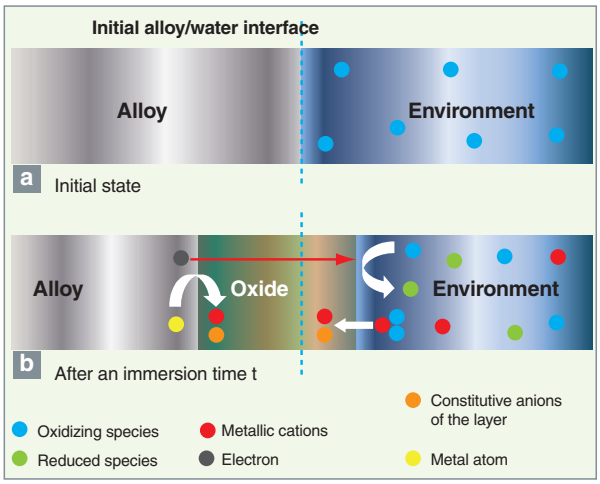

Fig. 2. Schematic representation of the uniform corrosion phenomenon in the passive state in an aqueous environment:
a) the initial metallic material / water interface,
b) and the passive layer formation after a given immersion time.

As material transport is faster in a liquid ionic conductor than in a solid one, species diffusion through the passive film generally acts as a mechanism that limits corrosion in the passive state.

Two cases are considered depending on the corrosive environment temperature:

- Low-temperature passivation for which diffusion phenomena within the passive film are slow; the films formed are thin, and the effect of the electric potential gradient is prevailing.

- On the contrary, in the case of high-temperature passivation, with diffusion being thermally activated, the films formed are thicker, and the effect of the electric potential gradient is negligible; so, the driving force of species motion is the chemical potential gradient.

Uniform corrosion phenomena in the nuclear steam supply system may refer to either of these two types of mechanism.

Thus, corrosion of nickel base alloys, used for steam generator tube fabrication, results in thin oxide films of approximately one hundred nanometers. Part of the oxidized metallic atoms is released towards the corrosive environment owing to the high solubility of the oxides or hydroxides formed. Species migration is driven by the electric potential gradient. The corrosion mechanism involved here is of the “low-temperature passivation” type.

In contrast, passivation of zirconium alloys, constitutive of fuel clads, does not lead to metallic species release (as zirconia solubility is negligible), and generates relatively thick passive layers (of several microns). In these layers, the corrosion mechanism involved is rather of the “high-temperature passivation” type.

Uniform corrosion of fuel clads

The **cladding*** material of the fuel rods used in the Pressurized Water Reactors (PWRs) is a zirconium alloy (Zr), which is oxidized on contact with primary circuit water (155 bar, 300-330 °C). Owing to its effects upon clad mechanical behavior, **fuel rod*** thermal behavior, and primary coolant system contamination, Zr alloy corrosion is a factor that limits the in-reactor residence time of fuel assemblies. Typically, the maximum allowable oxide thickness is approximately a hundred micrometers.

The CEA’s studies dealing with fuel rod clad corrosion are mainly conducted as part of the Zirconium Alloy Project, most ofen within the framework of a partnership with EDF and Areva NP. Their aim is to provide the relevant knowledge, data and models relating to fuel rod clads that are required to meet the nuclear industry’s improved competitiveness and safety needs in the short and medium term.

Concretely, their main goals are the following:

- The global analysis of the PWR feedback (quanfying and understanding in-reactor alloy performances);

- The assessment of Zr-alloy robustness with respect to an evolution of PWR operating conditions (environmental impact on corrosion kinetics);

- A contribution to the development and qualification of higher-performance, new cladding materials (metallurgical impact on corrosion kinetics);

- Knowledge capitalization and corrosion kinetics modelling.

These investigations are based upon:

- Acquiring data on the corrosion of clads arising from reactors (observations carried out in DEN's hot laboratories);
- Performing corrosion tests in autoclaves and in the **test loops*** CORAIL and REGGAE[1] (parametric studies, hypothesis tests);
- Characterizing oxide layer microstructure (mostly through optical and electron microscopies, SIMS, DRX, and Raman spectroscopy);
- Developing and using corrosion codes.

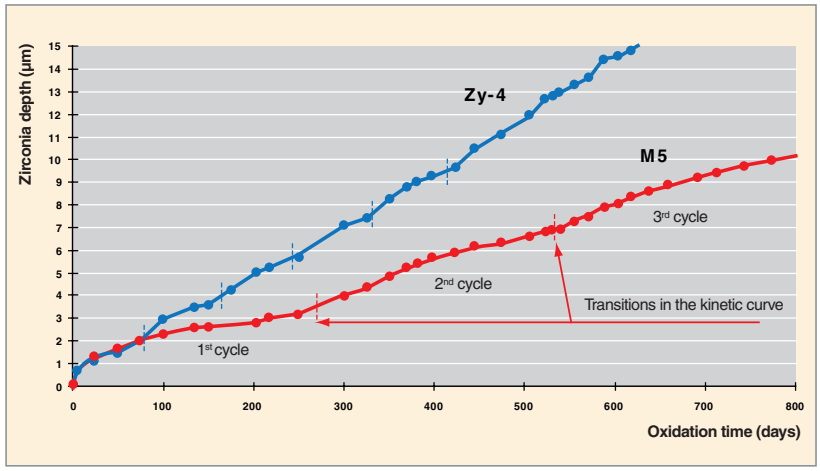

Fig. 3. Zircaloy-4 and M5TM oxidation kinetics determined through oxidation tests that were performed in an autoclave at 360 °C, with 10 ppm Li and 650 ppm B in water. The kinetics appear as cyclic. M5TM oxidation rate, the slowest on the average, displays the highest transition thickness.

Oxidation kinetics of zirconium alloys

Zr alloy[2] oxidation kinetics exhibit a succession of cycles (with a decreasing oxidation rate) and transitions in the kinetic curve (which bring the cycles to an end) (Fig. 3).

The major difference between alloys with distinct oxidation rates lies in the thickness of the oxide which has grown between two transitions in the kinetic curve (the so-called transition thickness). The lower the average oxidation rate, the higher the transition thickness. For example, alloy M5TM, which displays a higher resistance to corrosion, shows the highest transition thickness (~ 3.1 µm for M5TM as against ~1.7 µm for Zircaloy-4, under the conditions of the test detailed on Figure 3).

This cyclic feature observed for oxidation kinetics is also evidenced in the oxide microstructure. For the SEM observation of the oxide films formed in an autoclave, a loop, or a reactor, reveals a stratified state in the oxide films (resulting from the oxide's periodic cracking) (Fig. 4a). Stratum thickness is then consistent with the transition thickness deduced from oxidation kinetics.

These observations (cyclic kinetics, oxide periodic stratification, stratum thickness comparable to the transition thickness) have led to propose a cyclic oxidation scenario consisting of the following successive steps:

Oxidation cycle: during the cycle, a protective oxide layer is formed at the metal-oxide interface, and limits oxidizing species diffusion, the latter controlling the oxidation rate. As its thickness increases during the cycle, the oxidation rate decreases. At this stage, the oxide layer features high compressive stresses (resulting from zirconia volume expansion) [2]. It then consists of mostly columnar crystallites of quadratic and monoclinic zirconia (Fig. 4b).

The transition in the kinetic curve is correlated with a loss of the oxide protective character, as well as a decrease in stress, a lower proportion of quadratic zirconia, and oxide

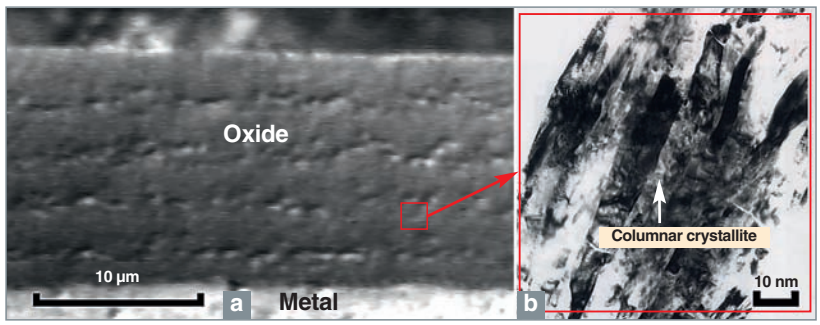

Fig. 4. An oxide film formed on the M5TM in an autoclave (360 °C, 10 ppm Li, 650 ppm B):
a) SEM image showing oxide stratification,
b) TEM image showing columnar zirconia crystallites with strong cohesion between them.

1. The test loops CORAIL and REGGAE allow to reproduce all the operating conditions of reactors, excluding irradiation, on the laboratory scale. Particularly, it is possible to control heat flow by inserting electrically heated elements into the clads.
2. The two main Zr alloys investigated by the CEA in relation to corrosion are Zircaloy-4 (Zr - 1.2-1.7 % Sn - 0.18-0.24 % Fe - 0.07-0.13 % Cr), and Alloy M5TM (Zr – 1 % Nb). The latter, developed by Framatome, is to replace current Zircaloy-4, as its performance is increased comparing with Zircaloy-4, especially in terms of corrosion resistance.

cracking [2, 3]. Given these facts, the scenario currently investigated to account for this oxide layer destabilization during the transition, is a mechanical type scenario. It is based upon an increase of stresses within the oxide, and / or a buildup of mechanical energy due to zirconia growth. A physico-chemical type hypothesis has also been considered, that implies the conversion of quadratic zirconia at the benefit of monoclinic zirconia.

New cycle: as the transition in the kinetic curve is correlated with a loss in the oxide protective character, the oxidizing species can then access nearly directly to the metal-oxide interface: a new oxidation cycle can start then.

Influence of metallurgical factors

Among the various metallurgical factors that affect oxidation kinetics in Zr4-type zirconium alloys, the precipitates Zr(Fe, $Cr)_2$ and tin play a key role in the uniform corrosion of Zr alloys (this role may be beneficial to the precipitates, and prejudicial to tin under standard PWR oxidation conditions).

Their incorporation into the oxide layer was investigated through transmission electron microscopy and Mössbauer spectroscopy. It was thus emphasized that the precipitates Zr(Fe, $Cr)_2$ underwent delayed oxidation in the oxide layer, the latter being accompanied with Fe progressive passing back into solution in zirconia (Fig. 5a). As for tin in zirconia, it exhibits various chemical forms, such as Sn^0, Sn^{2+}, Sn^{4+}, mostly under the form of nanoparticles of β-Sn, SnO_2 and $Sn(OH)_2$ (Fig. 5b) [4].

These findings have made it possible to put forward several hypotheses to explain the role of these elements: modified electrical and mechanical properties of zirconia, modified oxide crystallites (size, crystallographic nature), or even anodic protection of the matrix (shift of the corrosion potential from the matrix to the passivity area).

Following tests performed in an autoclave for coupling pure Zr samples and an alloy mimicking the precipitates Zr(Fe, $Cr)_2$, the third hypothesis was favored to account for the beneficial impact of the precipitates Zr(Fe, $Cr)_2$ on the corrosion of Zr4-type zirconium alloys. For the high oxidation rate characterizing pure Zr significantly decreases after Zr coupling with an alloy that mimicks the precipitates Zr(Fe, $Cr)_2$ (Fig. 6).

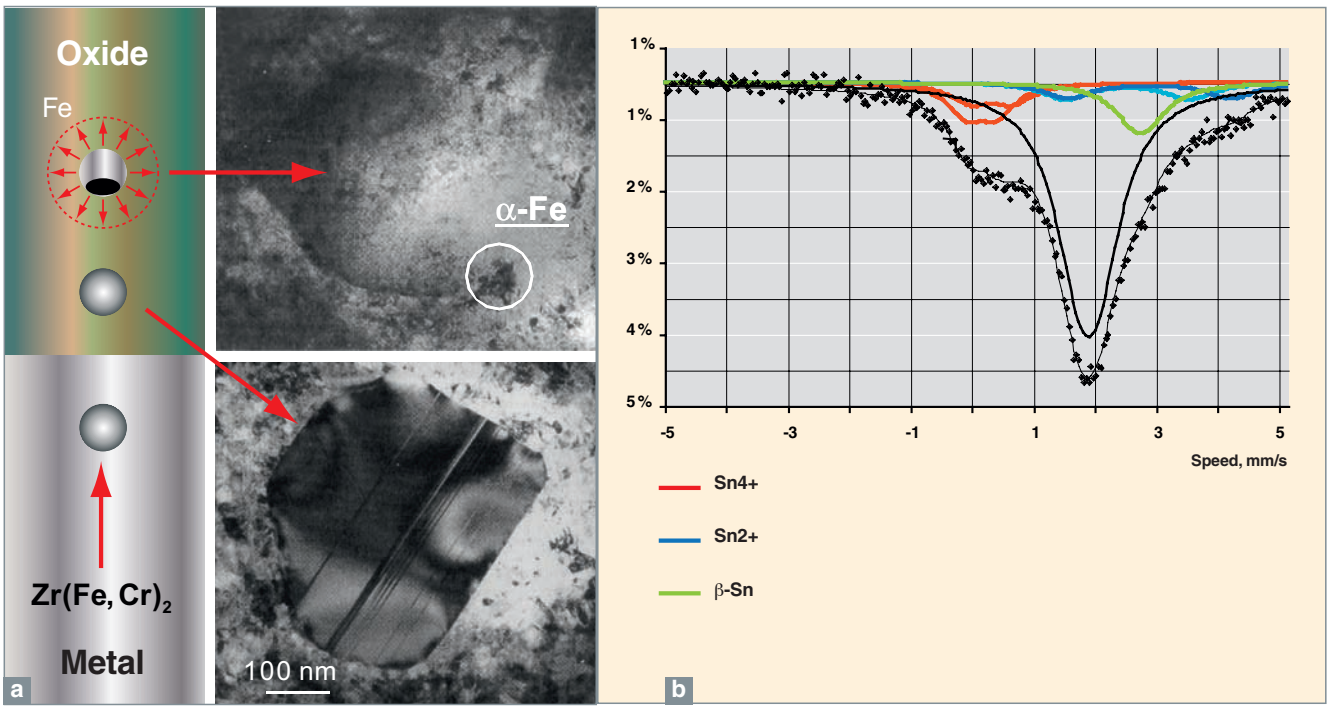

Fig. 5. Precipitates of Zr(Fe, $Cr)_2$ (a) and tin (b) in an oxide layer which has been formed on a Zircaloy-4 type alloy in an autoclave (the scans have been respectively achieved through **TEM*** and Mössbauer spectroscopy in transmission mode at 77 K).

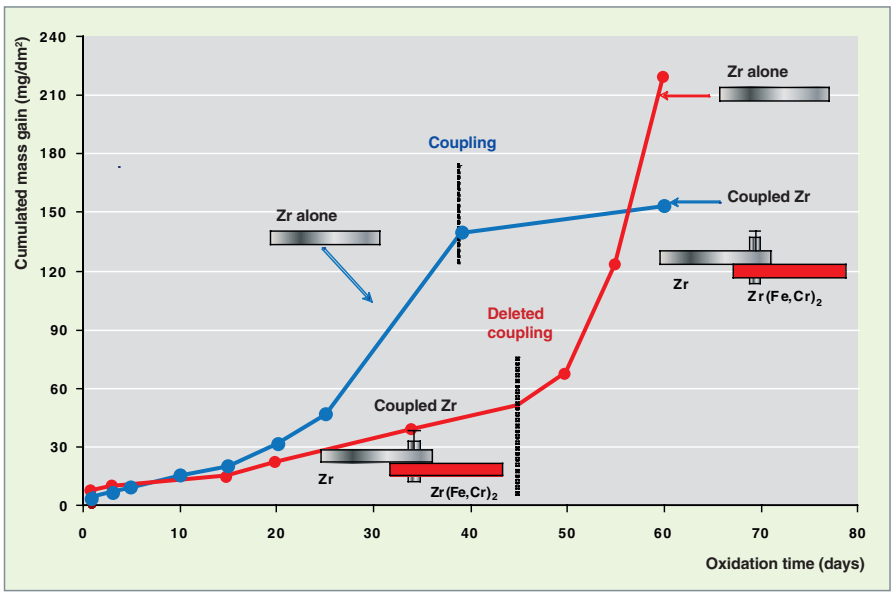

Fig. 6. Oxidation tests performed in an autoclave (360 °C, with a PWR-type chemical composition of water) on Zr specimens alone or coupled with an alloy simulating the precipitates $Zr(Fe, Cr)_2$. In the absence of coupling, the oxidation rate of pure Zr is high. In the opposite case, if pure Zr is coupled with the alloy representative of the precipitates $Zr(Fe, Cr)_2$, its oxidation rate significantly decreases.

Under chemical conditions very close to those observed in PWRs (boron presence, Li ≤ 10 ppm), any slight rise of the Li content beyond the current value of 2.2 ppm, typically up to 10 ppm, does not display a significant effect on corrosion.

In contrast, under chemical conditions very far from those encountered in PWRs (Li = 70 ppm, B = 0 – i.e. under very basic conditions), a strongly accelerated corrosion phase can rapidly take place.

Influence of the chemical environment

Increasing nuclear power plant competitiveness requires the following items:

- Extending operating cycles from 12 to 18 months, which implies increasing boron and lithium contents in primary water (for reasons related respectively to neutronics and primary coolant system contamination);

- Increasing the coolant temperature as well as heat flows (so as to improve energy yield in reactors), which may possibly entail nucleate boiling on clad surface in the hotter channels;

In these evolutions under consideration fuel faces more stringent conditions with respect to corrosion. So, in order to assess Zr alloy robustness in such new conditions, oxidation tests have been performed in autoclaves and loops under thermal-hydraulic and chemical conditions selected as envelope conditions of those currently imposed on PWRs.

Impact of water chemistry

As shown in autoclave tests, Zr alloy oxidation kinetics depends upon the solution composition (that is, whether boron is present or not), the lithium content, the thermal-hydraulic conditions and the oxidation time (Fig. 7).

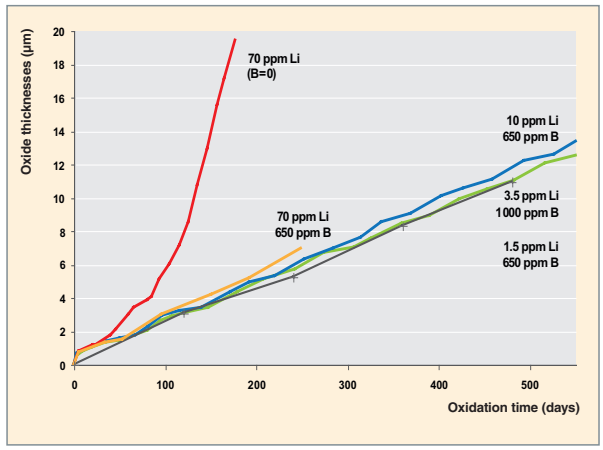

Fig. 7: Impact of water chemistry on the Zircaloy-4 oxidation kinetics (tests performed in an autoclave at 360 °C). High increase in the oxidation kinetics can be observed only in the case of the highest chemical stresses (Li = 70 ppm, B = 0).

As evidenced by the (**TEM***, SIMS, Raman, impedance spectroscopy) observations associated with these tests, the increase of corrosion rates is due to progressive degradation in the protective film which controls oxidation kinetics [2, 5]. Concretely, the oxide film is dense prior to the oxidation kinetics acceleration. It consists of mainly columnar quadratic and monoclinic zirconia crystallites (Fig. 8a). During oxidation kinetics acceleration, the thickness of the protective film slightly decreases until it nearly vanishes (Fig. 8b). The oxide layer that is formed at the metal-oxide interface, exhibits a strong intergranular porosity. It then consists of thin, mainly monoclinic equiaxed zirconia crystallites (Fig. 8c).

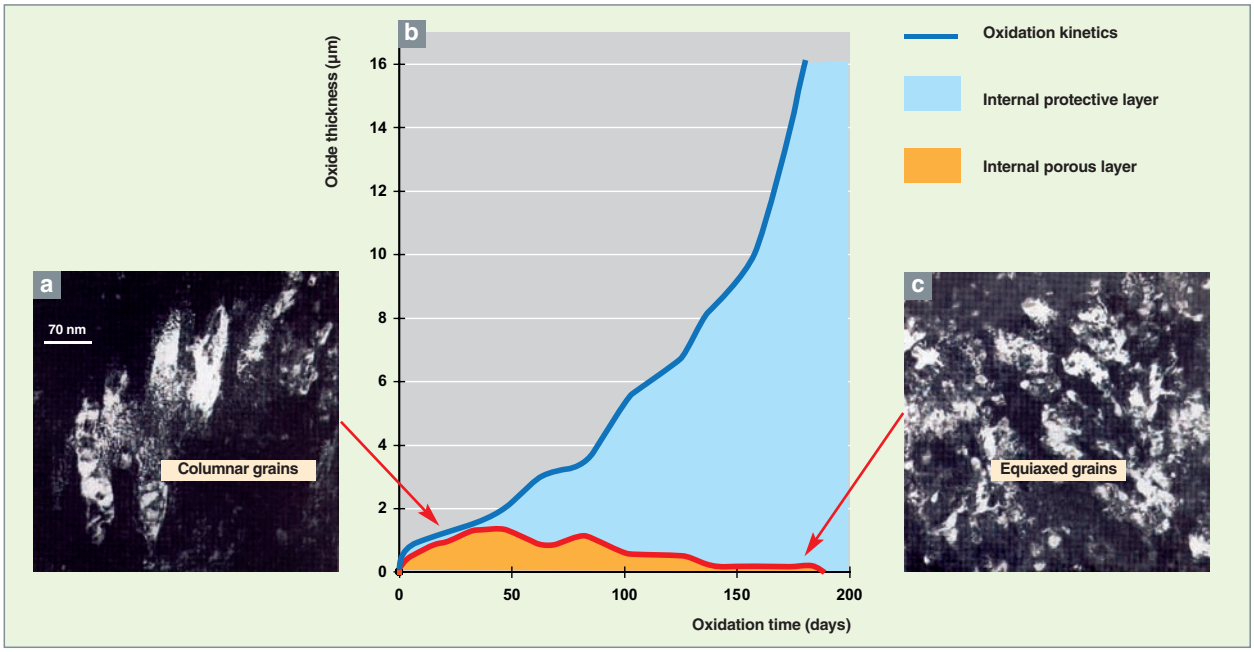

Fig. 8. Evolution of the microstructure in the oxide layer formed on Zircaloy-4 after autoclave oxidation with 70 ppm Li, and without boron (360 °C). Prior to corrosion acceleration, zirconia crystallites are columnar (a), and the protective oxide layer is thick (b). During acceleration, the protective layer thickness decreases (b), and the zirconia crystallites are equiaxed (c).

Boron effect on oxidation kinetics counterbalances the harmful effect of high lithium contents. For example, with 70 lihium ppm the oxidation kinetics obtained in presence of boron is not strongly accelerated, contrasting with that obtained without boron (Fig. 7).

Temperature impact

Temperature rise in the water of the primary coolant system strongly accelerates oxidation kinetics (Fig. 9). The activation energy of the oxidation reaction is then close to 137 kJ/Mol: the oxidation rate is nearly twofold as a result of a temperature rise of 20 °C.

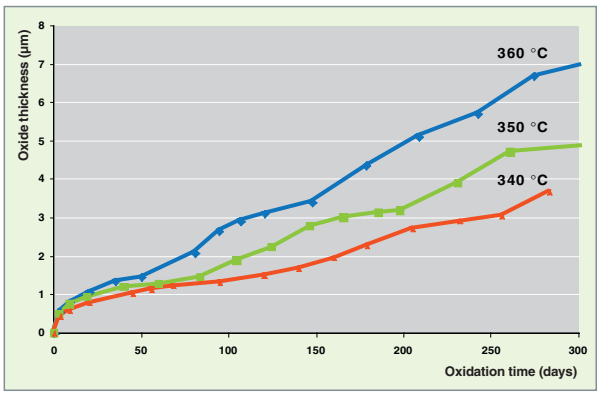

Fig. 9. Temperature effect on Zircaloy-4 oxidation kinetics. Results issued from oxidation tests carried out in an autoclave, in a chemical environment simulating that to be found in PWRs.

Influence of the heat flow

Oxidation kinetics depends upon the temperature of the metal-oxide interface T_i. In presence of a heat flow, T_i is equal to the wall temperature (water-zirconium oxide temperature), with the addition of the temperature increment resulting from the growth of the zirconia layer, the latter acting as a thermal barrier (Fig. 10).

So, as the oxide thickness increases, the heat flow accelerates the oxidation kinetics by increasing the temperature of the metal / oxide interface. In PWRs, due to high heat flows (50-60 W/cm^2, or even beyond occasionally), the temperature rise through the oxide layer is high. For example, taking the case of a heat flow of 55 W/cm^2 and for a thermal conductivity of the oxide layer equal to 0.022 W.cm^{-1}.K^{-1} (case of

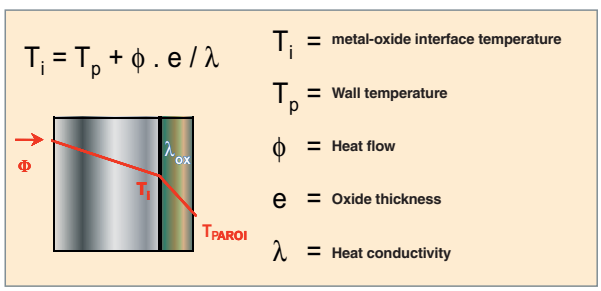

Fig. 10. Zirconium oxide acting as a thermal barrier.

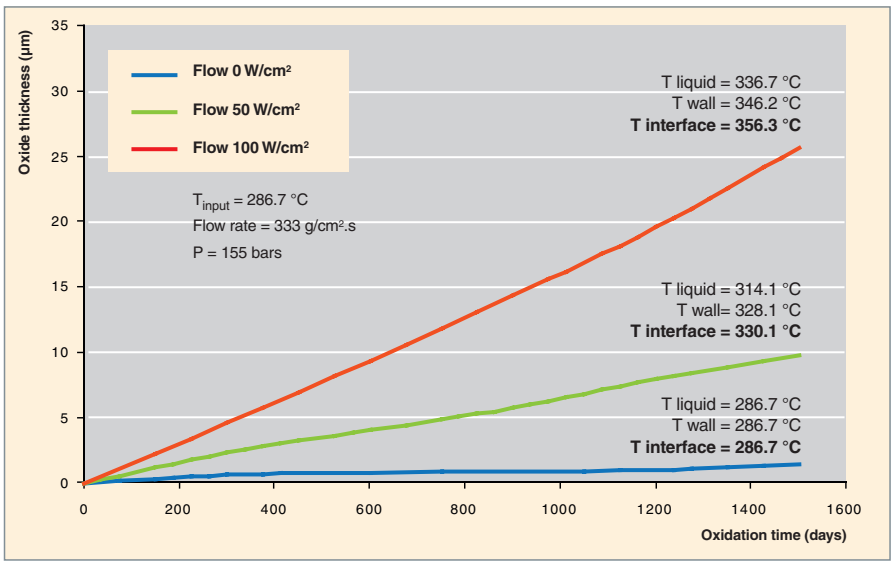

Fig. 11. Heat flow impact on Zircaloy-4 oxidation kinetics. Results issued from calculations carried out with the CEA's corrosion code CORCY for different heat flow values (oxide heat conductivity is equal to 0.022 W/cm.K).

Zircaloy-4), the interface temperature rises by 1 °C when the oxide layer grows by 4 µm.

The heat flow impact is not limited to the temperature increment related to the zirconium oxide growth. It also alters the clad surface temperature (wall temperature) through the fluid-wall exchange coefficient ($\phi = h.(T_p - T_{fluid})$, where h is the heat transfer coefficient). Yet it is worth noting that when the wall reaches the saturation temperature (344.5 °C under PWR pressure conditions, at 155 bars), a heat flow increase only results in a very slight temperature rise, but may lead to a wall boiling phenomenon. Heat flow impact on oxidation kinetics, including the increase in wall and metal/oxide interface temperatures, is shown on Figure 11.

Apart from this strictly thermal effect, heat flow induces in the oxide layer a temperature gradient which may be high (5000 K/cm at 100 W/cm²), and may have an impact on corrosion. Through the Soret effect, it constitutes an additional transport force liable to accelerate diffusion and, so, oxidation kinetics (assuming that diffusion is the limiting step in the oxidation process).

This additional effect of heat flow can be assessed through comparing the oxide thicknesses obtained in **test loops***, with or without heat flow, at the same interface temperature. The oxidation test performed in the loop REGGAE in presence of a 100-110 W/cm² heat flow (with lithium concentrations of 3.5-10 ppm and boron concentrations of 650-1000 ppm in the primary water) revealed that Zircaloy-4 oxidation rate was increased from +15 to +30% under heat flow. Now, under the REGGAE test conditions, occurring heat flow was related to the presence of nucleate boiling on the clad wall. Therefore, it is uncertain whether the observed acceleration is strictly due to the heat flow: boiling may possibly contribute to such an acceleration. Investigations are being carried out in the CORAIL loop in order to discriminate the respective effects of flow and boiling upon corrosion.

Boiling effect

Occurring boiling on the clad wall results in a local alteration of water chemistry. As a matter of fact, in a two-phase system (that is, during boiling) subjected to a heat flow, the liquid phase can be enriched in lithium (a low-volatility species) at the liquid/vapor interface, as is shown on Figure 12.

Under thermal-hydraulic conditions very close to those encountered in PWRs, i.e. with a relative bubble volume in the coolant (the void fraction) lower than 5%, the enrichment factor is close to 3. This entails alterations in water chemistry on the clad wall. However, in water with a typical PWR chemical composition, this change is not sufficient to strongly accelerate the oxidation kinetics of zirconium alloys (with boron still present and a lithium content on the wall still lower than 10 ppm), as is illustrated on Figure 13 (void fraction < 25%).

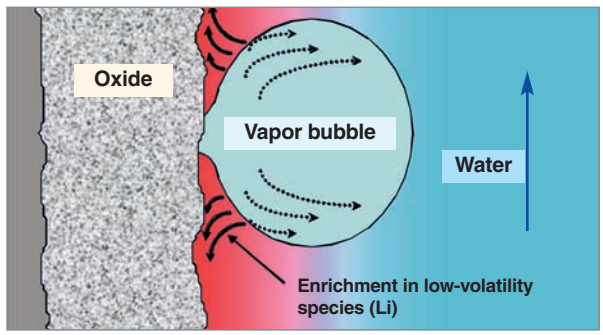

Fig. 12. Schematic representation of enrichment ("sequestration") in low-volatility species (e.g. Li) on the clad wall, a phenomenon that follows boiling.

In contrast, in the case of a very high void fraction (> 25-30%), not found in current PWRs, the conditions on the wall are very different from those existing for lower void fractions (vapor on the wall, an enrichment factor far higher than 3, a possible precipitation on the clad surface of corrosion products arising from the primary coolant system…). As observed in loops, the effect of such conditions is a very sharp acceleration of oxidation

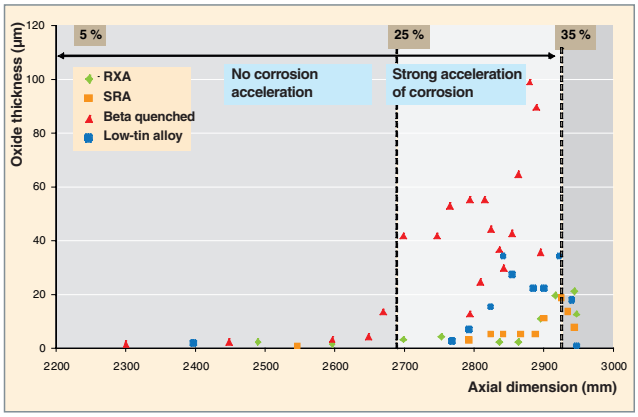

Fig. 13. Axial profile of oxide thicknesses measured along different Zircaloy-4 clads (RXA – recrystallized, SRA – stress-relieved, β– quenched, low-tin alloyed), cyclically oxidized in a chemical environment simulating that to be found in PWRs (Li = 2.2 ppm, B = 1000 ppm). Overoxidation could be pinpointed (only) for void fractions higher than 25%.

kinetics, even in the case of water with a PWR type chemical composition (Fig. 13, 25% < void fraction < 35%).

Inpile alloy behavior (irradiation effect)

As shown on this figure, for higher burnups, the thickness of the oxide films formed on Zircaloy-4 is far higher than that measured on M5™. As a matter of fact, for a burnup higher than 55 GWd/tU, it may reach 100 µm for Zircaloy-4 while it does not exceed 25 µm for M5™.

An analysis of the PWR oxidation kinetics, comparing it with the data collected in an autoclave (out of pile), shows that the reactor environment, especially irradiation, strongly accelerates Zr alloy oxidation kinetics.

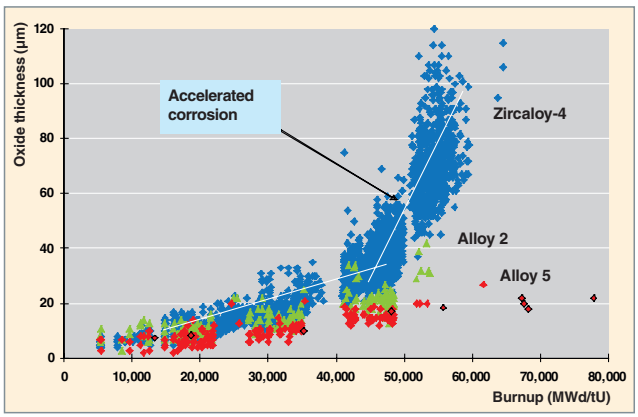

Fig. 14. Onsite and hot-laboratory eddy-current measurements of oxide thicknesses on fuel rod clads of Zircaloy-4 (1.3 % Sn), M5™ (Alloy 5) and Alloy 2 (0.5 % Sn) arising from pressurized water reactors. (Data from Areva-NP and CEA).

In the case of Zircaloy-4, the corrosion acceleration factor K^{REP}, defined as the ratio between the inpile and out-of-pile oxidation rates (at the same temperature) is close to 2 during the first two cycles of irradiation (Fig. 15). Beyond this step, the acceleration factor increases, and may reach values neighbouring 5 after 5 or 6 irradiation cycles. For example, concerning Zircaloy-4, the prejudicial effect of the PWR environment on oxidation kinetics is strongly enhanced after 2 to 3 irradiation cycles, which means an additional phase of accelerated corrosion is initiated, to be seen on Figure 14. This accelerated corrosion limits the Zircaloy-4 performance in PWRs with high burnups, whereas Alloy M5™ is not affected by this drawback.

Analyzing the microstructure of irradiated materials made it possible to put forward several hypotheses to interprete increased corrosion rates observed in reactors, as well as the dissolution under irradiation of the precipitates $Zr(Fe, Cr)_2$ initially present in Zircaloy-4, hydride buildup at the metal-oxide interface, or again the modified Sn distribution [6].

These different hypotheses were tested with separate-effect oxidation tests performed in laboratory (oxidation of prehydrided specimens, re-oxidation in a shielded autoclave of specimens irradiated in PWRs with different precipitate dissolution levels…).

Obviously, precipitate dissolution under irradiation and, mostly, the high amount of occurring hydrides accelerate Zircaloy-4 oxidation kinetics. However, the major metallurgical parameter which affects the initiation of corrosion acceleration, is tin. Concretely, the lower the tin content, the further the accelerated corrosion phase is delayed (Fig. 14, difference in behavior of Zircaloy 4 and Alloy 2).

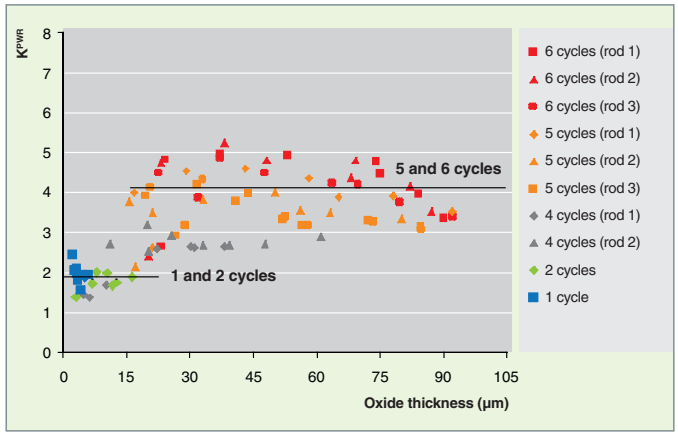

Fig. 15. Corrosion acceleration factors in a PWR as compared with the autoclave (K^{REP}) calculated for Zircaloy-4 with the CORCY Corrosion Code. The high increase in this factor beyond 2 cycles emphasizes the occurrence of a further corrosion acceleration at high burnups.

Uniform corrosion simulation

Corrosion kinetics can be calculated using the two codes COCHISE and CORCY developed at the CEA. In these two corrosion codes, the oxide growth, which is a thermally-activated phenomenon, is described with semi-empirical Arrhenius-type laws.

COCHISE is the first corrosion code developed for zirconium alloys [7]. In this code, overall oxidation kinetics is shown as a succession of two kinetic laws: pseudo-parabolic pre-transient kinetics, assumed to represent the initial growth phase of the oxide layer, and post-transient kinetics, which stands for further evolution, assuming its thickness to grow linearly with time. The whole set allows the evolutions observed to be modelled as on Figure 16.

These two oxidation kinetics are expressed in the code by the following semi-empirical relationships:

- Pre-transient phase:

$$dS^n / dt = K_{Pre} \exp(-Q_{Pre} / T_i)$$

- Post-transient phase:

$$dS / dt = K_{Post} \exp(-Q_{Post} / T_i)$$

where:
- S is the zirconia thickness formed,
- t is time,
- n is the order of the cycle kinetics, determined empirically,
- K_{Pre} is the kinetic constant in a pre-transient phase, empirically determined,
- Q_{Pre} is the activation energy in a pre-transient phase, empirically determined,
- K_{Post} is the kinetic constant in a post-transient phase, empirically determined,
- Q_{Post} is the activation energy in a post-transient phase, empirically determined,
- T_i is the temperature at the metal-oxide interface.

Semi-empirical correlations have been established from the numerous experimental results issued from the inpile operation feedback and the autoclave and loop tests. They express the oxidation constants (activation energies, kinetic constants, transition thickness) as a function of the main parameters acting upon corrosion (temperature, heat flow, water chemistry, irradiation, material nature, hydride precipitation).

The COCHISE code is a qualified industrial code, which is integrated in the METEOR (CEA) and CYRANO (EDF) computer codes for modelling PWR fuel rod thermomechanical behavior.

CORCY is a new modelling approach initiated by the CEA and EDF, the aim of which is to provide a more phenomenological, "physical" code.

As the oxidation process exhibits a cyclic component (see the paragraph dealing with oxidation kinetics), the CORCY approach (CORCY standing for *CORrosion CYclique*, cyclic corrosion) is based upon an oxidation scenario where oxidation kinetics is cyclic, and transitions are governed by the periodic failure of the oxide layer. Being closer to real kinetics, it thus differs from COCHISE, which assumed the post-transient phase to be described through a linear kinetics beyond the first pre-transient cycle.

Besides, this modelling approach is characterized by modularity, as it separately assesses the effects of the different parameters that influence corrosion in PWRs (irradiation, heat flow, clad hydrogen uptake…).

Oxidation kinetics are expressed in the code by a periodic repetition of the following phenomena (Fig. 16):

- Oxide growth by diffusion described by an empirical law of the Arrhenius-type:

$$dS^n / dt = K_{CYCLE} \exp(-Q_{CYCLE} / T_i)$$

where:
- n is the order of the cyclic kinetics, empirically determined,
- K_{CYCLE} is the kinetic constant of the cycle, empirically determined,
- Q_{CYCLE} is the activation energy of the cycle, empirically determined,
- T_i is the temperature at the metal-oxide interface,

- Kinetic transition characterized by a rupture oxide thickness (e_r) empirically determined.

The "material" effect is then taken into account determining a given set of parameters for the cycle (n, Q_{cycle}, K_{cycle}, rupture thickness), referring to the oxidation tests performed in the CEA's autoclaves.

The PWR environment effects are represented by a given in-reactor corrosion acceleration factor, comparing the in-PWR and in-autoclave oxidation rates for a same temperature. The first CORCHY Version V1 has been available since late 2005. Its validity range is larger than that of COCHISE since it includes, in particular, the monitoring program results collected in hot laboratories on M5™ clads irradiated during 6 and 7 cycles (~ 80 GWd/tU) and on Zircaloy-4 clads with a MOX fuel. An example of calculation obtained with the codes COCHISE and CORCY is shown on Figure 17.

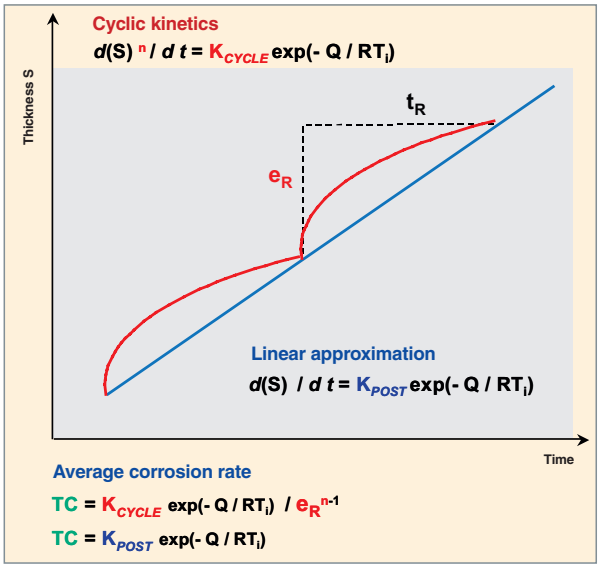

Fig. 16. Comparison of thickness evolutions according to the model used: the cyclic model, in the CORCY Code, or the linear model, in the COCHISE Code.

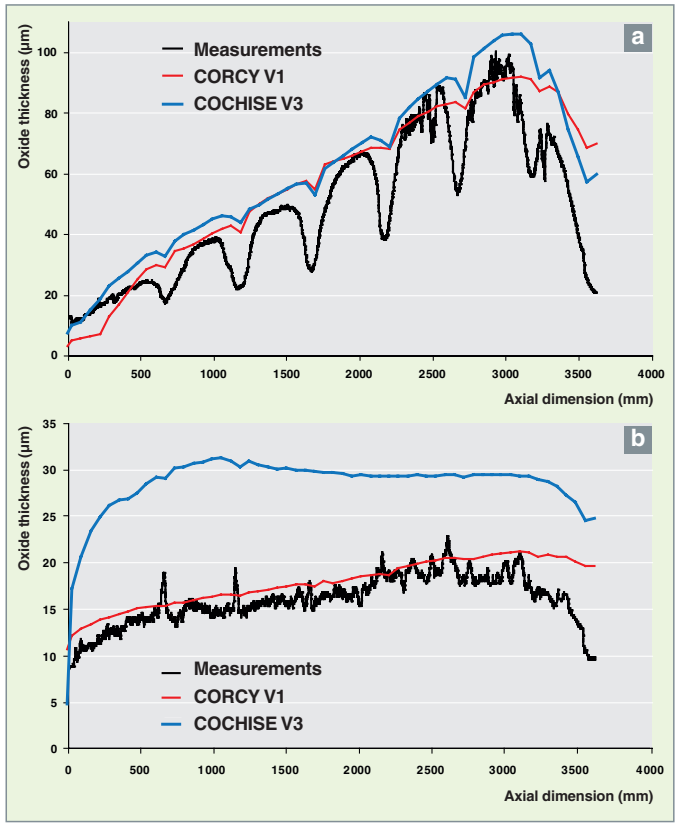

Fig. 17. Comparison of the hot-laboratory eddy-currents measurements of oxide thicknesses with the simulations performed with the CORCY V1 and COCHISE V3 Codes: (a) Zircaloy-4 clad rod exposed to 6 irradiation cycles in the Cruas-2 reactor, (b) M5™-clad rod exposed to 6 irradiation cycles in the Gravelines-5 reactor. The difference in oxide thickness between the two alloys is obvious. In both cases, the oxidized thickness is higher in the upper than in the lower part of the rod, for, similarly, water temperature is higher at the top than at the bottom.

The following step in the CORCY development process consisted in expressing the in-reactor corrosion acceleration factor as a combination of the effects of temperature, heat flow, neutron flux, and hydride precipitation in the clad. The effects of each of these parameters on corrosion were assessed through separate-effect tests carried out in laboratory, especially in CEA's corrosion loops and autoclaves (in order to quantify the effects of heat flow, temperature and hydride precipitation), and in experimental reactors, the CEA's OSIRIS reactor and the Halden reactor in Norvegia (in order to quantify the neutron flux effect).

These effects thereby determined separately were coupled in CORCY Version 2 [8]. Without any interpolation with the PWR data, CORCY V2 allows the whole of the corrosion data issued from PWR irradiated rod hot-cell characterization (Fig. 18) to be reproduced quite satisfactorily. The CORCY V2 Code is also an industrial code integrated in the ALCYONE (CEA) and CYRANO (EDF) Computer Codes for modelling fuel rod thermo-mechanical behavior.

CORCY Version 2 stands as an intermediate step paving the way for future versions likely to make CORCY more mechanistic and, so, more predictive, with the help of basic studies especially aimed at understanding the origin of oxide film failure, and identifying the oxidation process limiting steps.

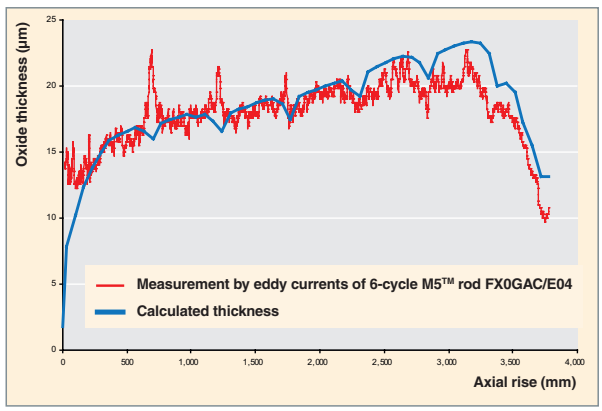

Fig. 18. Comparison of the model CORCY V2 with the thicknesses measured for Alloy M5™ on a rod exposed to 6 in-pile irradiation cycles.

In situ measurements of general corrosion rate through electrochemical techniques

The out-of-pile monitoring of corrosion in zirconium alloys under PWR-representative conditions is generally achieved through discontinuous techniques such as mass-gain measurement, or oxide film thickness measurement through Scanning Electron Microscope (SEM) images. For temperature and pressure conditions in pressurized water reactors (320 °C and 155 bars) make it impossible to perform *in situ* monitoring of oxidation in these alloys through **thermogravimetry*** under PWR-representative conditions, though this technique is still used to investigate such phenomena at low pressures. Therefore, in order to follow up *in situ* the electrochemical properties of the oxide layers formed on the clad surface using impedance spectroscopy, instrumented autoclaves have been made for a few years in many research organisms and, especially, at the CEA. It must be kept in mind, however, that this technique describes the electrochemical system in its whole through a complex impedance, indeed. The difficulty for interpreting the resulting spectra mainly lies in assigning a given feature observed on spectra to a specific physico-chemical process which takes place within the reactional system under investigation. Yet, despite these operating difficulties, it is still possible to know how the thickness of the oxide film formed on these alloys evolves as a function of time, with a measurement uncertainty of about 20% [9].

In a liquid environment, the corrosion of an alloy at rest potential (that is, the potential taken by a metal when put in a given solution) occurs under null current conditions, with the anodic current (oxidation current) being then equal to the opposite of cathodic current (reduction current). Consequently, the current (and so the corrosion rate at free potential) cannot be directly accessed through experiment. Observing a measurable current requires to polarize the specimen in such a way as to reduce and, even, annihilate the reduction current, thereby accessing to the anodic current under such polarization conditions. However, the latter is not equivalent to that obtained at rest potential.

This general approach has been undertaken on alloy Zircaloy-4. Figure 19 shows the evolution in the thickness of the oxide film formed on Zircaloy-4 at rest potential, as determined from impedance spectra (SI), comparing it with the findings obtained under the same conditions with the CORCY code. The results based on this method are globally in accordance with computer code calculations and, generally speaking, with data from literature.

As regards Figure 20, it displays variations of the anodic current on a specimen polarized at 270 mV above the free corrosion potential. This curve shows the relatively low influence of the potential on Zircaloy-4 oxidation rate under PWR primary conditions. In addition, it enables the kinetic transition to be observed *in situ* and in real time, a first-time observation at the CEA. These results validate the approach adopted, and pave the way for new outlooks for understanding corrosion mechanisms in zirconium-based alloys.

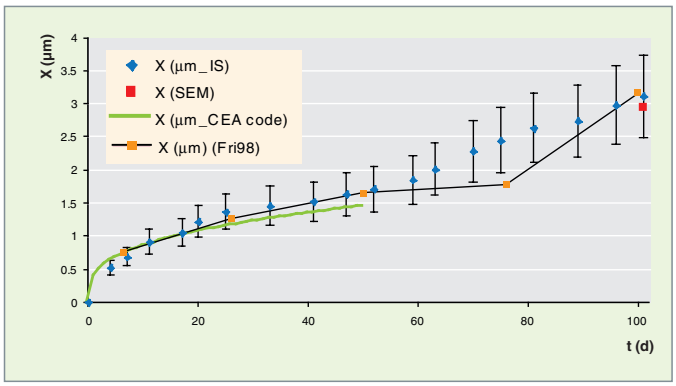

Fig. 19. Variations between the oxide thickness experimentally determined through impedance spectroscopy (IS) for the unpolarized specimen (full blue triangles) and the thickness measured basing upon SEM images (square dots). Comparison with the kinetic curve calculated under these conditions from the CEA's CORCY Code and that proposed by A. Frichet et al. (black continuous curve and orange dots [10]).

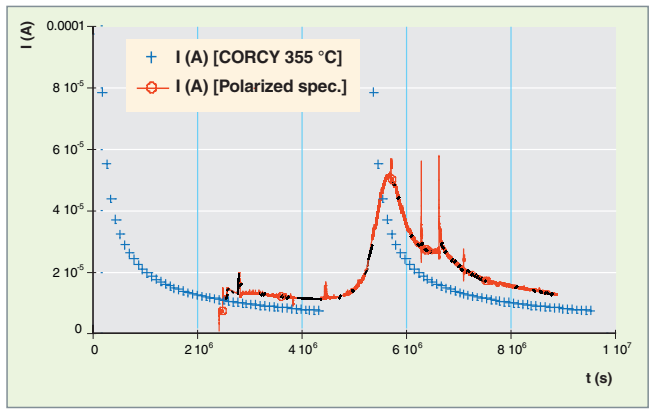

Fig. 20. Evolution of the anodic current for a zirconium alloy polarized at +270 mV, and comparison with the current curve deduced from the corrosion kinetics modelled with the CORCY Code: the transition in the kinetic curve (peak at 6 10^6 s) is made evident *in situ* and in real-time.

Uniform corrosion of nickel alloys: characterization of the passive layer and growth mechanisms

Passivable alloys, such as stainless steels and nickel alloys, are widely used in the PWR primary coolant system owing to their high uniform corrosion resistance. This behavior is related to the formation of an oxide layer, the so-called passive film, which consists in a continuous, protective film. Under PWR-type primary conditions, the phenomenon depends on both the alloy's nature and metallurgy and the environmental physico-chemistry. This dependence has an impact on both corrosion kinetics, with respect to oxidation and release, and the oxide film nature (composition and morphology).

The relevant parameters often fall into three main categories:

- The first deals with the characteristics of the materials under investigation: **alloy*** composition, surface roughness, surface grain size, cold working rate;
- The second deals with the environment's chemical characteristics: pH, H_2 partial pressure, dissolved O_2 content, metallic cation content, boron content, lithium content;
- The third is related to the environment's thermal-hydraulic features: chiefly, temperature and flow rate.

Improved understanding of corrosion processes requires, on the one hand, better knowledge of the structure of the oxide film formed in the primary environment, and, on the other hand, better comprehension of the mechanisms involved in layer growth.

Oxide films can be characterized through analyses which allow films from a few nanometers to a few dozen nanometers to be investigated. This purpose led to implementing a whole set of analyzing methods, such as Scanning Electron Microscopy (SEM), X Photoelectron Spectrometry (XPS), PhotoElectroChemistry (PEC), and MicroPhotoElectroChemistry (MPEC).

As displayed on Figure 21, on a TEM observation of an oxide film formed on an Alloy 690 under PWR primary conditions, the oxide layer includes two sublayers. The internal layer is a continuous layer which primarily consists of chromium-rich spinel (mixed chromite $Ni_{(1-x)}FexCr_2O_4$). Moreover, chromine (Cr_2O_3) nodules also occur at the alloy-spinel interface. According to the results obtained through microphotoelectrochemistry, these nodules are uniformously distributed within the oxide layer. In addition, TEM examinations achieved on specimens displaying surface defects evidence a higher amount of nodules. This proves that nucleation in this phase is to be related to the occurring surface defects [11].

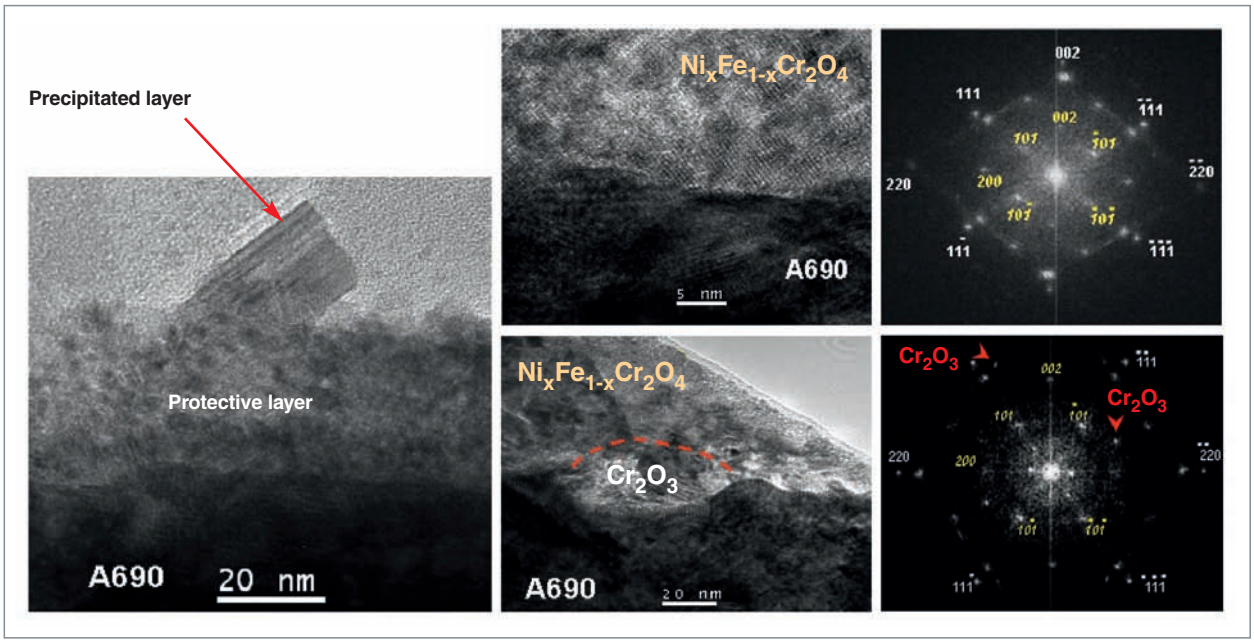

Fig. 21. TEM, high-resolution TEM and local-scattering observations of the oxide layer formed on an Alloy 690 corroded for 858 hours in a PWR primary environment (325 °C, 1000 ppm boron as H_3BO_3 with 2 ppm lithium as LiOH, i.e. a pH of 7.2 at 325 °C, and a dissolved hydrogen concentration of about 1.7×10-3 mol.L^{-1}). Observations carried out par Mr Sennour (ENSMP).

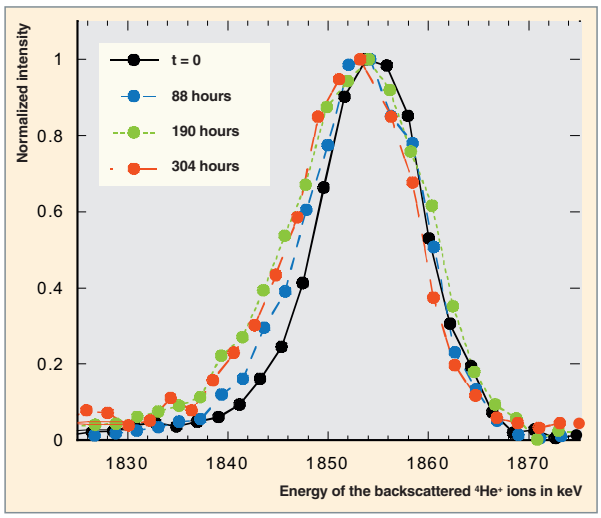

Fig. 22. Evolution of the energy of $^4He^+$ particles backscattered by gold atoms, measured by Rutherford backscattering depending on the corrosion time.

The discontinuous outer layer consists of precipitates which contain big crystallites of iron-rich spinel ($Ni_{(1-z)}Fe_{(2+z)}O_4$) on the one hand, and hydroxides (particularly, $Ni(OH)_2$) on the other hand. As shown by surface SEM observations, the quantity of precipitated spinel depends from both the alloy surface defects (playing the role of preferential nucleation sites for emerging precipitates), and the crystalline orientation of the metallic substrate grains. It is worth noting that, contrary to the internal layer, this layer does not look like a "barrier" against corrosion [12].

Last but not least, the alloy underlying the oxide layer may display a chromium-depleted area.

Thus, the passive film of nickel alloys corroded in a primary environment coincides with the chromium-rich internal layer. In order to improve knowledge of the layer growth, marker and tracer experiments have been implemented.

As a first step, gold markers have been deposited on the surface of Alloy-690 specimens. Then, the latter have been corroded in a PWR primary environment. Finally, the marker has been pinpointed in the oxide layer using **RBS*** spectroscopy (RBS standing for Rutherford Back Scattering). These experiments make it possible to determine whether the oxide lattice is built at the internal interface (internal / anionic growth), or at the outer interface (external / cationic growth).

The energy of the $^4He^+$ particles backscattered by gold, which has been measured through RBS and is represented on Figure 22, makes evident an anionic mechanism of oxidation: the maximum of the gold peak does not change, which implies that gold remains located at the ultimate outer surface, i.e. an internal growth mechanism. Referring to this result related to the internal layer's anionic growth, as well as to the photoelectrochemical investigations that revealed an n-type semiconduction for the internal layer oxides, it could be concluded that the defect diffusing through the layer was a substitutional defect in the anionic sublattice. Thus, it might be either an oxygen vacancy, or a hydroxyl group substituting for oxygen.

Experiments of corrosion sequences were also performed with an isotopic tracer ^{18}O. First, specimens were corroded in a "conventional" PWR aqueous environment $H_2{}^{16}O$, then in a primary coolant environment enriched with $H_2{}^{18}O$ (mixture 20% $H_2{}^{18}O$ – 80% $H_2{}^{16}O$). The oxide layer so formed during these two corrosion sequences was then analyzed through Secondary Ion Mass Spectrometry (SIMS). The ^{18}O buildup at the alloy-oxide interface (Fig. 23) shows that the oxide layer growth primarily takes place at the metal/oxide interface. This growth mostly originates in an anionic mechanism through short-circuit diffusion paths (grain boundaries).

As a conclusion, the growth mechanism of the spinel continuous layer results from an anionic diffusion at the oxide grain boundaries [13]. These experiments enabled a boundary grain diffusion coefficient of an approximate 1.10^{-17} $cm^2.s^{-1}$ to be determined using the Whipple and Le Claire method.

Such results related to the characterization of oxide nanometric layers and their growth mechanisms provide essential data likely to be used for mechanistic modelling of nickel alloy corrosion processes. They pave the way for describing a reactional mechanism for passive layer formation, as schematized on Figure 24, expressing the considered mechanisms as equations, and thus modelling the passive behavior of nickel alloys in PWR environment.

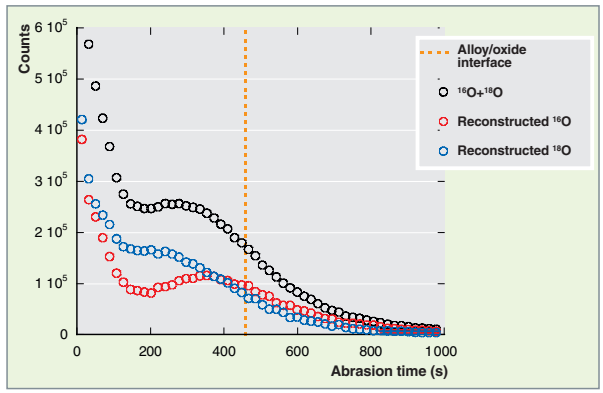

Fig. 23. Reconstructed SIMS Profiles of ^{16}O, ^{18}O and total oxygen measured on an Alloy 690 corroded for 406 hours in $H_2{}^{16}O$, and for 144 hours in a $H_2{}^{16}O$-$H_2{}^{18}O$ mixture.

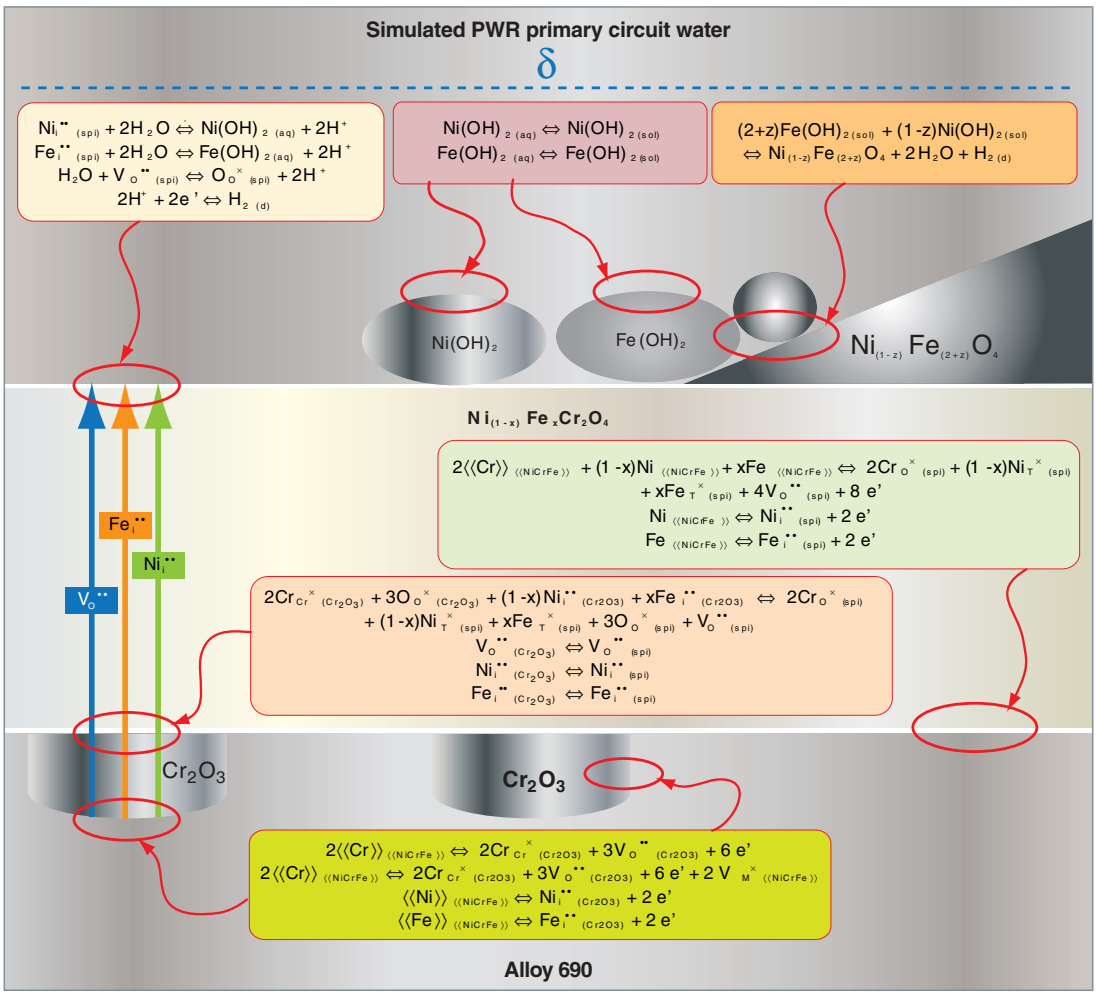

Fig. 24. Reactional schematic of nickel base alloy oxidation in a PWR primary environment.

The PACTOLE code, an integrating tool

General corrosion in the primary coolant system of Pressurized Water Reactors (PWRs) can be minimized through a suitable selection of materials constituting the various components, and using boric acid / lithine and dissolved hydrogen coordinated chemistry, which ensures operation in a basic and reducing environment during normal operation and hot shutdowns. General corrosion is low, and does not jeopardize the integrity of the various components in the primary coolant system. Yet, it results in releasing metallic ions into primary circuit water, though in low concentrations (of the order of the µg.kg^{-1}). These ions are carried through primary water (it is worth recording that primary circuit water accounts for a volume of 200-300 m^3 depending on reactors, and flows throughout the whole circuit in 20 seconds). The ions may precipitate in this water, thereby forming particles, or on the wall surface, where they form a solid deposit. The latter may itself be worn away as particles, which are likely to cling to other walls later on. These main mechanisms are illustrated on Figure 25.

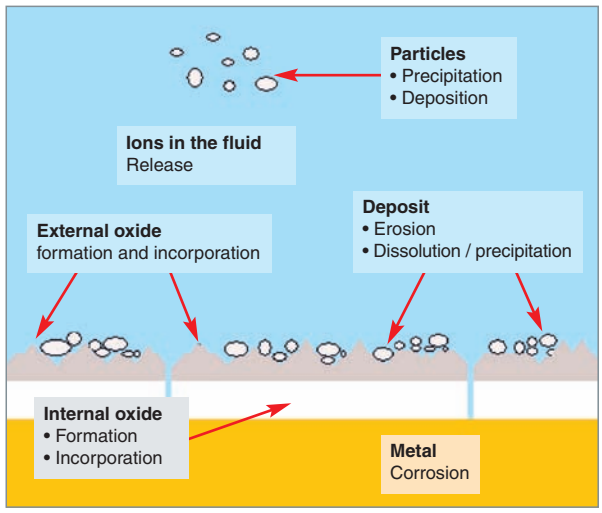

Fig. 25. The main mass transfer mechanisms which affect the various environments in a reference volume.

In the reactor core some chemical elements such as nickel may turn into radioisotopes under neutron flux, which can give birth to a fission-products radioactive contamination likely to deposit throughout the coolant circuit later on, hence the phrase *contamination transfer*. These different steps are schematized on Figure 26. Reducing this contamination stands as a key challenge for NPP operators and builders, as it is the main source (85%) of the dose received by staff during loading and unloading operations [14]. More than 80% of operational dosimetry is due to two cobalt isotopes, Co 58 and Co 60, which respectively arise from activation of nickel and cobalt (two elements resulting from corrosion of the various primary circuit components):

$^{58}Ni + n \rightarrow {}^{58}Co + p$ (^{58}Co, half-life = 71 days)
$^{59}Co + n \rightarrow {}^{60}Co + \gamma$ (^{60}Co, half-life = 5.3 years)

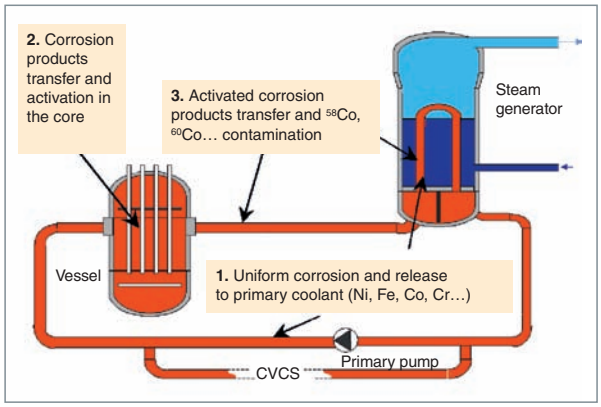

Fig. 26. Principle of contamination transfer by corrosion products activated in the PWR primary coolant circuit.

Assessing long-lived radionuclides (^{59}Ni, ^{63}Ni, ^{94}Nb …) is also of major interest for managing waste issued from NPP deconstruction.

Predicting primary coolant system activity due to corrosion products constitutes one of the CEA's goals in its effort to support industrialists. It is based upon understanding corrosion products behavior in the primary coolant circuit. Numerical simulation of the resulting contamination transfer by activated corrosion products is a true challenge, since it means taking into account numerous mechanisms which may be physical (neutronics, thermal-hydraulics, thermophoresis, erosion, turbulence, Brownian diffusion…), and chemical (speciation, precipitation, dissolution, corrosion…). In addition to the difficulties intrinsic to multi-physics modelling, the primary system of a nuclear reactor faces unusual, severe conditions (250 °C - 340 °C, 150 bars, high neutron flux, water flow rate up to 10 $m.s^{-1}$). This explains why measurements are difficult to perform and, so, rather scarce.

However, it is already 30 years since the CEA undertook to develop an R&D aimed at investigating the impact of PWR design and operational parameters on contamination transfer. This effort encompasses several topics:

- Acquisition of solubility data with the SOZIE Facility, and development of thermodynamic databases in relation to aqueous-phase ionic species at high temperatures,
- New modelling of chemical speciation in aqueous phase taking into account the various occurring solid phases,
- Experiments on test loops (e.g. CORELE or CIRENE) under PWR representative conditions,
- Reactor contamination measurements with the EMECC process (EMECC standing for *Ensemble de Mesures et d'Études de la Contamination des Circuits*: circuit contamination measuring and investigating system),
- Modelling and numerical simulation.

As a matter of fact, the PACTOLE Code has been developed since the seventies (PACTOLE standing for *Prédiction du comportement et de l'ACTivation des produits de corrosion dans le circuit primaire des réacteurs à eau (O) légère*: Prediction of corrosion products behavior and activation in LWRs primary coolant system). This code is aimed at determining surface activity deposited on the various surfaces, and water volume activity in the primary coolant system. It is worth noting that, regarding many physical mechanisms, modelling has not only benefited from past knowledge already published in literature (dealing with corrosion, hydro-dynamics, particle transport [mass transfer], activation…), but also from the experiments performed, particularly, in France (CEA, EDF…) and the United States (Westinghouse) as part of the quadripartite agreement (CEA, EDF, FRA, Westinghouse), and from the expertise gained from a large number of in-pile measurement cycles.

Since then the PACTOLE Code has been used by the CEA and its industrial partners for NPP design and operation aid. Nowadays, not only is the PACTOLE Code considered as a numerical simulation tool with a predictive approach, but also as a tool which is to federate all data useful for advances in controlling activated corrosion products contamination. In order to reach this goal, the PACTOLE Code has become an object-oriented code (since Version V3.0) using C++ as a programming language to allow physics related to specific mechanisms to be easily updated as soon as new advances in knowledge have been achieved in a given topic. The primary coolant system is modelled as reference volumes, and mass balance unstationary equations are solved for each isotope i in an environment j for a given reference volume:

$$\frac{\partial M_j^i}{\partial t} = \sum_s source - \sum_p sink + \dot{m}_{input} - \dot{m}_{output}$$

where:
M_j^i is the mass of isotope i in environment j,
$\sum_s source$ and $\sum_p sink$ respectively are the sum of mass transfers leading to an increase or decrease of isotope i mass in environment j,
$\dot{m}_{input} - \dot{m}_{output}$ is the mass variation of isotope i in environment j in relation to primary water convection.

A typical discretization of the primary coolant system is performed. The volumes are determined so as to give a relevant representation of the wetted surfaces, fluid rates, and materials composition under and out of neutron flux.

As part of the same reference volume, interactions between environments (metal, internal oxide, external oxide, deposit, ion, particle, filter and resin), which entail mass transfers (source terms and wells in the mass conservation equation), are represented on Figure 27. The modular nature of the code (object-oriented language) makes it easy to add an isotope, an environment or a new interaction between environments. So new physico-chemical models can be integrated as soon as they become available, which paves the way for a continuous improvement loop: upstream research, models development, experiments for data acquisition, experiments for model validation, simulation / system measurement confrontation (respectively in CYRENE-type test loops or in reactor). Today, quantitative modelling of general corrosion in the various materials of the primary coolant system is still a challenge to be taken, indeed. Metal corrosion ratios and release rates of ions into the primary circuit water are now decoupled, and introduced into the input data set basing upon correlations from test loop measurements. It is worth mentioning that influences of the various state surfaces can so be respectively taken into account, which may explain differences in overall activity between reactors assumed to be identical.

One example of simulation / in-pile measurement comparison is given on Figure 28. Five operation cycles of a French 1300-MWe PWR were modelled. The measured values (the rounds with the error bars) refer to refueling shutdowns. These gamma spectrometry measurements can only be carried out during reactor shutdowns, for the neutron flux under normal operation gives rise to nitrogen-16, a very short-lived radioisotope (with a half-life of 7.17-seconds), which emits a highly energetic gamma radiation. Not only does this radiation make it impossible to access to the primary coolant system, but it also forbids to carry out gamma spectrometry online measurement of contamination deposited and volume activities during reactor operation. The squares stand for the value simulated at the very moment of in-pile measurement (that is, during the shutdown). The results show good agreement between simulation and measurement.

It is worth noting that the problem is strictly the same for the coolant system of tokamak-type fusion machines. For example, regarding the ITER tokamak, the coolant system under consideration also contains water. Yet, some materials (e.g. copper) are different, and operating temperatures are lower, which requires further data input to the thermodynamic data-

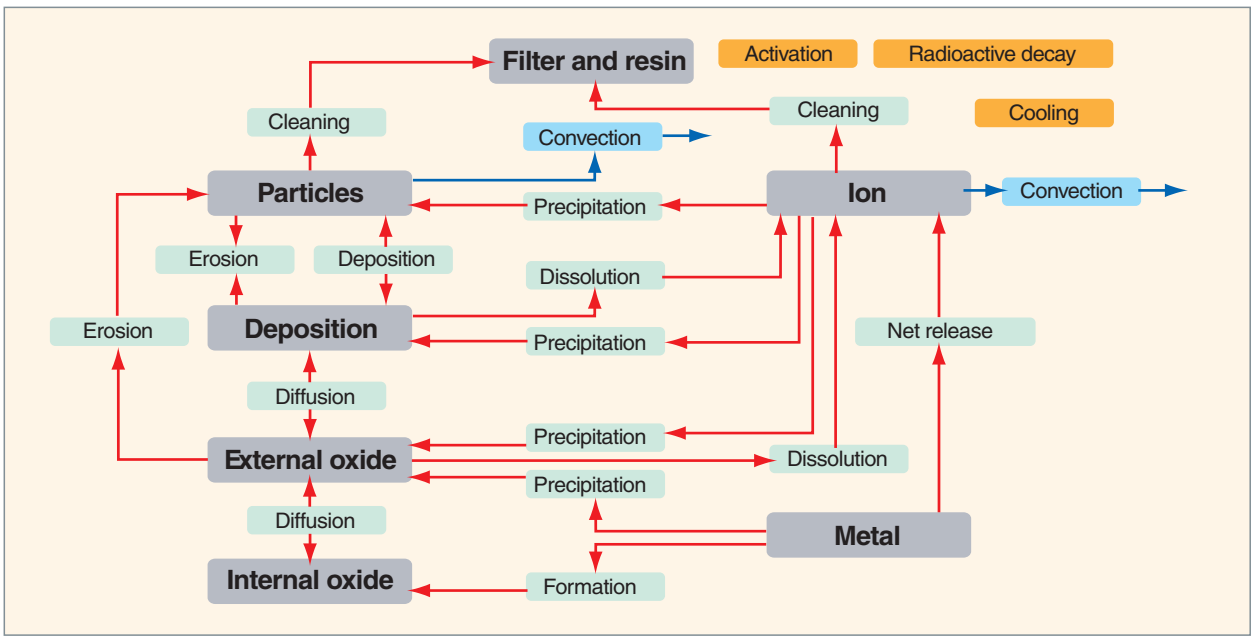

Fig. 27. Interactions between the various environments in a reference volume in the PACTOLE V3.0 Code (environments are in purple, convection in light blue, neutronics-related mechanisms in orange, and the others in green).

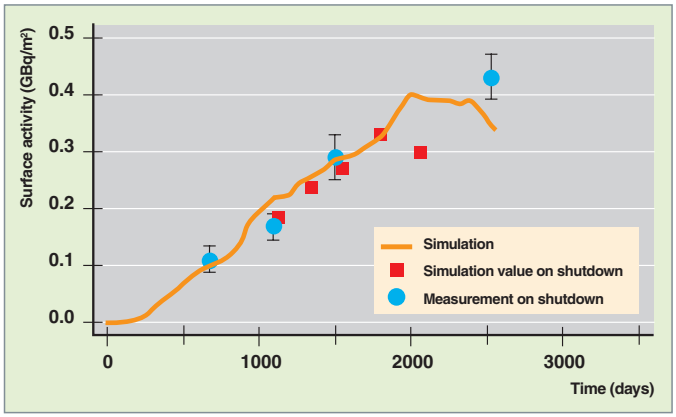

Fig. 28. Comparison between PACTOLE V3.0 Code simulation and measurements of Co 60 activity deposited on a 1300-MWe French PWR steam generator.

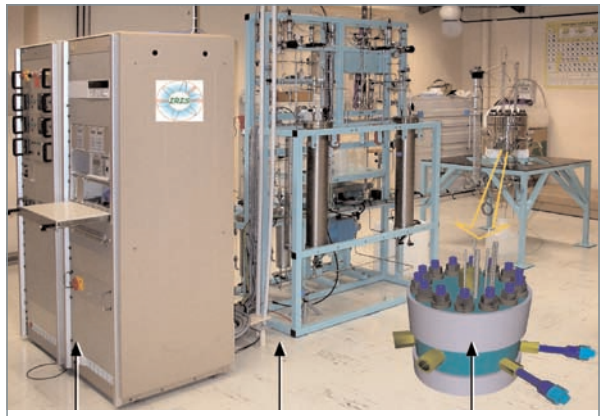

Fig. 29. The IRIS-AHT research instrument for investigating speciation in aqueous environments at high temperature and high pressure (IRIS-AHT: Instrument de Recherche pour l'Investigation de la Spéciation en milieu Aqueux à Haute Température).

base for copper-containing oxides. The neutrons generated exhibit an initial energy of 14.7 MeV, which changes the calculation of the activation ratio. So a "tokamak" version of PACTOLE was derived (PACTITER [15]), and is used for dose rate assessment in relation to the ITER safety case. Last but not least, let us quote that the CEA is developing a new application, the OSCAR Code, with the purpose of integrating modelling of contamination transfer by actinides, fission and corrosion products into a same tool. This code is an improved version of PACTOLE modelling for corrosion products. As regards fission products and actinides, the primary coolant system volume is used together with a new module relating to the source term, so as to get a better physical description of modelled phenomena and an extended validity range (high burnup and MOX).

Water chemistry influence on corrosion and contamination

Predicting materials-fluid behavior lies in taking account of complex systems, such as, e.g., mixed oxides with a spinel structure $(Ni,Fe,Co,...)_1(Fe,Cr,...)_2O_4$ occurring on nickel alloys (Alloy 600, 690, 800), as well as in getting reliable thermodynamic data for reaction-free enthalpies under thermo-mechanical and physico-chemical reactor conditions. In our laboratories, this means data acquisition under reactor representative conditions (Fig. 29): measurements of equilibrium concentration, liquid-vapor partition constant, redox potential, or pH.

Making use of these data implies two types of measures: first, feeding bases such as the generic thermodynamic database ATHENA, and, secondly, developing tools dedicated to aqueous-environment thermodynamics at high-temperatures, as e.g. THERMODY (Fig. 30).

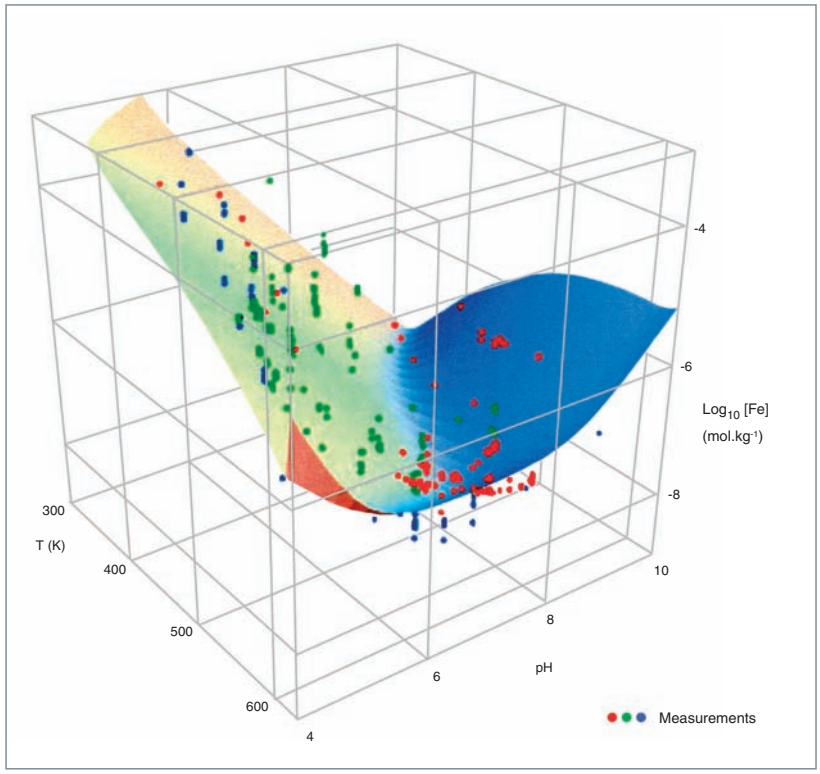

Fig. 30. Example of comparison between experimental measurements of magnetite solubility and the values computed by the PHREEQCEA Code.

Following these steps, a knowledge transfer to industrial tools can be achieved through the chemistry module *PHREEQCEA*. This module has been developed for the CEA's OSCAR Simulation Code by tailoring the US Geological Survey's PHREEQC Geochemical Code to PWR problems. The aim was to rely on a robust computational system designed for intensive calculations. For several thousands of calls to the chemistry module are required to model radioactive contaminants in a reactor coolant system over several operating cycles.

This approach enabled us to issue a comprehensive, reliable simulation of cold shutdown as experimentally reproduced in laboratory, including a temperature decrease of 300 °C-25 °C, the environment's acidity change following fluid boration, redox potential change when passing from a reducing to an oxidizing environment, and the sudden increase in corrosion products release into the fluid during this transient. Figure 31 illustrates this twofold experimental and simulated result.

The following step consists in taking into account a broader variety of degradation products potentially occurring in PWR primary coolant system, i.e. other corrosion, activation and fission products (Mn, Mo, Zn, Ag, Zr, Nb, Xe, I, etc.).

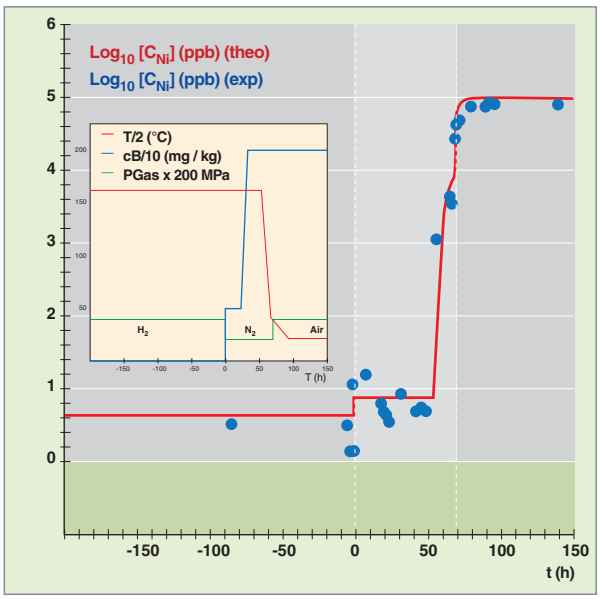

Fig. 31. Comparison between the laboratory experimental results and the simulation results relating to a PWR cold shutdown transient. The nickel concentration evolutions measured and calculated (on a logarithmic scale) are presented as a function of time, with the zero coinciding with simulation onset for a shutdown whose evolutions in temperature and chemistry (boron content and redox through the hydrogen, nitrogen and air contents) are shown in the small diagram inside the figure.

Radiolysis* impact on uniform corrosion

Since the commissioning of the first reactors in 1945, a high number of works have been carried out to evidence the fundamental processes that take place in solids or liquids – especially water – irradiated by radioelement-emitted particles. Using beams of particles (electrons or ions) produced from various accelerators instead of external radionuclide sources made it possible to conduct model experiments in broad ranges of fluxes, fluences and energies. Thanks to the resulting advances, basic mechanisms on the microscopic scale could be revealed, and macroscopic effects of long-term irradiations could be modelled. It is worth noting that, in contrast with literature dealing with solids or water, literature devoted to irradiated solid/water interfaces seems to be rather limited. The works presented hereafter illustrate the investigations which have been initiated as part of a fundamental approach based upon a co-operation between the Physical Sciences Division and the Nuclear Energy Division. The aim is to evidence, then identify the basic reactions controlling the electrochemical properties of the irradiated metal/water interfaces in water-cooled reactors [16].

The experiments use various types of particle beams differing in their initial energy and the particle nature:

- Electrons (CEA/DSM/DRECAM, 0.2-2.5 MeV and 10 MeV, CNRS/LCP 5-9 MeV),

- Ions (CNRS/CERI H^+ 34 MeV or He^{2+}45 MeV).

A few experiments have also been performed with external gamma sources.

It is essential to carry out *in situ* electrochemical measurements that allow direct comparison between the values obtained on the same electrodes before, under, and after irradiation. The electrochemical cells used under ion or electron beams of low energy 0.2-5 MeV were designed for *in situ* measuring the open-circuit potential and the current response as a function of an imposed variable potential (voltamperometry) at a disk / water interface; this interface is irradiated in such a geometry that ions or electrons are relased from solid to water. The input window is replaceable. As regards high-energy electron beams, the disks are immersed and put on the path of electrons, which irradiate the water contained in the electrochemical cell.

The electrochemical response of the interfaces under the beam simultaneously depends on the radiolytic species generated in water, the species released by the electrode into water, and metallic surface alteration. Other processes described in literature may also be involved according to whether the layer on the disk surface is metallic or not.

Figures 32 and 33 illustrate the behavior of a platinum (Pt) electrode immersed into a Na_2SO_4 solution in the absence or presence of ethanol 0.08 M (with the ethanol reacting with radiolytically-generated radicals OH) before, during, and after irradiation by 10-ns, 10-MeV electron pulses, sent at a 10-Hz repetition frequency. Prior to beam arrival, the free potential in presence of pure water (Fig. 32) displays a stable value of 290 mV_{SCE} (this potential being measured with respect to a Saturated Calomel "reference" Electrode - SCE -). The beam arrival entails an immediate rise of the potential which reaches a maximum value of 422 mV_{SCE} within a few seconds. Later on, the potential decreases, and rapidly tends to a nearly stationary oxidizing value of 347 mV_{SCE} after 20 minutes of irradiation. Once the beam is cut off, the potential drops, and reaches a 310 mV_{SCE} value, i.e. only 20 mVSCE above its value before irradiation. In presence of ethanol, the free potential prior to irradiation is of 136 mV_{SCE}. Under beam irradiation it goes through an oxidizing maximum value of 300 mV_{SCE} before reaching a nearly stationary reducing value of -457 mV_{SCE}.

Comparing Figures 32 and 33 shows that the solution's chemical composition plays a predominant role in the evolution of the electrode potential.

The second illustration (Fig. 34) deals with the electrochemical behavior of an AISI 316L stainless steel under irradiation. The corrosion potential is substantially increased under irradiation, and reaches a value of 120 mV_{SCE} within a few minutes, before slowly reaching 130 mV_{SCE}. After irradiation, the potential slowly drifts as it keeps on rising: within about 40 minutes after the beam cut, the potential has thus reached a 140 mV_{SCE} value. The polarization curves before and after irradiation make evident an increase in the cathodic reaction rate under irradiation, presumably due to the presence of new oxidizing species.

The corrosion currents determined from Figure 34 are under a $1.1x10^{-7}$ $A.cm^{-2}$ irradiation, i.e. approximately an order of magnitude higher than before irradiation ($1.71x10^{-8}$ Acm^{-2}). As shown in Figure 35, with 316-L stainless steel electrodes, the corrosion current under a 10-MeV, 10-ns, 1-40 Hz pulsed electron beam linearly rises with the flux for irradiations in which fluxes have veen varied with no solution renewal.

All these results evidence a strong influence of radiolysis upon the corrosion potential of passivable materials such as stainless steels, or zirconium or nickel alloys. This implies that uniform and localized corrosion phenomena are affected by radiolysis. In accordance with this outlook, a cell has been developed for investigating radiolysis in aqueous environment

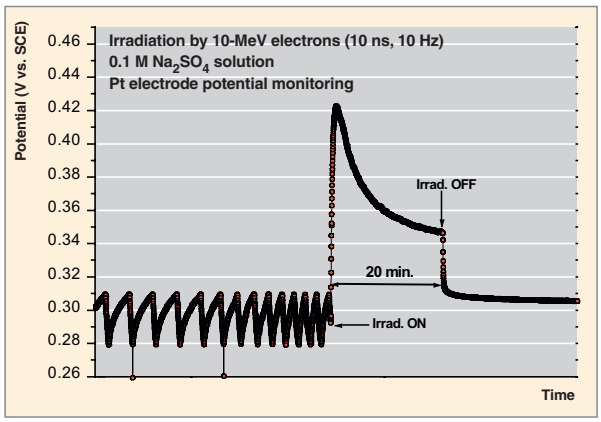

Fig. 32. Evolution of the potential of a platinum electrode immersed into a 0.1 M Na_2SO_4 solution before, during, and after irradiation. The solution is irradiated at a 10-Hz frequency by 10-ns pulses of 10-MeV initial energy electrons.

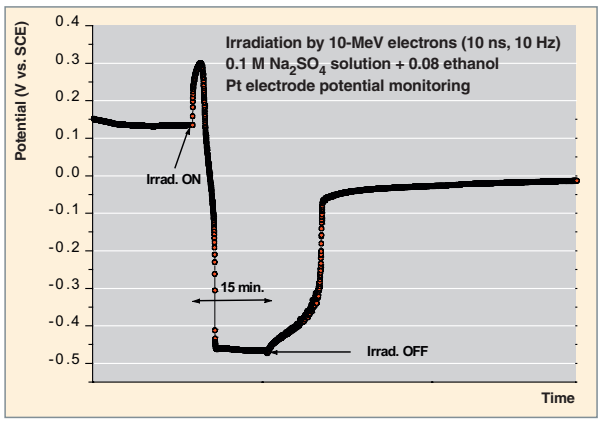

Fig. 33. Evolution of the potential of a platinum electrode immersed into a 0.1 M Na_2SO_4 solution and 0.08 M ethanol before, during, and after irradiation. The solution is irradiated at a 10-Hz frequency by 10-ns pulses of 10-MeV initial energy electrons.

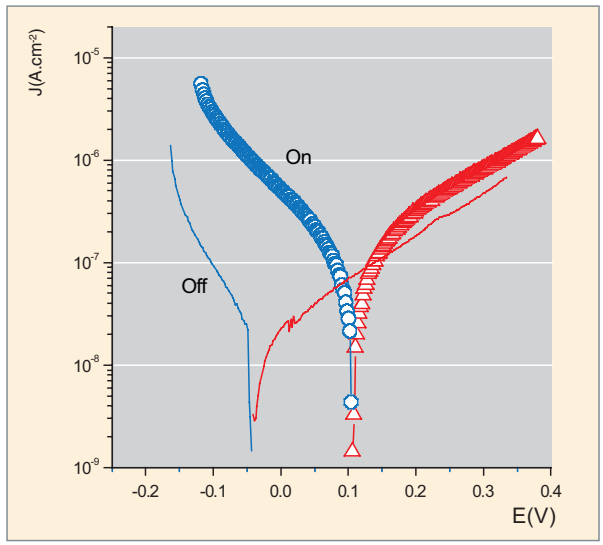

Fig. 34. Current density as a function of polarization before and under irradiation for a 316L steel after nine polarization scans.

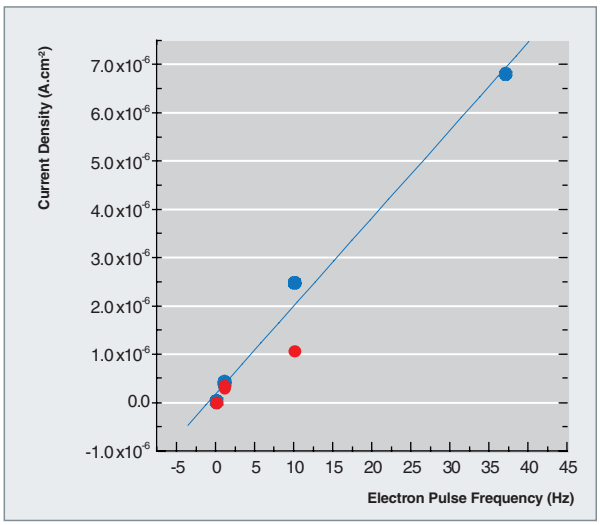

Fig. 35. Variation of the corrosion current under pulsed electron beams of 10-MeV energy, 10-ns pulse time, 1-40 Hz repetition frequency for two 316L electrodes irradiated in a water / electrode / water geometry, and prepared at the same dates under the same conditions. The flux ratio is within the ratio of the pulse repetition frequencies.

at high temperature (300 °C) and high pressure (10 MPa) (Fig. 36). This cell allows electrochemical monitoring to be carried out under temperature and irradiating flux in order to evidence radiolysis and its effects on the alteration of an electrode.

The first experiments of stainless steel radiolysis and corrosion were thus performed successfully under a proton flux on the CERI cyclotron, Orleans, in February 2008. The investigated environment simulated the primary environment of nuclear PWRs. Good operation of the device could be checked through this first test cycle, which helped start investigating stainless-steel behavior under radiolysis in a 25 °C-300 °C temperature range. Knowledge of irradiation effects on water physico-chemical properties at high temperature and high pressure will also be improved through *in situ* measurements and medium sample analyses. Such data will be very useful for developing electrochemical models of alloy behavior under radiolysis at high temperatures and high pressures.

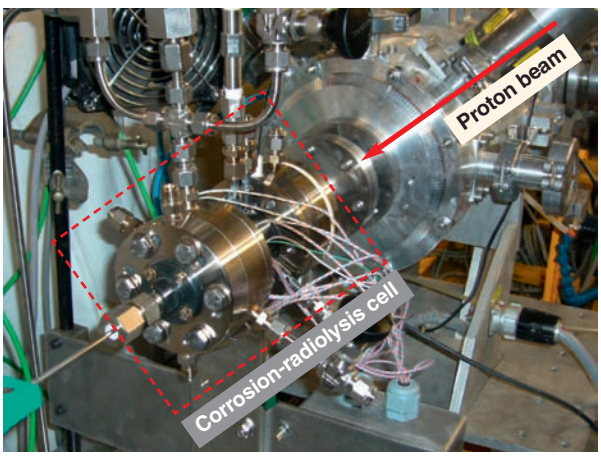

Fig. 36. High-temperature corrosion-radiolysis cell connected with the CERI accelerator.

References

[1] ISO 8044, avril 2000, *"Corrosion des métaux et alliages – Termes principaux et définitions / Corrosion of metals and alloys – Basic terms and definitions", AFNOR 2000*.

[2] J. Godlewski, P, Bouvier, G. Lucazeau and L. Fayette, "Stress distribution measured by Raman spectroscopy in zirconia films formed by oxidation of Zr-based alloys." *Zirconium in Nuclear Industry: Twelfth International Symposium*, ASTM STP 1354, G.P Sabol and G. Moan, Eds, ASTM International, West Conshohocken, PA, 2000, pp. 877-900.

[3] P. Bossis, F. Lefebvre, P. Barberis and A. Galerie, "Corrosion of zirconium alloys: link between the metal/oxide interface roughness, the degradation of the protective oxide layer and the corrosion kinetics", *Materials Science Forum*, 2001, n° 369-372, pp. 255-262.

[4] D. Pêcheur, V.P. Filippov, A.B. Bateev and J.J. Ivanov, "Mössbauer investigations of the chemical states of tin and iron atoms in zirconium alloy oxide film", *Zirconium in the Nuclear Industry: thirteen International Symposium*, ASTM STP 1423, Gerry Moan and Peter Rudling Eds, ASTM International, West Conshohocken, PA, 2002, pp. 135-153.

[5] D. Pêcheur, J. Godlewski, J. Peybernès, L. Fayette, M. Noé, A. Frichet and O. Kerrec, "Contribution to the understanding of the effect of the water chemistry on the oxidations kinetics of Zircaloy-4 cladding", *Zirconium in the Nuclear Industry: Twelth International Symposium*, ASTM STP 1354, G.P Saboland G. Moan, Eds, ASTM International, West Conshohocken, PA, 2000, pp. 793-811.

[6] P. Bossis, D. Pêcheur, K. Hanifi, J. Thomazet and M. Blat, "Comparison of the High Burn-up Corrosion on M5 and low Tin Zircaloy-4", *Zirconium in the Nuclear Industry: fourteen International Symposium*, ASTM STP 1354, Journal of ASTM International, June 2005, in press.

[7] A. Giordano and J. Peybernès, "*COCHISE – code de prévision de la corrosion externe des gaines d'assemblages combustibles*", Journal de Physique IV France 11, 2001, pp 151-164.

[8] V. Bouineau, A. Ambard, G. Bénier, D. Pêcheur, J. Godlewski, L. Fayette and T. Duverneix, "A new model to predict the oxidation kinetics of zirconium alloys in PWR", *ASTM 15th International Symposium on Zirconium in the Nuclear Industry*, June 24-28, 2007, Sunriver, Oregon, Paper ID JAI101312-07.

[9] "High temperature corrosion of Zircaloy-4 followed by *in situ* impedance spectroscopy and chronoamperometry. Effect of an anodic polarisation" par M. Tupin, C. Bataillon, J.P. Gzlan and P. Bossis, chapitre 7 dans *Electrochemistry in Ligth Water reactors* (pp. 134-163), EFC publications N°49, Woodhead publishing limited, Cambridge, GB (2007, ISBN 978-1-84569-240-7).

[10] A. Frichet, P. Barberis and N. Petigny, *12th Symposium on Zirconium Industry*, Toronto, Poster Session, June 15-18 (1998).

[11]. L. Marchetti, Thèse de l'École des Mines de Saint-Étienne, "*Corrosion généralisée des alliages à base nickel en milieu aqueux à*

haute température: apport à la compréhension des mécanismes", n° d'ordre 455 GP, 2007.

[12] M. Sennour, L. Marchetti, S. Perrin, R. Molins, M. Pijolat and O. Raquet, "Characterization of the oxide films formed at the surface of Ni-base alloys in pressurized water reactors primary coolant by transmission electron microscopy", *Materials Science Forum*, Vols. 595-598 (2008), pp. 539-547.

[13] L. Marchetti, S. Perrin, O. Raquet and M. Pijolat, "Corrosion mechanisms of Ni-base alloys in pressurized water reactor primary conditions", *Materials Science Forum*, Vols. 595-598 (2008), pp. 529-537.

[14] S. Anthoni and P. Ridoux, "Origin of Corrosion Products in PWR Primary Circuits", proceedings of Eurocorr'96, Nice 24-26 September 1996, *Session IX Nuclear Corrosion and Protection*, IX OR 1.

[15] L. Di Pace, F. Dacquait, P. Schindler, V. Blet, F. Nguyen, Y. Philibert and B. Larat, "Development of the PACTITER code and its application to safety analyses of ITER Primary Cooling Water System", *Fusion Engineering and Design* **82** (2007), pp. 237-247.

[16] E. Leoni, C. Corbel, V. Cobut, D. Simon, D. Féron, M. Roy and O. Raquet, "Electrochemical behaviour of gold and stainless steel under proton irradiation and active redox couples", *Electrochimica Acta, Volume 53, Issue 2,* 1 December 2007, pp. 495-510.

Bibliography

[A] G. Béranger and H. Mazille, *Corrosion des métaux et alliages – mécanismes et phénomènes*, Lavoisier, Paris, 2002.

[B] K.E. Heusler, D. Landolt and S. Trasatti, *Electrochemical corrosion nomenclature, Pure and Applied Chemistry*, 61 (1), pp. 22-29, 1989.

[C] J. P. Diard, B. Le Gorrec et C. Montella, *Cinétique électrochimique*, Coll. "méthode", Hermann, 1996.

[D] D. Landolt, *Corrosion et chimie de surface des métaux, Traité des matériaux*, Presses polytechniques et universitaires romandes, 1993.

Christian Bataillon, Damien Féron, Loïc Marchetti,
Stéphane Perrin, Dominique You,
Physico-Chemistry Department
Vincent Bouineau, Dominique Pêcheur,
Fuel Studies Department
Catherine Corbel,
CEA / DSM / IRAMIS / Irradiated Solid Laboratory
Joël Godlewski, Frédéric Nguyen,
Nuclear Technology Department
and Marc Tupin,
Nuclear Materials Department

Stress Corrosion Cracking

In pressurized water reactors, the **alloys*** used (nickel-type alloys or **stainless steels***) are usually covered with a very thin protective layer, called "passivation layer" or "passive layer", which has been formed on the metal surface by reaction between this metal and the environment. It is often because the metal's or alloy's good resistance to general corrosion is only due to passive layer protection that this metal or alloy is sensitive to the various forms of localized corrosion: so, localized corrosion may be assumed to be some kind of "disease" of the passive state. As a matter of fact, local alteration of protective properties in the passive layer may result from a chemical aggression – such is the case of pitting corrosion, usually induced by the action of some chemical species such as chloride ions – or from a mechanical stress, such as in stress corrosion cracking. Practically, investigating the initiation of localized corrosion phenomena (including stress corrosion cracking) therefore implies studying the passive layer, its evolution, defect generation within this layer, and its local destruction. The initiation of localized corrosion is followed by its propagation. The latter will involve specific, different mechanisms for pitting corrosion and stress corrosion cracking.

Stress corrosion cracking: overview

Among the various occurrences of corrosion, no doubt **Stress Corrosion Cracking*** (SCC) is one of the most feared forms of corrosion. For it appears as a cracking, the propagation of which may be relatively fast, and take place after a more or less long incubation phase, with no precursor sign. Moreover, it often occurs in poorly aggressive environments. It is defined in Standard ISO 8044 (April 2000) as a "cracking due to stress corrosion" Three main factors are thus involved: the material and the environment (as often in corrosion), as well as the stress. This is illustrated by the Venn diagram (Fig. 37).

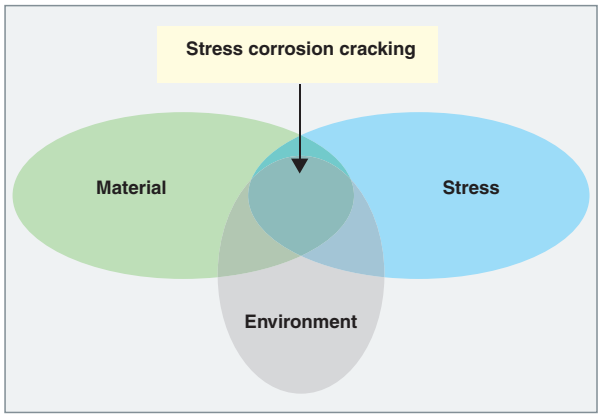

Fig. 37. Venn diagram as an illustration of the three factors of stress corrosion cracking.

No material can be considered as sensitive or insensitive to SCC (even though pure metals have long been considered insensitive). However, materials may be more or less sensitive in a given environment. This is the reason why, for instance, **Alloy 600***, an SCC-sensitive alloy in a PWR primary environment, was finally replaced by **Alloy 690***, considered as nearly insensitive in primary environment.

On the other hand, no environment may be considered as an intrinsic SCC promoter, even though many cracking cases originate in chlorinated environments or some sulfurized species. So, in reactors, great care should be taken to limit oxygen and chloride contents, for example, so as to keep them well under concentrations likely to induce stainless-steel cracking.

Cracking initiates when the stress goes beyond a limiting value, or it propagates on an already existing crack when the **stress intensity factor*** exceeds a critical threshold (K_{1SCC}). The limiting stresses are sometimes very low; yet, in our in-reactor applications, they are often neighbouring materials elasticity limit. In addition, residual stresses should not be omitted when assessing the stress level, which justifies stress-relieving treatments systematically performed. Cracking induces brittle fracture (or brittle failure) in materials, with no apparent strain. Cracks may be transgranular or intergranular, as shown on Figure 38, or mixed, as displayed on Figure 39, depending on the material and its environment.

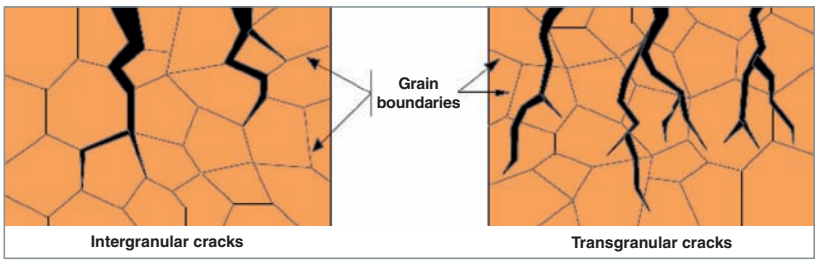

Fig. 38. Schematic representation of intergranular and transgranular cracks.

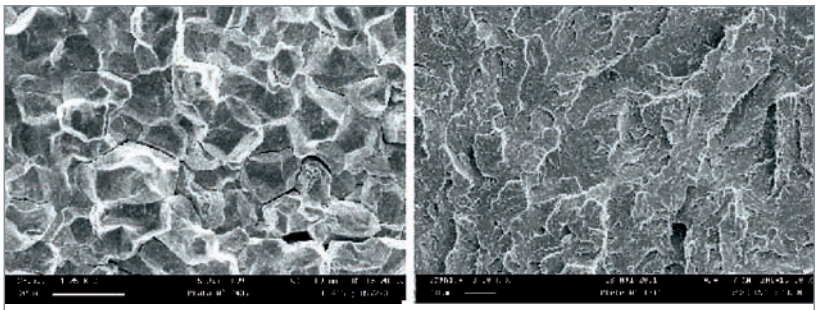

Fig. 39. An example of intergranular corrosion cracking (Alloy 600, PWR primary environment, 325 °C) and transgranular cracking (austenoferritic stainless steel, chloride-polluted environment) observed on PWR materials.

Stress corrosion cracking has often been described as a disease of the passive state, for it mostly affects materials protected by a surface oxide film (that is, materials in the passive state). Thus, in many systems, cracking occurs within very narrow ranges of corrosion potentials, as displayed on Figure 40.

These potentials fall within the following categories:

- Very low potentials for which hydrogen generated by water reduction is involved in the cracking mechanism (hydrogen embrittlement);
- Potentials close to the active-passive transition, and corresponding with potential values at which the passive film is under formation and, so, of poor stability; such is the case of **Alloy 600*** under PWR primary conditions, where the maximum sensitivity threshold is located at potentials neighboring Ni/NiO equilibrium;
- High potentials, neighboring the breakdown potentials for the passive film; such is the case of austenitic stainless steels in neutral chlorinated environments.

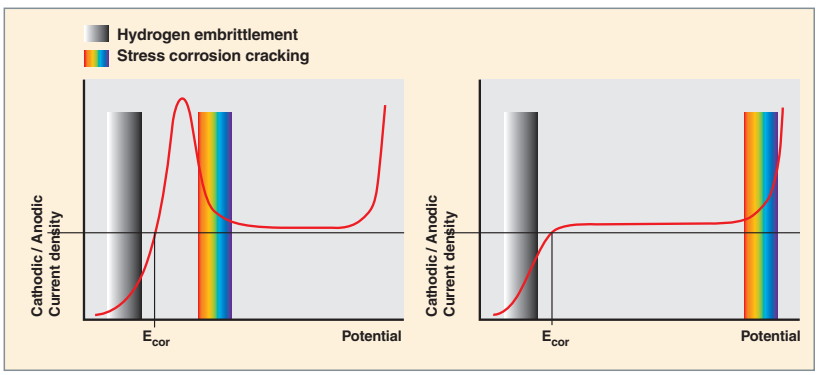

Fig. 40. Cracking preferential ranges: the influence of corrosion potential and passivity.

In practice, the phenomenology of SCC mechanisms is complex (Fig. 41). Once the electrochemical and mechanical conditions required by the phenomenon have been set up, cracks are initiated after the so-called *incubation phase*. In relation to this point, it is worth keeping in mind that Alloy 600 in a PWR primary environment is known to display very long incubation times likely to last several years. From a practical viewpoint, the issue of apparent initiation time is often used. It includes incubation itself, initiation, and some degree of crack propagation, a necessary condition for the cracks to be detectable. So the incubation phase is followed by crack initiation and propagation. Crack propagation usually includes two stages: a first stage of growth at a moderate rate, followed by a fast growth stage. Last but not least, beyond a given size some cracks may happen to branch, while others may gather.

This complexity is also illustrated by the temperature effect: generally, SCC phenomena are thermally accelerated, and there often exists a threshold temperature under which cracking does not occur. Yet, a maximum **sensitivity*** (or susceptibility) may be observed for a given temperature.

Many models have been proposed to explain brittle fracture in ductile materials as a result of mechanical stresses and corrosive environments. Owing to multiple parameters, their interactions, and the need for a pluridisciplinary approach, none of the models developed to date has been able to account for all the features of this cracking phenomenon. Nevertheless, in the latest years, real advances have emerged in the building of theories and the development of methods to validate them.

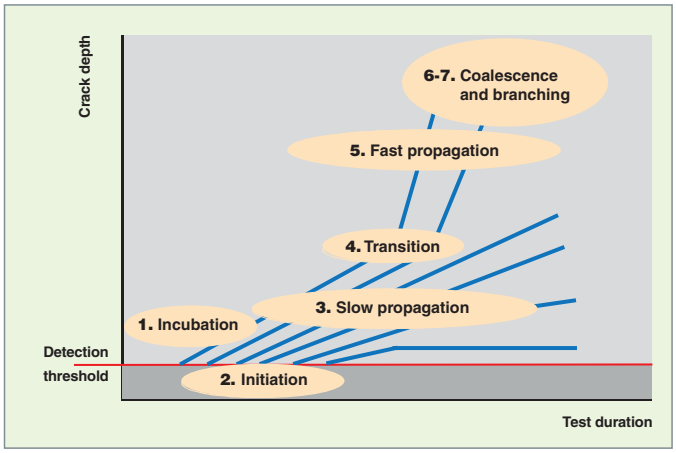

Fig. 41. Schematic representation of the various stages of stress corrosion cracking.

Among the models put forward to explain Alloy 600 cracking, two model families are favored today: models involving local hydrogen concentrations, and internal oxidation models. The oxidation / hydrogen alternative is still a highly controversial issue.

Test tools for investigating stress corrosion cracking

Test tools implemented for investigating corrosion phenomena are intended to achieve in-laboratory reproduction of the environment's main physico-chemical features, as well as the stresses which reactor component materials are subjected to.

As the incubation period of the phenomenon may last several years under operating conditions, laboratory tests are accelerated. Two techniques are generally used: temperature rise and/or increase in the applied stress. The experimental devices containing the test bars are, if need be, connected with systems which can recondition the environment, i.e. purify it or, reversely, pollute it.

Tests for investigating corrosion initiation

These tests are performed on tensile-stressed smooth test specimens using devices that subject the material to constant strain, constant loading, or to a constant strain rate. Cyclic stresses may also be used sometimes to reproduce the effect of reactor power transients.

There exists a broad range of test specimens under imposed strain:U-bend, Reverse U Bend (Fig. 43), C-ring, Bent-Beam, and out-of-round specimens…

The "Coriou effect"

As soon as the choice of **Alloy 600*** was known for PWR steam generator tubes, the CEA's "Corrosion Department", headed then by Henri Coriou, started a large number of autoclave tests to investigate the behavior of this new material in an aqueous environment at high temperature. The first observations made on test bars subjected to bending stresses evidenced substantial intergranular cracking on some specimens after a few months' exposure in both pure water and an environment simulating PWR primary water (water + boric acid + lithium hydroxide), and at temperatures ranging from 300 to 350 °C (Fig. 42). This result issued in 1959 at the 3rd Metallurgy Conference on Corrosion, Saclay, was the starting point of a controversy which was to last for about twenty years. Not until the 1970s-1980s, when numerous cases of cracking could be observed in plants, did scientific community as a whole acknowledged the reality of what is now named the "Coriou effect". This led to the replacement of many steam generators in France and abroad. The following pages of this monograph give an explanation of the phenomenon…

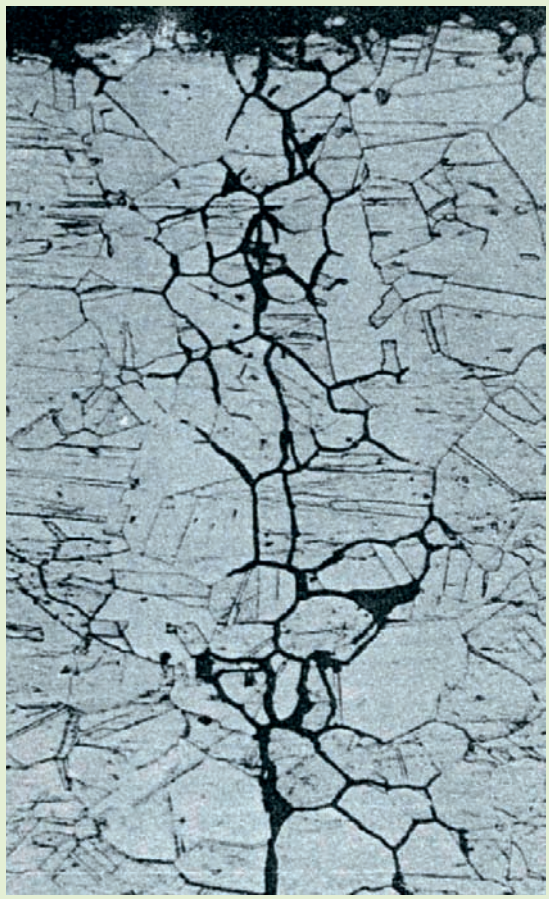

Fig. 42. **Alloy 600*** SCC pattern displayed at the 3rd Metallurgy Conference on Corrosion (Saclay, 1959), and observed after 90 days in "high-purity" water at 350 °C (X250).

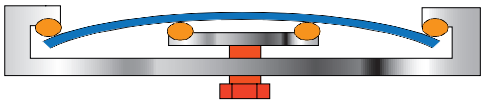

"Four-point loaded" specimen for plates

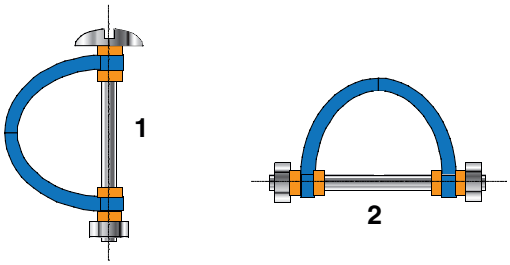

"C-ring" specimen (tubes) or "U-bend" specimen (plates)

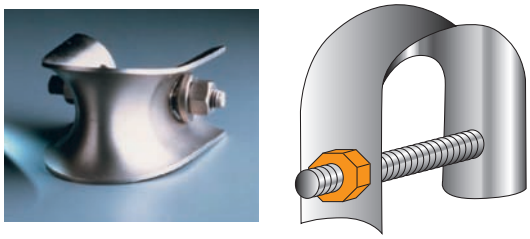

Reverse U Bend (RUB) specimen for tubes

Fig. 43. Constant-strain test specimens.

Reverse U Bend (RBU) specimens are made using a SG tube piece bent in two stages. This type of specimen enables the material to be subjected to very high stresses. Strain at the specimen apex reaches 30-40%. Stress levels obtained are assessed through X-ray diffraction. In the case of an Alloy 600 tube, longitudinal and circumferential stresses may respectively reach 1000 and 700 MPa.

Like all other test specimens under imposed strain, 'Reverse U Bend' specimens are placed in sufficient quantity in an autoclave which contains the test environment and is brought to high temperature and pressure. Tests of this type are more especially dedicated to the parametric and statistical study of material susceptibility to crack initiation.

The latter can also be characterized using tests under an imposed load. Specimens used may be capsules fabricated by welding plugs to both ends of a tube section. The test environment is introduced into the capsule, which is then put into an oven. The circumferential stress is proportional to the pressure prevailing in the capsule and to the capsule internal diamer, and reversely proportional to the tube thickness.

Tests under imposed strain may also be performed using axisymmetric or flat tensile specimens subjected to an applied force. This type of specimen can also be tensile-stressed under imposed strain rate condition. In the case of Alloy 600 in a PWR primary environment, at about 340 °C, the imposed strain rate generally ranges between 2.5 10^{-8} s^{-1} and 2.5 10^{-7} s^{-1}. According to the susceptibility of the alloy heat tested, the duration of the tensile test ranges from 1 to 3 months. For some applications, the test environment has to be continuously reconditioned. As an illustration, Figure 44 presents an autoclave fitted with a slow strain-rate tensile machine and a schematic of the specimen assembly in the autoclave.

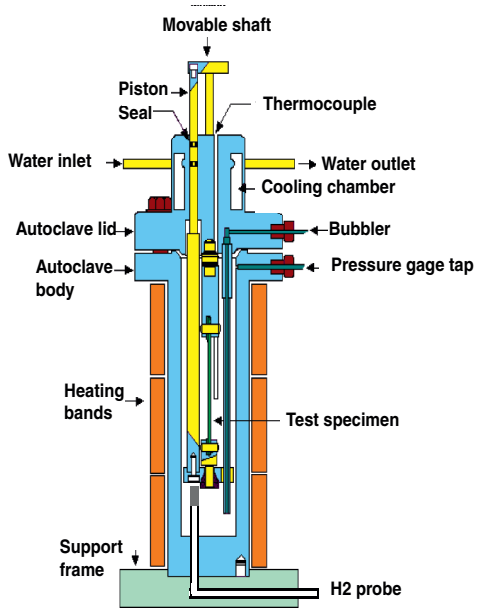

Fig. 44. Autoclave fitted with a slow strain-rate tensile machine for testing at a constant strain rate or under cyclic stresses.

The tensile machine may also impose cyclic stresses. Such tensile tests on smooth specimens entail multiple cracking in the latter. Since the late eighties, a model [2] has been developed, and is currently used to collect quantitative data on crack initiation and propagation rates basing upon the evolution of the crack population over time. This model assumes the existence of a one-to-one relationship between a function characterizing the evolution of crack depth distribution and a couple of functions characterizing crack initiation and propagation.

Tests for investigating crack propagation

Tests devoted to investigating crack propagation rates are generally performed using sheared specimens, which have been most often fatigue precracked. Regarding smooth specimens dedicated to crack initiation studies, the fabrication of these specimens is described by standards that give their precise dimensions and the related elaboration procedures. As in the previous case, these specimens may be subjected to an imposed strain (Double Cantilever Beam specimens, Wedge Opening Loaded Specimens…), or to an imposed load (Compact Tensile specimens…). The theory of continuous medium mechanics makes it possible to deduce the stress intensity factor characterizing mechanical stress in the crack tip from the imposed mechanical loading, shear depth, and material properties. It is worth keeping in mind that these calculations are valid only if confined plasticity criteria have been checked, and strictly for rectilinear crack fronts. Otherwise, finite-element calculations have to be performed to assess the local mechanical stress (Fig. 45).

During the corrosion test, crack growth may be followed by an electric method (Direct Current Potential Drop - DCPD) or by acoustic emission. The VENUS loop shown on Figure 46 is instrumented with the related devices. It also includes 4 autoclaves which may contain several specimens fitted end to end.

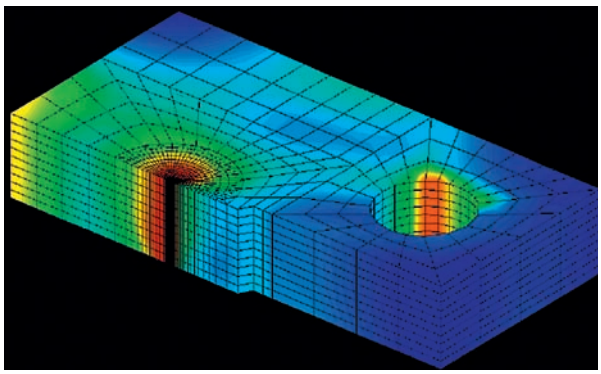

Fig. 45. 3-D representation of mechanical stresses in a CT specimen.

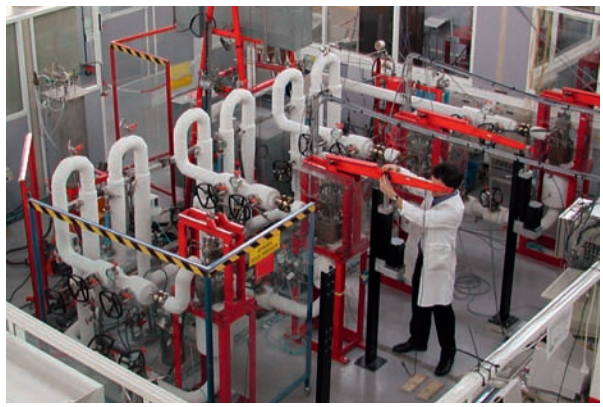

Fig. 46. View of the VENUS loop.

All the autoclaves are equippped with a programmable mechanical jack likely to impose the required mechanical stress on the material. The facility is equipped with devices likely to monitor and maintain the chemical conditions imposed during tests (continuous purification, hydrogen injection…).

The “Corrosion” hall at the Center of Saclay houses one part of the test tools devoted to stress corrosion cracking, together with the equipment for electrochemical monitoring and specimen observation (Fig. 47).

Fig. 47. View of the “Corrosion” Hall of the Physico-Chemistry Department.

Experimental techniques

Acoustic emission

Stress Corrosion Cracking (SCC) initiation and propagation induce microscopic motions of material. These motions act as emitters of acoustic, transient and elastic waves, which propagate through the material up to the free surfaces where they can be detected. Detection of the Acoustic Emission (AE) signal is carried out using a sensor acoustically coupled with the AE sources, and consisting of a piezoelectric ceramic which converts the transient elastic wave generated by the AE event into an electrical signal. The latter is then amplified and processed.

The processing consists in extracting from the "global" electrical signal the component which corresponds with initiation and propagation of stress corrosion cracks. For there is quite a number of potential AE sources during a SCC test. They may particularly originate in the test environment (boiling, convection, circulation), and the various processes involved in the SCC phenomenon:

- Hydrogen release resulting from the cathodic reaction,
- Oxide film rupture (in case of high thickness),
- Rupture or decohesion of phases (precipitates or inclusions),
- Phase transformation,
- Mechanisms of plastic strain (slip, twinning),
- Anodic dissolution (though of low energy).

CARON's thesis [1] highlights all the interest of this technique for *in situ* monitoring and characterizing the SCC phenomenon under PWR primary conditions.

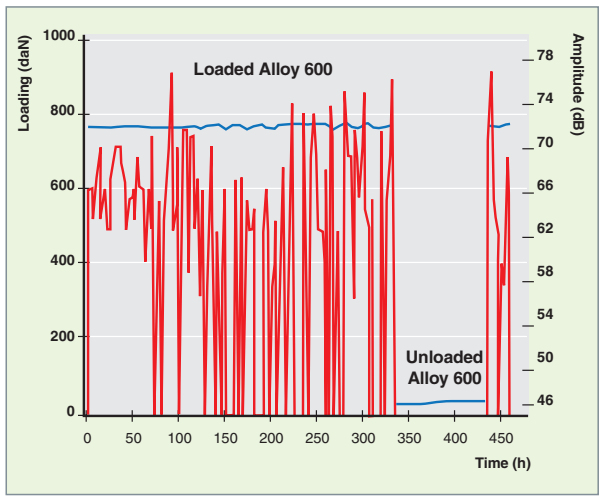

Fig. 49. Acoustic emission bursts during mechanical loading and unloading phases of Alloy 600 samples in a primary environment. Filtered data [1].

Identifying the acoustic signature of the various acoustic emission sources is not always required for AE to be used as a technique of *in situ* monitoring of cracking. For it may be sufficient to refer to the acoustic response obtained under similar experimental conditions with a material not sensitive to SCC, but displaying mechanical and metallurgical features close to those of the material to be investigated (Fig. 48). When Alloy 600 is tensile-stressed, acoustic activity is high, consistently with propagation of stress corrosion cracks. On the contrary, burst energies and amplitudes are kept low with Alloy 690 on which no crack has developed.

Figure 49 displays the amplitude variation of bursts emitted during periods of mechanical loading and unloading of Alloy 600 in a primary environment. As previously, when Alloy 600 is tensile-stressed, acoustic activity is significant. Then, this activity stops as soon as the material is no longer tensile-stressed. Finally, it starts again as soon as stress is renewed. Signal processing makes it possible to keep only the acoustic emission bursts associated with SCC propagation.

Implementing this experimental technique is always very simple (Fig. 50). Yet, processing recorded signals may prove to be difficult, especially when the device includes parasitic emission sources not clearly identified, or when characterizing the acoustic signatures for each of the occur-

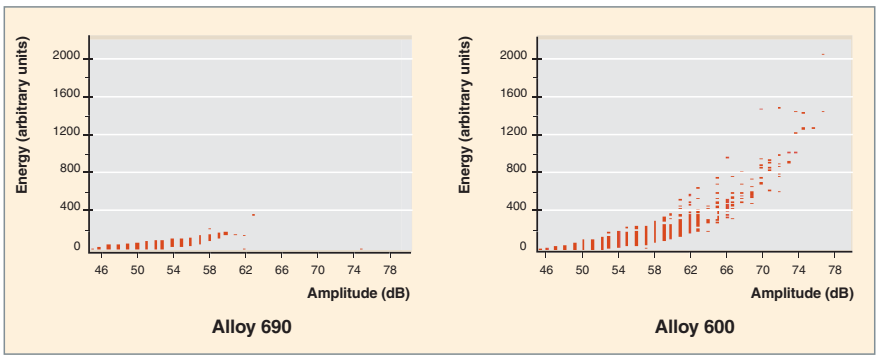

Fig. 48. Comparison of the energy/amplitude (dB) characteristics in the acoustic emission bursts recorded with **Alloy 690*** (no SCC) and **Alloy 600*** (SCC) during a 258-hour tensile test in primary environment (K_I = 30 MPa$\sqrt{m}$, T = 330 °C, [H_2] = 30 mL TPN.kg^{-1} H_2O). Unfiltered data [1].

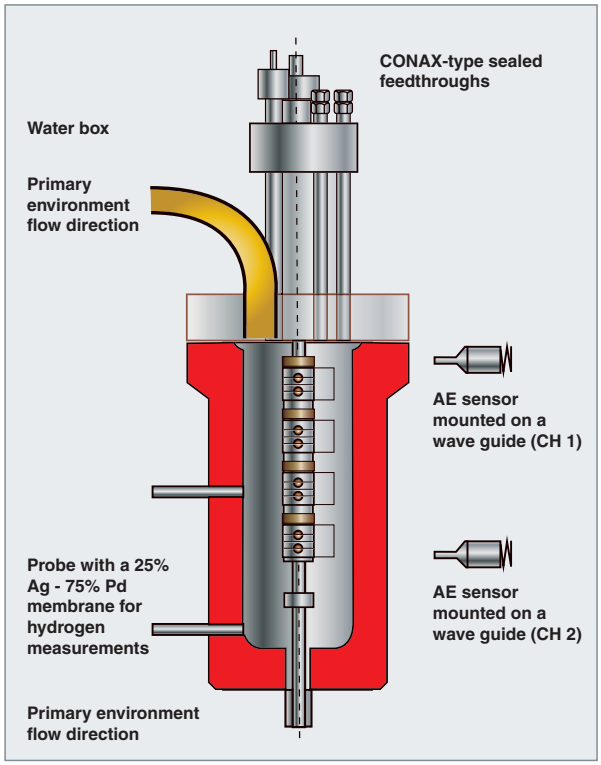

Fig. 50. Schematic representation of an autoclave fitted with two waveguides for acoustic monitoring of cracking propagation.

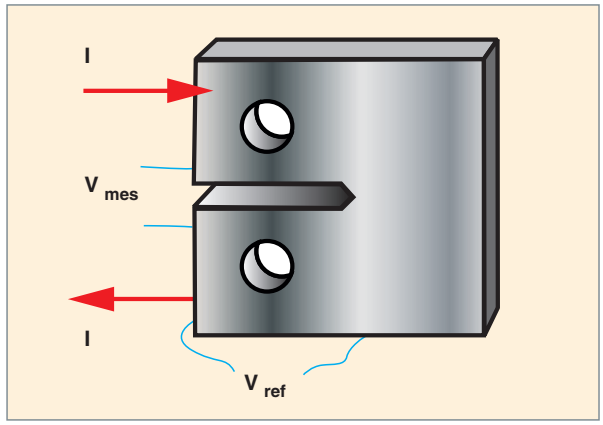

Fig. 51. Example of instrumentation for a CT-type specimen.

ring sources is required. To sum up it all, AE is a technique which is used for detecting the initiation of a SCC crack and following its propagation. However, its implementation is not easy in very noisy environments, which today circumscribes this technique to laboratory testing.

Monitoring cracks using potential drop (PD) measurement

Principle

The crack monitoring method using direct current potential drop (DCPD) measurement is based upon electrical resistivity variation in a cracked body. It consists in applying a high-intensity direct current (usually 1.5 A - 10 A) to a conducting test specimen insulated with respect to the remainder of the facility, and measuring a potential difference (V_{mes}) at the crack terminals using two electrodes (Fig. 51). When the crack is propagating, the apparent resistance of the specimen also increases, which induces a rise of V_{mes}. During SCC testing, a reference measurement (V_{ref}) is used for offsetting temperature and pressure variations which alter the material's resistivity. It is positioned in such a way that this measurement is not affected by crack propagation. Besides, this reference measurement avoids taking into account intensity variations of the applied current, as well as other variations related to instrumentation.

This technique may be used to detect SCC crack initiation *in situ* (that is, in an aqueous environment at 300-350 °C and, so, at a high pressure of 120-150 bars -), or to follow its propagation. Concerning crack initiation, any type of specimen may be instrumented. However, the area in which cracks will be initiated has to be predetermined so as to conveniently position the measuring wires. As regards propagation monitoring, there is a need to use specimen geometries for which the crack is unique and localized on a plane. Such is the case for specimens of type CT (Compact Tensile) or WOL (Wedge Opening Loading) used in fracture mechanics tests.

Preliminary calibration makes it possible to calculate crack length (a) referring to measured potential difference, and so deduce from it a propagation rate da/dt.

This monitoring is ensured through various techniques, which rely on relating measured parameters to crack length.

Once the test has been performed, the specimen undergoes destructive examination to check the cracking depth revealed by electrical monitoring. Corrective factors may be applied if need be.

Figure 52 illustrates the experimental device as in practice, with the specimen fitted with its current and potential drop wirings.

Figure 53 displays an example of electrical monitoring results as obtained on an **Alloy-600*** specimen tested in a PWR primary environment. The average rate obtained by processing the potential values measured through electrical monitoring is in agreement with the rate determined on the failure pattern after testing.

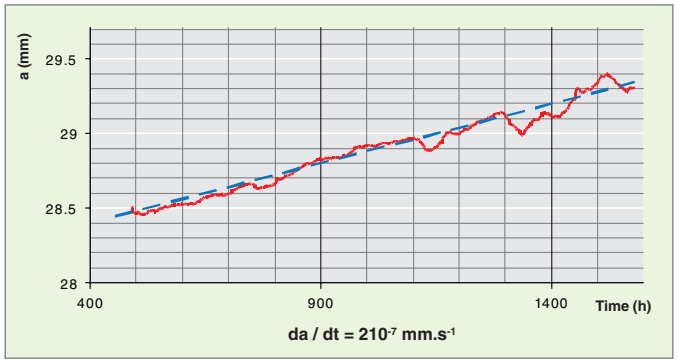

Fig. 53. Evolution of the length a of a crack deduced from the electrical signal after calibration with the overall crack length at the end of the test (red curve). The linear evolution of the crack length during the test is shown in blue for comparison.

Limits and benefits of the method

In its principle, this technique allows the average length of a crack to be evaluated through specimen thickness. So it is particularly efficient in the case when the propagation front is rectilinear and localized in a unique plane. On the contrary, it is less relevant in the following cases:

- Crack branching,
- Heterogeneous propagation front (large-grain materials, heterogenous microstructure).

Such cases can be encountered in particular during SCC cracking of deposited materials (Alloy 82, Alloy 182) or strongly cold worked materials (cold worked stainless steel). Figure 54 shows an example of rupture pattern obtained on a cold-worked 316L-stainless steel CT specimen tested in a PWR primary environment. The fatigue precracked zone formed outside this environment is followed by a homogeneous propagation zone and a highly heterogeneous propagation zone. The last two zones are obtained through cracking in a PWR primary environment.

In addition, in the case of little opened cracks such as most of those resulting from SCC, it can sometimes be observed after testing that there remain traces of former ligaments unbroken at the back of the propagation front during the SCC test. These ligaments act as electric short-circuits and induce a decrease in potential values, so that the real length of the crack may be underestimated. As a general rule, all contacts between crack edges (closed cracks, little opened cracks, occurring oxide…) entail inaccuracies.

Last but not least, signal instabilities have often been observed, which do not always have identified causes, and cannot be attributed to crack propagation. These instabilities generate a background noise which is not easily distinguishable from crack progress.

Despite these limitations, the crack length monitoring technique based upon direct current potential drop measurement is widely used: it makes it possible to access to cracking rate values, and be quickly informed about cracking rate depend-

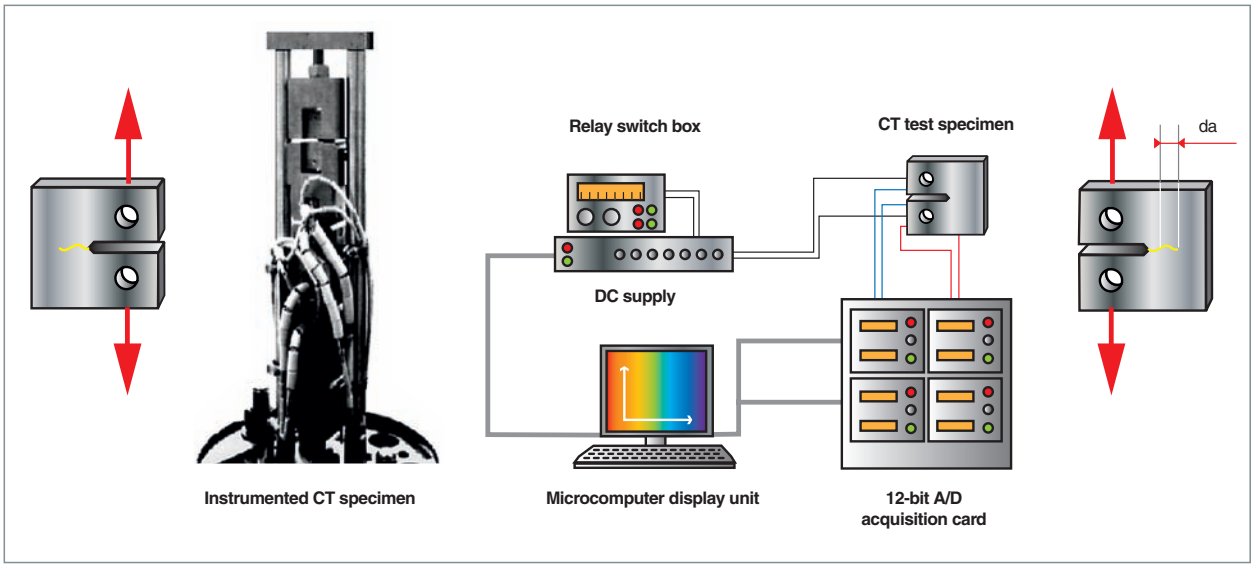

Fig. 52. View of a specimen instrumented for monitoring crack growth rate through potential drop measurement, and schematic representation of the data acquisition system.

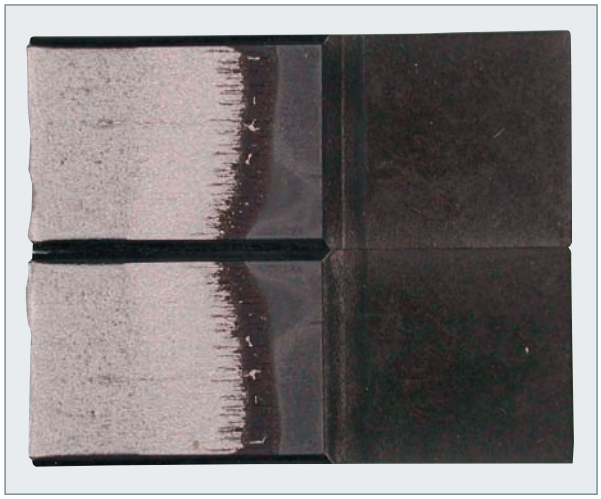

Fig. 54. View of a SCC rupture pattern of a cold worked stainless steel (cracking in a PWR primary environment).

ence on such parameters as temperature, solution chemistry (pH, redox…) by varying these parameters during tests. However, it is worth mentioning that the absolute rate values so determined should be considered cautiously and counterchecked with other methods, particularly rupture pattern observation after testing.

Internal corrosion of Zircaloy clads: iodine effect

In pressurized water reactors, after long-term rated power operation, the clad is deformed by creep, and comes into contact with the **fuel pellet***. This contact most often takes place in the middle of the second irradiation cycle: the pellet/clad gap is then closed. From this state, any significant variation in linear power density induces high thermal expansion in the pellet, thereby causing its deformation due to the strong contact and the nearly constant clad temperature. Coupled stresses will be the highest in pellet-to-pellet gap. On the whole, referring to fuel rod standard geometry, diameter expansions induced by power density variations are about 17-25 µm per increment of 100 W.cm^{-1}. In addition, this high rise in power density and, so, in fuel centerline temperature entails an increase in fission products release. Among the latter iodine plays a major role, for it may induce stress corrosion cracking in zirconium alloys, and may cause clad failure. In the early ages of water-cooled reactors (PWRs, BWRs or CANDUs), series of similar failures took place following sharp startups. Today power increase rates as well as instantaneous local power levels are limited. Many stress corrosion tests of zirconium alloys in presence of iodine have been conducted on a variety of Zr alloys, both irradiated and not irradiated. They have demonstrated that initially intergranular cracking is propagated through quasi-cleavage and plastic deformation (grooves) (Fig. 55). Quasi-cleavage preferentially occurs on the base planes of zirconium crystals. Consequently, clad tube susceptibility will be very highly dependent on their crystallographic texture. The more radial the texture will be, the less sensitive the clad will be to iodine-induced stress corrosion cracking (I-SCC).

Experiments undertaken at the CEA to describe the phenomenon of I-SCC have first consisted in internal pressurization testing of irradiated or unirradiated cladding hulls in iodine atmosphere. These tests have been performed, first, on smooth clads in order to determine materials sensitivity to I-SCC as a function of dose and the environment (Fig. 56), and secondly, on pre-cracked clads so as to determine crack propagation rates (Fig. 57).

The CEA's latest research efforts in relation to iodine-induced SCC have focused on developing a I-SCC phenomenological model liable to be set up in Codes TOUTATIS, METEOR and ALCYONE dedicated to fuel rod behavior description in power ramp situations [3]. This I-SCC model is based upon a local approach of damage mechanics, featuring both a viscoplasticity / damage coupling and a mechanics / iodine diffusion coupling. It is defined using a local damage law (Kachanov's law) coupled with the clad viscoplastic behavior. This coupling is displayed as the full loss of material stiffness in the areas where damage has reached a critical value (that is, where the

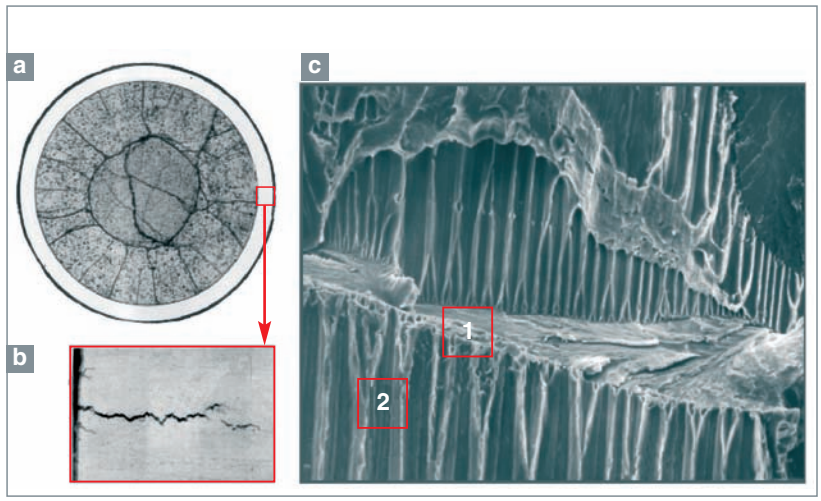

Fig. 55. Stress corrosion cracking of a clad during a power transient.
a) and b) Clad cracking during a power variation in a test reactor.
c) Stress corrosion cracking in presence of iodine during a laboratory test.
Mark 1: quasi-cleavage on Zr base planes.
Mark 2: plastic deformation grooves.

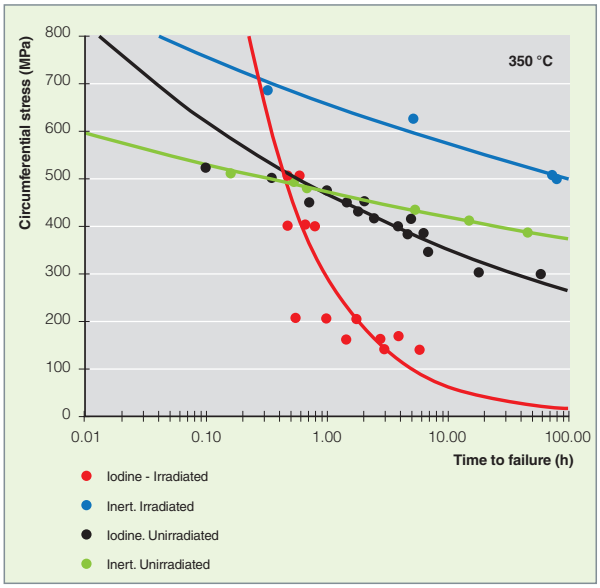

Fig. 56. Evolution of time to failure as a function of circumferential stress for irradiated or unirradiated Zircaloy-4 alloy, stressed under internal pressure at 350 °C in inert or iodine atmosphere. From [2].

material has undergone failure). Besides, the local damage law depends upon the evolution of local iodine amount. It is worth mentioning, too, that the latter is taken into account using a diffusion equation dependent on local mechanic quantities.

A new pressurization device in iodine environment has also been developed as part of the PELLECI project. The interest of this device is to enable cold working / stress-relieving tests to be performed on irradiated fuel rod clad hulls in iodine atmosphere (Fig. 58). This type of test makes it possible to better account for the type of stress imposed on clad by fuel under pellet-clad interaction conditions and, so, to better describe the I-SCC phenomenon.

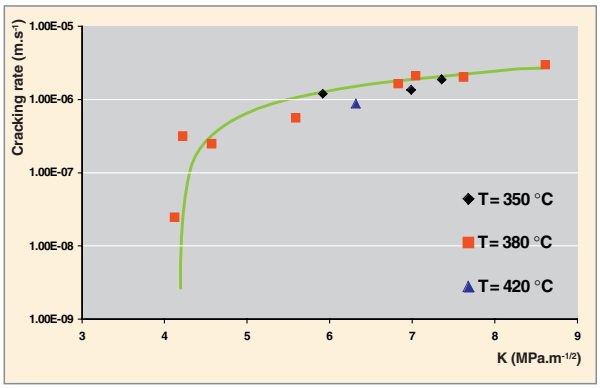

Fig. 57. Evolution of the cracking rate in I-SCC versus the initial stress intensity factor applied for Zircaloy-4 alloy stressed under internal pressure, at different temperatures. From [3].

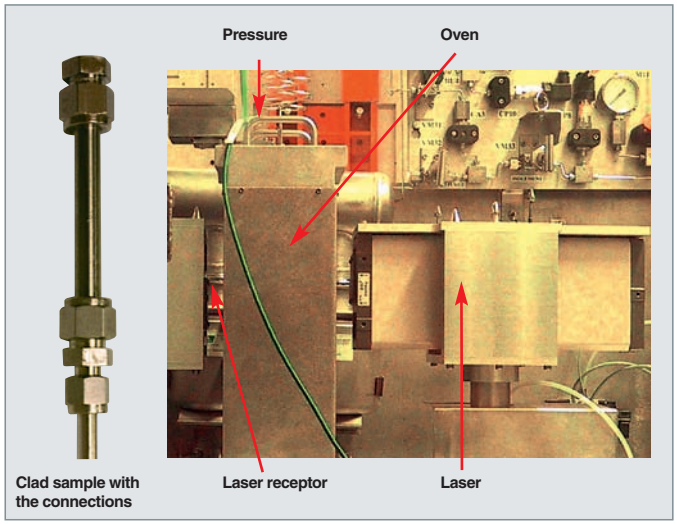

Fig. 58. View of the new device designed to investigate iodine-induced SCC of zirconium alloys in a shielded cell.

Stress corrosion cracking of nickel base alloys: hydrogen influence

Hydrogen introduced into the primary coolant circuit of pressurized water reactors is intended to avoid occurrence of oxidizing species (mainly oxygen and hydrogen peroxide) generated by water radiolysis, that may entail prejudicial effects for both primary system materials and fuel clad corrosion status. In order to maintain these reducing conditions a dissolved hydrogen concentration of 25-50 mL(TPN).kg^{-1} is prescribed in specifications for chemical conditioning of primary environment.

Laboratory results available in the late eighties had evidenced that an increase in the H_2 content had a rather prejudicial influence on stress corrosion cracking (SCC) of **Alloy 600***. Therefore, it had been recommended to target a nominal hydrogen content of 25-35 mL(TPN).kg^{-1} even though the overall range of authorized dissolved hydrogen contents was kept broader, as mentioned in the previous paragraph. These findings were issued from initiation tests performed at temperatures higher than or equal to 360 °C, and covered a wide range of hydrogen concentrations. Since those early findings, new tests have been carried out at temperatures and dissolved hydrogen contents more representative of PWR operating conditions, thereby allowing the effect of high hydrogen contents on alloy sensitivity to cracking to be adjusted and precised.

*Hydrogen and apparent crack initiation in Alloy 600**

Laboratory tests which aim at evidencing SCC crack initiation dependence on dissolved hydrogen content, are conducted with overall imposed strain specimens, most often of type RUB ("Reverse U-Bend") (see *supra*, on page 37, "Test Tools for Investigating Stress Corrosion Cracking"). Results obtained are plotted as time to cracking versus hydrogen partial pressure. The fast propagation phase of stress corrosion cracks is short if compared with the cumulated phases of incubation and slow propagation. So tests allow a "time to failure" to be determined, this term referring to the time required for the main crack to reach the fast propagation stage, generally termed "apparent initiation time". Yet, these results do not make it possible to study the dependence of the "real" incubation time or slow propagation stage on hydrogen partial pressure.

Analyzing the obtained results enables the following main points to be evidenced:

- Whatever the temperature may be, **Alloy-600*** sensitivity to SCC is strongly enhanced when hydrogen partial pressure increases from a few tenths of kPa to an approximate 10 kPa;

- As regards the highest temperatures (360 °C), a lower sensitivity seems to occur at partial pressures higher than 100 kPa. Nevertheless, experimental data are lacking to know whether the same phenomenon takes place at temperatures lower than or equal to 330 °C;

- Concerning partial pressures between 10 and 100 kPa, some results show that the material's sensitivity does not evolve significantly, especially at high temperatures. Yet, other results show a decrease in this sensitivity (Fig. 59).

As shown in the analysis of results available in literature, the maximum susceptibility to initiation can be observed for a hydrogen partial pressure range including the thermodynamical equilibrium potential of Ni / NiO. This redox equilibrium Ni / NiO corresponds with a partial pressure of about 35 kPa, at a temperature of 360 °C. In this very range, too, are to be found the highest values for the thickness of, respectively, the oxide film and the substrate's chromium-depleted layer (that is, the area located immediately under the oxide layer). According to this assumption, susceptibility to initiation would be correlated with the thickness of oxide layers occurring on materials. In other terms, the thicker these oxide layers, the higher susceptibility to SCC initiation.

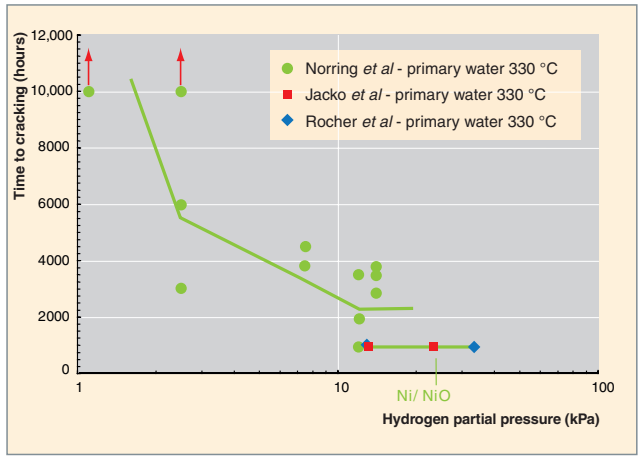

Fig. 59. Influence of hydrogen partial pressure on crack initiation in Alloy 600. Laboratory testing performed at 330 °C.

*Hydrogen and crack propagation in **Alloy 600***

Most of the investigations conducted in this context were performed on pre-cracked specimens. This type of test is chiefly intended to measure propagation rates relating to the fast crack propagation regime. In particular, a few results were gathered using smooth specimens tensile-stressed at slow strain rates. Detailed analysis of slow strain-rate tensile tests may enable crack propagation rates respectively associated with slow and fast propagation phases to be distinguished. Early investigations relating to SCC crack propagation were focused on tubular materials. Most tests were performed with notched tubular specimens. The aim was to assess crack propagation rate through the **roll*** transition zones of steam generator tubes (these tube zones being strongly cold worked as a result of the internal expansion treatment during tube fixation through partition plates). The first tests were carried out at 360 °C. For faster crack propagation rates can be obtained at high temperatures, which makes it easier to conduct parametric experimental tests. Later on other investigations were performed on bulk materials behavior following in-service observation of cracking on PWR **vessel*** head adapters. These last studies were carried out at temperatures between 290 °C and 330 °C.

The results obtained with notched tubular specimens make evident a slower rate of propagation for low hydrogen partial pressures (< 10 kPa) as well as for high hydrogen partial pressures (> 100 kPa). As regards partial pressures ranging from 10 to 100 kPa, i.e. concentrations of 15-150 mL(TPN).kg^{-1}, the propagation rate does not seem to evolve significantly.

As for crack initiation, most of available results dealing with crack propagation at 360 °C (Fig. 60) give evidence of the existence of a hydrogen partial pressure range in which the material's sensitivity is maximum. This partial pressure range corresponds with the thermodynamic equilibrium range Ni / NiO. For some tests, the very low (or even null) propagation rates observed for low hydrogen partial pressures (< 10 kPa) could result from an increase in the threshold **stress intensity factor*** K_{ISCC}: its value corresponds to the threshold at which the intergranular cracking phenomenon occurs. The same phenomenon could also account for the decrease in crack propagation rate with high hydrogen contents. According to this hypothesis, the stress intensity factor applied during the tests would thus get lower than the threshold K_{ISCC} at high and low dissolved hydrogen contents.

Regarding temperatures of 290 °C and 330 °C, there is not a sufficient number of results to inform precisely about the influence of hydrogen partial pressure on crack propagation. However, available results are not in disagreement with the existence of a maximum rate for an intermediate partial pressure of about 30 kPa, as is apparently the case at a higher temperature.

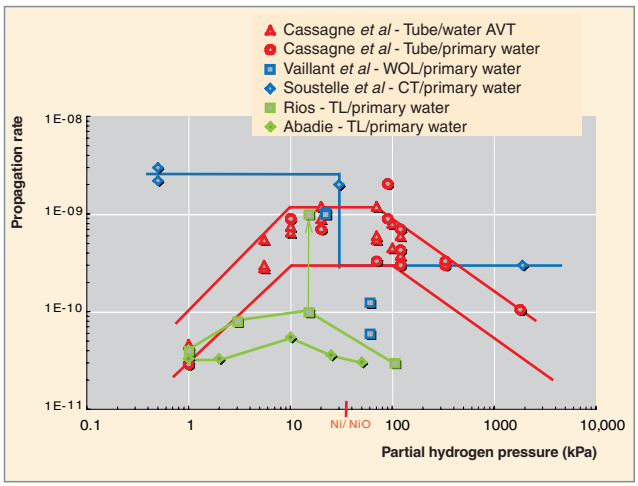

Fig. 60. Crack propagation rate dependence on partial hydrogen pressure. Tests performed at 360 °C.

At the temperature of 330 °C, the threshold stress intensity factor K_{ISCC} increases when hydrogen partial pressure decreases from 25 kPa to about 1.3 kPa. Similarly, for high partial pressures of dissolved hydrogen higher than 30 kPa, the threshold stress intensity factor K_{ISCC} increases with partial pressure. Thus no crack propagation can be seen for a stress intensity factor K of 15 MPa.m$^{1/2}$ when hydrogen partial pressure is of 1,900 kPa, while a K_{ISCC} of only 9 MPa.m$^{1/2}$ can be observed for a hydrogen partial pressure of 30 kPa.

Concerning the role of dissolved hydrogen in the case of Alloy-600 intergranular cracking, results of the various laboratory tests corroborate a direct effect of the corrosion potential on material susceptibility to the cracking phenomenon. Historically, sensitivity to the phenomenon of Alloy-600 stress corrosion cracking at imposed potentials was first mentioned by Coriou *et al.* [4]. As shown on Table 1, the cracking phenomenon increases at the cathodic potentials imposed by coupling Alloy 600 with less noble materials such as carbon steel.

Table 1.

Occurrence of the Alloy-600* cracking phenomenon under galvanic coupling conditions		
Galvanic couple	Number of cracked specimens after 12,000 hours (optical microscopic examination)	
	Water	LiOH to pH = 10.5
No coupling	0/9	0/9
Gold-coupled	0/9	0/9
Platinum-coupled	0/9	0/9
Coupled with stainless steel 10/18	1/10	0/9
Coupled with mild steel	4/10	2/10

This high sensitivity to corrosion potential is expressed on Figure 61, which emphasizes the strong dependence of Alloy-600 intergranular cracking on the different values of corrosion potential [5].

Optimum hydrogen content in the primary circuit water of nuclear reactors is still a highly debated issue, even though operating specifications (currently 25-50 mL(TPN).kg^{-1}) have not evolved. Today it is a well-known fact that Alloy-600 sensitivity to stress corrosion cracking (SCC) is particularly pronounced for hydrogen contents ranging from 25 to 50 (TPN).kg^{-1}, which induces to leave this hazardous range. For instance, in the EPR reactor [6], the hydrogen content of the primary coolant circuit could be held between 10 and 20 mL(TPN).kg^{-1}.

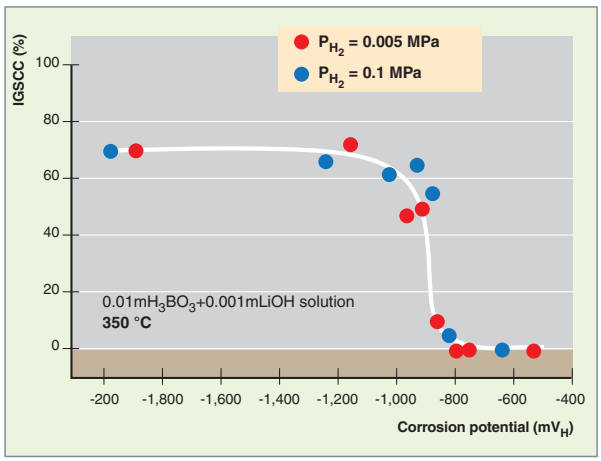

Fig. 61. Evolution of **Alloy-600*** sensitivity to intergranular cracking versus the corrosion potential values and two values of hydrogen partial pressure [5].

Influence of metallurgical state on stress corrosion cracking

Hydrogen concentration in primary environment, primary environment temperature, and mechanical stress applied to components deeply influence Alloy-600 sensitivity to SCC, and so do the material's metallurgical properties. The analysis of the microstructure role distinguishes "thin" materials such as Steam Generator (SG) tubes, and representative "bulk" materials such as vessel head adapters or partition plates.

As displayed on Figure 62, SCC sensitivity of Alloy-600 tubular materials substantially varies from one alloy heat to another. This "heat-to-heat variability" (or "metallurgical variability") has spurred a number of studies, the main results of which are fully described hereafter.

Steam generator tubes in the "Mill Annealed" (MA) state

It is difficult to pinpoint the grain size influence on Alloy-600 resistance to SCC, as this size is also related to carbon content, carbide precipitation and MA temperature. Yet, it can be seen that small-grain structures generally exhibit poor resistance to SCC, even though the latter cannot be dissociated from the influence of higher mechanical characteristics.

Tubes with the best SCC resistance display the following characteristics:

- A grain size lower than 20 or 30 µm, with a carbon content higher than 180 ppm,
- Or a carbon content lower than 180 ppm (whatever the grain size may be).

The studies carried out made evident a relationship between tube sensitivity to SCC and the localization of the chromium carbides contained in these tubes. It could be observed that tubes with the best corrosion resistance display a semicontinuous distribution of intergranular carbides and few intragranular carbides. In contrast, carbides in the most sensitive materials are mostly intragranular and uniformly distributed (Fig. 63 and 64).

It is assumed that grain boundary sensitization to SCC does not exert any harmful effect upon the material's SCC in a reducing environment. A beneficial effect may even be assigned sometimes to the presence of the chromium-

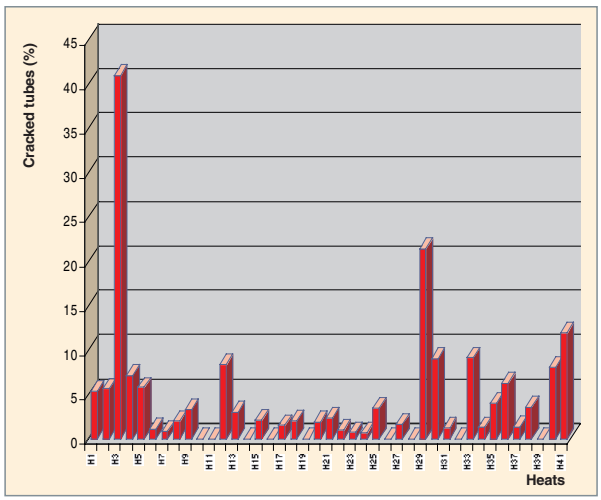

Fig. 62. Percent of cracked tubes in the roll transition zone after about 40,000 hours in operation.
Illustration of the "heat-to-heat variability" [1].

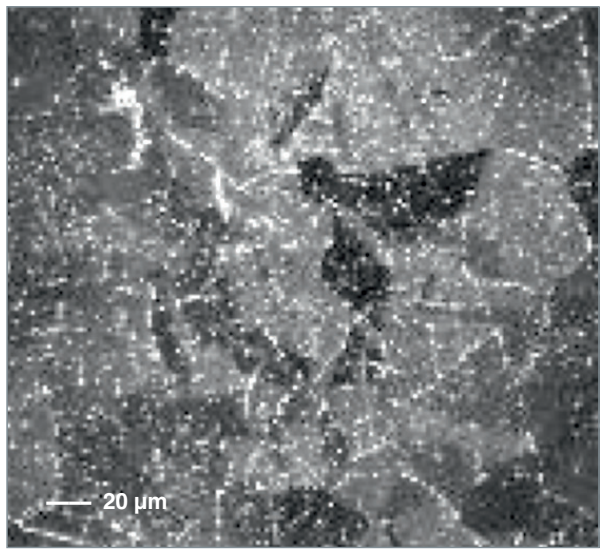

Fig. 63. Typical example of *a priori* SCC-sensitive microstructure.

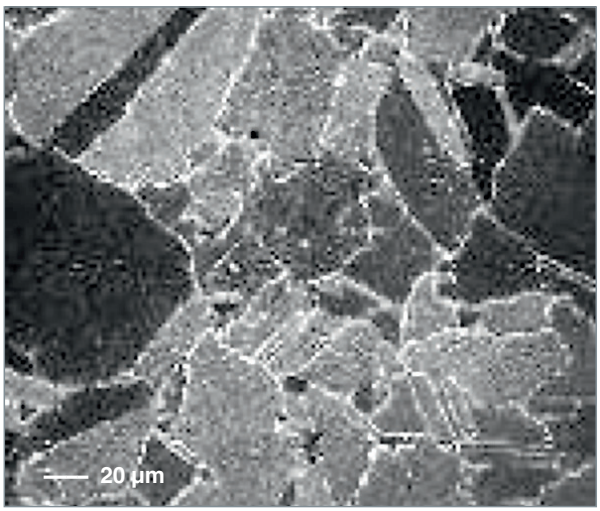

Fig. 64. Typical example of *a priori* SCC-insensitive microstructure.

depleted area at the grain boundary. Yet, this effect cannot be directly attributed to the chromium-depleted area itself (a nickel-rich area, too), although it contains intergranular carbides whose beneficial effect upon SCC is well-known.

Steam generator tubes after thermal treatment (16 hours at 700 °C)

The aim of the 16-hour thermal treatment at 700 °C is to reduce residual stresses in the tube. It is also intended to increase intergranular carbide density and intragranular carbide size. It is worth noting that after this treatment the tubes are little or not **sensitized***.

The effect of this thermal treatment differs according to the products considered. For tubes with the highest sensitivity, a beneficial effect can generally be observed. For the others, it may happen sometimes that no significant effect can be observed.

Bulk materials

A multivariate analysis of the structure (taking into account inter- and intragranular precipitations) and a statistical analysis of the corrosion test results allowed correlations to be set up for these bulk materials, which may sometimes be very heterogeneous.

It can be clearly seen that:

- Materials with a substantial intergranular precipitation (> 40%) and a low intragranular precipitation (< 2%) display good resistance to SCC;
- SCC may occur in materials which exhibit either a low intergranular precipitation (< 40%) or a high intragranular precipitation (> 2%). The products with the highest sensitivity are those with a carbide distribution reproducing a former grain boundary network.

Influence of surface cold working on stress corrosion cracking

During their fabrication, tubular or bulk components may be cold worked in volume or in surface. Surface cold working may result from mechanical machining (milling, lathing, grinding…) or surface treatment (sandblasting, peening…), and may introduce residual tensile or compressive stresses into the surface of materials. Compressive stresses generated by peening or shot peening processes prevent the occurrence of SCC cracks, but in the case of plastic strain they are turned into tensile stresses, and the resulting stress levels may be extremely high.

Constant-load tensile tests were performed on specimens displaying layers which had been cold worked at different depths (20 µm, 140 µm and 270 µm), but showed identical surface stresses (about 1050 MPa) for a true internal stress of about 650 MPa. Hence the following results [7]:

- A low-depth cold worked layer (Fig. 65) does not significantly affect the material's time to cracking and the component lifetime. On the contrary, a high-depth cold worked layer reduces the material's time to cracking by a factor 3 (Fig. 66);
- As shown by the "morphological model" [8], the slow crack propagation rate is accelerated by the cold worked layer while the fast propagation rate is not;
- As also displayed in this model, the slow propagation rate / fast propagation rate transition takes place for depths which are all the lower as the cold worked layer is deeper. The value of the corresponding threshold stress intensity factor does not seem to be substantially affected by the material's cold working.

SCC resistance of Alloy 600 in the MA state is considerably improved by the presence of intergranular carbides, whereas the presence of intragranular carbides may degrade it. On the other hand, high mechanical characteristics and small-sized grains are generally prejudicial to SCC resistance. If the material has not been strongly cold worked, the additional 16-hour thermal treatment at 700 °C considerably improves the material's SCC resistance.

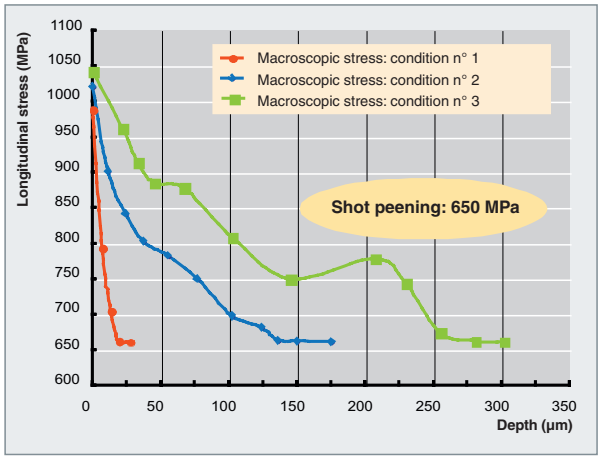

Fig. 65. Longitudinal stress versus cold worked layer depth [7].

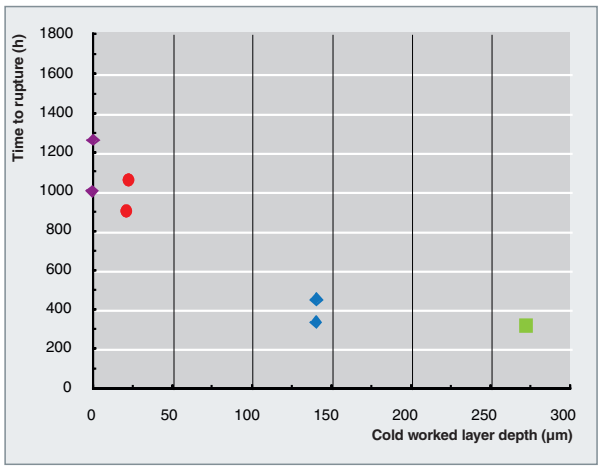

Fig. 66. Influence of cold worked layer depth on time to cracking [7].

*Modelling stress corrosion cracking of Alloy 600**

Since Alloy-600 SCC in PWR primary environment was evidenced (see the inset "The Coriou effect" in the introduction to this Chapter, p. 37), a number of mechanisms has been proposed in literature to account for this phenomenon. Among these models, two are considered as the most suitable for the case of Alloy-600 cracking in PWR primary environment, i.e. the model based on internal oxidation, proposed by Scott, and the models relying on hydrogen embrittling effect and hydrogen / material interactions. The basic physico-chemical processes liable to occur in these models are the following: oxygen and hydrogen diffusion, vacancy / diffusion kinetics interactions, hydrogen / plasticity interactions, and embrittlement mechanisms related to oxygen and hydrogen diffusion through the material [9].

In order to improve knowledge of these mechanisms, targeted experiments were carried out. Their aim was to collect the data still lacking, especially as regards oxygen and hydrogen transport, and validate the steps in the models. Some of the experiments were conducted on model microstructure materials obtained through thermal treatment of a presumably SCC-sensitive alloy heat. Last but no least, oxygen and hydrogen isotopes were used to improve hydrogenated and oxygenated species detection.

As a result of these targeted experiments, fine characterizations could be achieved through Scanning Electron Microscopy, Transmission Electron Microscopy (conventional imaging and high-resolution High-Angle Annular Dark Field (HAADF) analysis), Secondary Ions Mass Spectrometry (SIMS), nano-SIMS, and hydrogen dosing. These analyses made it possible to evidence oxygen and hydrogen isotope penetrations at the grain boundaries of uncracked materials which might coincide with SCC crack initiation sites. This raises the question as to whether these penetrations are continuous: in some cases, they might occur as nodules distributed discontinuously at the grain boundaries. On the other hand, no oxygen penetration could be evidenced at the crack forefront on cracked materials.

A fine description of the oxides present in cracks and crack initiation sites was put forward taking into account crack specific features (active or inactive cracks). An example of these characterizations is shown on Figure 67. The features (nature and distribution) of the oxides present at the crack tip as well as the morphology of the chromium-depleted area enable assumptions to be advanced regarding mechanism steps. For instance, the dissymmetrical aspect of the chromium-depleted area, which is only localized on one side of the grain boundary, is to be related to the strain difference between the grains located on either side of the grain boundary. The most deformed grain is the one that contains the highest number of flaws, which might accelerate species diffusion kinetics. Besides, hydrogen present in the material might interact with local strains, and alter species transport phenomena [10].

Last but not least, oxygen diffusion calculations based on SIMS profiles show that in PWR primary environment and for a deformed material, coefficients of oxygen diffusion at alloy grain boundaries could be several orders of magnitude higher than those proposed in literature, and would thus be consistent with experimentally determined cracking rates. In addition, as shown by calculations of hydrogen absorption and desorption, the hydrogen content in the material experiences a very fast rise, and gets saturated after four hours (Fig. 68). Given hydrogen fast diffusion, the influence of hydrogen from primary environment cannot be negligible.

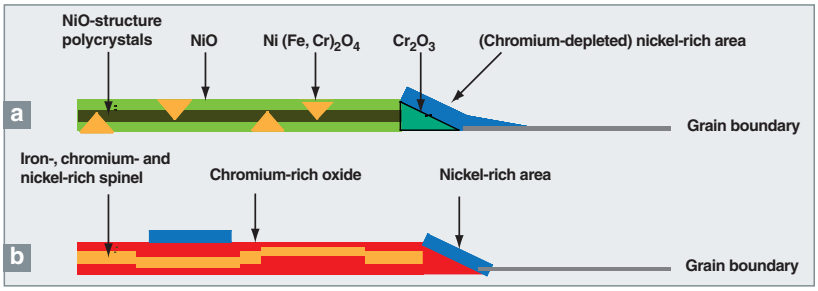

Fig. 67. Schematic representation of oxides contained in a stress corrosion crack, which has been formed in a U-bend Alloy-600 specimen exposed to PWR primary environment. (a) Case of an active crack in a typical grain boundary. (b) Case of a passive secondary crack [11].

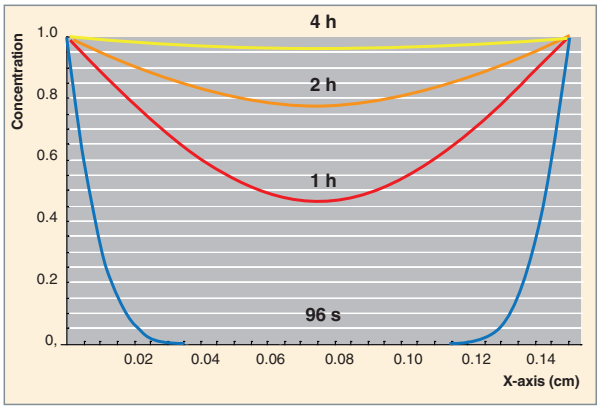

Fig. 68. Hydrogen concentration profile in a specimen of Alloy 600 1.4 mm thick immersed into a PWR primary environment at 340 °C, after 96 s, 1h, 2h, and 4h.

The final goal of targeted experiments, characterizations and calculations is setting up correlations between the microstructure of these materials, their oxidation, their local micromechanical behavior, and SCC crack localization. This whole set of data, coupled with corrosion data, should enable SCC behavior of nickel base alloys to be modelled.

Stress corrosion cracking of stainless steels

As regards Pressurized Water Reactors (PWRs), only in relatively recent times have concerns been expressed about the risk of stress corrosion cracking in stainless steels. Such is not the case for Boiling Water Reactors (BWRs), in which the intergranular cracking phenomenon affecting austenitic stainless steels in the reactor coolant pipe could be observed as early as the 1950-1960s. In the case of BWRs, this cracking phenomenon is mainly due to the conjunction of the following parameters: residual stresses present in welded areas, stainless steel sensitization due to chromium carbide intergranular precipitation related with ill-managed welding operations, and occurring residual oxygen contents coupled with radiolysis in the BWR environment (i.e. an average of 200 ppb), which only consists of high-purity water. As regards PWRs, 304L and 316L austenitic stainless steels make up the major part of internals components and the reactor coolant pipe, as well as components of the emergency core cooling systems (ECCS) and the residual heat removal systems (RHRS) with the associated valves. Cracking cases observed on austenitic stainless steels have first been related to accidentally occurring pollutants in the primary coolant circuit, mainly oxygen (introduced during unit outages), chlorides, and, less frequently, sulfates.Theses cases have generally proved to be sporadic (e.g. ECCS and RHRS dead legs) or, more rarely, generic (CANOPY-type connections). In the late nineties, a new case of stress corrosion cracking started to affect austenitic stainless steels, this time in a primary environment with a nominal composition, but strictly in the case of materials that seemed to be strongly cold-worked (which is the case of pressurizer heating cane clads). Jointly with EDF teams, the CEA dedicated several of its programs to the various cases of SCC cracks in austenitic stainless steels [12, 13]. The latter are summarized hereafter for the two main conditions investigated, i.e. the nominal primary environment, and the non-nominal primary environment.

Impurity influence in the primary system of water-cooled reactors

The investigations conducted were intended to determine the SCC susceptibility ranges of quenched austenitic stainless steels assessing them in terms of allowable concentrations in chlorides, sulfates and oxygen. Most of the tests were performed on the SCCME's CoPo loop (Fig. 69), and enabled slow-strain-rate tensile SCC tests to be carried out on austenitic stainless steels in flowing environment, with online measurement of the dissolved oxygen content. The tests were generally conducted at a 200 °C temperature (i.e. the operating conditions of CANOPY connections) in presence of, respectively, chlorides and oxygen, and sulfates, and, towards the end of the research program, in presence of complex pollutions, typically chloride / sulfate / oxygen pollutions. As revealed in these tests, relatively high chloride contents are needed to start stress corrosion cracking of quenched stainless steels in presence of chlorides alone and of oxygen. Yet, when these contents have been reached, a very fast transgranular cracking can still occur for low values of applied stress (Fig. 70). By comparison, if cracking in presence of sulfates alone does not require oxygen, it is worth mentioning that stainless steel sensitivity remains lower than that observed in chloride-polluted primary environment. Last but not least, austenitic stainless steels prove to be highly susceptible in the case of a mixed pollution of chlorides/sulfates (even for moderate contents), and in presence, simultaneously, of dissolved

Fig. 69. SCCME / LECA's CoPo Facility in which primary environment testing can be performed in presence of pollutants and with online measurement of dissolved oxygen contents.

oxygen. In the latter case, a synergetic effect of the occurring pollutants can be observed. The various resulting diagrams display the different SCC susceptibility ranges of steels in terms of pollutants dissolved in primary environment (Fig. 71 and 72).

Cold working influence on stainless steel SCC

Cold working is the first factor that favors emergence of SCC cracks in austenitic stainless steels put in nominal hydrogenated primary environment. The investigations performed have first allowed the cracking observed on site to be reproduced through slow-strain-rate tensile tests on steels which had undergone a complex cold work (pressing or

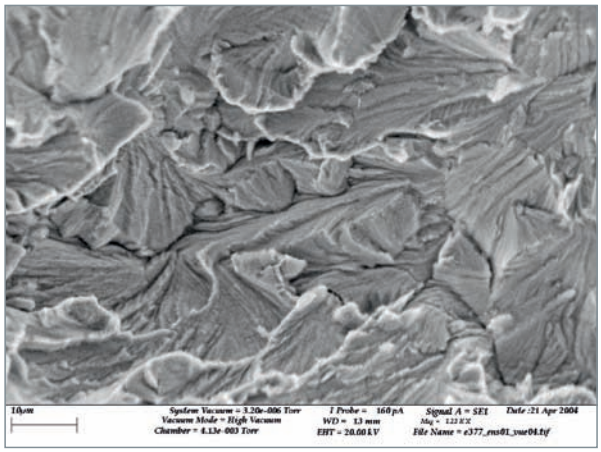

Fig. 70. Transgranular stress corrosion cracking as obtained on steel-304L in presence of chlorides and oxygen dissolved at 200 °C.

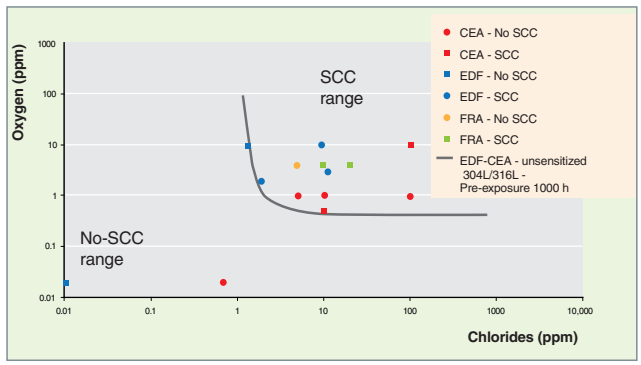

Fig. 71. Ranges of sensitivity to stress corrosion cracking of stainless steel in a primary environment that contains dissolved chlorides and in presence or absence of oxygen.

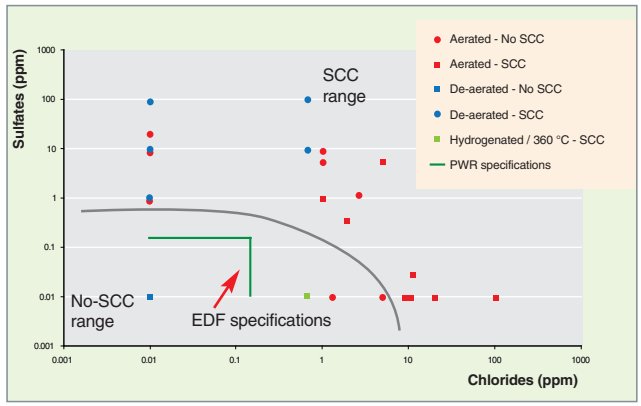

Fig. 72. Ranges of susceptibility to stress corrosion cracking of stainless steel in a primary environment containing dissolved sulfates and chlorides, and in presence or absence of oxygen.

rolling+pressing). These first tests have demonstrated that, in the case of complex cold work, fast cracking with an intergranular or transgranular mode could take place in austenitic stainless steels, even in a strictly nominal primary environment (Fig. 73). Cold working is not a pre-required phenomenon *stricto sensu*, as its effect on steel sensitivity to cracking is strongly determined by the mode of cold work imposed. Thus, steels that have undergone a fairly severe cold working (e.g. 90% rolling) may show no susceptibility to cracking. In contrast, initial compressive stresses (prior to a tensile test) do exhibit a critical penalizing effect on the sensitivity of austenitic stainless steels, hence the strongly sensitizing effect of modes of cold work such as shot peening and pressing. For a given cold work mode, a sensitivity threshold in terms of initial hardeness before test can be observed around 300 Hv on 304L steel (Fig. 74). This threshold also corresponds with that observed in the case of cold-worked materials exposed in boiling water reactors (BWRs). As displayed in long-time initiation tests (e.g. 18,000 hours) under strictly static loading (imposed deformation, constant load), initiation is quite difficult in austenitic stainless steels under static conditions, even though tests on various grades are still pending to scrutinize this issue. In contrast,

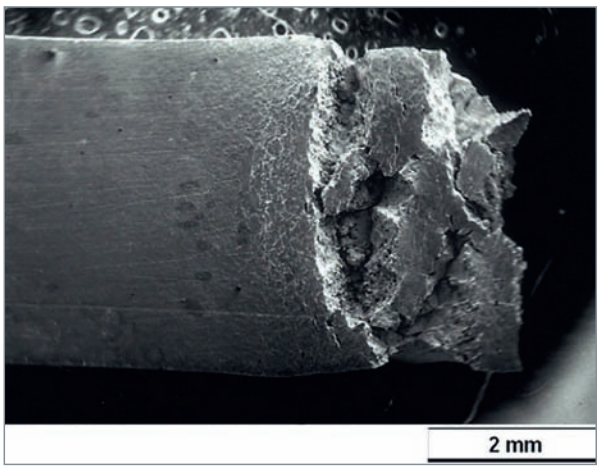

Fig. 73. Cracking observed on a V-pressed specimen which has been subjected to a slow tensile test in a primary environment at 360 °C.

intergranular propagation on CT specimens can be observed on 316L steel under constant load and at temperatures of 290 °C and 325 °C in a primary environment [14]. As a matter of fact, the temperature effect already seems to be very different from that observed in the case of, e.g., **Alloy 600***, as cracking can be seen for relatively low temperatures (e.g. 200 °C).

Ongoing works will allow SCC crack initiation conditions to be better defined for austenitic stainless steels in nominal primary environment, a major step, indeed, in the assessment of this type of risk for the whole nuclear power reactor fleet.

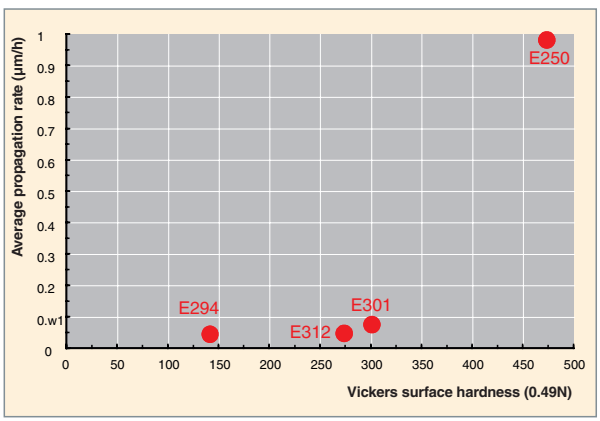

Fig. 74. Influence of surface hardness on the average crack propagation rate in steel-304L pre-cold-worked through shot-peening and subjected to tensile tests in a primary environment at 360 °C.

Irradiation influence on stainless steel SCC

Lower internals of pressurized water reactors (PWRs) are made out of 304 / 316 stainless steels, materials which have long been deemed to be unsensitive to stress corrosion cracking (Fig. 75). However, in the French PWRs of the first design (900 MW - CP0 series), a few baffle-former bolts of these structures (also referred to as “baffle bolts”), which are the most irradiated and tensile-stressed, have displayed intergranular cracking at the bolt head / body knuckle (Fig. 77).

EDF and CEA expertise provided on 316L steel cracked bolts revealed strong hardening of the material due to a significant evolution of the irradiation-induced **microstructure*** (disappearance of the initial **dislocation*** network, formation of dislocation loops and intergranular segregation). As a result of such expertises, this craking could be attributed to irradiation-assisted stress corrosion craking in PWR primary environment.

Such phenomena of Irradiation Assisted Stress Corrosion Cracking (IASCC) are complex: they can be seen as a multi-physical phenomenon, as illustrated on the opposite page (Fig. 76). For not only the three major promoters of stress corrosion cracking, i.e. the environment, the material and the stress, are to be considered, but also the irradiation effects on the material (**creep***, swelling, intergranular segregation…) and on the environment (**radiolysis***).

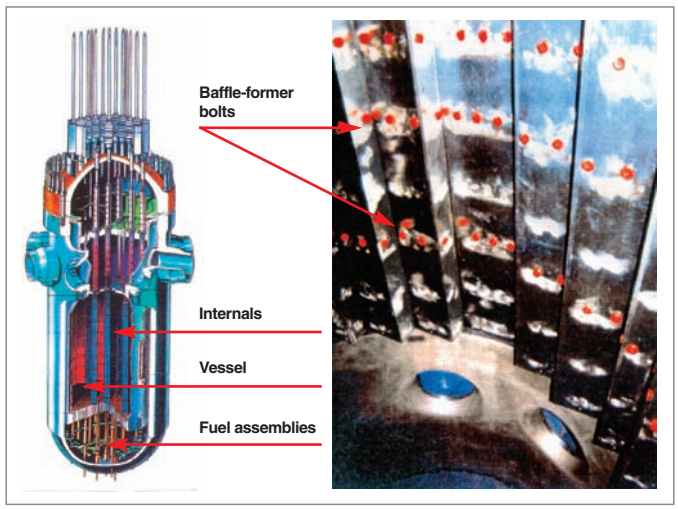

Fig. 75. View of PWR internals.

Irradiation-Assisted Stress Corrosion Cracking: a complex multi-physics phenomenon

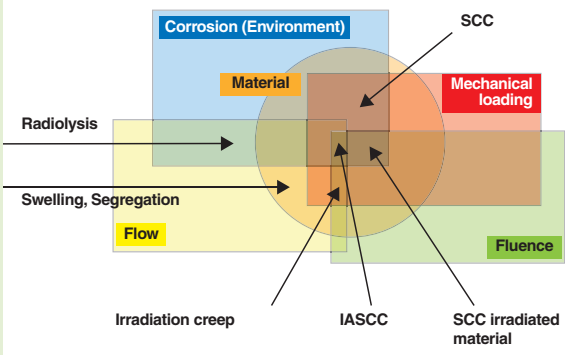

Fig. 76. The diagram hereabove displays the various phenomena likely to affect an irradiated material subjected to stress, and in chemical interaction with the environment. The IASCC (Irradiation Assisted Stress Corrosion Cracking) is a combination of all of these phenomena.

This is the reason why, in parallel to inspections and expertises conducted by EDF on PWR internals bolts, the CEA has started a R&D program, jointly with EDF and Areva NP, with the aim of studying austenitic susceptibility to irradiation-assisted stress corrosion cracking. This program consists in the following items:

- Mechanical and microstructural characterization of austenitic steels irradiated at temperatures representative of PWR operation, i.e. 300 - 400 °C;
- Specific experiments in the OSIRIS reactor (CEA Saclay) in order to investigate IASCC;
- Autoclaves set up in shielded cells (CEA Saclay's hot labs) so as to achieve stress corrosion tests on materials previously subjected to irradiation.

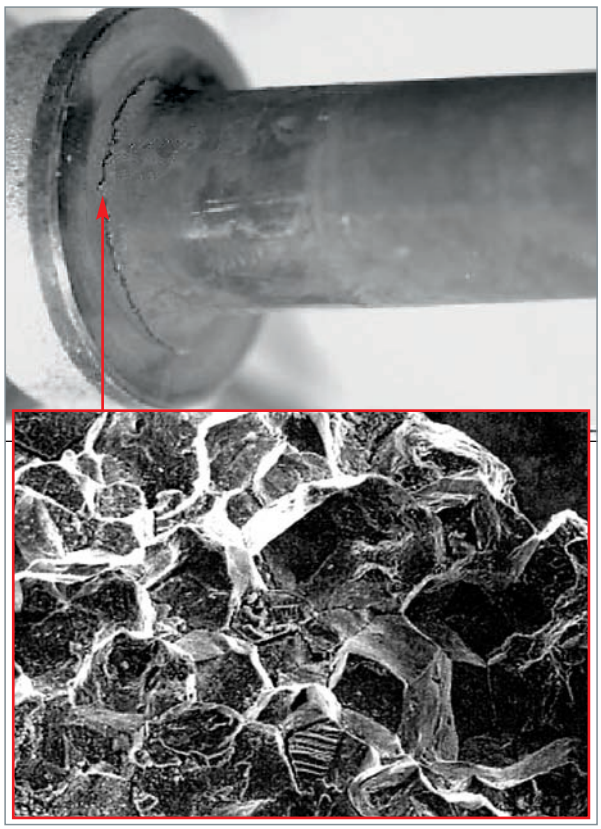

Fig. 77. Intergranular cracking of internals bolts of the CPO series. - Intergranular pattern of cracked bolts.

Susceptibility to cracking under irradiation has been tested in the OSIRIS reactor at 330 °C (the average operating temperature of PWR internals), using tubular specimens containing Al_2O_3 cores with various B_4C contents. Under the neutron flux the Al_2O_3 cores swell with rates depending on the B_4C content. Ceramic swelling induces loading with imposed strain rate, under irradiation, of austenitic-steel tubular specimens. Two experiments have been conducted in parallel, one in a neutral environment (NaK), and the other in a pressurized water representative of the PWR environment (155 bars - hydrogenated water, 350 ppm boron and 1.5 ppm lithium). Both experiments have been unloaded at regular intervals (≈ 2.5 dpa) for visual examination and diameter measurement of tubular specimens.

Cracks were made evident in austenitic steel specimens stabilized with titanium and irradiated in PWR water environment from the very first irradiation phase, i.e. for a dose lower than 2.5 **dpa***, while the same specimens irradiated in an inert environment (NaK) do not exhibit any crack, even for much higher doses, i.e. 5 dpa. Specimens made out of austenitic steels 304 and 316 do not display any crak, whether irradiated in a neutral environment or in a PWR-representative environment.

The presence of several cracks in the tubes could be made evident through visual observation of cracked specimens. These cracks possessed an intergranular feature (Fig. 78).

These observations were confirmed by metallographic expertises (Fig. 79) which have shown that cracks are fully intergranular, and are initiated in the outer face of the tube, i.e.on the surface in contact with the environment. As this cracking does not occur on specimens irradiated in a neutral environment, it is obviously due to irradiation-assisted stress corrosion cracking.

The analysis of uncracked tube diameter measurements presented on Figure 80 has been achieved on materials representative of PWR internals, i.e. steel-304 and -316, taking into account the following two items:

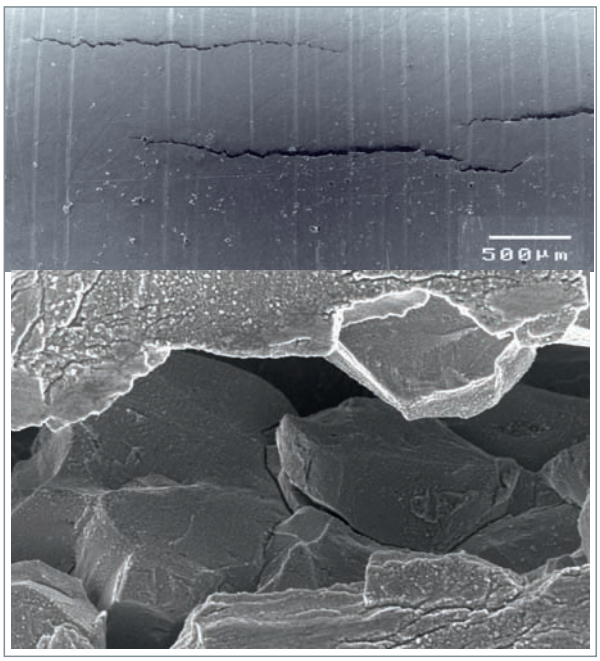

Fig. 78. Cracks in a titanium-stabilized steel following irradiation under stress in a PWR-representative environment, i.e. hydrogenated water with 150 ppm boron and 1.5 ppm Li , at 155 bars.

- The evolution of the material properties due to irradiation, i.e. the hardening of the material which evolves depending on dose, and gets saturated for doses ranging from 5 to 10 dpa depending on materials. The saturation level observed also depends on the material and its metallurgical state;

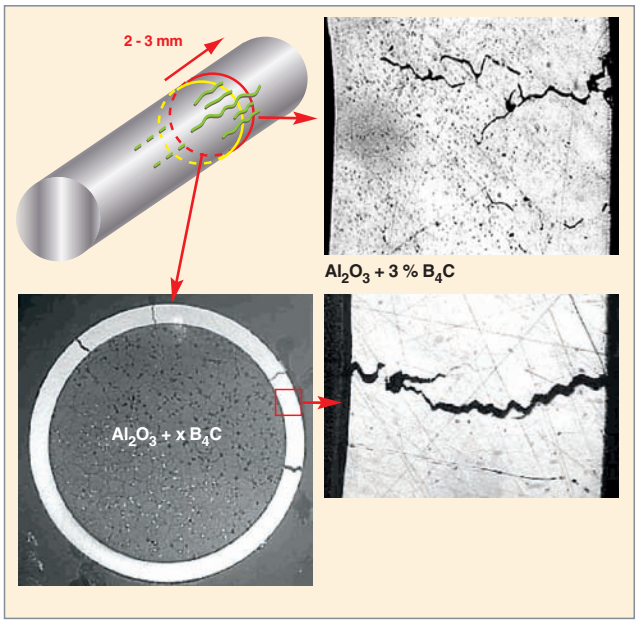

Fig. 79. Metallographical expertise results of cracked specimen of titanium-stabilized austenitic steel.

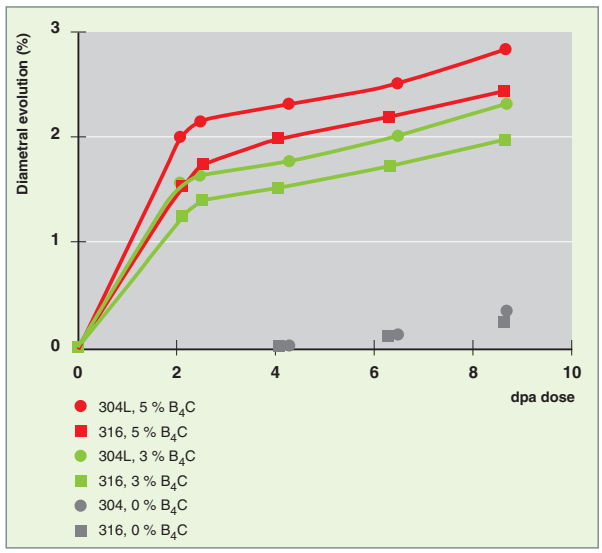

Fig. 80. Diametral strain of steel-304 and -316 tube specimens induced by irradiation in OSIRIS.

- Irradiation creep. After an incubation period, the strain induced by irradiation creep is linear with dose and stress. The value of the incubation range and the evolution rate also depend on the material and its metallurgical state.

These features have been set up for the same materials after irradiation at different doses during the two same irradiations in the OSIRIS reactor as well as after experimental irradiations at higher doses and different temperatures, conducted in the experimental reactors EBR II (USA), BOR 60 (Russia) and Phénix (France).

This analysis based upon a “finite-element” modelling made it possible to trace back to the stress status in steel-316 tubular specimens as a function of dose (Fig. 81). It can be observed that stress reaches a maximum value, apparently not dependent on the loading rate imposed by core swelling, and then

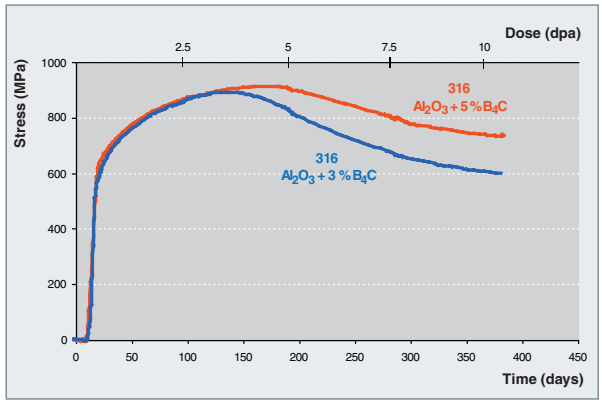

Fig. 80. Diametral strain of steel-304 and -316 tube specimens induced by irradiation in OSIRIS.

decreases for higher doses. This behavior as a function of dose results from irradiation creep, which allows for stresses induced in tubular specimens by ceramic swelling to be partially relieved. For higher doses, an equilibrium could thus be reached between stresses induced by ceramic core swelling and stress relieving induced by irradiation.

These results obtained under irradiation will be confronted with stress corrosion cracking tests on irradiated materials, especially tests under constant loading. This should help determine whether there exists a "thresthold" stress, as apparently shown by the tests performed in the OSIRIS reactor.

The corrosion loop set up in a shielded cell at the CEA Saclay's hot laboratories was licensed for operation in 2006. It consists of three autoclaves of 3 liters each, in which primary environment conditions of light water reactors (pressurized water for PWRs, or boiling water for BWRs) can be reproduced, with instantaneous monitoring of temperature, hydrogen and oxygen partial pressures, and conductivity. Water chemistry is monitored by periodic sampling. One of the three autoclaves is fitted with a tensile machine which makes it possible to conduct SCC investigations under slow strain rates, constant loading, crack propagation… (Fig. 82a and b).

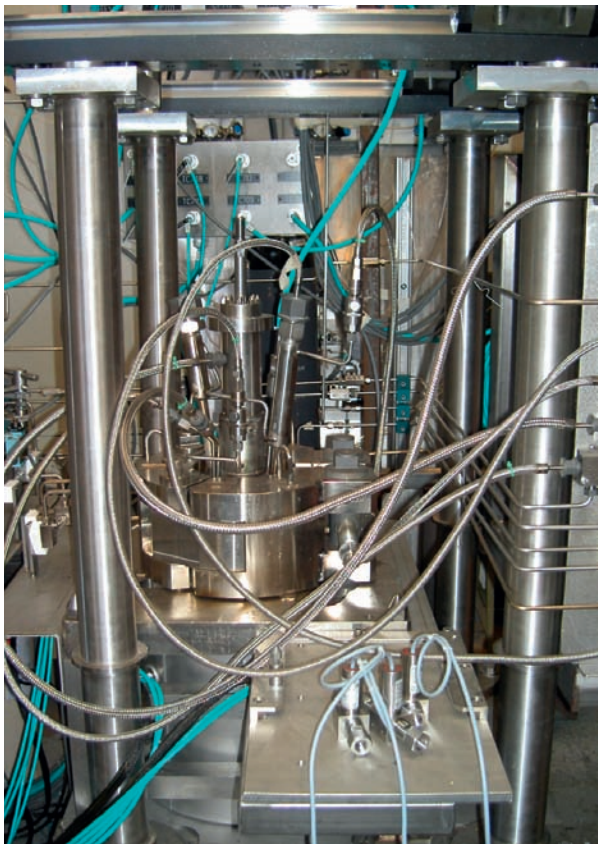

Fig. 82a. View of the autoclave fitted with a tensile testing machine and set up in a shielded cell (CEA Saclay – DMN / SEMI).

Fig. 82b. View of the autoclave fitted with a tensile testing machine and set up in a shielded cell (CEA Saclay – DMN / SEMI).

Qualifying of the shielded-cell loop started in late 2006 on specimens similar to those irradiated in the experimental reactors Phénix (CEA-EDF) and BOR 60 (RIAR – Russia), as part of the program "PWR Lifetime". The first SCC tests show that strain rates ranging from 10^{-9} to 10^{-6} s^{-1} can be reached for SSRT (Slow Strain Rate Test) tests on "small" specimens, and that the required conditions could be reached to achieve constant-load tests with a stable applied force (e.g. of an approximate 2 N).

Tests on irradiated specimens are being initiated (mid-2009). With the help of specimens previously irradiated in experimental reactors, they will make it possible to investigate the influence of irradiation parameters (temperature, dose…), and water chemistry, as well as the role of the initial metallurgical status of steels (quenching, cold working, grain size), and low variations in these materials' chemical composition.

Stress corrosion cracking has been a major industrial issue in ligh water nuclear power plants, e.g. cracking of stainless steel piping in boiling nuclear power plants, and of Alloy-600 steam generator tubes in pressurized water reactors. If laboratory tests have been conducted primarily to find remedies (surface treatment, coolant chemistry, steels of lower susceptibility…), they are increasingly oriented to initiation and propagation mechanisms. A broad range of experimental, characterization and calculation tools are now available at the required scales (from the nm to the µm), liable to pave the way to better understanding of these phenomena, and controlling chemistry / mechanics / transport couplings. One of the main goals of these studies is developing models that enable crack initiation and propagation to be predicted with a view to optimizing inspections and replacements. In all these cases, mechanism studies corroborate the semi-empirical models currently used, and enable the relevant parameters involved to be discriminated.

Bibliography

G. Santarini, *"La corrosion sous contrainte des alliages de nickel"*, Clefs du CEA, N° 38, Spring 1998.

R.W. Bosch, D. Féron and J.P. Celis (editors), "Electrochemistry in Light Water Reactors: Reference Electrodes, Measurements, Corrosion and Tribocorrosion Issues, EFC N° 48, Woodhead publishing, Oxford, 2007.

D. Féron and J.M. Olive (editors), "Corrosion issues in Light Water Reactors: Focus on Stress Corrosion Cracking and Practical Experience", EFC N° 51, Woodhead Publishing, Oxford, 2007.

References

[1] D. Caron, "*Influence de l'hydrogène sur la vitesse de propagation des fissures de corrosion sous contrainte dans l'Alliage 600 en milieu primaire de réacteurs nucléaires à eau sous pression"*, N° d'ordre 2000 INSAL 0064, Institut National des Sciences Appliquées, Lyon, 2000.

[2] G. Santarini, Corrosion, Vol. 45, 1989, p 369.

[3] D. Le Boulch, L. Fournier and C. Sainte-Catherine "Testing and modelling iodine-induced stress corrosion cracking in stress-relieved Zircaloy-4 Proc". *International Seminar on Pellet-Clad Interactions in Water Reactor Fuels*, 9-11 March 2004, Aix en Provence, France.

[4] H. Blanchet, H. Coriou, L. Grall, C. Mahieu, C. Otter and G. Turluer, "Historical review of the principal research concerning the phenomena of cracking of austenitic nickel base alloys, Stress corrosion cracking and hydrogen embrittlement of iron base alloys" NACE-5, R.W. Staehle, J. Hochmann, R.D. McCright, J.E. Slater eds., NACE Houston 1977 editions.

[5] N. Totsuka and Z. Szklarska-Smialowska, "Hydrogen induced IGSCC of nickel-containing FCC alloys in high temperature water", *Proceedings of the 3rd Symposium on Environmental Degradation of Materials in Nuclear Power Systems-Water Reactors*, G.J. Teus, J.R. Weeds eds., TMS, Warrendale, Pennsylvania, 1988.

[6] M. Berger, C. Brun and M-H. Clinard, "PWR to EPR: Evolutionary Chemistry for the New French Nuclear Power Plants Design and Operation at Flamanville 3", paper PS1-14, *International Conference on Water Chemistry of Nuclear Reactor Systems*, Jeju, Korea, 23-26 October 2006.

[7] O. Raquet, D. Féron, G. Santarini and J.M. Boursier, "IGSCC of alloy 600 in PWR primary water – Influence of a cold worked layer on crack initiation", *15th Int'l Corrosion Congress*, Grenada, Spain, 22-27/09/2002, Paper n° 447.

[8] O. Raquet, J. Daret, D. Féron and G. Santarini, "Quantitative characterization and modelling in initiation and growth of stress corrosion cracks", *EPRI Workshop A600*, St Petersburg, USA, 14-16 February 2000.

[9] P. Laghoutaris, J. Chene, C. Guerre, O. Raquet, M. Sennour, R. Molins, F. Vaillant and P. Scott, "Contribution to understanding of stress corrosion cracking of Alloy 600 in PWR primary Water", *Energy Materials*, Vol. 3, N° 2, pp. 119-125, 2008.

[10] P. Laghoutaris, J. Chene, C. Guerre, O. Raquet, R. Molins, F. Vaillant and P. Scott, "The role of hydrogen on the stress corrosion of the alloy 600 in PWR medium", 2e colloque 3M "Matériaux, Mécanique, Microstructure" *L'hydrogène dans les matériaux*, 18-19 juin 2007, Saclay, 2007.

[11] P. Laghoutaris, *"Corrosion sous contrainte de l'Alliage 600 en milieu primaire des réacteurs à eau sous pression: apport à la compréhension des mécanismes"*, thesis, ENSMP, 2009.

[12] O. Raquet, E. Herms, F. Vaillant, T. Couvant and J.M. Boursier, *12th International Symposium on Environmental Degradation of Materials in Nuclear Power Systems* – Water Reactors, Snowbird-Utah, August 2005.

[13] T. Couvant, E. Herms, O. Raquet, F. Vaillant, J. M. Boursier and O. de Bouvier, *13th International Symposium on Environmental Degradation of Materials in Nuclear Power Systems* – Water Reactors, to be presented, August 2007.

[14] C. Guerre, O. Raquet, E. Herms and M. Lecalvar, *12th International Symposium on Environmental Degradation of Materials in Nuclear Power Systems* – Water Reactors, Snowbird-Utah, August 2005.

Jean-Philippe Bossis, Philippe Dubuisson, Lionel Fournier,
Nuclear Materials Department
Damien Féron, Catherine Guerre, Emmanuel Herms, Pierre Laghoutaris, Olivier Raquet,
Physico-Chemistry Department
and Jacques Chêne,
CNRS and Physico-Chemistry Department

Wear Corrosion

Wear corrosion – also called tribocorrosion – is defined as a "process involving conjoint corrosion and friction between two sliding surfaces in contact" (Standard ISO 8044, April 2000). In pressurized water reactors (PWRs), this phenomenon has aroused special interest since fast wear could be observed on the (Stellite-6-coated) teeth of latch arms in control rod drive mechanisms (CRDMs) as well as on (steel-316L) clads of Rod Cluster Control Assemblies (RCCAs).

A coupled phenomenon

Wear corrosion in a passive alloy consists in the periodic removal of the **passive layer*** by mechanical or electrochemical attack, followed by alloy repassivation during the latency phase, e.g. between two impacts. Repassivation, or the rebuilding of the oxide which the passive layer consists of, is sometimes accompanied with loss of matter through dissolution in an aqueous environment. Depassivation may result from friction and impact; it may also take place in presence of wear debris that have turned "abrasive" and remain between the surfaces in contact, thereby erasing them. The phenomenon is generally termed "tribocorrosion" when the coupling of both phenomena (corrosion and wear) results in a loss of metal substantially higher than under the sole mechanical wear.

A research work related to extended lifetime of the French nuclear power reactor fleet

This research topic is a response to the goal of extending fuel cycles as well as the French PWR fleet lifetime. The issue of whether rod cluster control (RCC) guide tubes are to be substituted, and how Stellite-coated latch arms will evolve, is under consideration. Among the PWR components likely to be affected by wear corrosion are the following:

- Cold-worked steel-316L locating pins, in contact with bottom nozzles;
- Nitride 316L-steel clads in Rod Cluster Control Assemblies (RCCAs), in contact with the 304L-steel RCC guide tube or the Zy4 guide thimbles;
- Stellite-coated teeth of CRDM latch arms, in contact with the drive rod made out of martensitic stainless steel;

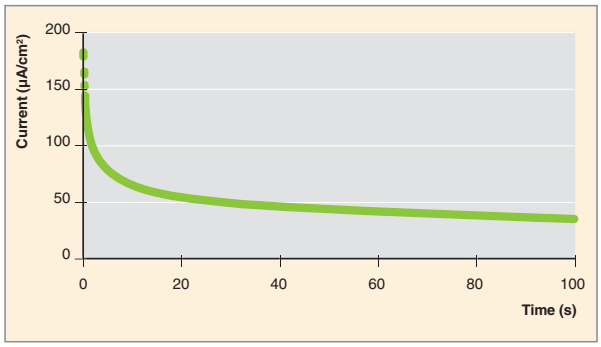

Fig. 83. Evolution of the repassivation current obtained on a Stellite (a cobalt alloy containing chromium and tunsten) under PWR primary conditions and after an electrochemical depassivation (-2000 mV with respect to free corrosion potential), thus displaying typical durations of about ten seconds for the oxide layer rebuilding in a PWR primary environment.

- Nickel-base alloy SG tubes;
- Zirconium alloy clads of fuel rods.

Without giving up tests dedicated to understanding wear at room temperature [1, 2], the CEA also conducts research works in PWR primary environment, i.e. in pressurized water (150 bars, 350 °C). Research works may be of the analytic type (electrochemical depassivation-repassivation, examination of oxide layers), and may be oriented to wear tests in specific machines (fretting corrosion in FROTTEAU 2 and machines of the "AECL[3]" type, or even tests on full-scale components (Stellite-coated latch arms of a real drive mechanism, and fuel rods qualified in representative loops) [3-6].

On passivable alloys such as cobalt-based alloys (Stellite - Fig. 83) or stainless steels, repassivation durations, as well as the involved currents, were determined under PWR primary conditions, which enabled characteristic frequencies and losses of matter to be traced back. In the case of steel-316L Rod Cluster Control Assemblies (RCCAs), it could be deduced by calculation that dissolving 10 nanometers after full depassivation would result in a wear 1 mm deep in one year, which had been formerly observed in an EDF reactor (a few clad failures in one year). Thus, wear corrosion may reach a very fast and, so, unallowable kinetics. Regarding nitride steel-316L control

3. Atomic Energy of Canada Limited.

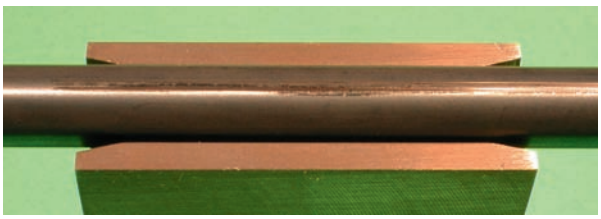

Fig. 84. Example of a worn clad in relation to the control rod / guide tube couple. Wear test performed with a steel-316L, nitrided clad pressing against a steel-304L housing over 50 mm, with an applied 3 N loading force and a continuous back-and-forth sliding motion of 128 mm per cycle, at a 0.38 Hz frequency, up to an overall path of 63 km.

rod assemblies, fretting tests in PWR environment (Fig. 84) show that wear corrosion exhibits specific wear pattern (Fig. 85) not to be encountered in cases of mechanical wear.

Concerning latch arms with Stellite-coated teeth (Fig. 86), two full-scale toughness tests were performed on the BACCHUS test bench,on which slow or fast loading paces can be imposed, likely to result in different wear corrosion mechanisms. Most of mechanical loading is an impact loading as the latch arm tooth is fit up against the grooved control drive rod. The final resulting wear is compared for an overall number of latch arm steps (260,000 steps). At the end of these two tests, as shown by wear measures (Fig. 87), wear is more pronounced when the operating pace is the lowest. These results bear out the assumption of tribocorrosion-induced wear.

High frequency of mechanical loading (lowering the frequency, inserting stop times), is also illustrated by fretting tests on the 316L / 304L couple carried out with an “AECL” type machine (Fig. 88). The resulting wear [4] is expressed as the amount of material loss per unit distance of sliding; it is typically of 20 µg/km under fast motion (18 Hz), and exceeds 5000 µg/km under very slow motion (0.2 Hz).

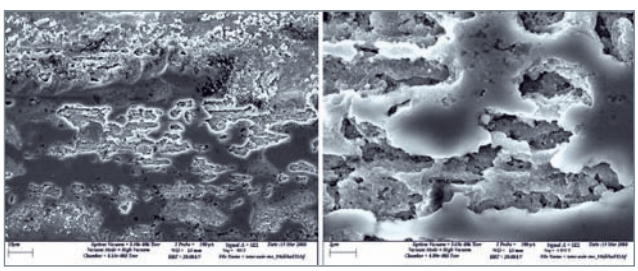

Fig. 85. SEM image of the wear pattern of the nitride steel clad shown on Figure 84, as exposed in a FROTTEAU 2 loop in a PWR primary environment. The bearing areas during the sliding motion are made evident by the dark, smooth plateaux, whereas corrosion is displayed by crevices with lighter oxidized debris.

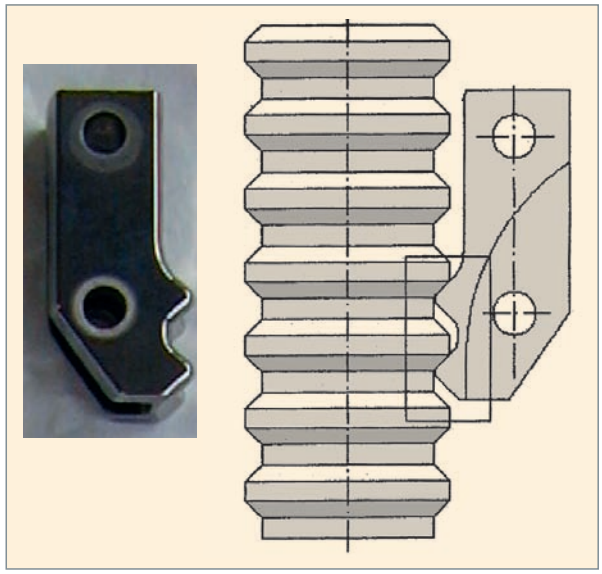

Fig.86. View of a Stellite-coated tooth latch arm (dim. ~5 cm x 1 cm), which is a part of control rod drive mechanisms (CRDMs), with the schematic representation of the contact surface between the latch arm and the grooved control drive rod.

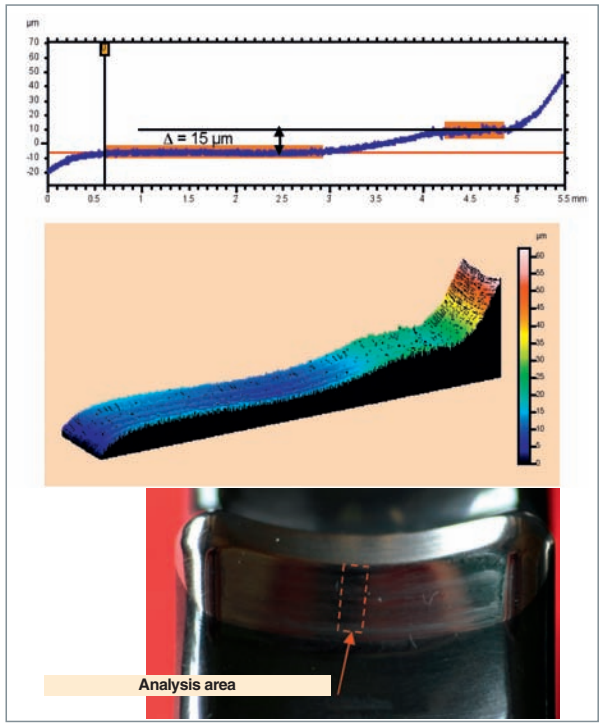

Fig. 87. Confocal microscopy images of wear on a Stellite-coated tooth. Maximum wear of the bearing side (center of light blue area): 15-µm deep after a 260,000-step, slow motion of a Stellite-6-coated latch arm against a Steel- Z12C13 grooved control drive rod in primary water at 285 °C.

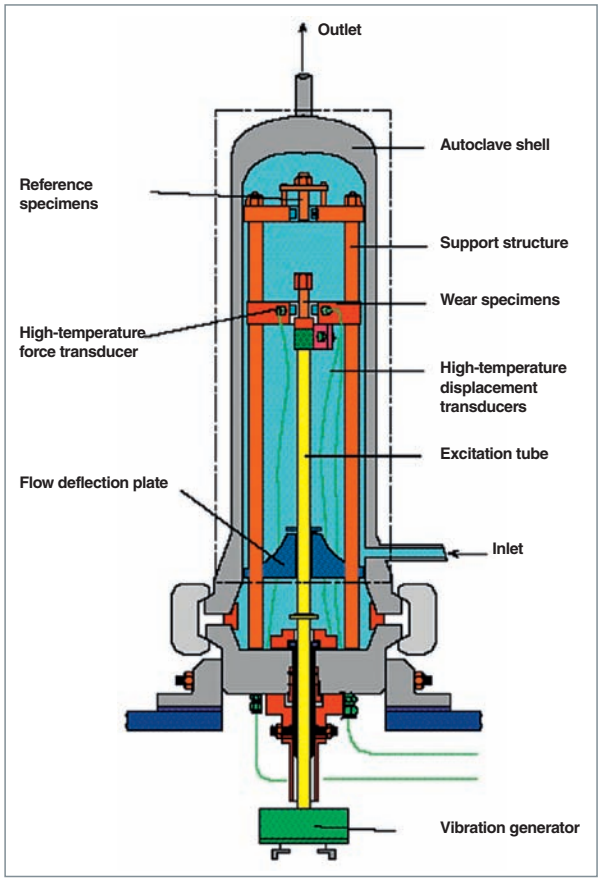

Fig. 88. The so-called "AECL" machine used at the CEA for investigating tribocorrosion (a machine designed and marketed by AECL).

Concerning zirconium alloy fuel clads, the form of deformation under tribocorrosion is different for the oxide formed is practically insoluble. Yet, there is still an effect to be understood of the aqueous environment and its chemistry. This topic is being investigated as part of a cooperation with Ecole Centrale de Paris.

As a conclusion, understanding wear corrosion phenomena lies in an approach coupling mechanics and corrosion. Passivation mechanisms of the alloys investigated play a major role, hence the influence of the solution chemistry, with such significant factors as pH, and species interfering with the solution redox potential (oxygen and hydrogen). Of equal importance, indeed, is the mechanical stress (frequency, applied force, surface under fretting…). Some more robustness is still needed to get fully reliable prediction of these phenomena.

References

[1] A. Van Herpen, B. Reynier and C. Phalippou, "Effect of test duration on impact/sliding wear damage of 304L stainless steel at room temperature: metallurgical and micromechanical investigations", *Wear* **249**, pp. 37-49, 2001.

[2] L. Benea, P. Ponthiaux, F. Wenger, J. Galland, D. Hertz and J.Y. Malo, "Tribocorrosion of stellite 6 in sulphuric acid medium: electrochemical behaviour and wear", *Wear*, **256**, pp. 948-953, 2004.

[3] A. Lina, D. Moinereau, X. Delaune, C. Phalippou, B. Reynier and P. Riberty, "The influence of water flow on the impact/sliding wear and oxidation of PWR control rods specimens", *Wear*, **251**, pp. 839-852, 2001.

[4] B. Reynier, C. Phalippou, P. Riberty and J. Sornin, "Influence of a periodic latency time on the impact/sliding wear damage of two PWR control rods and guide cards specimens", *Wear*, **259,** pp. 1314-1323, 2005.

[5] J. Vallory, "Methodology of PWR fuel rod vibration and fretting evaluation in HERMES facilities", *International Topical Meeting on LWR Fuel Performance*, Orlando, Florida, USA, September 2004, Paper 1091, 2004.

[6] J. Vallory and N. Baillon, "Grid to rod fretting wear: new designs qualification method", *Proceedings of Fontevraud VI (Colloque International Fontevraud VI)*, Vol. 2, pp. 899-908, 2006.

Christian Phalippou
Systems and Structures Modelling Department

Corrosion in the Nuclear Reactor Systems of the Future

The selection of the fourth generation nuclear reactor concepts can be summarized as five main stakes: economics, safety, waste management, resource upgrading, and safety in its broad meaning, including fight against proliferation risks. Several technological options are available; one of the main structuring items is the choice of reactor **coolant***, which is a key factor in the system's overall design, the choice of operating parameters (especially temperatures and pressure), and, consequently, the choice of materials.

Six nuclear systems have been selected by the **Generation IV*** Forum [1]:

- **GFR** (Gas-cooled Fast Reactor system): a gas-cooled fast neutron reactor with fuel recycling,
- **SFR** (Sodium-cooled Fast Reactor system): a sodium-cooled fast neutron reactor with fuel recycling,
- **LFR** (Lead-cooled Fast Reactor system): a lead or lead-bismuth-cooled fast neutron reactor with fuel recycling,
- **VHTR** (Very High Temperature Reactor system): a helium-cooled, thermal neutron reactor with a very high core outlet temperature (1000 °C) dedicated to hydrogen generation, without fuel recycling in the initial version under consideration,
- **SCWR** (SuperCritical Water-cooled Reactor system): a supercritical water-cooled reactor with a thermal or fast neutron spectrum and fuel recycling,
- **MSR** (Molten Salt Reactor system): a molten salt thermal neutron reactor with fuel recycling.

These systems are mostly aimed at generating electric power, but some of them are also able to supply high-temperature heat for industrial processes.

This chapter will review the major issues relating to interactions between structural materials and coolant.

Corrosion in Gas-Cooled Reactors

Corrosion by helium impurities

Helium in a gas-cooled fast reactor constitutes an original environment with a very low oxygen partial pressure and a high carbon activity. Competition takes place between the growth of a protective superficial oxide, i.e. a “passive” oxidation regime ensuring alloy integrity in the long term, and carburization or decarburization reactions, which irreversibly alter microstructure and properties. As shown by the experience gained in the seventies and eighties with helium-cooled experimental reactors (HTR for High Temperature Reactor), traces of pollutants such as H_2, CO, CH_4, and H_2O contaminate the coolant. Although only minute concentrations are involved, approximately ranging between one ppm and a few dozen ppm, these gases interact with metallic materials at high temperatures.

Experience issued from HTR-related studies provides a rich corpus of both theoretical and practical data dealing with corrosion phenomena in impure helium. Nevertheless, essential knowledge is lacking for selecting and, *a fortiori*, qualifying materials for Generation IV Gas-cooled Fast Reactors (GFR). For in these innovating systems, structures will be exposed to temperatures considerably higher than formerly. Moreover, materials themselves might be particularly different from those of early HTRs, i.e. mainly Alloy 800 and chromium-rich nickel alloys reinforced with Co and/or Mo (IN617, Hastelloy X…). Nowadays, other grades are assumed to be *a priori* more performing at high temperature, particularly owing to their optimized creep resistance, that is: Cr-rich nickel alloys reinforced with tungsten (typically, Alloy 230), coated materials featuring a three-layer system (typically, substrate / bond layer / yttria-stabilized zirconia thermal barrier), oxide-dispersion-strengthened (ODS) steels or nickel alloys, molybdenum alloys… Therefore, corrosion studies under representative atmospheres and at upper-bound temperatures are required to know new materials behavior, select materials compatible with the environment to be encountered in gas-cooled fast reactors, prescribe optimal operating conditions with associated margins (temperature, pollution in helium), and, further in time, propose parameterized laws for in-service prediction of lifetime.

Corrosion process in nickel base alloys

With a view to describing nickel alloy reactivity and, most particularly that of alloy IN617, research work is focused on chromium and carbon reactions, excluding other alloying elements: Cr oxidation by water, C oxidation by water, Cr oxidation with methane or carbon monoxide. Given the high dilution of impurities in helium and the very short residence times at high temperature, the gaseous phase does not reach an equilibrium. Beyond a certain temperature, carbon present in the material – under dissolved form or incorporated within metallic carbides – reacts with surface oxide, thereby inducing CO release. The superficial layer is damaged, which discards any possibility of passivity. Various approaches have been developed to plot the physico-chemistry of reactions at the alloy IN617 / gas interface as a function of the relative contents of oxidizing gas and carbonate species. For example, Figure 89 reproduces the stability diagram of chromium proposed by Quadakkers [2], and illustrates the various corrosion modes of IN617 – simplified as the Ni-Cr-C system with a Cr activity of 0.6 – at 950 °C as a function of atmospheric oxygen and carbon potentials.

A difficulty in this representation lies in assessing the oxygen potential and carbon activity specific of the environment. For, as the gaseous phase is out of equilibrium, these quantities have to be assessed through coupling data relating to thermodynamics and surface reaction kinetics.

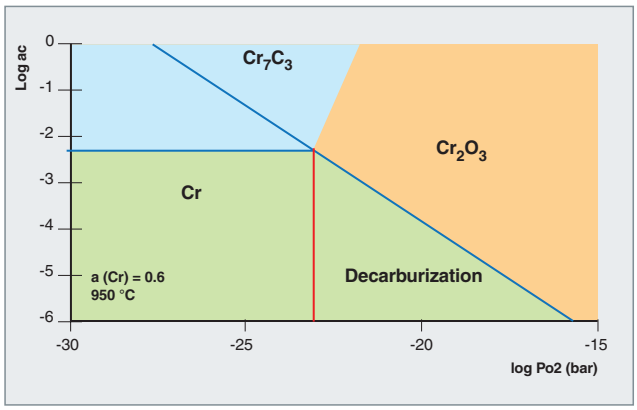

Fig. 89. Chromium stability diagram at 950 °C, with a chromium activity a(Cr) = 0.6, as a function of oxygen pressure and carbon activity [1].

Other test runs based upon a more technological approach are focused on depicting the microstructure of nickel alloys exposed to the helium atmosphere of gas-cooled reactors, and identifying the corrosion effects on their mechanical properties. Various morphologies are typical: "passive" oxidation, featuring a very slow evolution of the microstructure, coarse carbide precipitation or "carburization", which entails embrittlement at room temperature, and metallic carbide dissolution or "decarburization", likely to lead to lower resistance to creep. In addition to these processes, "active" oxidation phenomena may take place, such as internal oxidation, superficial oxide evaporation, layer scaling…

Practically, the only behavior likely to guarantee durable use of structural materials is "passive" oxidation, excluding any passing through the range of "carburization" or "decarburization". It is worth mentioning, however, that changes in corrosion mechanisms ("switch-over" phenomena) could be observed in the long term.

Experimental devices: CORALLINE and CORINTH

High sensitivity of the corrosion mode to operating parameters has led to a considerable dispersal of the results formerly published. Therefore, it seemed of paramount importance to us to preserve atmospheric conditions during the laboratory tests of exposure, which implied designing dedicated devices, as well as stringent handling protocols. The critical point is to adjust and measure the water vapor contents ranging between 0.5 and a few ppm. As a first step, we adapted the CORALLINE Facility so as to expose small coupons under a helium flux up to 1,050 °C. The test sections are made out of quartz, an inert material with respect to the environment. Special attention is given to circuit and component leaktightness. The gas mixture of required composition is directly supplied in bottles. Concentrations in helium are analyzed at the inlet and outlet of two testing sections using two hygrometers, one with a capacitive probe (accurateness of the dew point, ± 3 °C), the other with a chilled-mirror probe (PR accuracy ± 0.3 °C), coupled with a gas-phase chromatograph (accuracy for constant gases, 0.2 ppm). The CORALLINE Facility proves to be leaktight and performing for controlling (even low) concentrations in permanent gases up to 1,015 °C at least, over several hundreds of hours. However, owing to its design, moistness cannot be adjusted, the latter ranging between 0.5-4 ppm approximately. In order to go beyond the limits of CORALLINE, an improved version, the so-called CORINTH Facility, has been recently commissioned (Fig. 90). Improvements especially lie in fabrication on demand of gas mixtures, in vapor content control and still more accurate measuring, and increased capacity for exposing specimens simultaneously (4 big-sized test sections) at higher temperatures (1,150° and 1,550 °C) and for longer times.

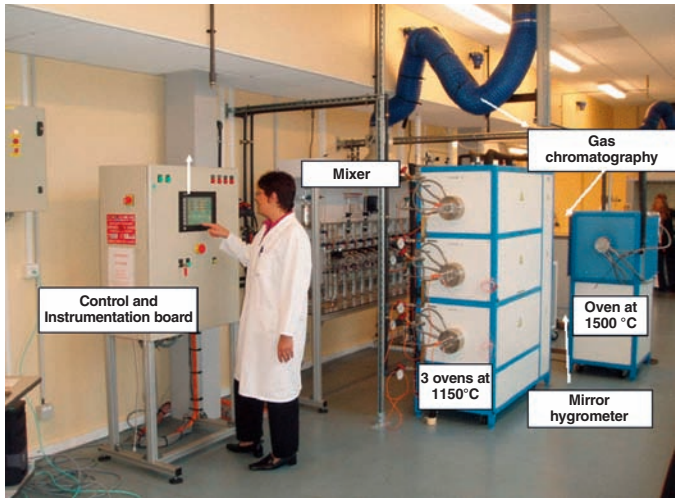

Fig. 90. View of the CORINTH Facility designed for investigating high-temperature corrosion in helium with controlled impurity contents.

A few results

In CORALLINE and CORINTH, a ("screening") program has been conducted, with the purpose of comparing candidate alloys for the GFR high-temperature applications. Corrosion tests have been carried out in atmospheres representative of the coolant, mainly at 950 °C. Tests were performed in a "slightly oxidizing" atmosphere (He+200 ppm H_2, 50 ppm CO, 20 ppm CH_4, ~2 ppm H_2O), the only range for a prolonged use of alloys which will be retained indeed in GFR nominal operating conditions. These tests have shown that at 950 °C "passive" oxidation leads to superficial oxide formation and internal oxidation. Under the surface is often formed a decarburized area, the depth of which may be related to the composition and thickness of outer oxides. Figure 91 illustrates the typical morphology of a Cr-rich Ni alloy after exposure in CORALLINE. The thickness, compactness and composition of the outer layer strongly depend on the alloy's contents in elements with a very high affinity for oxygen: Al, Si, Ti, Cr, Mn… For example, with titanium contents of a few weight per thousand, titanium is incorporated into chromine and forms mixed oxides, thereby inducing an increase in the oxidation rate. In addition, aluminium enhances proneness to internal oxidation.

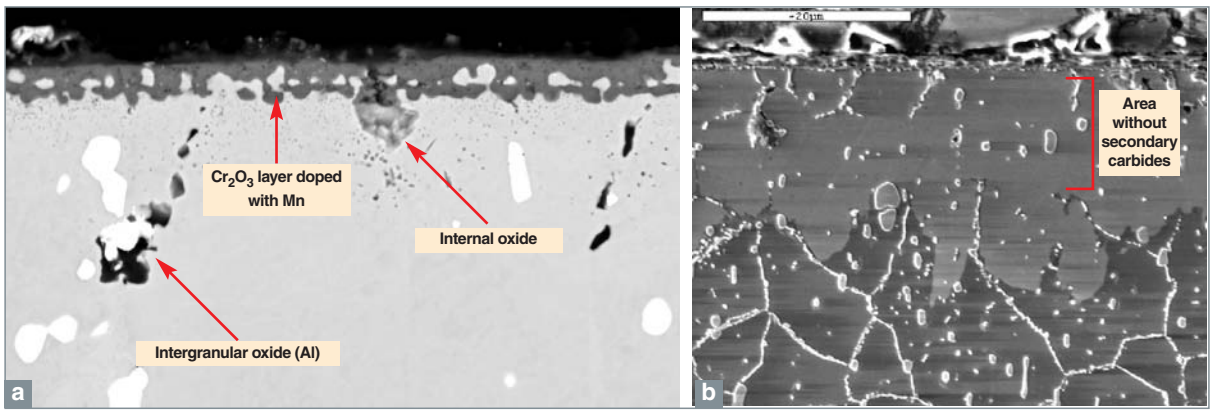

Fig. 91. SEM images of a surface section of a Haynes 230 sample exposed for 813 h in CORALLINE in slightly oxidizing He at 950 °C; a) backscattered-electron contrast; b) secondary-electron contrast after an electrochemical attack.

These first tests have enabled alloys to be classified as a function of corrosion toughness in GFR "little oxidizing" helium environment at 950 °C. For a same exposure time, Figure 92 gathers values measured on several grades for oxide layer thickness, internal oxidation depth, and depth without secondary carbides.

According to an order of increasing resistance to oxidation, there can be found: 800H< IN617 < Haynes 230 < Hastelloy X. Nicrofer 6025 cannot be compared with others, for, initially, an alumina superficial film is formed, and then the oxidation mechanism changes with the fast growth of Cr-rich nodules. In addition, two ODS materials, the alumino-forming PM 2000 and the chromino-forming PM1000, have exhibited damaging rates lower than those of Hastelloy X. Such good properties are assigned to the positive effect of yttria dispersoids on the formation and quality of superficial oxide layers. The previous categorization shall also be assessed with respect to the extent of the passive oxidation range for each grade. For our research is aimed at reaching, not only a suitable resistance to oxidation at low oxygen partial pressure (Po_2), but also an alloy likely to be oxidized within a very broad range of operating conditions, and able to withstand incursions into carburizing or decarburizing atmospheres without any risk of change in corrosion mechanism.

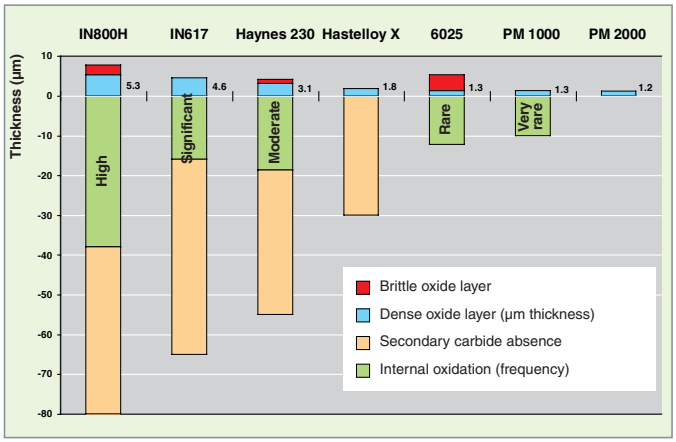

Fig. 92. Morphological features of samples exposed in CORALLINE for 813 h or 1027 h (PM 1000 and PM 2000) in slightly oxidizing He at 950 °C.

On the other hand, another investigating route is devoted to fine study of interactions beween helium impurities and alloy **Haynes 230***, approximately between 850 and 1000 °C. The aim is appraising the validity, for this grade, of the models developed for IN617, and issuing recommendations about the conditions of use in a GFR.

Figure 93 depicts both the temperature program and the CO content analyses at the test section outlet of two rather short tests under helium (He +200 ppm H_2, 50 ppm CO, 20 ppm CH_4, ~2 ppm H_2O).

In both tests, a first peak fo CO consumption can be observed during the rise in temperature to 900 °C. This peak corresponds with the alloy oxidation by CO. If exposure goes on, a plateau emerges, followed by a CO generation around 965 °C (TA). This release is then progressively reduced. Figure 93 is to be related to Figure 94, which presents the surface of specimens.

Microprobe analyses and SEM-FEG observations helped identify an oxide layer, about 0.7 µm thick and of the spinel type $(Cr,Mn)_3O_4$, on the surface of the oxidized specimen up to 900 °C. In contrast, after treatment at 980 °C, superficial oxide is only 0.25 µm thick, and is much chromium-depleted though it still contains Mn and Al. It could be thus evidenced that, alike alloy IN617 under some helium atmospheres typical of gas-cooled fast reactors, **Alloy Haynes 230*** displays either "passive" oxidation at T<TA, or undergoes destruction of the oxide layer above the critical temperature TA. In our

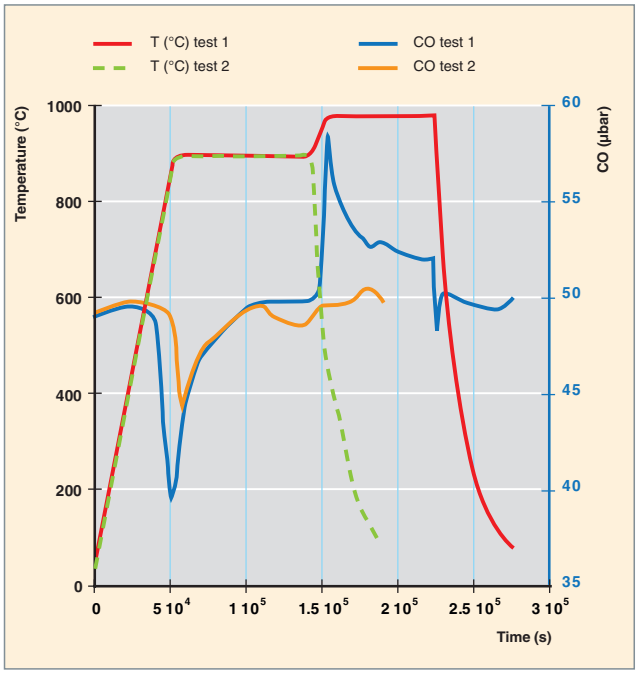

Fig. 93. Temperature program and analyses of CO concentration at the end of the test stage versus time during the exposure of alloy-**Haynes 230*** samples in the CORALLINE test loop. Alloy carburization and decarburization areas are clearly shown on this figure. No corrosion can be observed between them.

case, (with 50 ppm CO), the critical value is 965 °C. Moreover, this oxide / carbon reaction in the material is selective: only Cr-rich oxides seem to react. Some authors named it a "microclimate reaction" [2-5]. This work is proceeding as tests with other helium GFR compositions, implementing enhanced characterization techniques for surface oxide layers.

How modelling helps understand the role of impurities

In order to account for the destruction of the oxide layer above a critical temperature T_A, it is assumed that carbon in solution in alloy C_{sol} can reduce oxide according to the overall following process:

$$Oxide + C_{sol} = CO(g) + Metal \quad (1)$$

Reaction (1) leaves the alloy without any protection: it can then exchange carbon with the atmosphere, and undergo fast decarburization with major consequences in its mechanical properties.

The aim of the latest works [6-8] was to identify and model the steps of the phenomenon of oxide growth and, then, destruction for a Ni-base alloy Haynes 230®. The study conclusions help determine specifications on optimum environment conditions in VHTR primary circuit containment, in terms of temperature and helium chemistry.

Approach and experimental work

The critical temperatures of reaction T_A were determined in typical VHTR helium atmospheres at various CO partial pressures for alloy Haynes 230® and for model alloys Ni-Cr-W-C. Table 1 gives the chemical composition of the alloys.

The tests were performed in the dedicated CORALLINE test loop, consisting of impure helium feed, high-temperature furnaces, and gas analyzers.

The measurement protocol of T_A consists in exposing specimens to a given gaseous mixture at 900 °C for approximately 25 hours, then steadily increasing temperature (e.g. by 1 °C/min). Helium analysis through gas chromatography at the furnace outlet shows a sharp rise in carbon monoxide partial pressure, which helps pinpoint the onset of Reaction (1) and, so, of the starting reaction temperature, T_A.

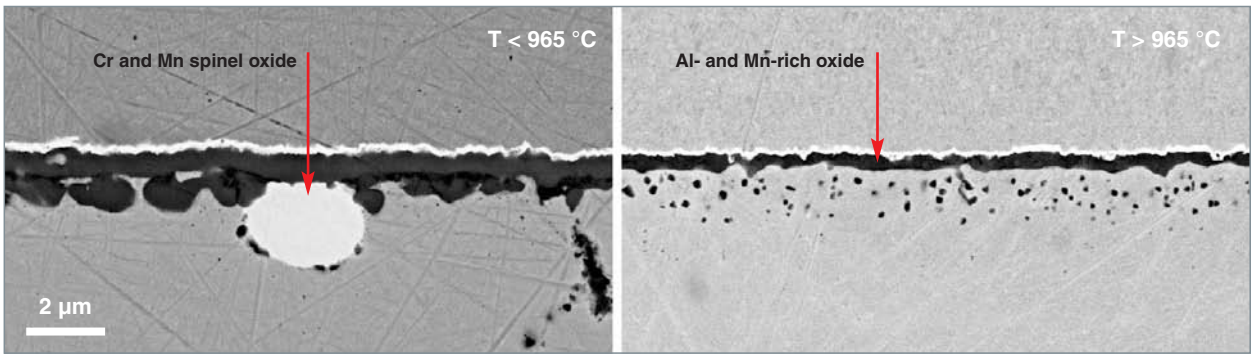

Fig. 94. Backscattered-electron-contrasted SEM-FEG images of a section of the surface of Haynes 230 alloy samples exposed in the CORALLINE Facility in slighly oxidizing He, at a temperature up to 900 °C (20 hours) and 980 °C (25 hours).

Table 2.

Wt% chemical composition of the tested alloys														
Alloy	**Ni**	**C**	**Cr**	**W**	**Mo**	**Fe**	**Mn**	**Al**	**Si**	**Co**	**Ti**	**Cu**	**La**	**S**
Haynes 230®	base	0.105	22.0	14.7	1.3	1.3	0.5	0.4	0.4	0.2	0.1	0.02	0.005	0.002
Ni22CrWC	base	0.103	22	14								< 0.001	< 0.001	< 0.001
Ni18CrWC	base	0.103	18	14										< 0.001

The evolution TA = f(P_{CO}) for the various alloys is displayed on Figure 95: for a given alloy, the higher CO partial pressure, the higher T_A. Measures on model alloys also indicate that there is a shift of T_A towards the lower temperatures when chromium content is decreasing.

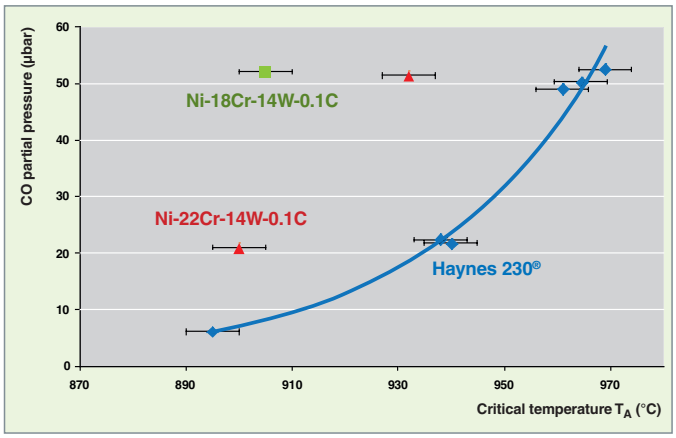

Fig. 95. Evolution of critical temperature T_A versus CO partial pressure in helium on the various Ni base Cr-rich alloys.

A reactional schematic diagram was put forth for Reaction (1): TA corresponds with the temperature from which the driving force is sufficient to achieve the reaction

$$Cr_2O_3 + 3C_{sol} = 3CO(g) + 2Cr \quad (2)$$

In Reaction (2), C_{sol} stands for carbon in solution in the alloy. It is assumed that an equilibrium has been established between: C_{sol}; stable carbides at high temperature – of type $M_{23}C_6$ and very rich in chromium, referring to TEM diffraction studies achieved at the CIRIMAT and the CEA/Grenoble –; and chromium within the alloy, including under the oxide layer (Cr-depleted area). Chromium formed by Reaction (2) is assumed to be pure in its phase (activity of 1), i.e. the effect of its following dilution in the matrix is disregarded. Yet, chromium and alloying elements very quickly interdiffuse, which explains why chromium cannot be detected at the alloy surface.

Figure 96 puts forth a schematic diagram of the approach developed to establish a theoretical relationship between T_A and P_{CO}. It combines a thermodynamic approach, that considers Reaction (2) and the equilibrium Csol/carbides/chromium in the alloy (using the sofwares HSC® and TermoCalc®), with fine analyses of the Cr local content at the alloy/oxide interface (through EDS-TEM). Step 2 on Figure 96 requires a Cr activity coefficient in the tested alloys. It was experimentally determined in the different alloys by the Physico-Chemistry Department, using multiple Knudsen cells associated with a High-Temperature Mass spectrometer (HTMS).

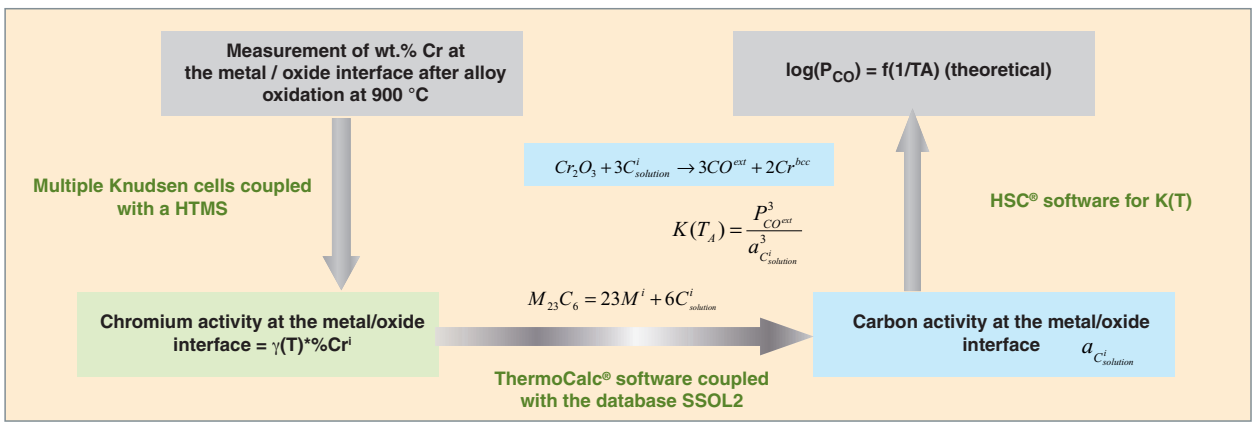

Fig. 96. Schematic representation of the approach adopted to know TA theoretical evolution as a function of PCO.

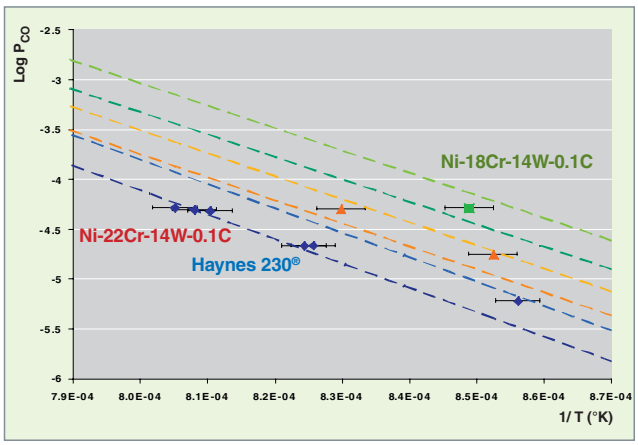

Fig. 97. Carbon monoxide equilibrium isotherm for various alloys of interest for gas-cooled reactors. Comparison between theoretical values (dotted lines) expressed by Log(P(CO))=f(1/TA) and experimental results.

Theoretical and experimental results are presented on Figure 97. Theoretical values are highlighted by a dotted band which takes into account experimental uncertainties. As regards the industrial grade and two model alloys, the experimental temperatures T_A are in very good agreement with the theoretical predictions derived from Figure 96.

It could be seen that the oxide layer which is formed on the surface of chromium-rich nickel-base alloys, at high temperature, in the impure helium atmosphere of VHTRs, is no more stable above a critical temperature T_A. Moreover, it was demonstrated that this oxide degradation temperature is dependent on carbon monoxide pressure and the chromium content of the alloy. It was thus proposed that in the first instants of the reaction, the relevant thermodynamic system be chromine reduction by carbon in solution within the alloy at the alloy / oxide interface. The model developed is based upon a thermodynamic study coupled with fine analyses of chemistry and of the local interfacial microstructure. An excellent agreement could be found between theoretical predictions and experimental direct measures of T_A.

As a conclusion, carbon monoxide P(CO) partial pressure in the VHTR atmosphere will be a key factor for determining the temperature range for which chromine is stable and, so, the possible protection of the structural alloy. Controlling helium coolant chemistry would enable to break dependence on Reaction (1): carbon monoxide partial pressure must be kept above a critical threshold to be set up according to data given on Figures 95 and 97 (still allowing for margins, of course).

Silicon carbide resistance to oxidation

Silicon carbide (SiC) and, more especially, ceramic matrix composites SiC / SiCf are contemplated as cladding materials for gas-cooled fast reactor fuels owing to their stability at high temperatures, their high thermal conductivity, and the stability of their properties under neutron irradiation.

In a reactor the cladding material will be under an overall pressure of several MPas in the helium coolant gas environment. Defining the allowable impurity rate in the coolant partly relies on determining the behavior of (monolith and composite) SiC elements facing oxidation by impurities present in helium under low partial pressures, in nominal operating conditions (between 1100 and 1500 K). In addition, investigations at higher temperatures and under different atmospheres are necessary to assess clad behavior in the case of an accident (> 1600 up to 2300 K), and contribute to accident scenario assessment.

SiC oxidation

SiC major particularity lies in its two distinct oxidation regimes, dependent on the oxidizing species partial pressure. For example, if the latter occurs in sufficient quantity, Sic oxidation is said to be “passive”, and a protective, dense, and homogeneous layer of silica (SiO_2) is formed on the material surface, thereby limiting its further oxidation. On the contrary, if the oxidizing species partial pressure is too low, silicon carbide oxidation is then active, and this is chiefly SiO, a gaseous oxide, which is formed. In this case, silicon carbide is not protected from the oxidizing environment, and its progressive degradation is expressed by a significant loss of mass over time [9, 10].

Oxygen is the main oxidizing species and the two active and passive oxidation regimes are respectively expressed by the two following chemical reactions:

$$SiC + O_2\ (g) = SiO\ (g) + CO\ (g)$$
$$SiC + 3/2\ O_2\ (g) = SiO_2 + CO\ (g)$$

In both cases, the oxidation kinetics is representative of the oxidation regime. When the reaction products are gaseous, oxygen directly reacts with silicon carbide, and the kinetics is linear. In the opposite case, if silicon is formed, the oxidation kinetics then becomes parabolic. This is due to the fact that oxygen has to diffuse through the oxide layer to react with silicon carbide at the substrate / oxide interface, and, similarly, the gaseous products of the reaction (here, CO) have to diffuse through silica to come out of the material. So the kinetics is slower as the oxide layer is growing.

In addition, for the two regimes, the kinetics depends on oxygen partial pressure, which confirms the fact that oxidizing species diffusion is the limiting factor of the reaction [11]. However, apart from oxygen partial pressure, the nature of the oxidizing species, as well as pressure and temperature are parameters which influence the material's behavior during its oxidation.

It has been proved experimentally that water vapor enhances the phenomenon of silicon carbide oxidation [12-15].

Thus, in an atmosphere consisting of oxygen for one half, and of water vapor for the other half, for temperatures between 1470 and 1670 K, water vapor proves to be the first oxidizing species according to the following reaction:

$$SiC + 3H_2O(g) = SiO_2 + CO(g) + 3H_2(g)$$

Another consequence of water vapor occurring in the atmosphere is the possible volatilization of silica according to the following reaction [16]:

$$SiO_2 + 2H_2O(g) = Si(OH)_4(g)$$

Possible reactions between carbon dioxide and silicon carbide are the following, respectively, according to whether oxidation is active or passive:

$$SiC + 2CO_2(g) = SiO(g) + 3CO(g)$$
$$SiC + 3CO_2(g) = SiO_2 + 4CO(g)$$

Experimental results show a behavior typical of the oxidation environment. Contrary to oxidation under air, in which there is always formation of a homogeneous, protective silica layer when the regime is passive, silica spheres can often been observed on the surface of the material for low CO_2 pressures, as a result of oxide reduction by carbon monoxide [17, 18]. So there is no uniform and passivating film on silicon carbide, and the so formed silica may react as follows:

$$SiO_2 + CO(g) = SiO(g) + CO_2(g)$$

As regards oxidation kinetics, a strictly parabolic trend can always be observed for passive oxidation under carbon dioxide, whereas kinetics successively exhibits a linear, then parabolic profile for passive oxidation under oxygen.

The case of He-cooled reactors

Helium in itself does not chemically interact with silicon carbide. Yet, it seems practically and thermodynamically impossible to remove all the impurities contained in the coolant. These residues can constitute oxidizing species such as oxygen or water vapor, in amounts up to 1000 ppm, which corresponds to relatively low partial pressures, thereby favoring active oxidation of the material [19]. In addition, the presence of polluting impurities coming from the other materials of the gas circuit cannot be excluded.

One way to approach the issue of the stability of silicon carbide under helium with a low impurity concentration is determining a critical passivation temperature and a critical temperature of silica decomposition.

Thus, SiC resistance to oxidation cannot be effective without the oxidizing species portion being present in sufficient quantity, thereby enabling silicon carbide to be passivated by the formation of a dense, homogeneous silicon layer. In the opposite case, oxidation is active, and the reaction products, in the gaseous state, do not protect the material, or the oxide layer formed is not uniform, and so does not act as a barrier against oxidation.

Literature gives no information about SiC behavior under the nominal operating conditions of a gas-cooled reactor: i.e. a 7-MPa helium pressure, a low, or even very low, oxidant partial pressure, a temperature around 1500 K, and, in incidental or accidental situations, a temperature rise up to 2300 K, with or without intrusion of different (oxidizing or not) atmospheres.

Consequently, investigations, which combined numerical simulation and high-temperature tests, had to be performed in order to define SiC behavior under various environmental conditions.

Investigation approach

The ceramic clad behavior is assessed under normal, incidental and accidental reactor operating conditions. Oxidation tests are performed under helium with different total pressures (0.1, then 0.3 and 7 MPa) and partial pressures of oxygen and water vapor. The approach is based on the following steps:

a. a thermodynamic approach of the system which uses the GEMINI 1 Computer Simulation Code, and aims at defining the temperature and pressure stability domains of the oxidizing products;

b. an experimental study of the ceramic clad oxidation behavior, which has required to use the solar test equipment of the Odeillo PROMES-CNRS Laboratory and the thermogravimetric analysis techniques (SPCTS-University of Limoges). This study is to define the role of the main reactor operating parameters on silicon carbide oxidation kinetics: oxygen and/or vapor partial pressure, total pressure, thermal cycle (holding temperature, temperature rise velocity), and the microstructural characteristics of the clad material (chemical composition of the grain boundary, average grain size…). This first research work is conducted on monoliths, which makes it easier to set up a correlation between resistance to oxidation, testing conditions, and the physico-chemical properties of the ceramic material;

c. a third part deals with interpreting the composite ceramics SiCf / SiCm behavior under oxidation under experimental conditions identical to those previously depicted. Experience gained following the works conducted on SiC monoliths (Part b) may simplify the analysis of the usual properties of composites, as it gives access to the silicon carbide matrix resistance to oxidation. Yet, oxidation resistance of these composite materials, which feature an architecture and a composition of high complexity; will be investigated with special attention to the role of the interphase and, more largely, of the secondary phases and the microporosities or microcracks.

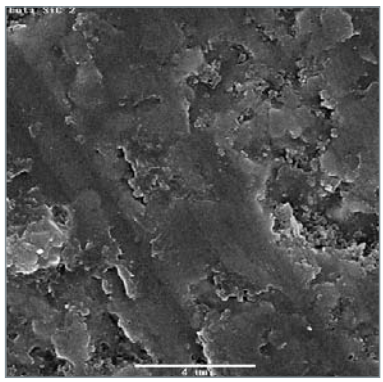

Fig. 98. SEM micrograph of a beta-SiC specimen treated at 1380 °C under an oxygen partial pressure of 2 Pa, which shows a passive oxidation.

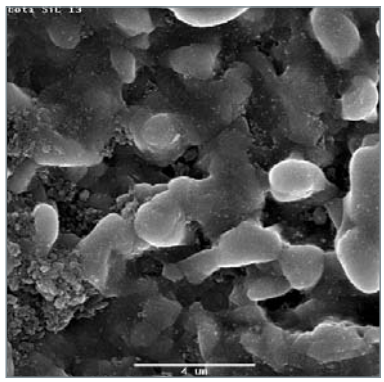

Fig. 99. SEM micrograph of a beta-SiC specimen treated at 1900 °C under an oxygen partial pressure of 2 Pa, which shows an active oxidation.

Assessing the physico-chemical performance of SiC-base ceramics at high temperature under various oxygen partial pressures is expected to provide guidance to R&D in making new composite materials and defining reactor operating scenarios.

Numerical simulation

As shown by the results of thermodynamic calculations, the transition temperature between passive and active oxidation is related to oxygen partial pressure by an Arrhenius law, with an activation energy of about 360 kJ.mol^{-1}. The results of the calculations performed with the GEMINI Code are consistent with those obtained with the Wagner model modified under helium [20], and under air [10].

The calculations also show that for an identical oxygen partial pressure, the influence of total pressure is negligible when passing from 0.1 to 7 MPa (nominal operating pressure).

Experimental study

The aim of the study is to distinguish the various factors which govern SiC oxidation: nature of the oxidizing species, pressure, temperature, and SiC fabrication process.

The tests performed on the MEXOS device at Odeillo's solar furnace (PROMES) and through thermogravimetry at the Limoges SPCTS confirmed the literature data and the trends displayed by computer simulation. It was also possible to assess the effect of the fabrication process by comparing the oxidation resistance of three silicon carbide grades with different microstructures and chemical compositions.

At low temperatures (1000-1200 °C), it can be noted that oxidation is low and causes silicon to be formed (passive oxidation), whatever the oxygen partial pressure and the SiC grade may be.

Between 1300 and 1550 °C, the effect of the oxygen content can be evidenced. For a passive oxidation/active oxidation transition temperature can be observed not only as a function of oxygen partial pressure, but also of specimens: the first results show clear evidence of a passive oxidation/active oxidation transition temperature of 1340-1700 °C for α-SiC, whereas it ranges between 1270 and 1380 °C for β-SiC. Figures 98 and 99 exhibit the (SEM-observed) difference in ***surface aspect*** between two β-SiC specimens treated under a 2-Pa oxygen partial pressure. At 1380 °C (Fig. 98), the surface is little altered (smooth surface), and is characteristic of a passive oxidation, which is confirmed by XPS analyses (SiO_2 signal). In contrast, at 1900 °C (Fig. 99), the surface exhibits strong alterations with a boundary grain attack, or even a loss of some grains; in such conditions, oxidation is active with SiO(g) formation and SiC consumption.

The protective role of the silica layer is clearly evidenced in the cycling tests at 1550 °C (treatment at 1550 °C for 10 hours after a 10-hour holding time at 1200 °C), since a decrease in SiC degradation can be seen, even under very little oxidizing conditions, with respect to direct treatment at 1550 °C.

It is also worth mentioning the effect of metallic impurities contained in one of the α-SiC specimens, which seem to stabilize the silica layer formed at 1200 °C and thus play a protective role during treatments at 1500 °C, even under active oxidation conditions.

At higher temperatures (1700 °C), oxidation is clearly active, whatever the oxygen content and the SiC grades may be. It can also be observed a higher degradation of α-SiC with respect to β-SiC: for a temperature of about 1730 °C, under an oxidizing atmosphere (1 mbar O_2), α-SiC loss mass is twice as high as that of β-SiC, and four times as high in a very little oxidizing atmosphere (2.10^{-3} mbar).

Considering these first results, it appears that beyond temperature and oxygen partial pressure, the SiC composition (reaction residues such as carbon or silicon, or impurities) plays a paramount role upon resistance to oxidation, by altering oxygen diffusion kinetics [21].

To sum up it all, the presence of metallic impurities therefore seems to be an advantage to preserve SiC from active oxidation conditions. In order to detail the role of these elements, additional tests were carried out on specimens containing variable amounts of metallic impurities [22].

Kinetic studies relating to longer periods of thermal treatment are conducted by thermogravimetric analysis so as to define **behavior laws*** likely to be used in the various operating scenarios. Analog oxidation tests have been carried out on composites with a SiC / SiCf ceramic matrix.

Corrosion of graphite and carbon-carbon composites

Graphite is an **allotropic*** form of carbon, in which carbon atoms are arranged in parallel hexagonal layers. Graphite possesses a high melting / sublimation point, high thermal conductivity, good mechanical stability up to high temperatures, and a low atomic number.

It is used in some reactor systems as a neutron moderator associated with various coolants: carbon dioxide in the Natural Uranium Graphite Gas (UNGG: *Uranium Naturel Graphite Gaz*) systems, or in the Advanced Gas cooled Reactor (AGR) system, water in the Soviet Type RBMK system, or again helium in reactor systems such as High Temperature Reactors (HTRs) or Very High Temperature Reactors (VHTR: a reactor selected amongst the 6 concepts of the **Generation IV*** initiative). Concerning helium-cooled reactors (HTR and VHTR), graphite is also used as a core structure component, that is for fuel "assemblies" (prismatic blocks or pebbles), as well as for reflectors, and for the core supporting structure. Last but not least, in helium-cooled reactors, graphite plays the role of a thermal barrier.

Graphite displays reduced resistance to oxidation at high temperature. Therefore, it is particularly important to ensure its good behavior, both in normal operation, i.e. in helium containing low concentrations of oxidizing species, and in accidental situation, e.g. in the case or air inflow into the primary coolant system following a containment failure.

Parameters of graphite oxidation by air

Carbon reaction with oxygen has been dealt with in many research works. According to Duval in 1960 [23]: *"For no chemical reaction has ever existed that has induced so many works without final conclusions being drawn on kinetic data as basic as order and activation energy. As a matter of fact, it is probable that many other heterogeneous reactions would prove to be more complex than is generally thought, were they investigated by so many research scientists and with so much care."*

From a kinetic viewpoint, the oxidation reaction of graphite by air consists of 3 successive steps: oxygen supply to the graphite surface, gas diffusion through the graphite porosity, and finally the properly said chemical reaction between oxygen and carbon. Three fields are generally identified, which correspond with three limiting steps (Fig. 100):

- At low temperatures (Area I), kinetics is controlled by the surface chemical reaction. Concentrations in reactants and products are more or less homogeneous in the pores and in the core of the gas environment. The material is oxidized homogeneously in the porosity. However, if there is no significant alteration of the specimen size up to 50% oxidation, a significant degradation occurs in the mechanical behavior of graphite (lower density and collapse strength). Finally, the specimen falls to dust.

- When temperature increases (Area II), the reaction rate increases more rapidly than diffusivity; any reactant molecule which penetrates into a pore, reacts as soon as it comes into contact with the pore wall. The reaction rate is thus controlled by pore diffusion. Graphite mechanical properties are less altered than in the previous case.

- At still higher temperatures (Area III), a reaction takes place at the outer surface of graphite owing to the reactivity of chemical species. As the concentration gradient gets increasingly higher between the gas and the wall, gas inflow to the solid's outer surface then becomes the limiting step. This oxidation mode entails an alteration in the solid's geometric dimensions, but has little effect on the specimen's mechanical properties. It is worth mentioning that the overall reaction rate then depends on gas renewal in surface (reactant inflow to the surface and reaction products outflow).

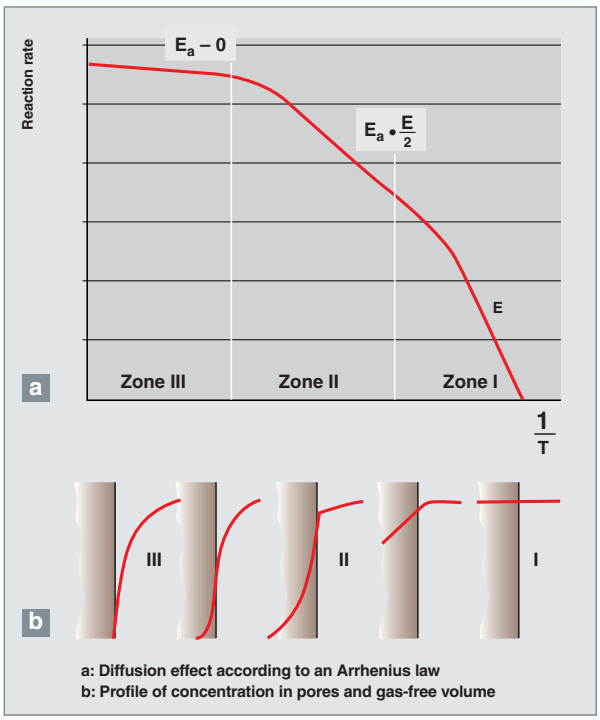

a: Diffusion effect according to an Arrhenius law
b: Profile of concentration in pores and gas-free volume

Fig. 100: Temperature ranges considered for the kinetics of graphite oxidation in air. Correspondence between activation energy and concentration profile [23].

The transition of a regime to another was the topic of many research works. The transition temperature is a function of numerous parameters, one of the most obvious being the porous structure of graphite. According to STAIRMAND [24], the Regime I / Regime II transition temperature is around 500 °C for a nuclear graphite, whereas the Regime II / Regime III transition is around 900 °C.

The temperature effect on the reaction has also been studied. NAGLE *et al.* [24] have thus observed that the oxidation rate increases with temperature prior to reaching a plateau. The temperature at which this plateau is attained, is a function of the graphite used and the experimental conditions. The values obtained by the different authors range between 1200 °C and 1800 °C. When the combustion reaction of graphite starts, the reaction may be self-sustained. Yet, it seems that the self-sustained oxidation of graphite cannot be held below 650 °C. Under this temperature, the self-sustained oxidation regime can be reached only if the air renewal rate is sufficient to bring oxygen and carry over combustion products, but not too high, so that convection cooling does not exceed heat input through chemical reaction.

The graphite oxidation reaction by air causes two gaseous compounds to be formed: carbon monoxide (CO), and carbon dioxide (CO_2). Carbon dioxide itself is also is an oxidizing species, but the CO_2 reaction rate with graphite is slower than the reaction rate between oxygen and graphite. Thus, at 800 °C, the reaction rate between graphite and CO_2 is 6 10^4 to 6 10^5 times lower than between O_2 and graphite.

At low temperatures, CO and CO_2 are two primary products of graphite oxidation. At higher temperatures, carbon monoxide becomes the main product. Besides, at T>1200 °C, CO is almost the only reaction product, and carbon dioxide is then the product of CO oxidation by oxygen in excess. Carbon dioxide so formed may in turn be reduced by carbon, according to the mechanism described in the Boudouard equilibrium ($CO_2 + C \leftrightarrow 2\ CO$, $\Delta H = -40{,}79$ kcal / mole).

Parameters of graphite oxidation by air

Graphite oxidation by air is influenced by various parameters that may fall into two major families:

- Graphite intrinsic factors, such as specific area, graphitization degree, porous structure, and present impurities (quantity and nature),

- Environmental factors, such as temperature, present ionizing radiation, mechanical stresses imposed to the graphite matrix, flow rate and pressure conditions, and gas composition.

All these parameters are not equally important as regards the phenomenon of graphite oxidation by air. As a matter of fact, the two main "intrinsic" parameters are the porous structure and impurities occurring in graphite, whereas the main "environmental" factors are temperature, the gaseous phase composition, and present ionizing radiation.

"Intrinsic" parameters

The graphite used in the industry is generally porous ($d_{theoretical} = 2.2$ and d_{real} for a nuclear graphite ~1.8). A major part of the surface accessible to gas is therefore located in the porosity (a specific area determined through the BET method ~ 0.1 to 1.1 m^2/g). Describing the steps involved in the reaction of graphite combustion in air helps evidence the fundamental role of porosity on reaction kinetics and its consequences. For a given temperature, the characteristics of the porous lattice will define the oxidation regime according to which the reaction takes place (Fig. 100): either the gas may go deep inside graphite (Regimes I and II), or its stays at the surface of the graphite block (Regime III), the transition between these regimes being a function of the pore diameter among other parameters. One part of porosity, initially closed, may be open during a temperature rise or during graphite oxidation. Thus, high-temperature purification of graphite causes the opening of a low portion of closed porosity, whereas the specific area of the specimens (BET surface) is practically multiplied by 2 (Table 3).

Table 3.

Evolution of graphite parameters during a high-temperature purification operation

	Prior to high-temperature purification				After high-temperature purification			
Graphite nature	Apparent density	Porosity open	Porosity closed	BET surface (m^2/g)	Apparent density	Porosity open	Porosity closed	BET surface (m^2/g)
Carbone Lorraine 3780	1.60	0.23	0.07	0.36	1.59	0.23	0.06	0.69
Carbone Lorraine 5501	1.61	0.17	0.11		1.59	0.22	0.06	
EDF type graphite	1.69	0.17	0.08	0.23	1.68	0.17	0.08	0.49

Table 4.

Comparison of methods used for calculating the graphite oxidation rate: surface rate ($g.cm^{-2}.h^{-1}$) and mass rate ($g.g^{-1}.h^{-1}$)

Oxidation regime	Side (cm)	Oxidation T (°C)	Air Q (l/h)	Rate $g/cm^2.h$	Rate g/g.h
Pore diffusion	1.5	780	400	0.14	0.41
	2.5	780	500	0.17	0.26
	1.5	800	800	0.18	0.55
	2.5	800	1000	0.22	0.32
Mass transfer	1.5	1050	800	0.70	1.90
	2.5	1050	1000	0.65	0.90
	1.5	1080	2000	1.00	2.90
	2.5	1080	2000	0.95	1.30

According to the units used, different conclusions may be drawn from the evolution of graphite porosity and the geometry associated with the various oxidation regimes. Table 4 thus indicates oxidation results obtained for the same specimens depending on whether they are given in surface oxidation rates ($g.cm^{-2}.h^{-1}$), i.e. relative to the specimen geometric surface, or in mass oxidation rates ($g.g^{-1}.h^{-1}$), i.e. relative to the specimen mass: if the specimen size has no influence on the surface rate ($g.cm^{-2}.h^{-1}$), reversely, it does have an influence on the mass rate ($g.g^{-1}.h^{-1}$), all the more as the temperature is higher.

The role of graphite impurities on the rate of oxidation by air was dealt with in quite a number of studies, not always converging. According to Lewis [25], *"the behavior of carbons containing a few percent impurities may be so complex that results, even if useful in practice, might be difficult to relate to those collected on materials of higher purity. [...] Catalyzing elements sometimes exhibit co-operative effects, which makes it difficult to predict the behavior of a graphite contaminated by a mixture of impurities. In an attempt to better understand the causes of this catalytic effect, impurity behavior on monocrystals and microcrystallites of graphite electrodes was investigated through electron microscopy and optical microscopy. The results have not brought clear answers; on the contrary, they have shown that catalytic effects are extremely elaborate and often of high specificity."*

Nevertheless, several results seem to have been acquired today. In particular, the impurity role on graphite oxidation by air is essentially and logically more sensitive during the phases controlled by the chemical reaction (Regime I) or, to a lesser extent, by diffusion through pores (Regime II). At higher temperatures, the impurity role disappears almost completely (Regime III: kinetics is controlled by gas phase transfer to the solid's surface).

Many authors have tried to classify impurities according to their catalytic effects. As an example, Amariglio and Duval [25] have measured the effect of adding various impurities (120 ppm) on the oxidation rate in air at 430 °C. The acceleration factors thus obtained are the following: Ba = 100, Cd = 90, Na = 130, Au = 240, Cu = 500, Mn = 86,000, Pb = 470,000. The presence of impurities in graphite results in lower activation energy. Thus, activation energy varies between 59 and 64 kcal / mole when determined from nuclear graphites purified by heating at 3500 °C up to reaching a non-dosable ash ratio. In the case of nuclear graphites with an ash ratio ranging from 100 to 200 ppm, activation energies measured are rather neighbouring 40 kcal / mol.

Last but not least, it is worth noting that if most of mineral impurities have a catalytic effect on graphite oxidation, some substances display an inhibiting effect; such is the case, especially, of phosphates, borates, and above all chlorine and chlorinated derivatives.

"Environmental" parameters

Gaseous atmosphere is characterized by the flow properties (flow rate and temperature) and the impurities present in the gas phase.

The gas flow rate governs the supply of oxidizing species and the sweeping of gaseous products (CO and CO_2); it enables the reaction-released heat to be eliminated more or less efficiently. On the other hand, the flow rate exerts an influence on the thickness of the gas boundary layer on the graphite surface, and so on mass transfer through this boundary layer. Figure 101 displays the findings of a study on the dependence of graphite oxidation rate on gas flow rate. For an oxidation temperature lower than 900 °C, kinetics is controlled by the chemical reaction and / or diffusion through pores. So there is no influence of the flow rate upon the graphite oxidation rate. In contrast, at high temperatures, it is not surprising to observe a flow rate effect, as kinetics is controlled by material transfer from gas to the graphite geometric surface.

Among the factors likely to influence graphite oxidation by air, the water vapor content of the gas phase seems to be very important. This point, mentioned by quite a number of authors [23, 26], seems however to be strongly dependent on the nature of the graphite under investigation. The two intrinsic parameters mentioned hereabove (present impurities and graphite porosity) are thus proposed for interpreting apparently contradictory results, i.e. a catalytic effect or an inhibiting effect of graphite oxidation by wet air (Table 5).

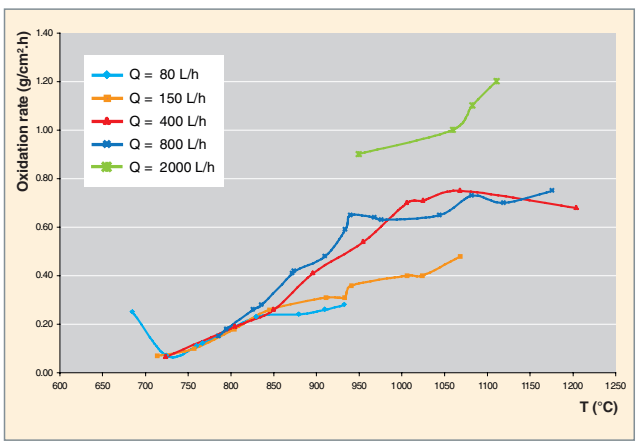

Fig. 101. Effect of gas flow rate and temperature on the rate of graphite oxidation by air [27].

Table 5.

Graphite oxidation rate in dry and wet air [23]

	Dry air at 637 °C	Wet air at 637 °C
Undoped graphite	1	0.6
Graphite doped with impurities	4	6.4

One of the consequences of graphite irradiation is energy storage related to carbon atom displacement out of their normal position in the crystal lattice.

The energy so stored may reach 120 J/g, which corresponds to the potential energy that tends to bring back atoms to their equilibrium position. The sudden release of this energy, generally referred to as "Wigner energy", may thus cause a rise of graphite temperature from room temperature to 1200 °C, thereby inducing the spontaneous ignition of graphite in air. This phenomenon is sensitive when oxidation under irradiation is brought to a temperature lower than 200 °C. In order to avoid this risk, periodic annealing enables atoms in an interstitial position to move back to their former position in the lattice. This very delicate operation has to be performed in an extremely rigourous manner, indeed. For it is in such an operation that a fire started at Windscale nuclear power plant. By contrast, in the case of operation at a higher temperature, for example in a HTR or VHTR, annealing takes place simultaneously with the irradiation phase, so that this step is no longer necessary.

Investigations have also been conducted by several authors on how the oxidation rate evolves under irradiation. The carbon oxidation rate is influenced by the defects of the crystal lattice. Thus, it could be observed that the oxidation rate of a graphite is multiplied by 6 between 250 °C and 400 °C if 2% of the atoms are displaced, whereas the reaction's activation energy drops from 48.8 to 36.1 kJ / mole. As a matter of fact, when oxidation directly occurs under flux between 200 °C and 300 °C, it is up to 30 times faster than that of unirradiated graphite, whereas the oxidation rate gets lower between 350 °C and 400 °C. This phenomenon could be explained by the radiolytic formation of ozone and higher nitrogen oxides.

Graphite oxidation, especially by air or oxygen, has always spurred numerous studies, and is still doing so. Indeed, the conclusions drawn by the various authors are not always converging. Yet, a certain number of key criteria can be pinpointed, which influence graphite behavior with respect to oxidation. Such criteria may be categorized into the following two families: intrinsic parameters of graphite, and criteria related to oxidation conditions.

Concerning the first category, the two main parameters to be retained are porosity and impurities present in graphite. The first one, in particular, will govern the kinetics of graphite oxidation by air, favoring or impeding oxygen access to the core of graphite. Though graphites are increasingly pure, some impurities may however act as an oxidation catalyzer or inhibitor. It is therefore critical to fully control this parameter. So, these parameters are now taken into account in studies for developing new graphites for nuclear reactors, in parallel with mechanical and thermal properties and the nuclear waste issue relating to activation of graphite and of its impurities.

As regards oxidation conditions, the main parameters are gas temperature, flow rate and quality (especially water content). At high temperatures, oxidation takes place chiefly on the surface of graphite blocks, whereas at low temperatures kinetics is governed by the chemical reaction: blocks may be attacked in their whole volume, hence the degradation of their mechanical properties. The gas flow rate will display two antagonist effects: first, air (oxygen) supply, to maintain the reaction and the combustion gas release (CO and CO_2), and, secondly, graphite cooling, which will tend to limit graphite oxidation. Presence of water vapor may exert an inhibiting, or, reversely, catalyzing effect on graphite oxidation, depending, particularly, on the impurities present in graphite. Purity of new nuclear graphites is expected to favor an inhibiting effect of water vapor, which is to be checked.

References

[1] Monographie DEN M0. *"L'énergie nucléaire du futur: quelles recherches pour quels objectifs ?"*, Éditions du Moniteur, Paris, décembre 2005.

[2] W.J. Quaddakers, "Corrosion of High Temperature Alloys in the Primary Circuit Helium of High Temperature Gas Cooled Reactors", *Werkstoffe und Korrosion*, 36 (1985), pp. 141-150 and 335-347.

[3] F. Rouillard *et al.*, Ox. Met. 68 (2007), pp. 133-248.

[4] F. Rouillard, C. Cabet, K. Wolski, A. Terlain, M. Tabarant, M. Pijolat and F. Valdivieso, "High temperature corrosion of a nickel base alloy by helium impurities", *J. Nucl. Mater.,* 362 (2007), pp. 248-252.

[5] C. Cabet, J. Chapovaloff, F. Rouillard, G. Girardin, D. Kaczorowski, K. Wolski and M. Pijolat, "High temperature reactivity of two chromium-containing alloys in impure helium", *J. Nucl. Mater.,* 375 (2008), pp. 173-184.

[6] F. Rouillard, C. Cabet, S. Gossé, K. Wolski and M. Pijolat, "Thermodynamic Modelling of the Destruction of the Surface Cr_2O_3 on Alloy 230 in the Impure Helium Atmosphere of a Gas Cooled Reactor", *Mater. Sci. For.,* Vol. 595-598 (2008), p. 429.

[7] C. Cabet, G. Girardin, F. Rouillard, J. Chapovaloff, K. Wolski and M. Pijolat, "Comparison of the High Temperature Surface Reactivity in Impure Helium of Two Materials for Gas Cooled Reactors", *Mater. Sci. For.*, Vol. 595-598 (2008), p. 439.

[8]. Gossé, T. Alpettaz, F. Rouillard, S. Chatain, C. Guéneau, C. Cabet *et al.*, "Direct Measurements of the Chromium Activity in Complex Nickel Base Alloys by High Temperature Mass Spectrometry", *Mater. Sci. For.*, Vol. 595-598 (2008), p. 975.

[9] M. Balat, G. Flamant, G. Male and G. Pichelin, "Active to passive transition in the oxidation of silicon carbide at high temperature and low pressure in molecular and atomic oxygen", *J. Mater. Sci.*, 27, pp. 697-703, 1992.

[10] M. J. H. Balat, "Determination of the Active-to-Passive Transition in the Oxidation of Silicon Carbide in Standard and Microwave-Excited Air", *J. Eur. Ceram. Soc.*, 16, pp. 55-62, 1996.

[11] N. S. Jacobson, D. S. Fox and E. J. Opila, "High temperature oxidation of ceramic matrix composites", *Pure & Appl. Chem.*, 70, pp. 493-500, 1998.

[12] E. J. Opila and R. E. Hann. "Paralinear Oxidation of CVD SiC in Water Vapor", *J. Am. Ceram. Soc.*, 80, pp. 197-205, 1997.

[13] E. J. Opila. "Variation of the Oxidation Rate of Silicon Carbide with Water-Vapor Pressure", *J. Am. Ceram. Soc.*, 82, pp. 625-636, 1999.

[14] K. L. More, P. F. Tortorelli, M. K. Ferber and J. R. Keiser, "Observations of Accelerated Silicon Carbide Recession by Oxidation at High Water-Vapor Pressures", *J. Am. Ceram. Soc.*, 83, pp. 211-213, 2000.

[15] P. F. Tortorelli and K. L. More, "Effects of High Water-Vapor Pressure on Oxidation of SiC at 1,200 °C", *J. Am. Ceram. Soc.*, 86, pp. 1249-1255, 2003.

[16] E. J. Opila, D. S. Fox and N. S. Jacobson, "Mass Spectrometric Identification of Si-O-H(g) Species from the Reaction of Silica with Water Vapor at Atmospheric Pressure", *J. Am. Ceram. Soc.*, 80, pp. 1009-1012, 1997.

[17] M. Balat, R. Berjoan, G. Pichelin and D. Rochman, "High-temperature oxidation of sintered silicon carbide under pure CO_2 at low pressure: active-passive transition", *Appl. Surf. Sci.*, 133, pp. 115-123, 1998.

[18] M. Balat and R. Berjoan. "Oxidation of sintered silicon carbide under microwave-induced CO_2 plasma at high temperature: active-passive transition", *Appl. Surf. Sci.*, 161, pp. 434-442, 2000.

[19] F. J. Perez and N. M. Ghoniem. "Chemical compatibility of SiC composite structures with fusion reactor helium coolant at high temperatures", *Fus. Eg. Des.*, 22, pp. 415-426, 1993.

[20] J. Eck, M. Balat-Pichelin and F. Audubert. "Étude du comportement du SiC à haute température sous différentes atmosphères", *Matériaux 2006*, 13-17 novembre 2006 (Dijon).

[21] J. Eck, M. Balat-Pichelin, E. Beche and F. Audubert. "Behavior of SiC at high temperature under helium with low oxygen partial pressure", *Journal of the European Ceramic Society*, Volume 28, Issue 15, November 2008, pp. 2995-3004.

[22] L. Charpentier, M. Balat-Pichelin, A. Maître, M. Gendre, S. Chehaidi, G. Di Vita, S. Foucaud and F. Audubert, "Influence of alumina on the passive oxidation at low oxygen pressure of hot-pressed a-SiC", *Scripta Materialia*, 60, pp. 481-484, 2009.

[23] P. Pascal, "*Nouveau traité de chimie minérale*", Tome VIII- 1er fascicule, Masson et Cie Éditeur.

[24] J. Nagle and R.F. Stricland-Constable, “Oxidation of carbon between 1000-2000 °C”, *Proceedings of the Fifth conference on Carbon* (Pennsylvania State University), 1962.

[25] J.B. Lewis, “Modern aspects of graphite technology”, *Academic Press* (1970).

[26] F.M. Lang, P. Magnier, P. Gilles, R. Pollet and M. Brie, “*Influence perturbatrice de la vapeur d’eau sur le mécanisme d’oxydation du graphite en présence d’oxygène (500-650 °C)*”, Seventh biennial conference on carbon, June 21-25, 1965, Cleveland (USA).

Fabienne Audubert,
Fuel Studies Department

M. Balat-Puichelin,
Promes, CNRS Odeillo

Céline Cabet and Fabien Rouillard,
Physico-Chemistry Department

A. Maître,
SPCTS, Limoges University

Jean-Charles Robin,
Nuclear Industry Support Department

Materials Corrosion in Liquid Metal-Cooled Reactors

Several coolants may be used as primary fluids for developing fast neutron reactors, such as: sodium, gas, lead, or lead-bismuth eutectic, supercritical water, etc. High power density requires using a coolant endowed with very good thermal properties (thermal conductivity, specific heat): this is the reason why liquid metals are very attractive for this type of application. Nowadays two paths are being investigated around the world. Sodium-cooled fast neutron reactors have been developed in the early fifties. Phénix has just been shut down in France, but some reactors of this type have still been in operation for many years. Others are under construction (CEFR in China, BN800 in Russia, PFBR in India). Lead-cooled fast reactors, which are especially studied by RDIPE (Research & Development Inst. of Power Engineering, Russia), within the frame of projects BREST 300 and BREST 1200[4], and the 6th-PCRD European project "ELSY" (European Lead-cooled SYstem), are an alternative to the sodium-cooled fast neutron reactor. They offer the advantage of a significant feedback from other reactor systems: lead or lead-bismuth eutectic are contemplated for hybrid reactors (Accelerator Driven Systems) designed for waste transmutation, both as coolants and for neutron generation in the spallation target. Lead-bismuth eutectics and Pb-Bi-Cd are also considered for the intermediate coolant circuit of sodium-cooled fast reactors, and the lead-lithium eutectic for tritium-generating blankets of fusion reactors.

In these reactors, controlling corrosion due to liquid metals stands as a major challenge. Corrosion by sodium, lead or its alloys may act according to various mechanisms: dissolution of the solid in the liquid metal, formation of intermetallic compounds, intergranular penetration of the liquid metal into the solid, embrittlement of the solid by the liquid… Moreover, in presence of a thermal gradient, dissolution-deposition phenomena may occur, thereby entailing transfer of material between hot and cold areas. This may generate materials degradation in hot areas, facility plugging in cold areas, and contamination by deposition or diffusion. Dissolved metallic species activity can thus have a preponderous influence on the kinetics of transfer phenomena. These phenomena may be influenced by present impurities, that is not only oxygen, but also carbon and nitrogen.

4. BREST 1200: BREST stands for "bystro reaktora židkost' tjaželo", i.e. "heavy coolant fast neutron reactor".

Corrosion in sodium-cooled fast reactors

Corrosion by liquid sodium

Sodium possesses neutron and physical properties attractive for its use as a coolant in a fast neutron reactor. It is in a liquid state at temperatures ranging from 97.8 to 880 °C. Its viscosity is comparable to that of water, which enables thermohydraulic studies in water to be performed, and its compatibility with metallic materials is satisfactory.

Generally, it is considered that ferritic or austenitic steels, or still alloys that do not contain more than 32% nickel (as nickel solubility is high in liquid sodium) can be used in sodium reactors.

It is however necessary to control the operating conditions in order to avoid stress corrosion cracking and to limit general corrosion and, so, mass transfer which generates primary coolant system contamination by activated corrosion products. Although this contamination is relatively moderate if compared with that developing in other types of reactors, such as light water-cooled reactors, it may however require suitable decontamination during handling and repair operations relating to main components.

Corrosion and mass transfer mechanisms are described hereafter, and the scope of our investigations is also extended to the influence of impurities (carbon, nitrogen) dissolved in alloys.

Embrittlement

Embrittlement by liquid metals is a type of stress corrosion cracking affecting metals and alloys which undergo a tensile mechanical stress and are in contact with liquid metals: this phenomenon stands as a major issue for metallic alloys exposed to liquid metals. Although data from literature vary significantly, it is generally considered that exposure of ferritic and austenitic steels to pure liquid sodium (with a low impurity content), under constant-load test conditions, does not produce a major effect on the rupture strength of these steels [1]. Moreover, regarding stainless steels containing nitrogen (added to steel to improve its mechanical properties at high temperature, and, so, its resistance to failure), such as those of Type 316L(N), they display comparable times to failure under creep in pure sodium and air, as shown on Figure 102.

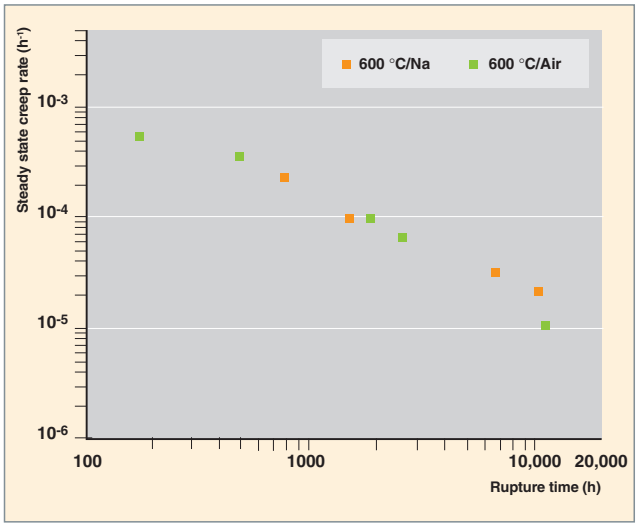

Fig. 102. Influence of the surrounding environment (Air/sodium) on the time to rupture of a stainless steel at 600 °C. In sodium, this time to rupture is comparable to that obtained in air at the same temperature [2].

With impurity concentrations typical of sodium-cooled reactors, a certain susceptibility of unalloyed or low-alloy steels (up to 9% chromium) can be observed during the very severe slow strain rate tensile tests, at temperatures between 200 °C and 400 °C, as displayed on Figure 103 for a low-alloy steel [3]. As evidenced by the observations carried out, microstructure and non-metallic impurities present in the alloy have a great impact on these phenomena of embrittlement by liquid sodium. At higher temperatures, a sharp change of behavior can be seen, so that embrittlement by liquid sodium no longer seems to ever take place [4].

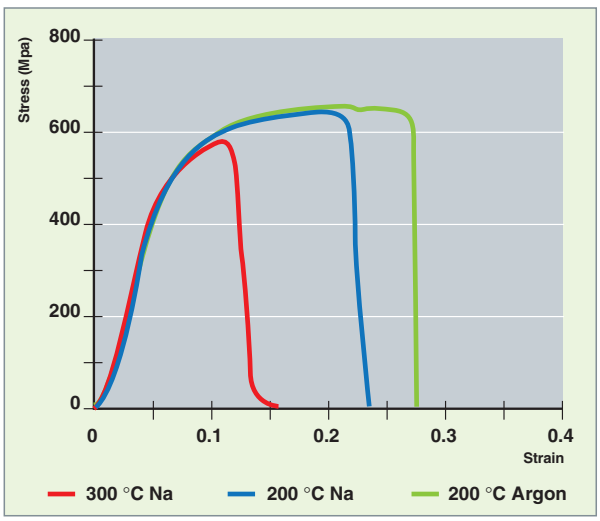

Fig. 103. Stress-strain curves relating to a low-alloy steel in sodium and argon at 200 °C and 300 °C, at 10^{-6} s^{-1} [3].

Accidents (e.g. water or air leaks) may increase impurity concentration in liquid sodium. Generally, sodium hydroxide may cause stress corrosion cracking (SCC) in ferritic and austenitic steels, including in liquid sodium, if NaOH concentration, temperature and stress are sufficiently high. A more detailed study was conducted into Alloy-800 behavior in liquid sodium at various concentrations, as shown on Figure 104, in which Alloy 800 susceptibility to intergranular SCC was determined as a function of stress intensity and NaOH concentration [5].

In addition, stress corrosion cracking phenomena may occur owing to the presence of aqueous soda when the component, covered by a residual sodium film, is polluted by moisture, with local generation of aqueous soda. At temperatures higher than 80 °C for ferritic steels, and higher than 110 °C for austenitic steels, transgranular cracking may take place very rapidly. Such temperatures may occur during facility preheating, and

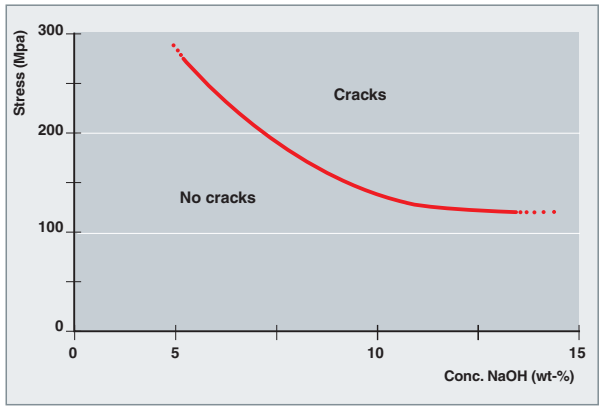

Fig. 104. Alloy-800 sensitivity to intergranular stress corrosion cracking in Na/NaOH mixtures [5].

then during sodium filling. It is therefore required to avoid any residual presence of aqueous soda on components, especially in gaps and clearances of structures and circuits, which is obtained through relevant washing and drying procedures. (In France, the aim is generally to reach a dew point lower than -20 °C in the sweeping gas prior to filling the facility with sodium).

General corrosion mechanisms in liquid sodium

General corrosion mechanisms of austenitic steels in liquid sodium were investigated in the seventies-eighties, and described in the literature devoted to this topic. They consist in a dissolution of the surface elements in steel (Fe, Cr, Ni, Mn, C), in contact with sodium, followed by their transfer and deposition, or diffusion, on the reactor structures. This deposition phenomenon represents the main vector of contamination of reactor structures by activated corrosion products. The dissolution phase can be divided into four successive time steps,

the existence and duration of which are temperature-dependent: surface cleaning, surface dissolution of austenite, formation of a ferritic layer, and access to a steady state. These local phenomena depend on various parameters such as temperature, oxygen concentration, and sodium rate. Consequently, they are strongly connected with mass transfer phenomena occurring between reactor hot and cold areas.

For an austenitic steel, four successive steps can usually be distinguished:

Step 1: surface cleaning. This step corresponds with dissolution of metallic oxides and superficial inclusions during the first hours. It is generally considered that surface cleaning starts at low temperature, but clean surfaces can only be obtained with temperatures of approx. 300-350 °C, in presence of sodium with a very low oxygen content ([O] < 5 ppm). This step results in a very good wetting of the metallic surface by liquid sodium.

Step 2: dissolution of austenite. The following step mainly occurs at temperatures equal to or higher than 570 °C, and consists in a selective dissolution of nickel present in the austenitic phase. This is the so-called "dissolution" of the austenitic layer in contact with sodium and the diffusion of steel elements towards sodium. If temperature is lower than 590 °C (which is the case for all of the structures excepting fuel clads), the following steps are generally too slow and do not occur in practice.

Step 3: formation of a ferritic layer. During a longer period of time, at a temperature higher than an approximate 590 °C, the preferential dissolution of the nickel present in steel from the outer austenitic layer causes steel to be ferritized. This ferritic layer is also dissolved, but at a slow rate, in liquid sodium (iron and chromium are also soluble in sodium, but at a lesser degree than nickel), and the various steel alloying elements diffuse to the surface.

Step 4: behavior in steady state (Fig. 105). The thickness of the ferrite layer has reached its threshold value; the rates of alloying element dissolution and diffusion towards sodium correspond with a stœchiometric corrosion of austenite. The contents reached at the sodium-steel interface are of about 1 to 2% for nickel, 5 to 7% for chromium, and less than 0.5% for manganese.

In Steps 2 and 3, the corrosion rate decreases until it reaches a constant value in Step 4. During Steps 2 and 3, the elements dissolved preferentially are alloying elements (mainly nickel, but also chromium). During Step 4, the relative quantities of metallic elements dissolved correspond with those of the initial alloy (Step 4 is commonly referred to as "stœchiometric corrosion").

In pure sodium (i.e. oxygen concentration $[O^{2-}]$ lower than e.g. 1 ppm), corrosion corresponds with a dissolution of metallic

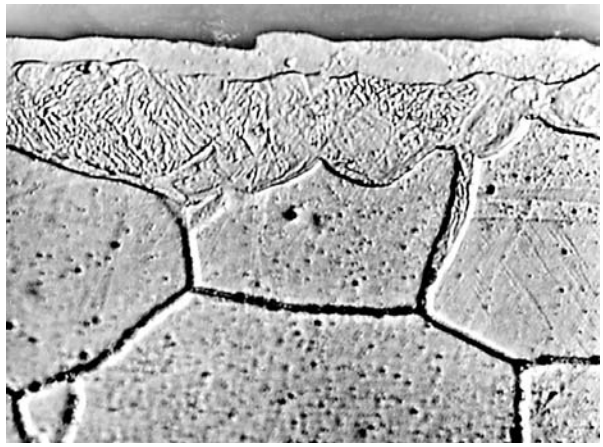

Fig. 105. General corrosion of an austenitic stainless steel in liquid sodium. The picture shows the emergence of a ferritic film in surface (Ferrite / Ferrite and austenite / Sound austenite).

elements in liquid sodium, as expressed hereabove. If temperatures are not too high (e.g. up to 550 °C), this phenomenon is relatively slow: corrosion is therefore limited.

For oxygen concentrations higher than 1-5 ppm, an oxidation reaction takes place, and entails a rise in corrosion rates with the following reaction:

$$2Na + O + 1/2\ M \rightarrow 1/2\ NaMO_2 + 3/2\ Na$$

where M stands for iron or chromium, whereas nickel is not involved in the oxidation reaction in presence of sodium.

General corrosion parameters

General corrosion kinetics is mainly a function of sodium physico-chemical parameters (temperature and flow velocity, oxygen content…).

- **Temperature:** temperature increases steel corrosion rate in liquid sodium, especially beyond 570 °C. Below this temperature, general corrosion is fairly reduced. In other terms, corrosion mainly affects the cladding material of fuel assemblies in the core, in the primary coolant circuit: the clad temperature reaches 600 °C on the average, for a sodium temperature ranging from 360 °C to 550 °C. Within the frame of the Generation IV International Forum (GIF), it is suggested to investigate the consequences of a rise of sodium temperature to 600 °C in the hot collector: it will be therefore necessary to assess the effects of this new stress on the corrosion phenomenon and, more generally, on the contamination level in the reactor.

- **Oxygen activity in sodium:** the alloying element content in the Na-steel interface area depends on the oxygen content of sodium: chromium, iron, nickel and manganese contents are increased with the oxygen content. In addition, the corrosion process changes when the oxygen content exceeds a threshold of about 5 ppm. The dissolution is then increased by oxidation reactions, thereby inducing complexes. According to the corrosion model considered, the exponent of the term [O], which stands for oxygen in the kinetic law, is between 0.8 and 1.8.

- **Sodium rate:** general corrosion increases with sodium flow velocity, up to a threshold beyond which it no longer rises significantly. This observed phenomenon could be explained by a mixed control of (dissolution) reaction and diffusion (through the boundary layer). At higher flow velocities, corrosion would only be limited by the reaction at the interface, and would no longer depend upon the flow.

In isothermal areas and in extreme cases, sodium saturation in dissolved elements may limit the corrosion process; in the sodium-cooled reactor core, this effect may be disregarded owing to the positive temperature gradient along the fuel clad.

Models of corrosion by liquid sodium

In order to reach a better understanding of the corrosion products and radionuclide behavior, a certain number of laboratories have launched research programs which mainly aim at developing corrosion models, particularly in France and in the United Kingdom, with special attention to various degrees of oxygen concentration [O]. Two semi-empirical models are used by the CEA to calculate general corrosion as a function of oxygen concentration for a Type 316 austenitic steel.

For an oxygen [O] concentration lower than 5 ppm (the maximum value allowed for reactor operation for a limited duration; recommended value: 3 ppm), the BAQUÉ model [6] is used, which considers that metal loss R is negligible under 450 °C approximately:

$R = 0$ (for temperatures lower than 817.13 K)

$R = 0.078 \cdot V^{0.435} \cdot [O] \cdot \exp(-150.5/(T-817.13))$

where: R = loss of metal in $kg.m^{-2}$ over one year
a = 0.078, a coefficient for a Type 316 austenitic steel
V = sodium flow velocity (m/s) (< 10 $m.s^{-1}$)
T = temperature in K (above 817.13 K and < 993.13 K)
[O] = oxygen content in ppm (Eichelberger's solubility law): the Eichelberger's law for oxygen solubility in liquid sodium is given by the following equation:
$\log_{10}[O] = 6.239 - 2447/T$
with [O] expressed in ppm, and T in K.

Beyond the 5 ppm of oxygen dissolved in sodium, the THORLEY model is used [7], given for [O] between 0 ppm and higher concentrations, but used in France beyond 5 ppm):

If $V \leq 4$ m/s, $R = (V/4)^{0.435} \cdot 10^{2,724 + 0.01106 \cdot \log10[O] - 39,13/(T)}$

If $V > 4$ m/s, $R = 10^{2,724 + 0,01106 \cdot \log10[O] - 39,13/(T)}$

where: R = metal loss in $kg.m^{-2}$ over one year
[O] = oxygen content in ppm (Thorley's law)
T = temperature in K

The main difference between the two models is that, in the BAQUÉ model, corrosion at temperatures lower than 544 °C is negligible.

These two semi-empirical models have been introduced into the Anacconda[5] Simulation Code developed by the CEA jointly with EDF and AREVA. This code, validated from experimental results, enables the corrosion products amount, and, so, contamination, to be assessed through describing in-core temperature and neutron flux profiles.

Other general models have been developed, i.e. phenomenological models of release / deposition of radioactive corrosion products [8, 9, 10]. They use mass transfer equations, which take into account dissolution and deposition phenomena: diffusion through the structural material, desorption or absorption at the interface between structural materials and liquid sodium, diffusion of the sodium flux through a laminar boundary layer.

Minor element impact in an alloy (carbon…)

The selective dissolution of nickel and chromium, as well as the resulting increase in iron amount at the surface of steels, are the main consequences of steel corrosion by liquid sodium. The effects of non-metallic elements, too, such as carbon and nitrogen arising from the bath or from the steel itself, have to be taken into consideration.

The transfer process by activity gradient leads to the formation of a metal layer affected by the diffusion of interstitial elements (carbon or nitrogen), inducing an alteration in mechanical properties. The properties of this layer are altered in such a way that they are hardened in the case of carburization (nitriding) or softened in the case of decarburization (denitriding). Carburization thus increases steel resistance, and reduces their ductility. Carburization and decarburization affect the clad outer part in depth, as shown on Figure 106 [5].

Absorption of carbon influences the microstructure as carbides precipitate in high-concentration areas (Fig. 107). As long as

5. Anacconda: *ANalyse de l'Activation, de la Corrosion, de la COntamination du sodium (Na) et de Dépôt de l'Activité*, ANalysis of Activation, Corrosion, COntamination of sodium (Na) and Deposition of Activity.

these layer thicknesses remain low with respect to the material thickness, the impact is considered as negligible. The threshold is generally fixed at a 10% thickness. Austenitic steels are rather sensitive to carburization owing to their initial low carbon content (0.04 to 0.08%). As the structure of ferritic steels is face-centered cubic, it favors a higher mobility of interstitial elements such as hydrogen or carbon (and nitrogen), and so, sometimes, an increase in diffusion coefficients by one order of magnitude (H) with respect to austenitic steels. Temperature dependence is critical for these phenomena. As a general rule, non-stabilized steels undergo decarburization at 600-700 °C, whereas stabilized steels absorb carbon from sodium, considering a sodium purity typical of sodium-cooled reactors. As a matter of fact, carbon activities in liquid sodium and in the metallic alloy counterbalance each other. Carbon exchange seems to be less high at lower temperatures (450 - 550 °C) [8,9]. The much slower diffusion affects areas of very low thickness at the surface of the material. Carburization and decarburization are thus dependent on material composition and sodium purity. For example, no decarburization could be observed for exposures up to 7000 h at 550 °C for ferritic steels containing 5% chromium or more, or for 2.25% Cr steels stabilized with niobium. As regards non-stabilized 2.25% Cr steels, decarburization could be seen only for temperatures higher than 475 °C, and did not become significant until 550 °C. Decarburization models are based either on diffusion in the solid solution, or on diffusion through grain boundaries [8].

Nitrogen exchange between steels and sodium generates effects similar to those resulting from carbon exchange. Nitriding risks are reported, especially in the case of primary blanket pollution by air: areas undergoing high temperature variations and stripped by sodium motion are *a priori* more sensitive to a possible nitriding, particularly in the case of a temperature rise. Stabilized austenitic steels are not much subjected to decarburization, but do undergo denitriding. Ferritic steels experience both decarburization and denitriding, the latter being especially significant. Niobium and vanadium, which form carbides and nitrides, partially inhibit decarburization, but nearly do not inhibit denitriding in ferritic steels. Nitrogen contained in steels quickly diffuses at 650-700 °C to and through grain boundaries, is quickly dissolved in sodium, and may favor the dissolution of other elements.

Generally, at temperatures of 800 °C or more, exposure to sodium entails chemical changes in exposed materials: concentrations in nickel, chromium, iron, carbon and nitrogen may increase or decrease within the outer layers of materials, as previously shown. Besides, other elements are also involved, such as, e.g., boron or manganese. Generally, these evolutions only have marginal effects on the corrosion behavior of steels at the 600 °C temperature, but they might have much more significant effects at higher temperatures.

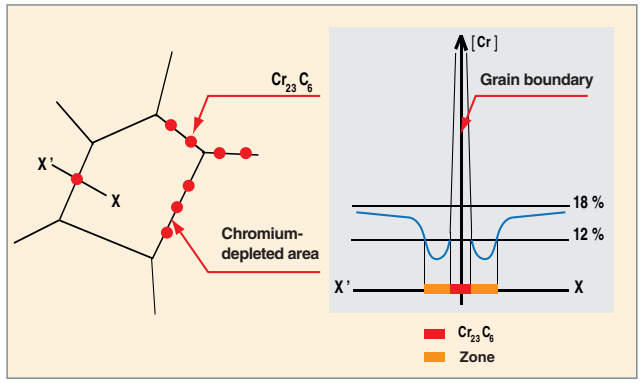

Fig. 107. The exposure of a steel to a high temperature in a carbon-rich sodium bath may entail the precipitation of chromium carbide $Cr_{23}C_6$ at grain boundaries, thereby causing the sensitization of the steel, which happens to be locally chromium-depleted.

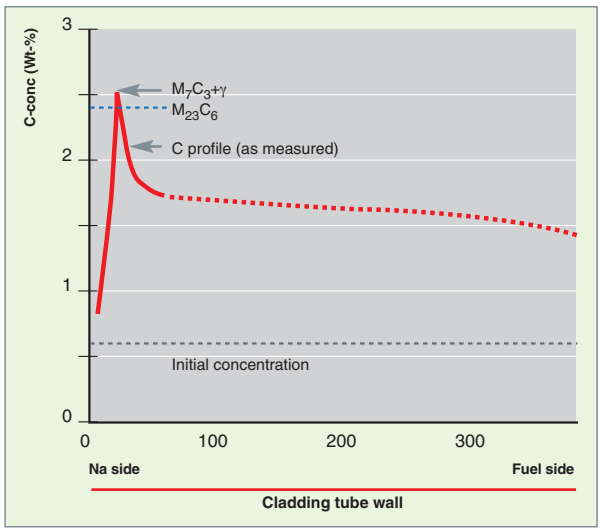

Fig. 106. Carburization of a cladding material in sodium, at 700 °C after a 5000-hour exposure [5].

Controlling corrosion and mass transfer phenomena

The major radionuclides generated by neutron-induced reactions in the core steels are: ^{51}Cr, ^{54}Mn, ^{59}Fe, ^{58}Co and ^{182}Ta. But, once reactor operation has been stopped, the main sources of radioactivity in the primary coolant system consist of isotopes with a much longer lifetime: ^{58}Co (71 days), ^{60}Co (1913 days), and ^{54}Mn (313 days). Activated corrosion products, such as ^{54}Mn, ^{51}Cr, etc., induced by core materials activation, are dissolved in sodium, and are deposited mainly in pumps and the coldest parts of the reactor, i.e. intermediate heat exchangers. Radioactive cobalts such as ^{60}Co are also released, and a small fraction is deposited on hot surfaces in primary components or structural materials. Moreover, CO release rate is a function of the oxygen content of sodium. More generally, comparing with other nuclear facilities, such as light water-cooled reactors, the degree of contamination is moderate, as shown by the corrosion rates assessed and the contamination induced by activated corrosion products and observed in sodium-cooled fast reactors, such as PHENIX, JOYO, BN600, PFR or EBR2. This is due to two factors: easy oxygen control in sodium during operation, and a very moderate solubility of steel-constitutive elements in sodium.

As shown hereabove, general corrosion is strongly dependent on oxygen content during operation. In several countries (France, Japan…), it is considered that an oxygen concentration of no more than 3 ppm allows for reactor operation with no unacceptable risk of contamination by corrosion products. But a concentration over 5 ppm is not acceptable. In contrast, in the United Kingdom, oxygen concentration is allowed to reach up to 10 ppm, as it is argued that, for concentrations of about 5-8 ppm, oxygen improves resistance to friction / wear (by a process of oxide layer stabilization on structural materials prone to friction). But then, oxygen generates more corrosion and mass transfer, and, so, more contamination.

Two main positive effects are therefore associated with the French strategy of sodium-cooled fast neutron reactors operating with “clean sodium”: dose reduction during operation or maintenance, and easier decommissioning and waste management [10].

Two main sodium purification processes have been developed concerning oxygen content control:

- “Cold trap” purification, i.e. through crystallization of dissolved oxygen as Na_2O by taking sodium temperature to under the oxygen saturation temperature, thereby creating the optimal conditions for Na_2O nucleation and growth on a steel wool packing put in an auxiliary container cooled by oil, nitrogen… This process also enables the hydrogen content to be efficiently controlled by crystallization of dissolved hydrogen as NaH. Purification kinetics depends, on the one hand, on the cold trap control parameters, i.e. freezing point temperature and sodium flow rate, and, on the other hand, on trap efficiency, which itself is a function of trap geometry and refill rate:

$$V = \eta.10^{-6}.D_{Na}.(Ce-C^*(Tpf))$$

where V stands for oxygen trapping rate ($kg(O).s^{-1}.m^{-2}$), η for purification efficiency (between 0 and 1), T for hot trapping temperature (K), Ce for the oxygen content in mg/kgNa, at the cold trap inlet, C*(Tpf) for oxygen solubility at the cold point temperature of the trap in mg/kg_{Na}, and D_{Na} for the sodium flow rate expressed in $kg_{Na}.s^{-1}$.

- “Hot trap” purification (the so-called “getter” effect) based on the oxidation capacity of the selected material (e.g. a zirconium-titanium alloy), when it is placed in presence of sodium that contains a given oxygen amount. This process is generally chosen when the aim is to purify small volumes of sodium, and when the Na_2O dissolution risk due to the cooling function loss in the cold trap is unacceptable. For example, alloy $Zr_{0,87}$-$Ti_{0,13}$ was chosen for hot trapping in an irradiation loop designed for Phénix [11]; the kinetics and the optimal operating conditions could then be set up as follows:

$$V = 41.26 \,.\, 10^{-3} \,.\, \exp(-40{,}3 \times 10^{3} / RT).[O]$$

where V stands for the oxygen trapping rate ($kg(O).h^{-1}.m^{-2}$), T for the hot trapping temperature (K), R for the ideal gas constant ($J.mol^{-1}.K^{-1}$), and [O] for the oxygen content in ppm.

The cold trap is the process most widely used for sodium purification in fast neutron reactors, owing to its outstanding benefits:

- Oxygen and hydrogen, which constitute the two most important impurities to be trapped in a sodium-cooled fast neutron reactor, can be held in the same component;

- A low oxygen concentration is easy to reach, as oxygen solubility (and that of hydrogen, too) is very low for temperatures neighboring the melting point;

- An optimized design of cold traps results in higher efficiency and retention capacity (Fig. 108);

- The cold trap can be regenerated by extracting the sole packing, or by *in situ* physical treatment using a suitable process based on the redissolution of O and H impurities and their separation, e.g. the PRIAM process, developed at the Research Center of Cadarache;

- The cold trap can also hold other impurities such as metallic impurities, even though efficiency is much lower for these elements than for oxygen and hydrogen.

In addition to oxygen control during normal operation, several recommendations have been taken into account in relation with the development and operation of sodium-cooled fast neutron reactors, in order to limit the corrosion phenomenon enhanced by oxygen dissolved in sodium:

- Supplying with extremely pure, nuclear "quality" sodium;

- Primary coolant system cleaning prior to sodium refill (structures, gas...);

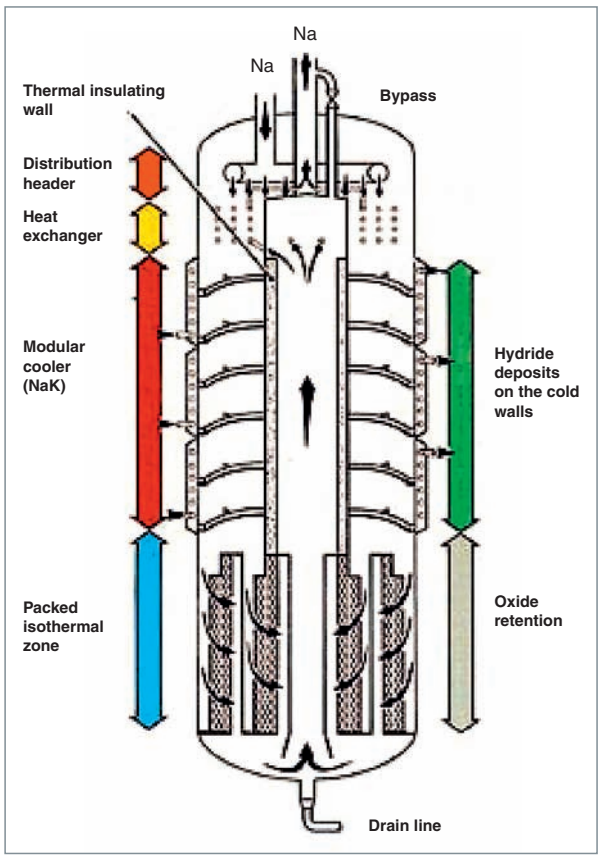

Fig. 108: A cold trap concept developed for sodium purification in Superphenix [17].

- Setting up a purification run during reactor startup, followed by purification operations during the reactor operating period;

- Limiting impurity (oxygen, moisture...) ingress into the cover gas using suitable methods;

- Continuously monitoring sodium quality with respect to oxygen with the help of efficient instrumentation.

Influence of corrosion and interstitial elements on present materials under conventional operating conditions seems to be rather negligible as regards potential structural damage under operating conditions of the sodium-cooled fast neutron reactors already built to date. Yet the phenomena presented hereabove are relatively complex, and the behavior of new candidate materials for future reactors will have to be validated; the kinetics of localized corrosion (including the phenomena of stress corrosion cracking and liquid metal embrittlement), as well as those of general or uniform corrosion will have to be determined and introduced in the models simulating materials behavior and contamination transfer.

Internal corrosion of fuel pins

Fast neutron reactors, which use a fuel consisting of mixed oxides of uranium and plutonium, have always displayed more or less significant effects of internal corrosion in the metallic clad which stands as the first barrier of fuel pins. In the late nineties this potential damage of a certain number of fuel pins in the fast reactor core still was one of the major impediments to reach the goals of the latest European fast neutron reactor project, EFR, i.e. a burnup rate of 190 GWd/tox and a dose of 190 **dpa*** [12].

Investigations were carried out at the CEA for the 20th century's last two decades in order to better understand the mechanisms inducing this internal corrosion, and pinpoint the parameters deemed to have the greatest influence. Today, however, no "mechanistic" model is yet available to extrapolate fuel pin behavior with respect to this corrosion concern, in order to reach the ambitious goals of the SFR 4th Generation reactor project, i.e. 200 à 250 GWd/tox and 250 dpa [13].

The history of fast reactor fuel elements goes back to the early seventies. During the first fuel reloading of the RAPSODIE reactor in its FORTISSIMO Version (40 MWth), a high number of fuel pins were affected by clad failures after only a few days of irradiation. This type of failure is induced by a deeply penetrating, intergranular corrosion, which has been named "early corrosion" (Fig. 109).

This phenomenon was triggered by fuel pin operation at high linear power density. This corrosion is due to concentration of corrosive fission products (iodine and tellurium) in some points of the clad, together with a high thermal state of oxide, which has allowed them to be released. Owing to thermodynamic conditions, these fission products are responsible for the chemical attack of the clad steel at grain boundaries. A remedy adopted at that time against this devastating corrosion, and used again later on for the PHENIX reactor, was to carry out a fuel "vaccination". The method consists in moderating the fuel thermal state for a few days so as to limit iodine and tellurium isotope migration, thereby giving them sufficient time to decay and generate caesium and rubidium, which form stable compounds with "fresh" iodine and tellurium isotopes (CsI and Cs_2Te). Consequently, introducing new assemblies during fuel reloading may entail a decrease of about 5-10 % in reactor power for some days, in accordance with the vaccination procedure.

Once the early corrosion issue could be tackled, performance of fast reactor fuel elements could be progressively increased thanks to better clad materials resistance to swelling (see the Monograph dealing with nuclear fuel). As a second step, many cases of "end-of-life corrosion" could be evidenced through post-irradiation examinations, both non-destructive (eddy current examination) and destructive (targeteted metallographic sections). The two main types of "end-of-life corrosion" currently observed in fuel pins have been respectively named **ROG*** (oxide-clad reaction), for the volume corrosion developing along the fissile stack in its upper part (Fig. 110), and **RIFF*** (fissile-fertile interface reaction), for the corrosion located in the immediate vicinity of the fissile stack upper part and at the level of the upper breeder UO_2 pellet (Fig. 111).

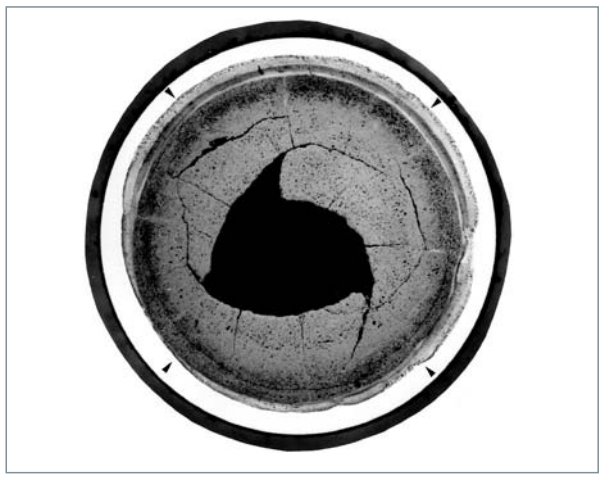

Fig. 110. Strong corrosion resulting from an oxide-clad reaction ("ROG"), that affects over 360° the cold-worked steel 15-15 Ti clad of a PHENIX pin irradiated at a very high burnup (17.2 at%, i.e. 146 GWd/t_{ox}). A fuel fragment has been torn off in the center during specimen preparation.

Experimental observations could thus be collected in relation with both types of end-of-life corrosion in PHENIX fuel pins. As demonstrated by their synthesis, the oxide-clad reaction and the fissile-fertile interface reaction may be explained by the same corrosion mechanism, in which the fission product tellurium plays a prominent role [14]. The latter is released by reactions of caesium telluride (CS_2Te), either with molybdenum (generated by fission, or possibly present in the clad as an alloying element), or with chromium, present as a major addition element of clad materials. These reactions take place at the fuel-clad interface, under some conditions which are as follows: sufficient molybdenum and CS_2Te amounts have to be locally present, and the fuel oxygen potential has to be sufficiently high: irradiation $\Delta G(O_2)$ is about -500 kJ/mol, but increases with the burnup rate; as a result, the critical area of $\Delta G(O_2)$ as defined hereabove,

Fig. 109. Intense early corrosion with no clad failure on a fast reactor fuel element irradiated in the RAPSODIE - FORTISSIMO reactor.

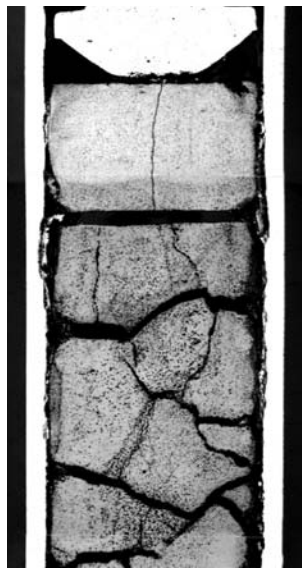

Fig. 111. Axial metallographic section of a corrosion phenomenon at the fissile-fertile interface on a cold-worked steel-15-15 Ti clad PHENIX pin after a 13.3 at% irradiation, i.e. 115 GWd/t_{ox}.

which enables free tellurium to be generated, may be reached as soon as an average pin burnup rate of 5-6 at% has been attained (Fig. 112).

Given the generally high operating regime of fast reactor fuel elements, the axial distribution of caesium compounds formed in the fuel is not homogeneous along the fuel pellet stack. During irradiation deposits are formed in some “cold” spots of the stack, at the fuel-clad interface. Perpendicularly to these deposits, if favorable conditions are gathered regarding temperature, burnup rate and oxygen potential, high availability of Cs_2Te entails localized and possibly deep attacks through the various reactions with molybdenum and chromium. Concerning fissile-fertile interface reactions, this condensation occurs at the end of the fuel pellet stack, in contact with the fertile pellet which induces a “cold” spot (Fig. 113). As regards the oxide-clad reaction, transfer will occur from an overheated fuel area, during an irradiation often induced by clad deformation as a result of swelling, towards the immediately neighboring fissile stack which has not undergone this overheating or deformation.

Identification of the main parameters which influence corrosion, and knowledge of thermodynamic and physico-chemical mechanisms which generate it, have enabled optimization paths and potential remedies to be proposed.

Strong oxide-clad reaction type alterations can be observed when the clad swells in its lower part without being deformed at the top of the fuel pellet stack. They can be significantly reduced using clad materials which do not swell much, such as ferritic-martensitic steels, and, in the longer term, oxide-dispersion strengthened (ODS) ferritic-martensitic alloys.

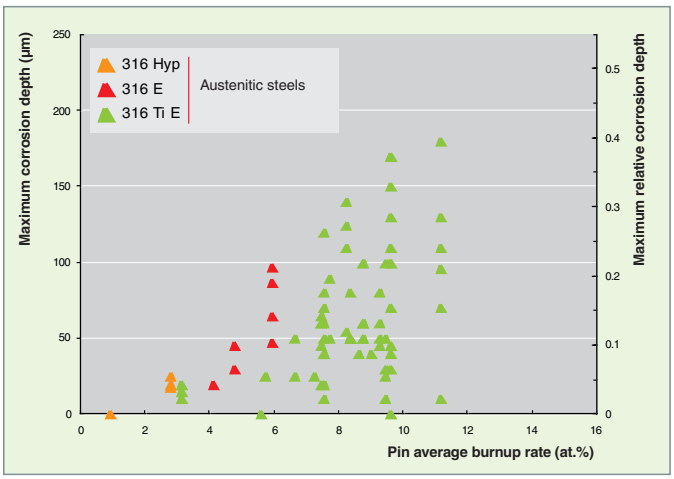

Fig. 112. Maximum depths of internal corrosion due to the oxide-clad reaction recorded through metallographic examinations of pins for various austenitic steel clad materials (source: the BREF Base of the Fuel Studies Department).

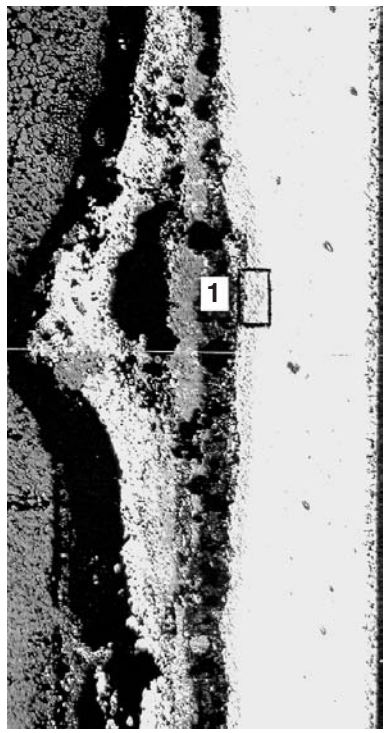

Fig. 113. Optical micrograph of a fissile-fertile interface reaction (RFFI) showing highly penetrating corrosion (e_{max} = 210 µm) perpendicular to this interface (Mark 1).

Fuel pins of the axial heterogeneous concept, $UPuO_2/UO_2/UPuO_2$, which have been the focus of the irradiation program ZEBRE in PHENIX, have displayed good behavior with respect to the oxide-clad reaction, as compared with homogeneous fuel pins, up to burnup rates of an approximate 13.5 at%. So, the heterogeneous-type fuel stack would be a rather favorable factor for mitigating clad internal corrosion. Similarly, the presence of the fertile pellet stack above the fissile stack is reported to be beneficial with respect to the fissile-fertile interface reaction. For it favors the spreading of corrosion over several centimeters along the clad, contrary to what can be observed on pins only featuring an upper breeder UO_2 pellet a few-millimeters long.

As for the remedies, they may be classified into two main categories:

- Action on mixed oxide fuel, by using “getters” to limit the increase of its oxygen potential under irradiation;
- Action on the clad, by applying a metallic deposit likely to withstand chemical attack of tellurium.

In most of processes tested to date for either of these remedies, no solution could be found that could ensure the absence or mitigation of clad corrosion at the high burnup rates considered for the 4th generation reactor systems. Finding a solution will require further investigations in this field, together with irradiation benchmarks.

Corrosion in lead (alloy)-cooled fast reactors

Given its hydraulic and thermal properties, liquid lead stands as a coolant of lower performance than sodium. However, the high chemical reactivity of sodium with respect to water and air makes sodium loops vulnerable to pipe leaks and breaks. On the contrary, a lead-cooled fast reactor would not face such an impediment: this is the reason why this type of reactor has been selected as one of the six Fourth Generation reactor concepts of the GEN IV Forum. Of course, the LFR exhibits other flaws: corrosion by liquid lead is precisely one of its Achilles' heels. On the other hand, lead or its alloys such as the lead-bismuth **eutectic*** may also be contemplated for the intermediate loop of a sodium-cooled fast reactor, with the advantage of avoiding any direct thermal contact between sodium and water in the secondary coolant system. Last but not least, the lead-bismuth eutectic is considered as a possible fertile blanket material for fusion reactors. These applications therefore justify a research activity in relation to liquid lead and its alloys, which may proceed according to various mechanisms, as follows: dissolution of the solid in liquid metal, formation of intermetallic compounds, intergranular penetration of liquid metal in the solid, embrittlement of the solid by the liquid… In addition, in presence of a thermal gradient, dissolution-deposition phenomena may occur, thereby entailing material transfer between hot and cold areas, and are thus likely to induce a severe degradation of materials in the hot area, and facility plugging in the cold area.

In lead and its alloys, the chief structural materials contemplated are type 316L austenitic steels and type T91 martensitic steels (Table 6).

Table 6.

Composition of structural steels (weight %)								
Steel	**Cr**	**Ni**	**Mo**	**Mn**	**Si**	**C**	**V**	**Nb**
T91	8.98	0.125	0.962	0.393	0.351	0.086	0.190	0.075
316L	17.0	11.66	2.7	1.53	0.42	0.022	–	–

Corrosion studies conducted in relation to lead, Pb-Bi alloy or Pb-17Li alloy have evidenced various corrosion mechanisms:

- In the case of Pb-17Li alloy, corrosion occurs as a dissolution phenomenon;
- Regarding pure lead and Pb-Bi alloy, the corrosion mechanism varies according to the dissolved oxygen content in liquid metal;
- For oxygen concentrations lower than a critical minimum content, corrosion takes place as a dissolution phenomenon, just as in Pb-17Li alloy;
- For contents higher than this critical content, an oxide layer may form on the steel surface. The properties of this layer depend upon the material, the oxygen content, temperature, hydrodynamics… Under some conditions, this layer may be protective, and act as a barrier against corrosion.

Dissolution phenomena

In the case of a corrosion mechanism acting through dissolution, two steps may be considered:

- An overall dissolution reaction at the solid-liquid interface, which results from two opposite partial reactions: a dissolution reaction, and a deposition reaction at the interface.
- Mass transfer of dissolved species from the solid-liquid interface into the liquid core: it results from the diffusion of dissolved species through a diffusion boundary layer, then from the transport by convection through the liquid alloy. This type of transport is also called "convective diffusion".

If the system is strictly isothermal, and if there is no circulation of the liquid alloy, its evolution stops as soon as dissolved metal solubility has been reached in the liquid alloy: the system is then in equilibrium. Excepting the case when the solubility limit is extremely high, which generally prohibits using the metal on the industrial scale, the loss of matter so calculated on the basis of purely thermodynamical considerations is moderate.

Yet, in most cases, the system is not isothermal. As metal solubility increases with temperature, the metal will tend to be dissolved in hot areas, and to be deposited in cold areas. The

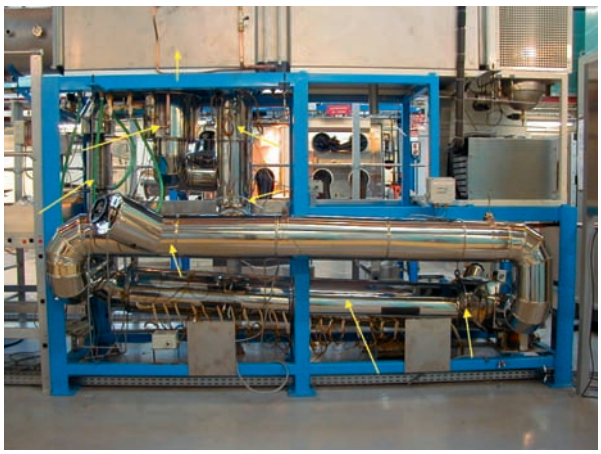

Fig.114. The CICLAD Facility for the experimental study of corrosion by lead alloys conducted at the Physico-Chemistry Department (CEA/Saclay).

resulting degradations may then be highly significant. In order to assess corrosion kinetics through this process, test loops are implemented, in which the solid metal is put in contact with the flowing liquid alloy under conditions representative of the expected operating conditions.

These tests can be achieved in the CICLAD Facility (Fig. 114) [15, 16]. In this facility, a rotating cylinder is implemented inside a liquid metal circulation loop. This rotating cylinder displays the benefit of being able to reproduce high circulation rates in piping under controlled hydrodynamic conditions.

A homogeneous dissolution of the material can be observed for steel-T91 and, more extensively, for ferritic/martensitic steels (Fig. 115a). This dissolution phenomenon is all the more pronounced as the temperature and flow velocity are high. As shown on Figure 115b, the corrosion rate varies as a function of the flow velocity of the liquid alloy (or the cylinder rotating rate, depending on the case considered). A quasi-linear variation in the corrosion rate can be observed, which confirms that the corrosion process is limited by dissolved iron diffusion.

For, in the case when the corrosion rate is limited by metal iron diffusion from the metal / liquid alloy interface to the medium, the corrosion rate is expressed as follows:

$$V_{corrosion} = K(C_i - C_o)$$

where K is the mass transfer coefficient ($m.s^{-1}$), and c_i the concentration at the solid-liquid interface: in any case, the overall reaction of dissolution-deposition at the interface will be considedered to be in equilibrium, and the concentration at the interface will be assumed to be equal to the solubility limit of the species dissolved in the liquid alloy: $c = c_s$ ($g.m^{-3}$), where c_0 is the concentration in dissolved species in the liquid alloy volume. If the latter has been sufficiently renewed, c_0 may be considered as negligible: $c_0 = 0$.

Coefficient K depends on the geometry of the flow under consideration. In the case of the rotating cylinder, a study carried out by EISENBERG on the mass transfer of nickel cylindrical specimens into alkaline aqueous solutions enabled the mass transfer coefficient to be expressed as follows:

$$V_{Eisenberg} = 0.0487 d_{cylinder}^{0.4} D^{0.644} \omega^{0.70} \nu^{-0.344}$$

where

ω: rotating rate of the electrode ($rad.s^{-1}$), $d_{cylinder}$: outer diameter of the cylinder (m), ν: kinematic viscosity of the fluid ($m^2.s^{-1}$), D: diffusion coefficient ($m^2.s^{-1}$).

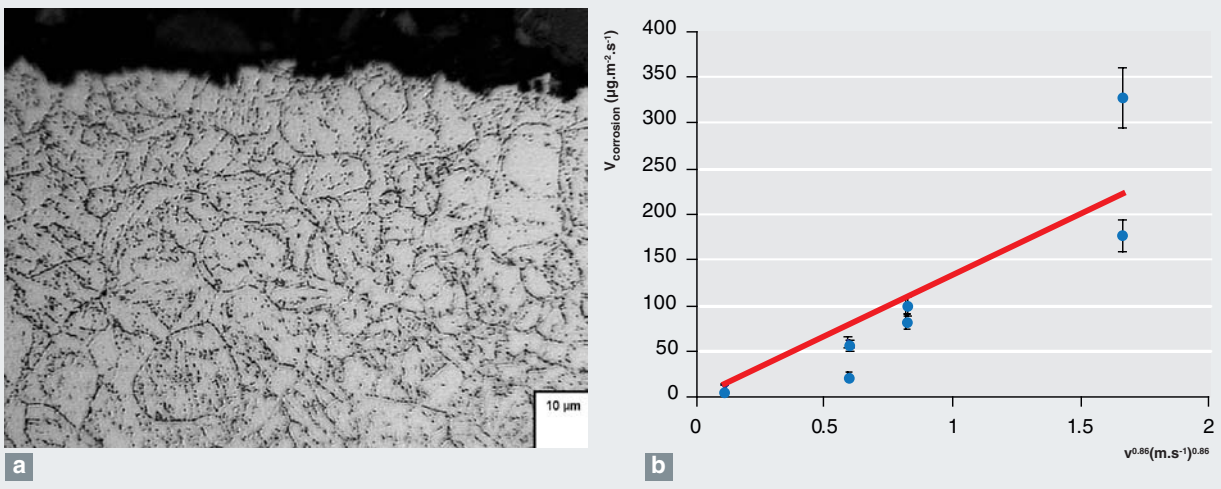

Fig. 116. a) Microscopic observation of martensitic steel-T91 after immersion for 1200 hours into Pb-Bi alloy at 470 °C and with an oxygen content of 10^{-11}-10^{-12} wt. %. (b) Variation in the corrosion rate of steel-T91 at 470 °C as a function of the flow velocities of liquid alloy Pb-Bi. As shown in this diagram, for the flow velocities typically considered in a coolant loop, the rate of steel dissolution is expected to be about a fraction of mm per year.

As regards flow in piping, different equations are put forth in literature, among which we have retained that developed by BERGER and HAU:

$$K_{B\text{-}H} = 0.0165 v^{0.86} d_{tube}^{-0.14} \nu^{-0.530} D^{0.670}$$

where v: liquid alloy flow velocity ($m.s^{-1}$), d_{tube}: hydraulic diameter (m).

So, it is possible to refer to these equations expressing the mass transfer coefficients, and relate the corrosion rate to the liquid alloy flow velocity, whatever the geometry of the facility under consideration may be.

Regarding 316L stainless steel, it undergoes a selective dissolution (Fig. 116). For, owing to the very high solubility of nickel in lead and lead alloys, it is preferentially dissolved, thereby inducing the formation on the steel surface of a ferritic porous layer consisting of a network of channels filled with liquid alloy. Analyses have evidenced a very high depletion in nickel, chromium and manganese, as well as an iron enrichment [17, 18].

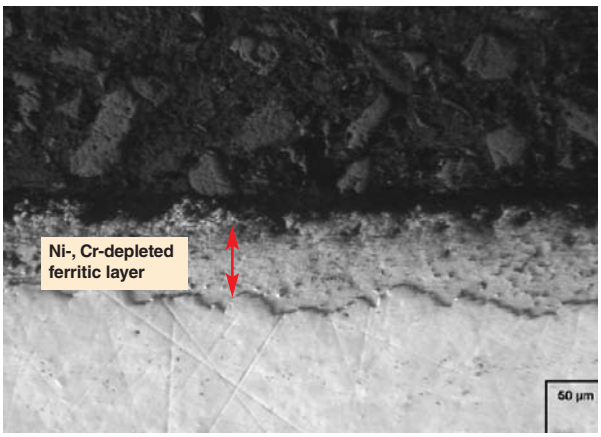

Fig. 116. 316L steel after immersion for 3000 hours at 500 °C into Pb-Bi with an oxygen content of 7 10^{-8} wt. %.

In Pb-17Li alloy, pure lead, as well as in Pb-Bi alloy (when the dissolved oxygen content is low), use of uncoated steel-316L is limited to moderate temperatures (below 350 °C approx.), at which it does not undergo any significant dissolution. So is it for ferritic / martensitic steels, and strictly in flow velocity ranges which do not induce high corrosion rates.

If temperatures are higher (above 400-450 °C approx.), steel dissolution rates become unacceptable, and materials protection has to be considered in order to ensure their corrosion resistance. This protection can be achieved either by outer coatings, or through *in situ* monitoring of liquid alloy chemistry.

Oxidation phenomena

One way of protecting materials against corrosion in pure lead and Pb-Bi alloy lies in the *in situ* formation of a protective oxide layer on the surface of materials (austenitic or martensitic steels). For such a layer can be formed on the solid's surface by finely controlling the dissolved oxygen content, while avoiding lead oxide precipitation within the liquid metal. Yet, only through a strict control and accurate measurements of the oxygen content in the whole facility can this method prove to be successful. Ensuring the good behavior and resistance of these oxide layers first requires to understand their formation mechanism, then modelling the oxidation kinetics in order to predict long-term steel behavior under given conditions.

Partly in cooperation with the Russian Research Center IPPE (Institute of Physics and Power Engineering, Russia), the CEA carried out oxidation tests on austenitic steels (316L: Fe-17.3Cr-12.1Ni-2.3Mo), as well as on martensitic steels Fe-9Cr-1Mo (T91), Fe-12Cr (EP823), and Fe-10.3Cr (Manet II) put in a liquid Pb-Bi alloy displaying various dissolved oxygen contents, under stagnation and circulation conditions and at different temperatures [18, 19].

Martensitic steels Fe-9Cr were particularly investigated in as much as they are considered as the candidate material for the spallation target window in hybrid reactors. In all the cases observed in literature and at the CEA, a duplex oxide layer is seen to form on contact with steel (Fig. 117): it consists of an internal layer of Fe-Cr spinel on which a magnetite outer layer is superposed on contact with the liquid alloy. The nature of these two layers is identical whatever the test temperatures may be (between 470 °C and 600 °C).

Stoichiometry of the Fe-Cr spinel was identified on alloy T91 oxidized in the Pb-Bi eutectic at 470 °C, in the liquid alloy 36Pb-64Bi at 460 °C, and in the liquid alloy 26Pb-74Bi at 634 °C for short oxidation durations (lower than 700 hours). In all cases, it is equal to $Fe_{2.3}Cr_{0.7}O_4$ and remains constant during oxidation. It is worth emphasizing that the same structure and the same oxide layer stœchiometries could be observed in the case of alloy T91 oxidation in oxygen-saturated liquid bismuth at 470 °C.

The magnetite layer seems to be porous, and lead penetrations can be observed through Scanning Electron Microscopy (Fig. 117). Lead traces can also be distinguished in the Fe-Cr spinel which, however, seems to be denser.

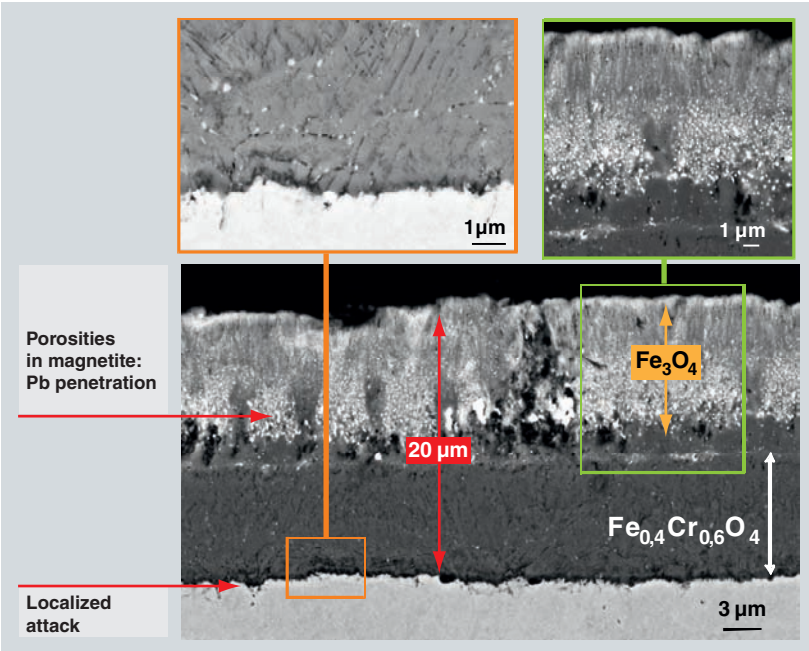

Fig. 117. Backscattered-electron image of a cross-section of a steel-T91 specimen immersed for 3600 hours into oxygen-saturated Pb-Bi alloy at 470 °C.

When the temperature is higher than 550 °C, an internal oxidation occurs, displaying chromium-rich oxide precipitates localized along grain boundaries. These precipitates can be observed under the Fe-Cr spinel layer and, sometimes, under the magnetite layer.

The thickness ratio between the Fe-Cr spinel and magnetite layers is the same, whatever the tested temperatures (460-600 °C), the oxygen content and the oxidation duration may be.

Experimental kinetics for the oxide layer growth in stagnant or circulating Pb-Bi alloy have been obtained at the CEA [20, 21] for the various steels, at different temperatures (300-600 °C) and different oxygen contents. The kinetics obtained over long oxidation durations exhibit a parabolic evolution, which suggests that the layer growth is limited by a diffusional process.

Successive steel-T91 oxidation experiments conducted at the CEA (jointly with the Technological University of Compiègne) in a liquid Pb-Bi alloy medium at 470 °C, with different oxygen isotopes, have shown that:

- The magnetite layer growth takes place at the magnetite / Pb-Bi interface, which implies iron diffusion through the oxide layer;
- The Fe-Cr spinel layer grows at the T91 / Fe-Cr spinel interface, which implies oxygen diffusion up to this interface.

On the other hand, the growth kinetics and morphology of the oxide layers obtained through the oxidation of steels-Fe-9Cr in Pb-Bi alloy look like those observed in water and vapor at high temperature. It can therefore be assumed that the growth mechanisms of these layers were similar. The main mechanism proposed in literature to explain Fe-Cr steels oxidation is named “available space model”. This mechanism suggests that the growth of two oxide layers is limited by cation diffusion of iron through the layers, and oxygen diffuses to the steel / oxide interface under molecular form, through nano-channels going across the oxide layer.

Several considerations based upon literature dealing with the “available space model”, simulations and experiments have led to propose the following mechanism for steel T91 oxidation in oxygen-saturated alloy Pb-Bi.

The magnetite layer grows at the oxide / liquid alloy interface by iron diffusion through the oxide layer lattice. The transfer of T91 iron atoms to the outer interface generates vacancies, which pile up at the T91/ Fe-Cr spinel interface as nano-voids (Fig. 118 a). Oxygen, the transport of which is not limiting through nano-channels, enters these nano-voids in order to directly oxide T91. So, once formed, these nano-voids are filled with the product of the T91 / oxygen reaction, i.e. spinel Fe-Cr (Fig. 118 a). When a nano-void has been filled, oxygen can no longer reach T91, for the channel is plugged, and the oxidation reaction comes to an end (Fig. 118 b). In other terms, the growth of the spinel Fe-Cr is stopped, and will not resume before other nano-voids are formed (through iron diffusion) (Fig. 118 c). So the spinel Fe-Cr grows in the metal consumption volume, accordingly with the “available space model”. Its growth is not limited by oxygen uptake, but by the kinetics of nano-void formation, i.e. that of vacancy diffusion

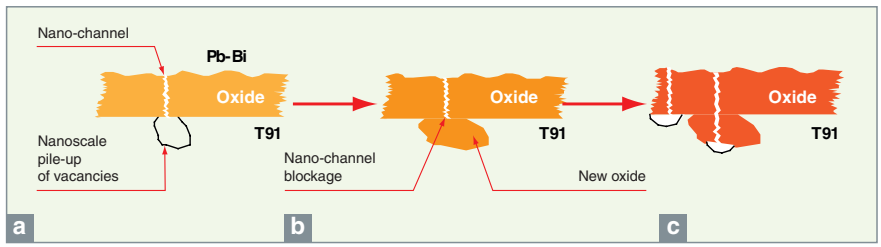

Fig. 118. The mechanism of steel-T91 oxidation by liquid alloy Pb-Bi.

within the oxide. A simulation was performed referring to this mechanisms. The results of these simulations at 470 °C and 600 °C are represented with the experimental results on Figure 119.

As shown on Figure 119, simulation accounts for the oxide layer growth kinetics in oxygen-saturated alloy Pb-Bi at both test temperatures. The proposed mechanism is underpinned

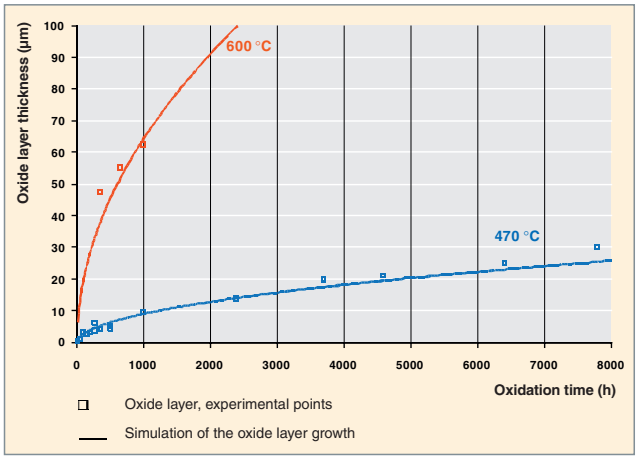

Fig. 119. Simulation of the oxide layer growth kinetics at 470 and 600 °C. Comparison with the experimental results.

by these results. However, in order to predict steel-T91 oxidation kinetics in lead alloys and thus help design and select reactor structural steels, the oxidation model has to be applicable to other experimental conditions. This is the reason why oxidation tests are underway for various lead-bismuth alloys (with various lead proportions in the alloy), over a temperature range of 400-600 °C and for different dissolved oxygen contents. The experimental results of these tests will be confronted with simulation.

On the other hand, these studies on oxidation mechanisms in alloy Pb-Bi help improve the understanding of oxidation mechanisms in water and vapor environments owing to the similar morphologies of oxide layers and their growth kinetics.

Controlling the dissolved oxygen content

Controlling the dissolved oxygen content in liquid lead alloys is aimed at creating the thermodynamic conditions required for the formation of a protective oxide layer on the structural steel surface, consisting of iron oxide and chromium, thereby reducing its corrosion kinetics by transferring the material from its dissolution to its oxidation domain in this environment. The formation of this layer is much alike the *in situ*

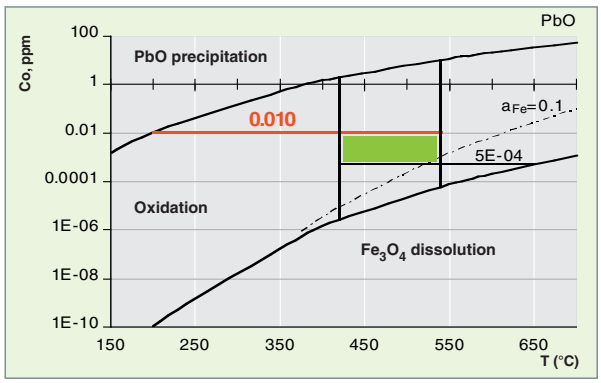

Fig. 120. Allowable range of oxygen concentration for the lead-bismuth eutectic of primary coolant (420 °C-540 °C). The picture pinpoints PbO precipitation areas, as well as steel oxidation and homogeneous dissolution areas. The allowable area is represented by the green section, circumscribed by the vertical (cold and hot collector temperature) and horizontal lines that stand for the threshold concentrations in equilibrium with lead oxide formation at the colder wall temperature (200 °C-0.01 ppm), and with iron oxide dissolution at the hoter wall temperature of the system (650 °C-5.10^{-4} ppm).

building of a barrier against material transfer, which significantly reduces diffusion of alloying elements (especially, iron) towards the liquid. Yet, a strict control of the oxygen content in the whole facility is the condition required for this method to be fruitful.

Moreover, dissolved oxygen activity has to be controlled within relatively narrow operating limits (Fig. 120), so as to reach an oxygen content not only higher than the threshold value for iron oxide formation – i.e. the condition required for protecting structures –, but also lower than lead oxide (PbO) solubility, that results in precipitation of solid crystals likely to be deposited on heat exchanger walls or to plug narrowed passage sections partially or even fully, thereby reducing the system's heat extraction power as well as its performance [22].

Dissolved oxygen measurement may be performed with an electrochemical probe [23], using a solid electrolyte (yttria-stabilized zirconia), i.e. a specific ionic conductor, in such a way that the reference (a metal / oxide couple or air) and the medium to be measured are placed into two separate boxes (Fig. 121). Measuring the electromotive force at null current with this type of assembly makes it possible to trace back to oxygen concentration through Nernst's relationship:

$$E_{th} = \frac{RT}{4F} \cdot \ln \frac{P_{O_2(ref.)}}{P_{O_2}}$$

So very low concentration levels can be measured continuously.

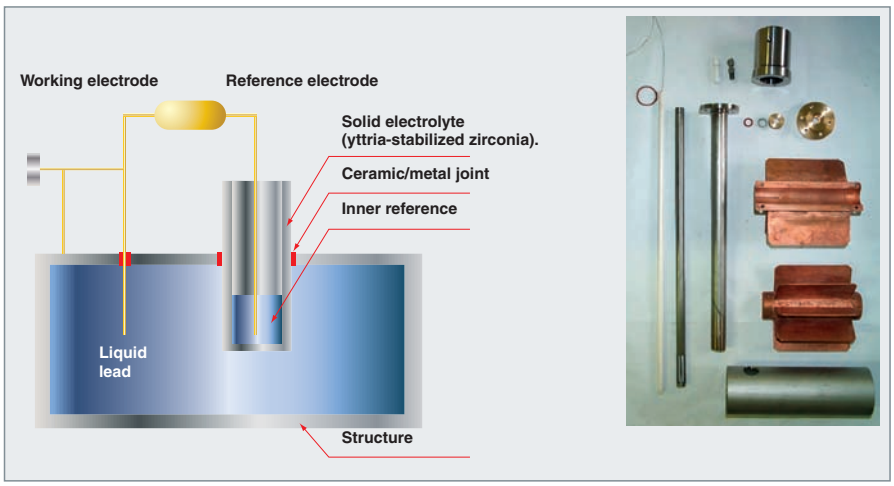

Fig. 121. A probe developed at the CEA for controlling oxygen content in liquid lead [3].

A calibration method in a static crucible, based on the research of the saturation point, and systematically applied for all the probes, enabled standard fixed operating lines to be determined for the reference probes In/In_2O_3, and Bi/Bi_2O_3, deemed to be more precise than those issued from a theoretical calculation. The whole of the validation tests in static crucibles or on loops enables the main operating characteristics of these probes to be defined: low temperature (T>350 °C), very low contents ($<10^{-10}$ ppm), short time of response, good reproducibility, as well as lifetimes likely to exceed several thousands of hours. The main limits are related to the reliability of these probes: signal shift in the long term, and relative embrittlement of the solid electrolyte. Dissolved oxygen measurement in the lead-bismuth eutectic may so be considered as validated on the test loop scale. Yet, better reliability is still required for its use to be contemplated on a nuclear system. In addition, online calibration methods would be a useful tool for steadily assessing the shift, and would considerably improve confidence in the measurement.

Corrosion in lead and its alloys – Protective coatings

Protection against corrosion in liquid lead and its alloys may be achieved either *in situ* by forming an oxide layer on steel surface through oxygen content monitoring in lead and its alloys, as previously seen, or through using protective coatings or forming surface alloys [24-29].

As regards protective coatings and surface alloys, different processes are considered: formation of surface alloys containing such elements as Al or Si, which form stable oxide layers at low oxygen contents (fairly lower than those required for *in situ* oxidation of structural materials), coatings with Type FeCrAlY alloys, coatings with materials likely to withstand corrosion in lead and its alloys, such as W, Mo and Nb.

Among the different protective devices, those which today appear as the most promising in terms of corrosion resistance and the most elaborate in terms of industrial process are the following:

- The processes which allow formation of aluminium-containing surface alloys: pack-cementation, based on a diffusion process of addition elements (Al), which was investigated for austenitic steels and developed for martensitic steels at the CEA, and the GESA process, developed by the Research Center of Karlsruhe (FZK), which relies on a pulsed electron beam technique;
- The FeCrAlY coating processes based upon the GESA process.

The coatings investigated at the CEA are made by pack-cementation. They were initially developed and studied as part of fusion-related programs for achieving tritium-permeation barriers, and their behavior in a Pb-17Li environment could thus be investigated.

Concerning 316L austenitic steels, the aluminizing process based upon pack-cementation is an industrial process consisting in the following steps:

- A deposit treatment in presence of the pack at 750 °C for 1h40,
- A step of diffusion under argon for 6 hours at 900 °C.

The resulting coating (Fig. 122), about 50-60 µm thick, consists of two layers.

The outer layer displays a uniform thickness of about 20 µm. It consists of steel-constituting elements, containing aluminium and oxygen. The aluminium content is higher than that of the internal layer which, in contrast, is richer in chromium. A high number of Ni-and Al-rich precipitates can be observed at the interface between the two layers. Their density decreases as they are closer to the matrix. Al and O enrichment is also seen on a thin (5-10 µm) layer on the coating surface. Figure 123 displays the corresponding microprobe profile.

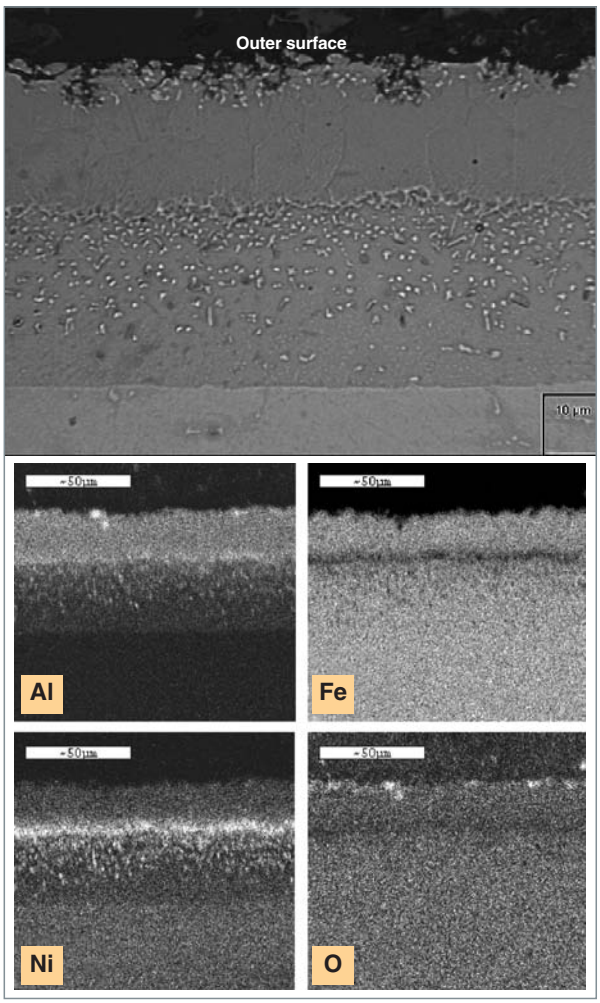

Fig. 122. Cross-sectional SEM micrographs and X-ray images of 316L austenitic steel following formation of an aluminized coating through pack-cementation.

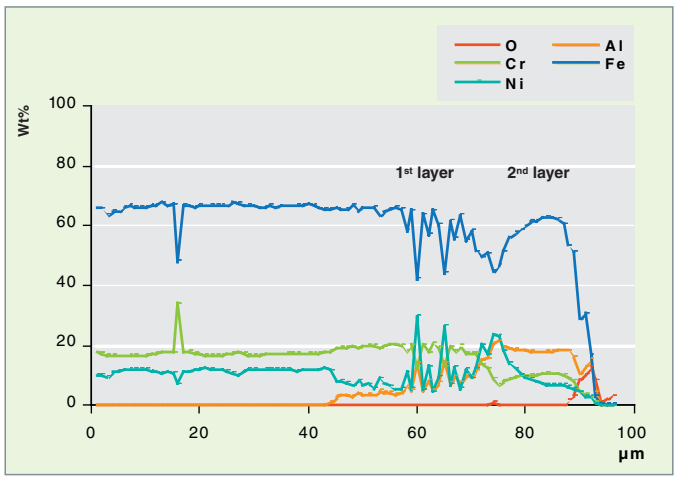

Fig. 123. Microprobe profile of type 316 austenitic steel after deposition of a coating by pack cementation.

As regards martensitic steels, in as much as no industrial process was available, different coating processes were investigated by the CEA/Grenoble, with the following goals:

- Obtaining a Fe-Al deposit at a temperature lower than or equal to 750 °C (temper temperature of the material) in order to avoid any alteration of the material's mechanic properties and avoid formation of brittle intermetallic phases;

- Getting a deposit with an extreme surface layer consisting of alumina.

Three processes were studied:

a) The deposit of the Fe-Al alloy through pack-cementation: thermal decomposition at 750 °C for 1 hour in presence of the pack;

b) The deposit of the Fe-Al alloy through pack-cementation followed by *in situ* oxidation at 750 °C for 1 hour to allow an alumina layer to be formed in surface;

c) The deposit of the Fe-Al alloy through pack-cementation followed by alumina deposition according to the Pyrosol process (treatment at 370 °C for 1 hour).

The thickness of the coatings, including an aluminium diffusion area within the steel, ranges between 40 and 120 µm depending on the process.

Concerning the three different processes, the coatings obtained are similar. A thin alumina layer (of about 1 µm) can be observed on the outer side in all cases. Then, different metallic phases can be seen on a layer 10-20 µm thick, i.e. Fe, FeAl, Fe_3Al, mixed with alumina and hematite in cases b) and c). Figure 124 displays the coating formed on martensitic steel T91 using the b) process.

The corrosion tests in lead and its alloys have led to the following results:

- Regarding Pb-Bi alloy, the coating achieved on an austenitic steel is always intact, and its thickness unchanged, after contact with the alloy between 400-450 °C for 15,000 hours at a flow rate of 50-100 $L.h^{-1}$. As a conclusion, the behavior of the aluminized coating in contact with liquid Pb-Bi alloy proves to be quite satisfactory.

- In stagnant Pb-Bi alloy, a very good behavior of the coating can be observed for austenitic and martensitic steels up to 500 °C, and the like up to 600 °C for oxygen contents higher than 10^{-8} wt%. At 600 °C, a significant degradation of the coating occurs for low oxygen contents (< 10^{-8} wt%).

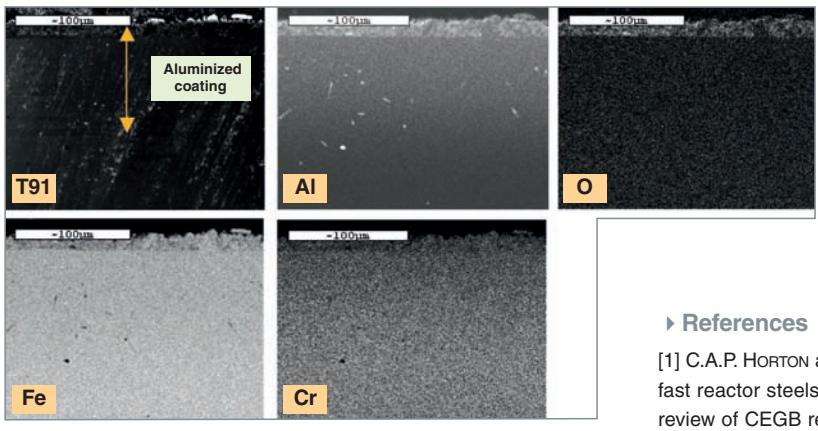

Fig. 124. Cross-sectional SEM micrographs and X-ray images of martensitic steel-T91 after coating through pack-cementation.

- In circulating Pb-Bi alloy, localized damage appears at 600 °C, whatever the oxygen content in the liquid alloy may be. This alteration is attributed to turbulence areas.

Steels protected by formation of an aluminium-containing surface alloy through the GESA process also exhibit a good behavior with respect to corrosion. This process was tested on austenitic and martensitic steels which display a good corrosion behavior in lead and stagnant alloy Pb-Bi up to 650 °C, for oxygen contents ranging between 10^{-4} and 10^{-6} wt%.

These various protective means have proved to be efficient with respect to corrosion by lead and its alloys; still, they will have to be investigated more thoroughly as regards their long-term behavior, mechanical strength and irradiation resistance.

To sum up it all, it seems useful to focus one's attention on cases of corrosion by liquid metals considered as candidate materials for nuclear applications. Corrosion by liquid sodium appears as controllable: the corrosion rate can be kept at very low values by only maintaining an oxygen content as low as possible in the bath. Dissolution or embrittlement phenomena by liquid metal penetration are also negligible providing a temperature lower than 570 °C is maintained. As a matter of fact, the major difficulty to be coped with is the risk of cracking corrosion induced by aqueous soda, which may be generated in the case of wet air ingress during maintenance or repair operations. This risk can be controlled through implementing suitable intervention procedures. This overall control stands as one of the benefits of the "sodium reactor system".

In contrast, corrosion by liquid lead alloys appears as a true problem, which will finally impose using coated materials, as well maintaining a highly controlled oxygen content in the bath. Despite significant advances, controlling corrosion phenomena in this environment has not yet been fully acquired, and here lies one of the major handicaps of the "lead reactor system".

References

[1] C.A.P. Horton and B.H. Targett, "The creep rupture behaviour of fast reactor steels, welds and transition joints in flowing sodium: a review of CEGB results", pp. 513-1 to 513-10, *Fourth International Conference on liquid metal engineering and technology*, 17-21 October 1988, Tome 2.

[2] M.P. Mishra *et al.* "Microstructural aspects of creep-rupture life of Type 316L(N) stainless steel in liquid sodium environment", *Journal of Nuclear Materials 200* (1993), pp. 244-255.

[3] J.P. Hilditch, J.R. Hurley, P. Skeldon and D.R. Tice, "The liquid metal embrittlement of iron and ferritic steels in sodium", *Corrosion science*, Vol. 37, N° 3, pp. 445-454, 1995.

[4] P. Skeldon, J.P. Hilditch, J.R. Hurley and D.R. Tice, "The liquid metal embritllement of 9Cr steel in sodium environments and the role of non-metallic impurities", *Corrosion science*, Vol. 36, N° 4, pp. 593-610, 1994.

[5] H.U. Borstedt and L. Champleix, "Corrosion in fast breeder reactors", *EFC publication* N°1, The Institute of Metals, 1989, ISBN 0-901462-73-X.

[6] F. Masse and G. Rouvière, "Activation, corrosion and contamination in Fast Breeder Reactors Validation of models with experimental data". *Conference on liquid metals systems*, Karlsruhe, 1993 March 16-18 Plenum Press New-York and London.

[7] A.W. Thorley, A. Blundell, S.A. Bardsley and R. Lloyd, *4th International Conference on Liquid Metal Engineering and Technology*, Avignon, France, Octobre 1988 (ed SFEN F75724 Paris, Vol. 3).

[8] J. Sannier, J. Paidassi and J. Dixmier, "*Decarburation des aciers ferritiques dans le sodium en circulation entre 475 et 550 °C*", *Journal of nuclear materials*, 55 (1975), pp. 169-176.

[9] J. Sannier, J. Paidassi, J. Dixmier, D. Leclercq and O. Konovaltschikoff (1975), "*Décarburation des aciers ferritiques dans le sodium en circulation entre 475 et 550 °C*", *Journal of Nuclear Materials*, Vol. 55 (2), p. 169.

[10] C. Laige, P. Baque, J. Waliers, K. Schillings and H. Runge, "FBR primary sodium chemistry control: control approach and experience", Kyoto Conference, 1991.

[11] C. Latge and S. Sellier, "Oxidation of zirconium-titanium alloys in liquid sodium: validation of a hot trap, determination of the kinetics, Material behaviour and physical chemistry in Liquid Metal Systems 2", Edited by H.U. Borgstedt, Plenum Press, 1993.

[12] European Fast Reactor 98: Outcome of Design Studies EFR Associates FRAMATOME.

[13] P. Anzieu *et al.*, "The CEA contribution to the Gen IV Sodium Fast Reactor (SFR)", P*roceedings of the Global 2003 ANS Conference*, New Orleans, Louisiana, November 16-20, 2003.

[14] J.-L. Ratier, "*Phénomènes de corrosion des gaines d'éléments combustibles de réacteurs à neutrons rapides*." EUROPCOR, juin 1992, Finlande.

[15] F. Balbaud-Célérier and A. Terlain, "Influence of the Pb-Bi hydrodynamics on the corrosion of T91 martensitic steel and pure iron", *Journal of Nuclear Materials*, 335 (2004), pp. 204-209.

[16] F. Balbaud-Célérier and F. Barbier, "Investigation of models to predict the corrosion of steels in flowing liquid lead alloys", *Journal of Nuclear Materials* 289 (2001), pp. 227-242.

[17] F. Barbier, F. Balbaud, Ph. Deloffre and A. Terlain, "Corrosion behaviour of materials in a liquid Pb-Bi spallation target", Global 2001, Paris, France (2001).

[18] F. Barbier and A. Rusanov, *J. Nucl. Mat*, 296, 2001, p. 231.

[19] F. Balbaud-Célérier, P. Deloffre, A. Terlain and A. Rusanov, *J. Phys. IV France 12*, 2002, Pr8, 177.

[20] L. Martinelli, Thèse de doctorat, Université Paris VI, 2005.

[21] F. Balbaud-Celerier, L. Martinelli, A. Terlain, A. N'gomsik, S. Sanchez and G. Picard, *Mater Science Forum*, pp. 461-464, 2004, 1091.

[22] J.L. Courouau and J.L. Robin, "Chemistry control analysis of lead alloys systems to be used as nuclear coolant or spallation target", *Journal of nuclear materials*, Vol. 335 (2004), pp. 264-269.

[23] J.L. Courouau, "Electrochemical oxygen sensors for on-line monitoring in lead-bismuth alloys: status of development", *Journal of nuclear materials*, vol. 335 (2004), pp. 254-259.

[24] Jean-Bernard Vogt, Arnaud Verleene, Ingrid Serre, Fanny Balbaud-Célérier, Laure Martinelli and Anne Terlain, "Understanding the liquid metal assisted damage sources in the T91 martensitic steel for safer use of ADS", *Engineering Failure Analysis*, 14 (2007), pp.1185-1193.

[25] L. Martinelli, F. Balbaud-Célérier, A. Terlain, S. Delpech, G. Santarini, J. Favergeon, G. Moulin, M. Tabarant and G. Picard, "Oxidation mechanism of a Fe–9Cr–1Mo steel by liquid Pb–Bi eutectic alloy" (Part I), *Corrosion Science*, 50 (2008), pp. 2523-2536.

[26] L. Martinelli, F. Balbaud-Célérier, A. Terlain, S. Bosonnet, G. Picard and G. Santarini, "Oxidation mechanism of an Fe–9Cr–1Mo steel by liquid Pb–Bi eutectic alloy at 470 °C" (Part II), *Corrosion Science*, 50 (2008), pp. 2537-2548.

[27] L. Martinelli, F. Balbaud-Célérier, G. Picard, G. Santarini, "Oxidation mechanism of a Fe-9Cr-1Mo steel by liquid Pb–Bi eutectic alloy" (Part III), *Corrosion Science*, 50 (2008), pp. 2549-2559.

[28] L. Martinelli, T. Dufrenoy, K. Jaakou, A. Rusanov and F. Balbaud-Célérier, "High temperature oxidation of Fe–9Cr–1Mo steel in stagnant liquid lead–bismuth at several temperatures and for different lead contents in the liquid alloy", *Journal of Nuclear Materials*, 376 (2008), pp. 282-288.

[29] L. Martinelli, F. Balbaud-Célérier, G. Picard and G. Santarini, "High temperature oxidation of Fe-9Cr-1Mo steel in liquid metal", *Materials Science Forum*, Vols. 595-598 (2008), pp. 519-528.

Bibliography

Handbook on Lead-bismuth Eutectic Alloy and Lead Properties, Materials Compatibility, Thermal-hydraulics and Technologies, Nuclear Energy Agency OECD (2007).

IAEA-TECDOC-1289 Comparative assessment of thermophysical and thermohydraulic characteristics of lead, lead-bismuth and sodium coolants for fast reactors.

IAEA-TECDOC-687 Fission and corrosion product behaviour in liquid metal fast breeder reactors (LMFBRs).

Fanny Balbaud, Jean-Louis Courouau,
Philippe Deloffre, Damien Féron, Laure Martinelli,
Physico-Chemistry Department
Christian Latgé,
Nuclear Technology Department
Michel Pelletier,
Fuel Studies Department
Anne Terlain,
Nuclear Materials Department

Corrosion in Molten Salt Reactors

Today investigations on Molten Salt Reactors – MSR – conducted within a European frame converge towards thorium cycle-based (epi)thermal spectrum concepts. The fuel consists of thorium 232 (the fertile isotope) and uranium 233 (the fissile element dissolved in a fluoride bath). This liquid fuel also ensures the function of a **coolant***, the fission-generated heat being directly released within it. Mixtures of LiF, BeF_2, NaF, ZrF_4... are under consideration. In a MSR, molten salt at the core outlet flows towards a heat exchanger in which it transfers its calories to a secondary coolant prior to coming back to the reactor vessel. In the version illustrated hereunder, the fluoride bath under atmospheric pressure comes into the core at about 550 °C, and leaves it at an approximate 700 °C. It is worth emphasizing here that a fraction of the fuel salt is deviated to a chemical treatment unit. There, **fission products*** - FPs - and actinides will be partially removed in order to limit their pile-up in the bath, harmful for reactor efficiency. Continuous extraction with helium will enable volatile products such as Kr or Xe to be removed, while online or batch processes are to remove part of dissolved species. Today the principle of spent fuel treatment is under investigation, so that its efficiency has not yet been quantified species per species. However, it would be an illusion to assume that any FP trace will be removed.

The molten salt reactor concept displays several assets. Nevertheless, developing this reactor system means using structural materials which can withstand heat on contact with molten salt. Our attention is focused on metallic materials for the primary coolant circuit, and salt for the processing unit. Now, ensuring corrosion resistance of alloys in liquid fuel seems to be all the more critical as the target lifetimes may reach several dozens of thousands of hours.

In the 1960s and 1970s, the USA (Oak Ridge), Japan (Furukawa), ex-USSR and Europe (EDF, CEA) conducted many studies on MSR-dedicated materials. In particular, Oak Ridge Laboratory (ORNL) designed an alloy optimized with respect to its properties of molten salt corrosion behavior, under the trade name of Hastelloy N [1]. This alloy is nickel-based and includes alloying elements such as molybdenum (15-17 wt% Mo), chromium (6-8 wt % Cr) and iron (4-6 wt % Fe); it also contains carbon (0.04-0.08 wt % C) and addition elements such as Mn, Si, Al, Ti... This alloy was used for building the structures of the experimental reactor MSRE, which operated successfully at ORNL in the 1960s. Since then, most of studies have been focused on Hastelloy N or similar grades. Part of former program data is accessible in open literature, and was analyzed within the frame of the European Project MOST, in the light of the aims targeted for the 4th-Generation reactor systems [2]. This feedback indicates that using molten fluorides at high temperature results in an environment highly aggressive to metallic materials. The degree of aggressiveness depends on various factors such as the temperature, nature and concentration of the molten bath pollutants... In addition, apart from damage due to molten salt and its oxidizing impurities, some FPs such as tellurium may also react with the MSR structures. Last but not least, substantial amounts of FPs will be carried into the treatment unit. Therefore, corrosion likely to be induced by FPs, especially tellurium, in solution in molten fluorides will have to be taken into account when selecting a structural material for the circuits of a 4th-Generation MSR.

Corrosion of nickel alloys (Hastelloy-N) by molten fluorides

Corrosion of an alloy by a molten salt mostly results from redox reactions between a metallic element and an oxidant in solution. Generally, these reactions are fast at high temperature, and a thermodynamic treatment can then provide information about corrosion processes. Assuming that the redox potential of a species in a molten bath is calculated referring to the free energy of formation of fluorides, Table 7 gives a scale of the oxidizing potential of some components in a fluoride system. It is clearly shown that the main fuel constituents, quite stable, do not react with conventional metals.

However, reactions involving the species UF4 may still take place [see Equation (1)]. Besides, the liquid fuel will inevitably contain impurities arising from the initial salt pollution, leaks, native oxide dissolution... O_2, H_2O, HF, OH^-, and metallic cations are powerful oxidants [see Equations (2) and (3)]. Progress in corrosion reactions chiefly depends on the bath "redox power", often assessed using the ratio between concentrations of quadrivalent and trivalent uranium ions:

$$Cr_{(alloy)} + 2\ UF_4 = CrF_2 + 2\ UF_3 \quad (1)$$
$$Cr_{(alloy)} + 2\ HF = CrF_2 + H_2 \quad (2)$$
$$Cr_{(alloy)} + FeF_2 = CrF_2 + Fe \quad (3)$$

This UF_4 / UF_3 ratio varies from 10 to 500 approximately. As corrosion products are highly soluble in molten fluorides,

Table 7.

Free energy of formation of fluorides at 1000 K expressed in kcal/mol F atom.

	ΔG°f		ΔG°f		ΔG°f		ΔG°f
CaF_2	-125	AcF_3	-113	NpF_3	-102	FeF_2	-67
LiF	-125	MgF_2	-113	ThF_4	-101	CoF_2	-67
BaF_2	-124	RbF	-112	UF_3	-100	SnF_2	-62
SrF_2	-123	NaF	-112	PuF_4	-98	PbF_2	-62
LaF_3	-121	PaF_3	-112	UF_4	-95	NiF_2	-58
CeF_3	-120	PuF_3	-111	ZrF_4	-94	WF_6 (g)	-58
PrF_3	-119	AmF_3	-110	AlF_3	-90	MoF_6 (g)	-50
SmF_3	-119	KF	-109	TaF_5	-82	TeF_4	-39
NdF_3	-118	CsF	-106	UF_6 (g)	-74		
YF_3	-114	BeF_2	-104	CrF_2	-74		

there is no case of passivity. In an isothermal, static and purified bath, metallic ions concentrations will reach their equilibrium values, and corrosion will come to an end. But in a renewed bath, it may go on indefinitely, indeed.

Mass transfer in non-isothermal fluoride systems

As the reactional constant K [see Equation (4)] is a growing function of temperature, equilibrium concentrations of corrosion products in the bath increase with temperature, which means that metal is dissolved in hot areas, and deposits are formed in cold areas:

$$\Delta G_r = -R.T.\ln[K(T)] = \Delta H_r - T.\Delta S_r \qquad (4)$$

This dynamic process is complex, for it includes several steps: ionic transport in liquid phase, redox reaction, diffusion in a solid phase… For a given system, the kinetically limiting step will strongly depend on environmental variables. Some factors have a considerable influence on the corrosion rate:

- **Temperature:** Hastelloy N specimens were placed in forced convection loops in which $LiF/BeF_2/ThF_4/UF_4$ were flowing at 700-500 °C, 760-560 °C and 815-615 °C [8]. For a constant value of ΔT, loss of mass in hot areas increases with the maximum temperature of the system (Fig. 125).

- **Thermal gradient:** temperature evolution along the metallic walls is the driving force of material transport [see Equation (4)]. It can be noted that the gradient of the constant ΔK varies with ΔSr. So any change in the bath composition may influence the corrosion rate.

- **Oxidants content:** supply of vapor (Fig. 126), HF, FeF_2 or CrF_2 in the natural convection loops carrying over (LiF/BeF_2, $NaBF_4/NaF$, NaF/ZrF_4 based) fluorides resulted in increased corrosion of metallic specimens. The mass transport rate rises with the metallic ion content, the latter being generated by oxidation reactions. Consequently, the contamination rate will exhibit a more harmful effect, here, than in the case of an isothermal system.

- **Exposure time, flow velocity of the fluid, salt composition, hydraulic conditions.** All these factors may play a role in material transfer.

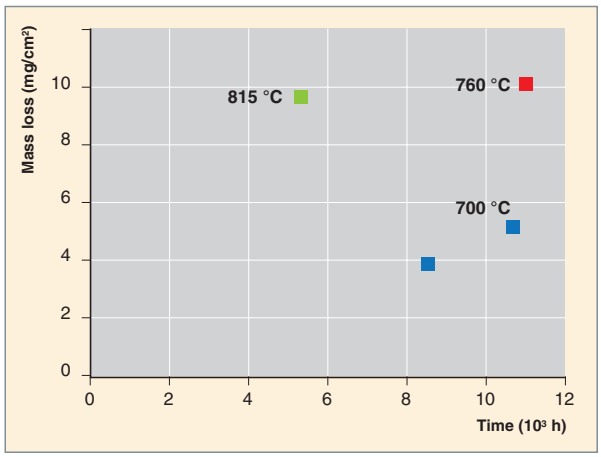

Fig. 125. Mass loss of Hastelloy N specimens put in three forced convection loops carrying $LiF/BeF_2/ThF_4/UF_4$ [1].

As shown by the MSRE operation and by laboratory tests as well, alloys type Hastelloy N and stainless steels were slowy corroded to 700° and 650 °C, respectively, in highly purified fluorides comprising beryllium salt (with the bath redox power being adjusted by contact with a Be bar). It is an absolute requirement to purify the salt and permanently adjust its oxidation potential. Therefore, concerning Be-depleted salts, a suitable, efficient purification method would have to be developed.

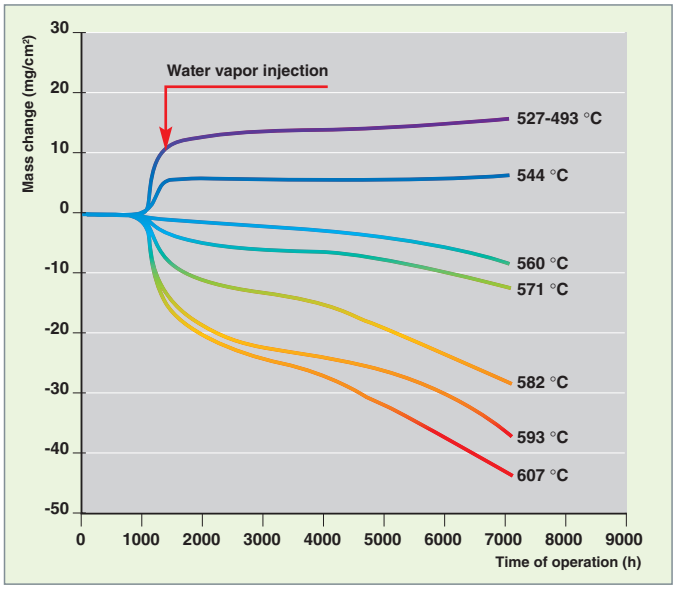

Fig. 126. Mass change of Hastelloy N specimens put in a natural convection loop comprising $NaBF_4$ / NaF at different temperatures. At t = 1000 h, water vapor is injected to the system [2].

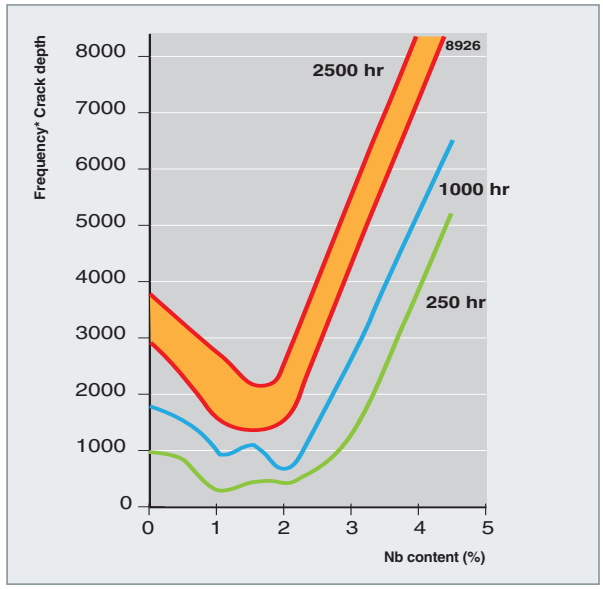

Fig. 127. Empirical cracking parameter as a function of the niobium content added to the Hastelloy N nominal composition. Cracking examinations were performed on specimens immersed for 250, 1000, or 2500 hours into Te-containing fluoride at 700 °C [3].

Tellurium-induced embrittlement

Apart from general corrosion, after contact with fluoride fuel, MSRE monitoring specimens displayed embrittlement in a particularly clearcut way during post-exposure tensile tests. Intergranular cracks reaching 330 µm could be observed. As this cracking occurred out of pile, it was assigned to the effect of a FP. As confirmed by controlled dissolution of a specimen, FPs penetrated Hastelloy N, with Te as the most concentrated element. In parallel, *in situ* Auger analyses on a fractured grain boundary enabled Te to be pinpointed. Although Te flow in the MSRE was relatively low (about 10^9 atoms Te/cm²/s), it was concluded that this FP was responsible for embrittlement, presumably out of formation of hard compounds at the alloy grain boundaries.

Following these observations, ORNL undertook a program to optimize Hastelloy N composition. First of all, a test method had to be developed. It was thus found that laboratory tests do not accurately reproduce the morphology obtained in a reactor, but enable alloys to be discriminated. As a general rule, specimens are immersed into a molten fluoride which contains a Te compound of Type Cr_xTe_y, Ni_xTe_y between 650° and 750 °C. Alloy heats enriched with Ti, Nb and Cr were tested. Most of them exhibited intergranular cracking. It is worth mentioning that Cr contents of 15% and more reduce proneness to cracking. Besides, adding 1 to 2% Nb fairly improves Te resistance (Fig. 127).

In contrast, not only is Ti inefficient, but it also annihilates Cr and Nb beneficial effect. It is worth noting, however, that Al is assumed to reduce damage caused by tellurium. In addition, stainless steels and Cu or Co alloys are insensitive to this corrosion mode.

In parallel, as illustrated on Figure 128, the tellurium effect can be overcome by controlling the fluoride bath chemistry. Specimens were immersed for 260 hours into a mixture of $LiF/BeF_2/ThF_4/UF_4$ salts with Cr_3Te_4 at 700 °C. In order to induce variations in the medium redox potential, a Be bar was immersed into the salt, and the UF_4/UF_3 ratio was assessed. Proneness to embrittlement was appraised using an empirical parameter based on metallographic observations. Hastelloy N displays a significant change of behavior: regarding UF_4 / UF_3~ 60, cracking is moderate, whereas it is strong for UF_4 / UF_3 ~100.

Controlling the oxidizing power of the environment therefore seems to be a promising route for protecting Ni alloys containing less than 15% Cr against tellurium embrittlement effect.

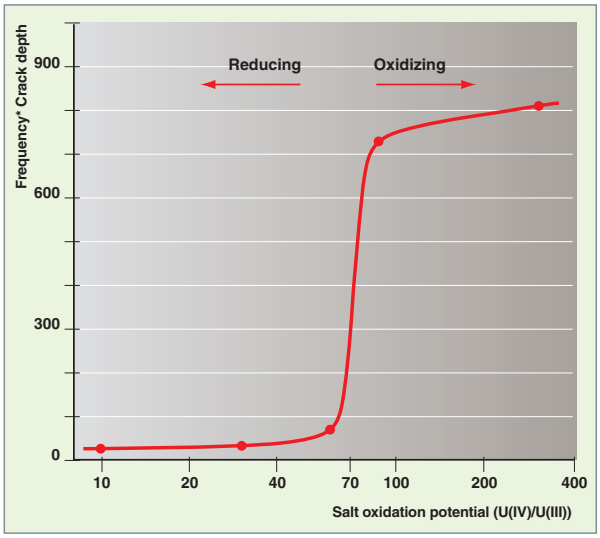

Fig. 128. Empirical cracking parameter as a function of the oxidizing power assessed through the UF_4/UF_3 ratio. Crack observations were performed on Hastelloy N specimens immersed for 200 hours into $LiF\text{-}BeF_2\text{-}ThF_4\text{-}UF_4$ + Te at 700 °C [3].

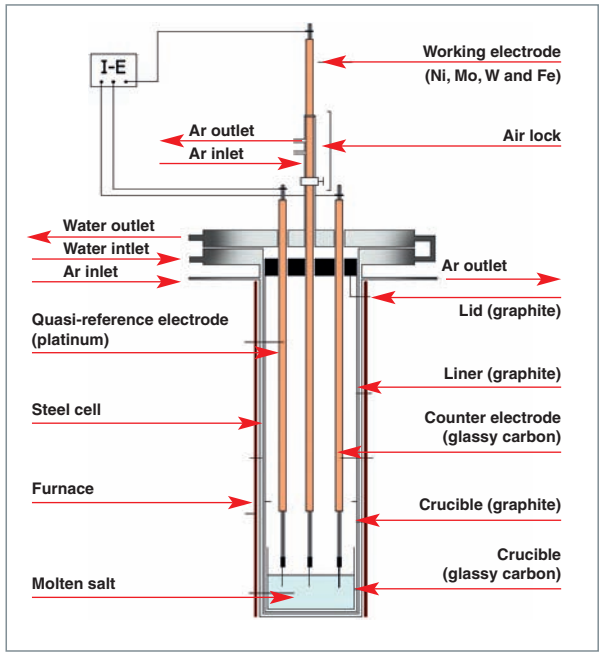

Fig. 129. Schematic diagram of the experimental device designed for the electrochemical study of pure metal behavior in molten fluorides.

Electrochemical study of pure metal corrosion in molten fluorides

With the aim of better characterizing physico-chemical interactions between materials and molten fluorides, the electrochemical behavior of several pure metals (iron, nickel, chromium, molybdenum and tungsten) was investigated in molten fluoride media (e.g. LiF-NaF) in a temperature range of 700-1000 °C. First, experimental techniques had to be developed, including the test device designed to ensure full confinement of the medium (no air contamination), as well as a stringent control of temperature (Fig. 129). The electrochemical methods used include cyclic voltammetry, Tafel's method (plotting of anodic and cathodic polarization curves), and polarization resistance measurement. They are associated with examination of the electrode microstructure after immersion.

A scale of apparent oxidation potentials was developed basing upon the linear-sweep voltamperograms plotted for several pure metals (Fig. 130). It shows the relative stability of the various metals in LiF-NaF at 900 °C. Experimental oxidation potentials are in good agreement with the predictions obtained with thermochemical calculations (Table 1), and so can be classified as follows: Cr < Fe < Ni < Mo < W, with tungsten as the most noble metal.

The electrochemical behavior of species of chromium, iron and nickel in solution could then be determined by adding metallic fluorides CrF_3, FeF_2 and NiF_2 to LiF-NaF at 900 °C. Under such conditions, species Cr(II), Cr(III) and Fe(II) are stable and soluble for concentrations up to an approximate

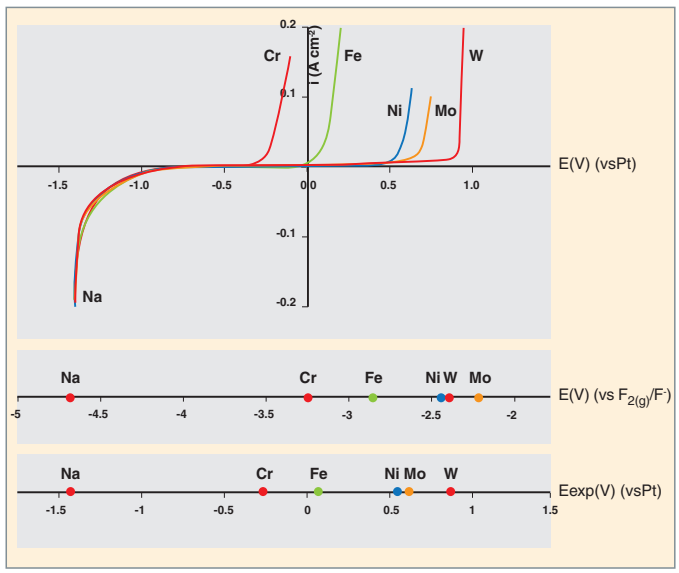

Fig. 130. Polarization curves for electrodes made out of chromium, iron, nickel, molybdenum, and tungsten in fluorinated salt (LiF-NaF) at 900 °C, and comparison of the thermochemical and experimental oxidation potential scales.

1.5 mol.kg^{-1}. In agreement with literature, diffusion coefficients of the various oxidized forms of metals are of about 10^{-6} cm^2.s^{-1} at 900 °C, and the activation energy associated with diffusion of chromium +III ions through the medium is of about 55 kJ.mol^{-1} in the 700-1000 °C temperature range. In contrast, it is noteworthy that Ni(II) ions are spontaneously reduced in the molten medium. These behaviors suggest that

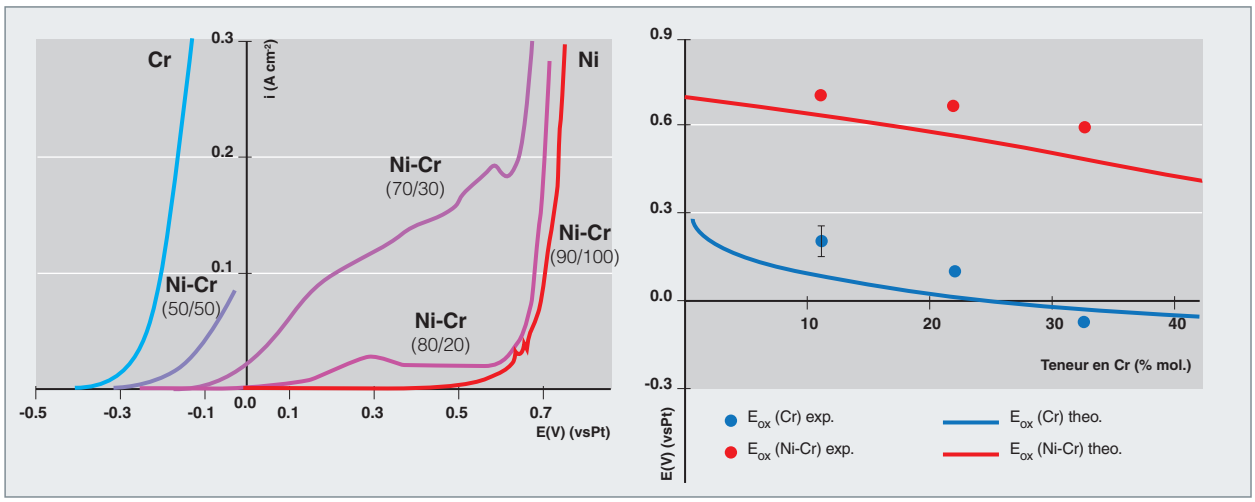

Fig. 131. Polarization curves for electrodes made out of chromium, nickel, and Ni-Cr alloys of various compositions (weight %) in LiF-NaF at 900 °C (scanning rate: 1 $mV.s^{-1}$), and the related thermo-chemical modelling.

there exists an electroactive species in the bath which is likely to control equilibria in the medium. Referring to experimental results, the electrochemical potential of this redox couple is assumed to be set up between iron and nickel oxidation potentials. Even if the nature of the redox species involved is still to be identified, this hypothesis helps rationalize the behavior of increasingly complex metallic materials in fluoride baths.

Thus, Figure 131 illustrates the anodic polarization curves of binary alloys Ni-Cr with an increasing chromium content in LiF-NaF. Oxidation proceeds in two steps: the first one occurs at intermediate potentials, and is displayed by selective chromium oxidation (checked through electrode inspection after testing); the second one takes place at more electropositive potentials, and is displayed by the congruent attack of the solid solution Ni-Cr. For each of these steps, a characteristic oxidation potential can be assessed: E_{ox}(Cr) and E_{ox}(Ni-Cr). The potential E_{ox}(Cr), significant for the behavior of the alloy immersed into NaF-LiF, is shifted to the more electronegative values when the Cr content of the binary alloy increases. This trend was validated by thermochemical calculations which account for, if only qualitatively, chromium activity influence on E_{ox}(Cr) (Fig. 131, right graph). Accordingly with the hypothesis hereabove mentioned in relation to the bath redox potential, it could then be observed that chromium-rich alloy heats behaved as Cr, and were oxidized in the environment, while nickel-rich heats were under immune conditions.

Corrosion is the Achilles' heel of molten salt reactors, and of **pyrochemical*** processes as a whole. Consequently, developing this reactor type will only be possible through developing new materials and ensuring the chemical (impurity) and electrochemical (redox) control of the molten medium, the whole being based upon a thorough understanding of corrosion mechanisms. Technological breakthroughs, such as exchangers without wall, coated materials…, also bring promising outlooks with respect to coping with implementation difficulties. All things considered, this is a research field widely open to innovation, in which significant R&D efforts can but prove fruitful.

References

[1] M.W. Rosenthal *et al.*, ORNL-4832 (1972).

[2] M.W. Rosenthal *et al.*, ORNL-4622 (1970).

[3] M.W. Rosenthal *et al.*, ORNL-4812 (1972).

[4] S. Fabre, C. Cabet, L. Cassayre, P. Chamelot, J. Finne, D. Noel and P. Taxil., "Electrochemical study of the corrosion of metals in molten fluorides Materials", *Science Forum*, Vol. 595-598, pp. 483-490, 2008.

[5] S. Fabre, C. Cabet, P. Chamelot, J. Finne and L. Cassayre, "Electrochemical study of the corrosion of metals in molten fluorides", *Proceedings of the 7th International Symposium on High Temperature Corrosion and Protection of Materials* (HTCPM - 2008), 18/05/2008 - 23/05/2008, Île des Embiez, France.

Bibliography

Baes Jr. (C.F.), "The Chemistry and Thermodynamics of Molten Salt Reactor Fuels", Proc. *AIME Nuclear Fuel Reprocessing Symposium*, Ames, Iowa, USA, August 25 (1969).

Renault (C.) and Delpech (M.), "Review of Molten Salt Reactor Technology", *MOST Final Report, European Commision Contract*, N°: FIKI-CT-2001-20183, March (2005).

Céline Cabet, Stéphanie Fabre,
Physico-Chemistry Department

Materials Corrosion and Alteration at the Back-End of Fuel Cycle

From spent fuel **treatment*** to **waste storage*** or **disposal***, the various steps of the back-end of nuclear fuel cycle make use of several types of materials: natural or artificial, metallic, mineral or organic materials. These materials may be subjected to very severe conditions of use in terms of environment (aggressive environments), required performance, or again required duration of performance.

- In spent fuel treatment / recycling facilities, the first aim is to enable the plant to operate properly. The main requirement relating to materials is their strength in acid environments which are chemically very hostile.

- In waste storage facilities, the other aim is, above all, to ensure good behavior of containers and overcontainers so as to guarantee their retrieval at the end of the storage period.

- In disposal facilities, the stake is to control, retard and limit alteration of containment barriers and confining matrices: for this alteration influences radionuclide release into the geosphere and, so, the chemical and radiological impact of the repository. Here, the constraint chiefly lies in the concept of long timescales (of several hundreds or thousands of years), that is far beyond the usual industrial range (a few tens of years), hence the need for robust, reliable predictive approaches in this field.

Within the frame of the former Act of December1991 and of the new Act of June 2006 relating to nuclear waste management, a substantial set of R&D programs has been undertaken, and is going on in order to understand and model the long-term behavior of materials under storage and disposal conditions. In terms of applications, investigations mainly focus on the long-term behavior of conditioning matrices made out of cement, bitumen, glass or ceramic, or of cement- or metal-made containers (or overcontainers), designed to host waste packages, as well as of concrete or swelling clay engineered barriers and/or structural components. The environments under consideration are of a wide variety and relate to applications of storage (unsaturated environment, temperature), disposal under reversible conditions (unsaturated environment), or post-closure disposal (saturated environment).

The material's physico-chemical environment (component, object, structure...) plays a crucial role in its evolution (mineralogy, metallurgy, microstructure, surface state, reactivity...) and its properties (transport, confinement, mechanics...).

It is also worth noting that the material and / or structural works heterogeneity may enhance these various processes, so that the interfaces of components and their chemical interreactivity in the long term appear as a critical field to be investigated for the purpose of understanding and modelling the ageing phenomenon.

Hence the development, through experiment and simulation, of often original multiphysics, multiscale and multimaterials approaches, which are based on phenomenological understanding and physico-chemical modelling.

Corrosion in a Concentrated Nitric Environment

In France, spent fuel **treatment*** is performed in AREVA La Hague plants using the **PUREX*** process. This process relies on the use of nitric acid to dissolve spent fuel. As a result, all along the process line can be found nitric environments with varied concentrations (up to azeotropic concentration), temperatures up to the boiling point and slightly above, and dissolved species such as oxidizing ions. In order to hold back these very acid and highly oxidizing environments, materials have been selected taking into account their corrosion resistance limits, and have been optimized and qualified before plant building. These materials, passive in their conditions of use, are the following:

- Zirconium, chosen for building the most critical equipment in terms of corrosion, such as fuel dissolvers and evaporators-concentrators of nitric acid;
- Austenitic stainless steels with a very low carbon content (type AISI 304L, 316L and 310Nb; C ≤ 0.02%) for most of equipment;
- A special 4% Si stainless steel for evaporators-concentrators of fission products.

Materials behavior in a nitric environment

These materials previously mentioned are protected with a **passive layer*** stable in nitric acid. Yet, all the phenomena likely to degrade this passive layer may entail severe corrosion phenomena.

Concerning zirconium, three types of phenomena may reduce the protective effect of the passive layer consisting of zirconia ZrO_2:

- The presence of a stress: under passive conditions, which are those of the process-related equipment, zirconium behavior in a nitric environment is little changed when is is subjected to a stress or strain;
- A mechanical degradation, e.g. due to friction or erosion;
- The presence in the environment of zirconium-complexing agents, especially fluorides. Zirconium dissolution rate strongly increases with their concentration, even on the scale of the mg / L in fluorides.

Although protected by a Cr(III)-rich passive layer, all stainless steels, excepting special silicon-based stainless steel, may undergo an intergranular corrosion when their corrosion potential is moved to the **transpassive*** domain (Fig. 132). This type of corrosion features a selective attack of grain boundaries, which may even result in grains getting loose under extreme conditions, although steel is not sensitized (no precipitation of chromium carbides at grain boundaries) and its composition is optimized in carbon, sulfur and phosphorus.

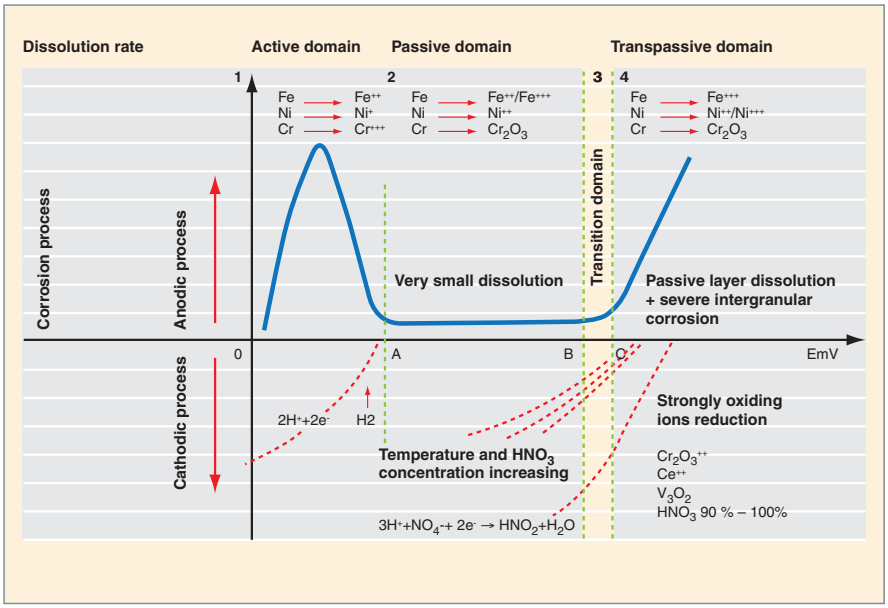

Fig. 132. Corrosion behavior of austenitic stainless steels in acid environments as a function of the redox potential.

Several circumstances may be responsible for the shift of a steel's corrosion potential to its transpassive domain [1].

- In most nitric environments, the reaction which fixes the material's corrosion potential is the overall reduction reaction of nitric acid HNO_3 to nitrous acid HNO_2:

$$NO_3^- + 3H^+ + 2\,e^- \text{ à } HNO_2 + H_2O$$
$$(E_0 \text{ (water, 25 °C)} = 934 \text{ mV/ENH})$$

This reaction uses an autocatalytic mechanism, which will be described in detail in the following paragraph.

- In nitric environments which contain oxidizing ions (i.e. with redox couples having a redox potential higher than that of the HNO_3/HNO_2 couple), the oxidant's reduction reaction is the one that fixes the material's corrosion potential. For example, for the Pu(VI)/Pu(IV) couple, the reaction is as follows:

$$PuO_2^{2+} + 4H^+ + 2e^- \text{ à } Pu^{4+} + 2H_2O$$
$$(E_0 = 1\,024 \text{ mV/ENH})$$

  The steel can remain in its passive domain or be carried to its transpassive domain depending on the redox potential of the couple considered and the oxidant concentration in the environment.

- Contact between these stainless steels with nobler metallic materials is another circumstance that may entail an increase in the steel's potential by galvanic coupling. Such is the case for platinoids (Tc, Ru, Rh, Pd) which are little soluble in nitric acid.

Once these three mechanisms are thermally activated, a temperature rise, e.g. on heated evaporator walls, is a penalizing circumstance with respect to the risk of intergranular corrosion.

Autocatalytic mechanism of nitric acid reduction

The thermodynamic study of the environment allows the prevailing species involved in the process of nitric acid reduction to be identified: these are two gaseous species (NO, NO_2) and an aqueous species (HNO_2) (Fig. 133) [2, 3].

When investigating the influence of nitric acid concentration on the nature of the species limiting the stability domain of nitric environment under reduction, it can be seen that the final reduction product is nitrogen monoxide for concentrations lower than 8 mol/L, and nitrogen dioxide for higher concentrations. The stability domain of nitric acid at 100 °C is represented on Figure 133.

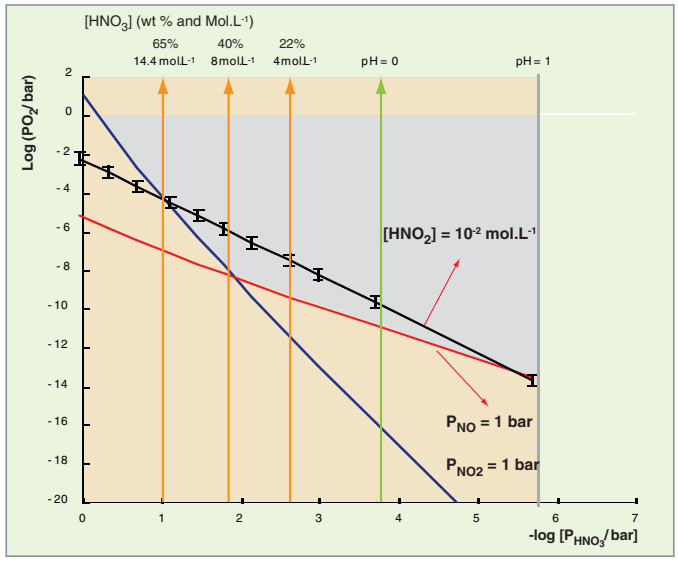

Fig. 133. Representation of the stability range of nitric acid at 100 °C (see the grey portion of the diagram) [2, 3].

The electrochemical study of the nitric acid reduction process performed on a platinum electrode, then on a stainless steel electrode, confirmed the results issued from the thermodynamic study, and enabled the mechanism to be further detailed [2, 4].

Nitric acid is indirectly reduced by an autocatalytic mechanism comprising a charge transfer step and a chemical reaction, which regenerates the electroactive species.

The electroactive species is nitrous acid, which is reduced into nitrogen monoxide:

$$(HNO_2)_{el} + H^+ + e^- + s \Leftrightarrow (NO)_{ads} + H_2O \qquad (1)$$

Nitrous acid is then regenerated by a heterogeneous chemical reaction between nitric acid and nitrogen monoxide:

$$HNO_3 + (NO)_{ads} \Leftrightarrow (HNO_2)_{el} + (NO_2)_{ads} \qquad (2)$$

A third reaction takes place between nitric acid and nitrous acid:

$$HNO_3 + (HNO_2)_{el} + 2\,s \Leftrightarrow 2\,(NO_2)_{ads} + H_2O \qquad (3)$$

Reactions (1), (2) and (3) are the basic reactions of the nitric acid reduction mechanism, which are valid over the whole concentration range.

For low to moderate (< 6 mol / L), concentrations of nitric acid, the reaction of nitrous acid regeneration (2) is slow. Nitrogen monoxide formed during the charge transfer step

(1) can then pile up. Reaction (3) is also shifted to HNO_2 formation, NO_2 not being stable for concentrations lower than 8 mol/L. For this concentration range, the mechanism of nitric acid reduction can therefore be expressed as follows (Fig. 134 a):

$$(HNO_2)_{el} + H^+ + e^- + s \Leftrightarrow (NO)_{ads} + H_2$$

$$HNO_3 + 2\,(NO)_{ads} + H_2O \Leftrightarrow 3\,(HNO_2)_{el} + 2\,s$$

For environments of higher concentration (> 8 mol/L), the reaction of nitrous acid regeneration (2) is fast, as it is made easier by the high nitric acid concentration, and induces an NO_2 gaseous release stable in this concentration range. The mechanism of nitric acid reduction can be therefore written as follows (Fig. 134 b):

$$(HNO_2)_{el} + H^+ + e^- + s \Leftrightarrow (NO)_{ads} + H_2O$$

$$HNO_3 + (NO)_{ads} \Leftrightarrow (HNO_2)_{el} + (NO_2)_{ads}$$

to be completed by Reaction (3) assumed to be at equilibrium

$$HNO_3 + (HNO_2)_{el} + 2\,s \Leftrightarrow 2\,(NO_2)_{ads} + H_2O$$

Nitric acid reduction kinetics can be altered by:

- The products arising from steel corrosion (i.e. Fe(III) ions and, to a lesser extent, Cr(III)) ions, which catalyze it);
- Dissolved oxygen, which makes it slower.

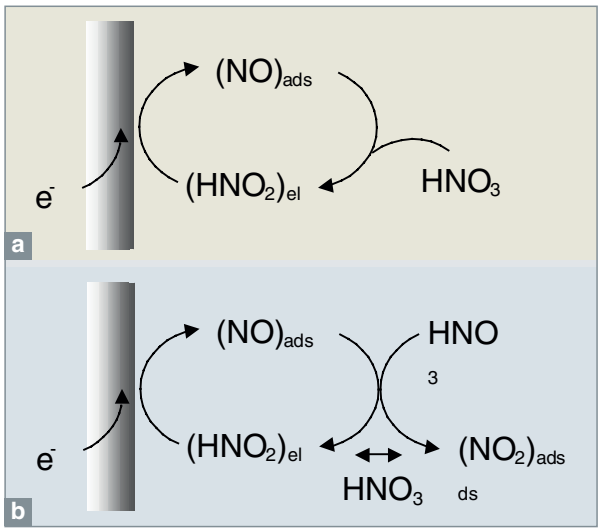

Fig. 134. a) Nitric acid reduction mechanism in an environment of low concentration. b) Nitric acid reduction mechanism in an environment of high concentration.

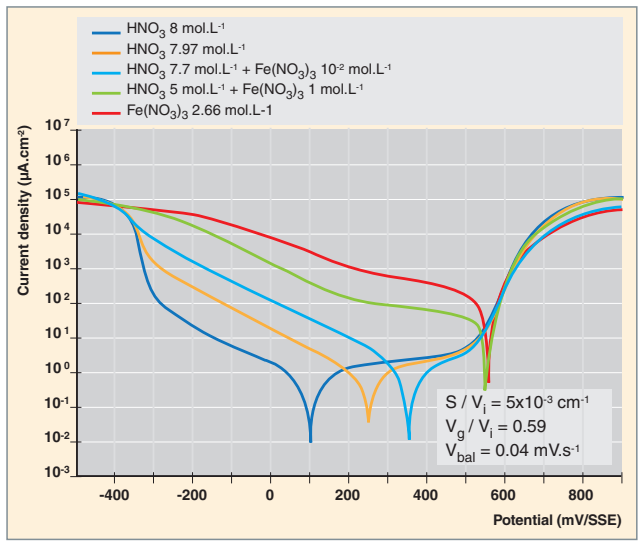

Fig. 135. Ferric ion influence upon the electrochemical behavior of stainless steel-304L in nitric acid of high concentration (8 mol/L) at 100 °C [5].

This mechanism can account for two practical cases. The first one is related to confined, little renewed nitric environments. In this case, nitric acid reduction products (nitrous acid, nitrogen dioxide) as well as Fe(III) and Cr(III) cations issued from corrosion itself, catalyze the nitric acid reduction reaction. This autocatalysis phenomenon shifts the steel corrosion potentials to the transpassive range (Fig. 135) [5].

A second practical case, very similar indeed to the previous case as regards intergranular corrosion causes, is related to corrosion by nitric condensates. The ratio of the metal surface over the very high solution volume and the low rate of condensate renewal entail a fast change in the steel's potential corrosion as soon as metal oxidation products and nitric acid reduction products start piling up in the condensate film (Fig. 136) [2, 6].

The various causes of the increase in steel's corrosion potential in a nitric environment, and so of the risk of intergranular corrosion, have been depicted in the two previous paragraphs.

Present research efforts focus on:

- Modelling intergranular corrosion: in a given environment, the model has to predict loss of sound metal in the long term on the basis of short-term morphological measurements (depth and angle of intergranular penetrations);
- Understanding steel passivation mechanisms across grains and along grain boundaries: the role of impurities and silicon, particularly, will have to be taken into account.

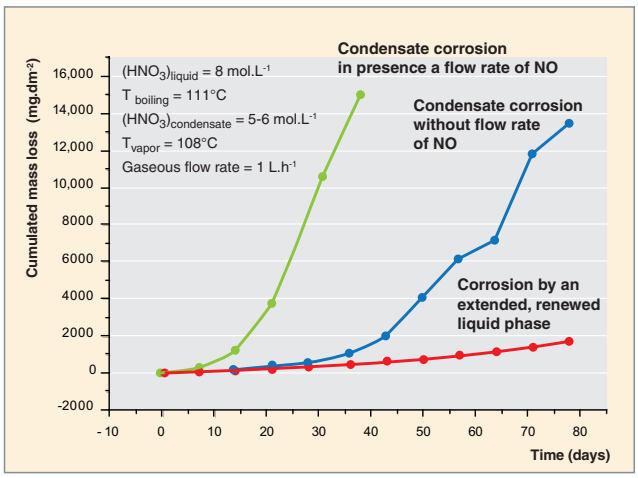

Fig. 136. Comparison of steel-304L corrosion in presence, respectively, of nitric acid condensates and of an extended, renewed liquid phase. Corrosion is far slower in the latter case. The influence of nitrogen monoxide NO shows the autocatalytic feature of corrosion [2, 6].

References

[1] P. Fauvet, F. Balbaud, R. Robin, Q.-T. Tran, A. Mugnier and D. Espinoux, "Corrosion mechanisms of austenitic stainless steels in nitric media used in reprocessing plants", *J. Nuclear Materials*, 375 (2008), pp. 52-64.

[2] F. Balbaud, "*Mécanisme de corrosion de l'acier inoxydable Z3 CN 18.10 en présence de condensats nitriques*", Thèse de doctorat, Université Pierre et Marie Curie, 1998.

[3] F. Balbaud, G. Sanchez, G. Santarini and G. Picard, "Equilibria between gas and liquid phases for concentrated aqueous solutions of nitric acid", *Eur. J. Inorg. Chem.* (1999), pp. 277-285.

[4] F. Balbaud, G. Sanchez, G. Santarini and G. Picard, "Cathodic reaction involved in corrosion processes occurring in concentrated nitric acid at 100 °C", E*ur. J. Inorg. Chem.* (2000), pp. 665-674.

[5] J.-P. Schosger, "*Contribution à la connaissance du comportement de l'acier Z3 CN 18.10 dans l'acide nitrique concentré, chaud et confiné*", Thèse de doctorat n° 1225, Institut National Polytechnique de Toulouse, 1996.

[6] F. Balbaud, G. Sanchez, P. Fauvet, G. Santarini and G. Picard, "Mechanism of corrosion of AISI 304L stainless steel in the presence of nitric acid condensates", *Corrosion Science*, 42 (2000), pp. 1685-1707.

Fanny Balbaud, Pierre Fauvet, Raphaël Robin
Physico-Chemistry Department

Corrosion in an Aqueous Unsaturated Environment

Corrosion in unsaturated environment is especially related to nuclear waste under **storage*** conditions, with generally room air as the "unsaturated" environment. Various types of waste package materials can be affected and will be successively examined here: metals, bitumens and reinforced concrete.

Metal corrosion in an unsaturated environment. The specific case of waste package storage

Under storage conditions, thermal power in some high-level vitrified waste is high enough to avoid condensation on the metal container surface. The outer container wall will then undergo a first step of so-called "dry" corrosion for about 100 years. As soon as temperature on the container surface will be sufficiently low for room moisture condensation to take place, a second step of "atmospheric" corrosion will be likely to occur. Materials considered for containers under storage conditions are alloyed or low-alloyed steels.

Dry corrosion

The term "dry corrosion" here refers to the phenomenon of oxidation of a metal surface by surrounding gases, that is room air in the present case. As a result of expected temperatures (maximum temperature of 300 °C on the outer wall), oxide layers so formed by room air oxidation are not expected to be very thick. However, in order to extrapolate data on laboratory timescales to century timescales (and validate these extrapolations), it is necessary to rely on suitable tools that enable oxide layer growth mechanisms to be modelled.

All existing models are based upon two main oxidation theories: that issued from Wagner's works developed between 1930 and 1970 (high temperatures and thick layer), and that issued from Cabrera and Mott's works in the sixties (low temperatures and thin layer).

Within the framework of container corrosion studies, given the (centennial) timescales examined and the nature of the alloys considered (low-alloy steels), it can be reasonably assumed that the layers are likely to be "rapidly" of sufficient thickness for their growth to be rather controlled by the mechanism proposed in Wagner's model. This model is chiefly based upon the hypothesis of a layer growth controlled by thermally activated diffusion phenomena within this layer. It results in parabolically-shaped kinetics, if only considering the system's pseudo-stationary solutions.

The mass gain of a sample per unit surface area ($\Delta m/S$) is then proportional to the square root of time:

$$(\Delta m/S)^2 = K_p\, t$$

where the K_p parameter, improperly called the "parabolic constant", is time-dependent according to the Arrhenius law (Fig. 137).

Thus, a conservative assessment of the oxide thickness expected over 100 years, of about a hundred microns, can be provided through extrapolating short-term experiments on iron at low temperature according to a parabolic law [1].

Dry corrosion mechanisms

This first estimate can be enhanced with a more robust model likely to take into account the basic mechanisms that jointly govern the layer growth, especially the layer morphological evolutions.

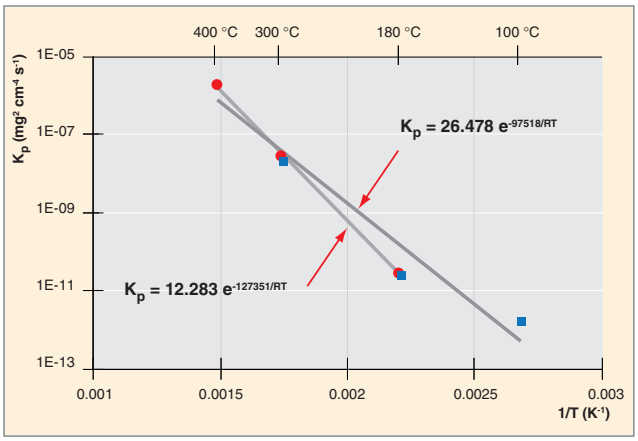

Fig. 137. Arrhenius graph of the parabolic constants (Kp) determined by iron specimen oxidation tests for 250 hours in air +2% vol H_2O.

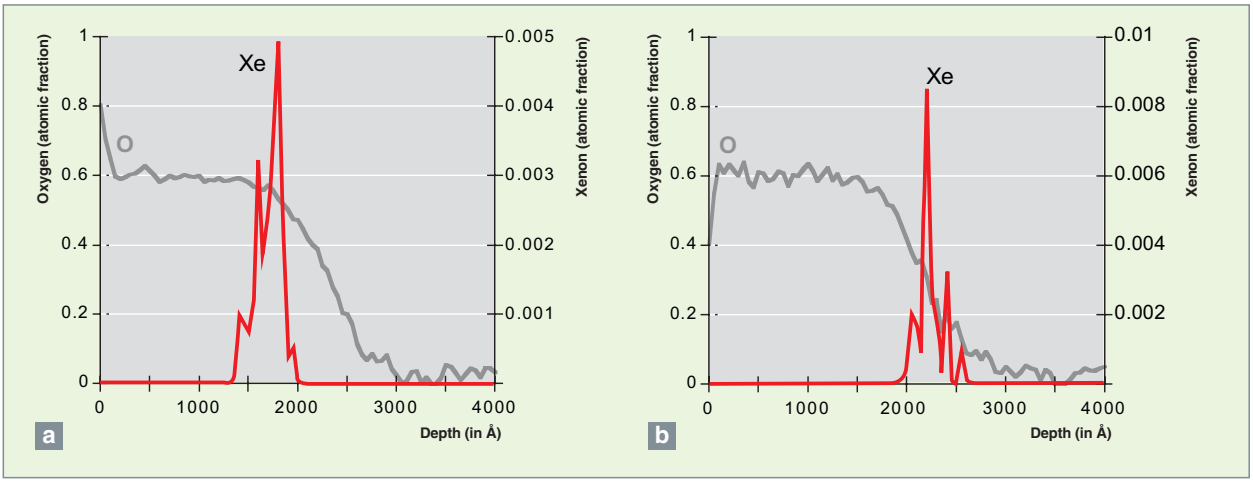

Fig. 138. Oxygen and xenon concentration profiles obtained through RBS analyses for two tests: a) after oxidation at 300 °C for 142 hours, b) after oxidation at 400 °C for 42 minutes. The xenon peak position is a marker of the interface initial position.

The oxide layer growth mechanisms are investigated and validated using so-called "marker" experiments. The principle consists in implanting inert ions at a given depth within the metal substrate, then studying the motion once the specimen has been oxidized. The shift of the marker plane affords information about the relative mobilities of the different (anionic and cationic) species within the oxide layer.

As an example, Figure 138 presents concentration profiles issued from a Rutherford Back Scattering Spectroscopy (RBS)[6] analysis with the Van de Graff accelerator, for two Xe^+ ion implanted samples displaying nearly equivalent layer thicknesses (220-250 nm), one oxidized at 300 °C, and the other at 400 °C.

As the metal / oxide interface is *a priori* located at the inflection point of the decreasing oxygen profile, xenon can be clearly seen in the bulk of the oxide layer in the case of the 300 °C-oxidized specimen, while it seems to be located at the metal / oxide interface in the case of the 400 °C-oxidized specimen. The oxide thickness formed between the xenon peak, marking the initial surface, and the metal / oxide interface can be assigned to a so-called "anionic" growth, i.e. resulting from diffusion through the oxide layer of oxygen anions which react at the metal / oxide interface, thereby inducing oxide growth at this interface.

In contrast, the oxide thickness located between the xenon peak and the surface can be assigned to a so-called "cationic" growth due to diffusion through the oxide layers of iron ions which react at the surface, thereby inducing oxide growth.

In all the tests performed at 400 °C, there does not seem to exist any anionic part, which is in agreement with the purely cationic transport mode usually attributed to magnetite (Fig. 138b). In contrast, at 300 °C, a non-negligible oxide thickness formed under the initial surface (Fig. 138a) can be measured. The thicknesses of the anionic and cationic parts proceed similarly by approximately following a parabolic evolution, with a faster kinetics in the case of the cationic part.

Oxygen 18 tracer experiments have allowed the part of anionic growth to be confirmed and show that oxygen transport takes place through grain boundaries, which act as short-circuit diffusion paths.

This has led to the development of numerical model EKINOX (Evaluation of Kinetics Oxidation), which simulates the growth of an oxide layer through dry corrosion on a mesoscopic scale (a few µm), and explicitly takes into account atomic scale defects (vacancies), these defects controlling diffusion in volume of (metallic and ionic) chemical species [2].

This model helps determine the concentration profiles of the chemical species and the associated defect not only in the oxide, but also in the underlying metal. The oxide growth relies on the equation that expresses the shift of an interface under the fluxes received by it (Eq. 1). The latter are calculated through time integration of the Fick's law, numerically resolved in the space discretized in a volume element of constant concentration. Based on the material balance equation (Eq. 1), a numerical algorithm dealing with the motion of

6. Rutherford BackScattering (RBS) spectrometry consists in analyzing the energy of He^+ ions backscattered by a target sample. The energy losses undergone by the backscattered He^+ ion are specific of the nature of the nucleus on which the He^+ ion is collided. RBS spectra thus make it possible to rebuild the concentration profiles of the target sample. Analyzing depths allowed by this technique are of the order of a fraction of micrometer.

metal / oxide and oxide / gas interfaces makes it possible to reproduce cases of growth through cationic, anionic or mixed diffusion.

$$\frac{\partial \xi^{\Phi 1/\Phi 2}}{\partial t} = \frac{J^{\Phi 1} - J^{\Phi 2}}{{}^{eq}C^{\Phi 2} - {}^{eq}C^{\Phi 1}} \qquad \text{(Eq.1)}$$

where $\frac{\partial \xi^{\Phi 1/\Phi 2}}{\partial t}$ is time variation of the position of interface ζ between phases ϕ1 (metal or oxide) and ϕ2 (oxide and gas), $J^{\Phi i}$ is flux in phase ϕi received by the interface, and ${}^{eq}C^{\Phi i}$ equilibrium concentrations at the interface in phase ϕi.

The model's basic parameters (shape and size of oxide grains, anionic and cationic parts...) are experimentally adjusted on model materials, such as iron, by fine (SEM or TEM) characterization of the developed oxide layers (Fig. 139) [1].

These results will be used for parameterizing mechanistic models, among others, relating to dry corrosion of waste containers under long-term storage conditions. To reach this goal, the model has to be completed with a term for short-circuit diffusion. Besides, assessing the part of anionic growth at a lower temperature (< 200 °C) will help improve the model's parameterization within the temperature range involved in the dry corrosion phase under storage conditions. These different evolutions of the model are under development.

Last but not least, it is worth noting that, as shown by the most pessimistic assessment of the oxide layer expected over a 200-year period, the thickness expected as a result of dry corrosion (~100 µm max.) has not to be taken into account as a design basis parameter for the integrity of low-alloy steel waste package containers. As will be seen hereafter, corrosion in wet air may be faster.

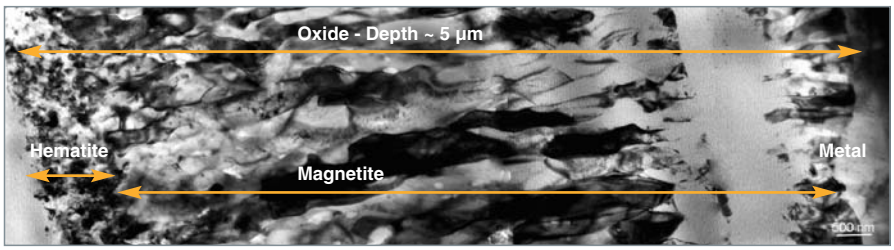

Fig. 139. Transmission Electron Microscopy (TEM) cross-sectional observation of an oxide layer formed on iron for 145 hours at 400 °C in dry air.
A small-grain zone consisting of hematite (Fe_2O_3) can be distinguished on the left.
The remaining part of the layer, made of columnar grains, consists of magnetite (Fe_3O_4).
(In collaboration with M.-C. Laffont, CIRIMAT, Toulouse).

Atmospheric corrosion

Atmospheric corrosion is an electrochemical interaction between a metallic material and oxygen in air in presence of a thin electrolyte (water) resulting from intermittent adsorption or condensation. So atmospheric corrosion is a corrosion of electrochemical type in which the electrolyte is the adsorbed or condensed water film.

Formation of the electrolyte film (just as its disappearance) depends on temperature variations and relative humidity. The latter lead to successive wet and dry periods named wetting-drying cycles. These cycles are an essential feature of atmospheric corrosion, and make its mechanisms deeply different from those of corrosion in aqueous solution.

In order to apprehend the characteristics of these cycles, it is first required and possible to describe the evolution of relative humidity on the container wall referring to the climatic data of the storage facility and the container properties (dimensions, volume mass, thermal conductivity...) and using a thermo-hydrodynamic model associated with a computer code (CASA) [3].

As a result, once relative humidity on the walls of a low-alloyed steel container is known, several approaches can be used to determine the thickness of corroded metal.

The first approach is of normative type, and complies with NF ISO (9223 and 9224) Standards which define the corrosiveness of an atmosphere as a function of three parameters: the duration during which relative humidity is higher than 80%, the sulfur dioxide content (SO_2), and the chloride ion content (Cl^-). The resulting corrosiveness can then help determine the thickness of corroded metal.

The second approach used is a semi-empirical method which makes it possible to apply the **behavior laws*** expressing corroded thickness as a function of time for various types of atmospheres (Fig. 140), under the following form:

$$P = kt^n$$

with P as corroded thickness (in µm), t as time (in years), k as corroded thickness after one year, and n as a factor characterizing the protective abilities of the corrosion products layer (generally within a range of 0.2-0.8). These laws can be adapted so that they may be expressed, no longer as a function of time, but as a function of wetting time, a more relevant parameter with respect to atmospheric corrosion:

$$P = k'\tau^n$$

where t is the normalized wetting time associated with the package walls.

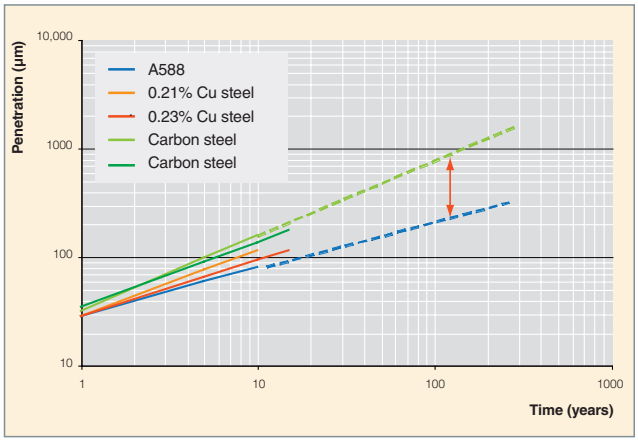

Fig.140. Evolution of corroded thickness for various low-alloy steels versus time, obtained with semi-empirical laws for rural atmospheres.

A mechanistic approach of atmospheric corrosion

The approaches previously described are empirical and rely on feedback (results of ageing over a maximum of twenty years, Fig. 140). They need to be corroborated on long timescales (hundreds of years), especially to take into account the corrosion rate dependence on the evolution over time, morphology and the structure of the rust layer formed [4].

With this aim was developed a third approach of a physico-chemical type, that describes the reactional mechanisms involved during a wetting-drying cycle (Fig. 141).

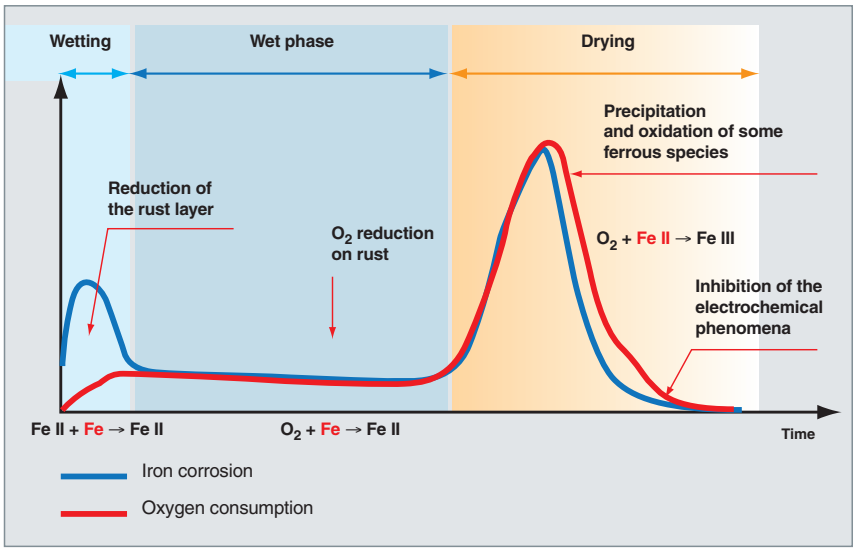

Fig. 141. Representation of iron corrosion and oxygen consumption rates during a wetting-drying cycle.

A cycle can be divided into three steps. The first one corresponds with the electrolyte formation. During this step, this is not oxygen, but the rust layer which through reduction enables iron to be oxidized. In the second step the thickness of the formed electrolyte is assumed to be constant, and then oxygen is the oxidant which entails metal oxidation. Last but not least, the film thickness decreases and oxygen re-oxidizes the rust that has been reduced during the first step.

For each step of the cycle it is possible to consider a limiting kinetic step and a related corroded thickness [5].

Thus, during the wetting step, the limiting step is assumed to be the reduction of lepidocrocite (the reducible phase of the rust layer). This reaction starts at the metal-oxide interface, then progresses towards the outer interface on the wall of the rust layer pores. During the period of wet phase, the kinetic limitation results from a mixed control between a step of oxygen diffusion in the electrolyte, then through the pores, and a step of reduction of this oxygen on the rust reduced during the first step.

Last but not least, during the drying step, the anodic reaction (iron oxidation) gets kinetically prevailing, and the corrosion process comes to an end as the aqueous phase vanishes.

Basing upon this mechanistic description, a model has been developed which takes into account the first two steps of the cycle and the onset of drying, and provides a thickness of corroded metal over several wetting-drying cycles.

Given the active participation of the rust layer to the corrosion process, the corroded thickness strongly depends on the properties (thickness, porosity, structure, morphology, electrochemical reactivity...) of these oxide layers, whose evolution over time can be apprehended as follows:

- On the one hand, by characterizing the layers issued from archaeological analogues (Fig. 142) which have undergone atmospheric corrosion under shelter;
- On the other hand, by climatic cell "ageing" of specimens of current (or archaeological) steels in order to determine an experimental corroded thickness as a function of a fixed number of wetting-drying cycles (Fig. 143).

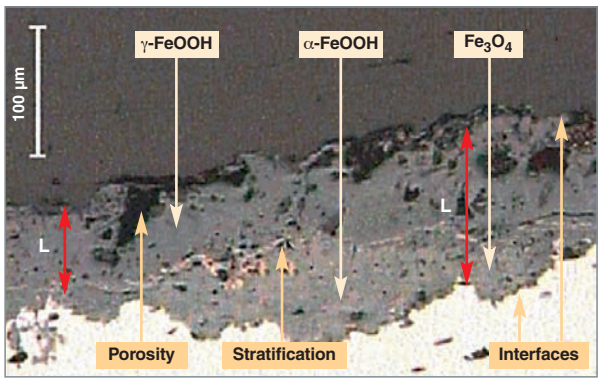

Fig. 142. Rust layer observed on an archaeological specimen: a metallic beam arising from the Popes' Palace in Avignon (800 years old).

Experimentally, for a specimen aged in a laboratory and initially displaying a rust layer of 150 µm, the corrosion rate is assessed to be about 0.2 µm.cycle^{-1} (Fig. 143), whereas the model brings about a value of an approximate 0.3 µm.cycle^{-1} under the same conditions.

This difference between the model and the experiment originates, in particular, in insufficient knowledge of the oxide layer characteristics and of their evolution over time. It confirms the importance of their role and of the need to take them into account for improving the model's parameterization: porosity (and its evolution over time), currently existing phases, their distribution across the layer, and their reactivity with respect to atmospheric corrosion. These data are under acquisition with the help of fine charaterization techniques (micro-Raman spectroscopy, synchrotron radiation-based X-ray-absorption analyses [µXANES]), as well as electrochemical methods. These data will be integrated into the model later on.

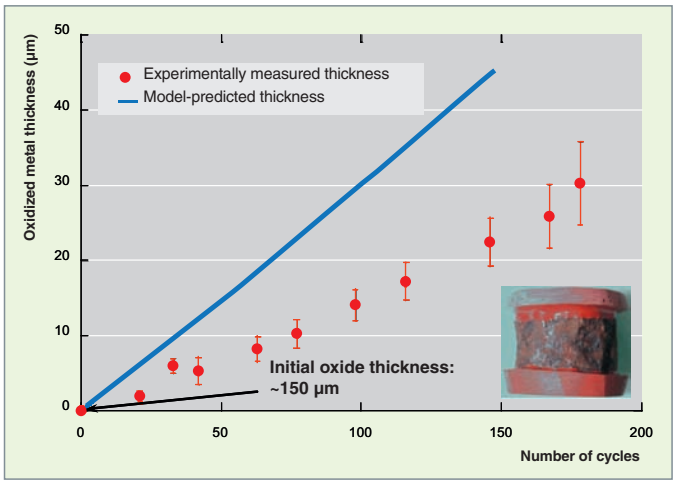

Fig. 143. Corroded metal thickness on specimens issued from Marly aqueduc (220 years old, with an initial rust layer of about 150 µm) versus the number of wetting-drying cycles achieved in a climatic cell. Comparison with the model.

As a conclusion, it may be noted that, starting from thermo-hydrodynamic models coupled with normative or semi-empirical approaches, a first estimate of consumed metal thicknesses leads to values ranging between 200 and 800 µm, depending on the selected environments (moisture, pollution...), following a 200 years' atmospheric corrosion.

These thicknesses, though corroborated by mechanistic modelling, remain low with respect to the wall thickness of a container.

Bitumen alteration

Bitumen is an organic matrix issued from oil distillation and used in particular for conditioning long-lived low-and-intermediate-level nuclear waste (**LILW-LL***). Its main advantages with respect to radioactivity containment are its high impermeability, chemical inertia, high incorporation rate, and easy industrial implementation.

Bituminized waste packages are industrially produced by radioactive sludge extrusion in La Hague and Marcoule workshops (see the DEN Monograph M5 "Nuclear Waste Conditioning"). This sludge is issued from coprecipitations of liquid effluents generated during the various steps of the spent nuclear fuel treatment process.

Extrusion, which is performed under hot conditions, consists in mixing sludge with bitumen in a liquefied state while ensuring sludge drying. Once the mixture cooled and solidified, it displays heterogeneities on the micrometer scale (Fig. 144), though looking homogeneous if observed with the naked eye. The bitumen matrix thus differs from other matrices such as glass matrix. In the first case, radioelements (RN) are precipitated under salt form and embedded in bitumen, whereas in the second case they are intimately incorporated into the glass network.

Embedded waste* industrially produced and poured into 220 L drums contain about 40 wt% salts as against 60 wt% bitumen. The major part of embedded salts arises from the reactants used during chemical treatments of radioelement insolubilization by coprecipitation. Concerning insoluble salts, they mostly are barium sulfate, ferrocyanides and cobalt sulfides, and, concerning soluble salts, sodium sulfate and sodium nitrate.

There exist various qualities of bitumen, which can be distinguished macroscopically by their rheological properties. Hence the need for a compromise between hot implementation conditions (a hard bitumen has to be extruded at a higher temperature) and radiolysis behavior conditions (a hard bitumen is less affected by swelling). In France, the selected bitumen is softer than that used in other producing countries (mainly, Belgium and Japan).

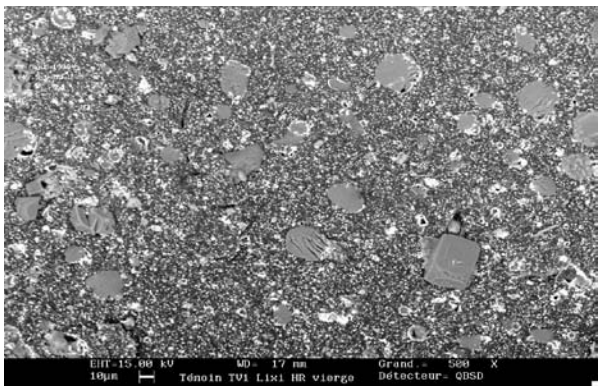

Fig.144."Environmental" SEM observation of a synthetic bituminized waste, representative of industrial embedded waste. Bitumen is shown as a dark grey background. Prevailing salts can be identified: sodium nitrate is displayed as light grey crystals of a few dozen micrometers, whereas barium sulfate occurs as small white dots (<1µm).

Today the bituminization process is less and less used. However, 70,000 drums currently exist, among which 60,000 produced and stored at Marcoule as early as the late 1960s, and 10,000 drums produced and stored at La Hague since the late eighties, which justifies carrying on studies on these packages.

Once packages have been produced and cooled, they are stored on production sites and periodically followed up pending their transfer to their disposal site. In these various situations, long-term behavior of bituminized packages is determined by two main phenomena: **radiolysis*** and **leaching***.

Radiolysis effect on bitumen alteration

Bitumen is a continuum of organic compounds, with a molar mass varying between 400 and 4000 g/mol, mostly unsaturated and polycyclic. This organic composition confers bitumen the property of emitting radiolytic gases, i.e. hydrogen for the very most part, as an effect of self-irradiation. These gases are issued from the breaking of the existing C-H bonds.

Depending on the incorporated activity, a drum generates 1-10 L of radiolytic gas per year during the first hundred years following its generation. As a result of radioactive decay, the source term gas gets lower than one liter per year after one thousand years. The volume cumulated over one thousand years is approximately one cubic meter per drum.

Swelling bitumens

The gases generated in the whole volume of the embedded waste are solubilized in the matrix up to saturation (1-5% in volume). Beyond this level gas bag nucleation is allowed and, as a second step, bubble growth can induce swelling of embedded waste. Some packages have displayed a swelling rate of about 1 centimeter per year.

In some cases (e.g. packages manufactured with no apical void), swelling evolution can cause embedded waste to overflow its container, or even induce a pressurization. This overflow does not fundamentally question bitumen confining properties, but may require new conditioning to avoid any mechanical degradation of containers.

Swelling kinetics follows a bell-shaped curve, with a maximum reached within a few dozen years following generation (Fig. 145), as a result of competition between radiolytic gas buildup (RN source term), and their release through various transport mechanisms.

Upward migration of gas bubbles, of a lower density than embedded waste, results in limited swelling. It is all the more efficient as bubbles are voluminous, and embedded waste viscosity is lower. As for diffusion / permeation, it contributes to the release of about 1 L/year of gas.

These various mechanisms have been experimentally evidenced on inactive synthetic embedded waste in which self-irradiation was simulated by outer irradiation, and on active embedded waste used for validation. A direct experimentation consists, for a controlled irradiation, in correlating gas generation (through sampling and dosing) with swelling (X radiography). Gas solubility in the embedded waste, bitumen surface tension, viscosity, and gas diffusion coefficients (of about 10^{-11} m^2/s) are also determined experimentally. The whole of phenomenologies and experimental data are implemented in a computational code, JACOB2, which enables swelling evolution to be determined over time (Fig. 145).

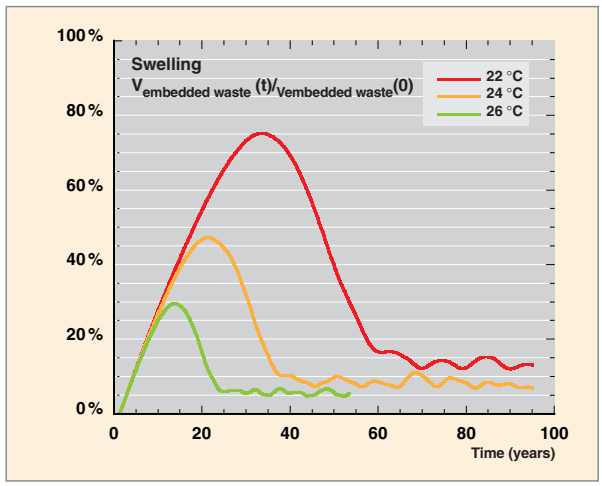

Fig. 145. Temperature dependence of swelling kinetics in a reference bituminized waste. Temperature has an influence on bituminized waste viscosity, and so impacts on the ability to give off radiolytic gases through upwards migration of the formed bubbles.

For instance, using the JACOB2 code can help optimize bituminized pakage fabrication parameters so as to control swelling (drum partial filling, limits of intake (activity), chemical trapping of radiolytic gases in the package's first years of lifetime…).

Adding a cobalt sulfide-based dopant, for example, is aimed at *in situ* oxidizing the hydrogen generated and inhibiting its pile-up in the embedded waste for a given time [6]. No swelling is then expected over the effective period of trapping, and the swelling amplitude can be decreased thanks to decay of the hydrogen source term.

*The role of **leaching*** in bitumen alteration* [7,8]

Although pure bitumen is of very low permeability to water and dissolved species, initially occurring salts favor water uptake through diffusion and osmosis. On contact with water inside the embedded waste, the most soluble salts are locally dissolved. Formation of salt solution bags results in development of porosity, which makes diffusion easier from dissolved species to the outer leachant.

Kinetics of water uptake and release of the most soluble salts follow square-root-of-time laws, typical of a given diffusion mechanism. Such kinetics are mainly controlled by the contents and solubilities of the various salt species embedded, on the hand, and leaching solution activity, on the other hand (Fig. 146). For increase in leaching solution activity, which is chiefly controlled by sodium nitrate concentration, generates an increase in water uptake and soluble salt release kinetics.

It is worth noting that, for a given alteration time, water uptake is about 100 times faster than the release of the most soluble salts, which is to be related to the values of the effective diffusion coefficients experimentally determined, of about 10^{-13} m²/s regarding water, and about 10^{-15} m²/s on the average regarding salts dissolved in water. This difference entails swelling of embedded waste due to the aging of the porous area and the leaching front progress (Fig. 147). The depth of the soluble salt dissolution front (which so materializes the thickness of actually degraded material) thus progresses through the embedded waste following a square-root-of-time law (approx. a few mm/year$^{1/2}$).

The whole set of experimental data obtained for a wide variety of boundary conditions (leaching under renewed or stagnant liquid water, pure water or water representative of a clay or cementitious environment, alteration by air moisture) was integrated into the operational code COLONBO, which conservatively determines material transfers between an embedded waste under leaching, its disposal package and the engineered barrier through a chemistry-transport coupling.

Last but not least, these investigations were performed taking as a reference the release of tracer salts of high solubility, such as sodium nitrate. Tests on active embedded waste have corroborated the conservative feature of this approach, since it was shown that radionuclide release rates are lower than those of tracer salts by two or four orders of magnitude.

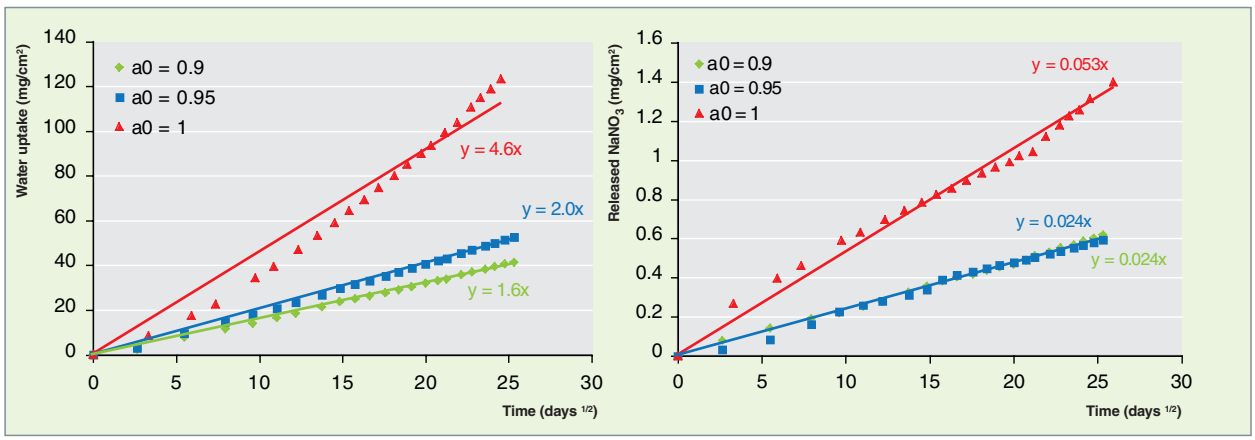

Fig. 146. Experimental kinetics of water uptake and salt release during the leaching of a synthetic bituminized waste versus square root of time, and for three activity conditions of the periodically renewed leachant.

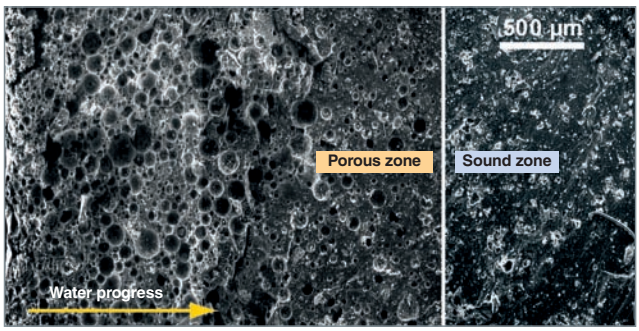

Fig. 147. "Environmental" SEM cross-sectional observation of a synthetic bituminized waste, altered for one year in a periodically renewed pure water. The dark craters, more numerous at the top of the embedded waste, highlight the salt solution bags resulting from water uptake. The white dots ocurring mainly in the lower part are dry salts, unreached by water by this date.

Robust operational predictions of bitumen alteration

Predicting the long-term behavior of confining materials (gas or RN source terms in the case under consideration) assumes an iterative coupling between experiments and numerical simulations, that can be divided into four steps: identification of prevailing mechanisms, phenomenological modelling, numerical simulation, experiment validation.

The robustness of this approach first lies in the selection of the most unfavorable alteration conditions for the material, chosen to be conservative and reasonably representative of evolution conditions. Then, as a second step, mechanisms and phenomenological couplings are refined in order to reduce margins (representativity gain) or extend the scope of prediction.

For example, coupling between radiolytic effects and leaching, which was dropped owing to sufficiently distinct characteristic times, is currently re-examined with a view to better representing the impact of matrix ageing on long-term evolution of its rheological and material transport properties (porosity-transport coupling).

Similarly, as finite expansion volumes (container, disposal package, engineered or geological barrier) potentially reached under radiolytic and leaching conditions are taken into account, the swelling pressures, the mechanical strength of the package and its environment, and the volume constraint feedback on gas source terms or leaching then emerge as new investigation fields [9]…

Reinforced concrete behavior and reinforcement corrosion

Reinforced concrete is one of the structural materials most widely used in the industry. It is the constitutive material of the containment systems of nuclear reactors and of the latter's atmospheric heat exchangers. It is also used for nuclear waste conditioning (see the DEN Monograph M5 "Nuclear Waste Conditioning"), with reinforced concrete structures playing a role not only in mechanical behavior, but also, in some cases, in radionuclide **containment***. This requires concretes able to keep their integrity over long timescales. Hence the need to study this type of material so that its degradation may be more easily predicted and, so, hindered.

The low-alloy steel is used as a material for concrete reinforcement, for it is in a passive state when the embedding material (concrete) has not been degraded. Yet, when the structure is exposed to the atmosphere, carbon dioxide reacts to be dissolved into an alkaline solution according to the following reaction:

$$CO_2(g) + 2\ OH^- \leftrightarrow CO_3^{2-} + H_2O$$

This reaction entails a physico-chemical evolution of concrete through calcium carbonate precipitation from portlandite, a constituent of the material.

In order to simulate the phenomenon, the atmospheric carbonation model implanted in the Cast3m code considers concrete as consisting of three phases - one solid (cement hydrates), one liquid (interstitial water), and another gaseous (CO_2) –: at the interfaces of these phases take place chemical reactions of dissolution, precipitation, vaporization and liquefaction associated with (water, CO_2) transport and microstructural evolution phenomena [10]. Simulations are relatively in good agreement with experimental results. Yet, validation efforts have to be undertaken in relation to carbonation in natural environments.

First extrapolations over periods of hundreds of years provide, for 300 years, carbonate thickness values of 10^{-30} mm on the average for a 15% porosity concrete (Fig. 148). It will be observed that these values are lower than the standardized embedding thickness of reinforcing bars in a reinforced concrete (40 mm).

Carbonation particularly induces a pH decrease in the concrete interstitial solution to values for which steel reinforced bars are no longer passive. This is then the so-called "corrosion in the active state". The effects of this reinforcement corrosion is of two kinds for the reinforced concrete work (Fig. 149):

- On the one hand, the formation of a layer of oxides more voluminous than initial steel will be likely to induce concrete

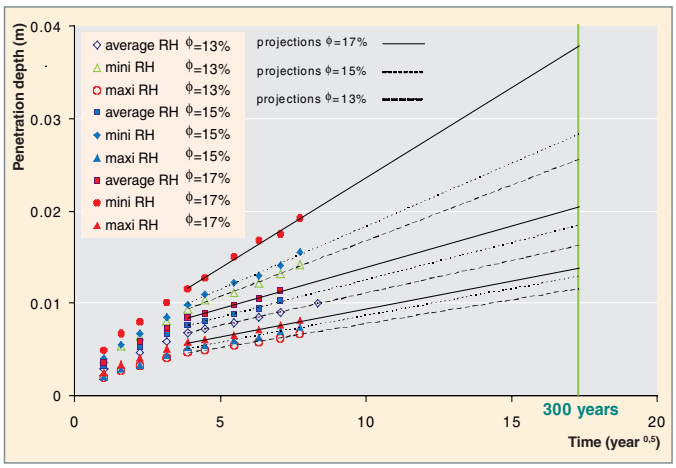

Fig. 148. Evolution of the calcite penetration depth versus time for concretes of variable porosities (13, 15, and 17%) and for different relative humidities (RH = 70, 75, and 80%). Projection over 300 years (linear regression analysis versus square root of time).

cracking, or even bursting. Under such conditions concrete transport and containment properties are altered.

- On the other hand, reduction in the cross-sectional area of reinforcing bars during the corrosion process results in a decrease in the structure's bearing capacity. Consequently, the work's lifetime is reduced.

As a "civil engineering" type approach, mainly based on a semi-empirical ("state-of-the-art") approach, does not enable long-term behavior to be satisfactorily predicted; a R&D program has been launched on the CEA's initiative, with the wish that it may welcome contributions of industrial partners and of the scientific community involved in the field (EDF and ANDRA, LMT-Cachan[7], LMDC Toulouse[8], CEBTP[9], LCPC[10], LRMH[11]…).

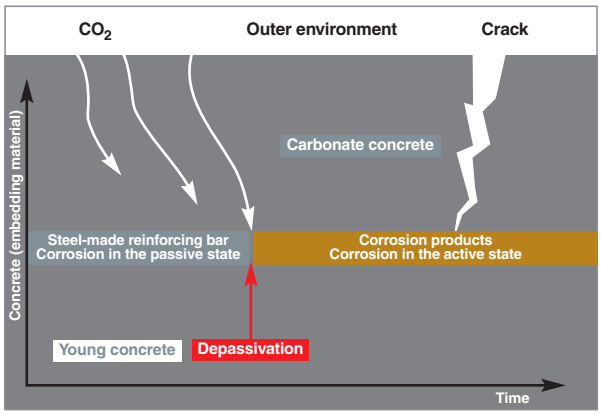

Fig. 149. Schematic diagram of evolution over time of the metal / concrete interface during the reinforcement corrosion process.

This program aims at investigating and modelling in the long term (hundreds of years) interactions between cementitious and metallic materials (CIMETAL: (matériaux) CIMentaires et METALliques) under atmospheric conditions as well as their impact upon the material's mechanical resistance (cracking, bearing capacity…). A micro-macro type of approach is used to set up a coupled model that takes into account aggressive agent transport through the cementitious environment, reinforcement corrosion mechanisms, and damage of embedding material (concrete) up to the works' residual bearing capacity. [11]. A few recent advances of the program are highlighted hereunder.

Phenomenology of reinforced concrete corrosion

On the microscopic scale - the so-called "scale of the material's microstructure"-, understanding concrete degradation phenomena and reinforcement corrosion is based upon quite a number of experimental data acquisitions on laboratory samples (pastes, reinforced concretes, reinforced bars considered separately…) or on ancient / archaelogical analogues, i.e. ancient irons embedded in binders aged 50 to over 600 years (ranging from the Saclay's water tower to the Popes' Palace in Avignon !...). Laboratory investigations are aimed at accelerating corrosion phenomena and studying the separate influence of well-controlled physico-chemical parameters (pH, chemical composition of the solution, redox potential…). Observations are carried out through a broad range of analytical techniques, among which some cutting-edge techniques (optical microscopy, dispersive-energy spectrometry coupled with scanning electron microscopy, mercury porosimetry, X diffraction and micro-diffraction…).

The pattern of the metal / concrete interface is always the same, irrespective of the age and origin of the samples, the nature of reinforcing bars (microstructure, inclusions), and that of binders (morphology, porosity, chemical composition), with a succession of four areas (Fig. 150 and 151) [12]:

- Metal;
- Dense (corrosion) products layer, mainly consisting of iron oxides and oxi-hydroxides;
- Transformed medium, in which iron has diffused from the metal into the cementitious material
- Binder.

7. LMT-Cachan: *Laboratoire de Mécanique et Technologie de l'ENS Cachan*, French ENS Cachan's Laboratory of Mechanics and Technology.
8. LMDC-Toulouse: *Laboratoire Matériaux et Durabilité des Constructions*, French Laboratory for Materials and Durability of Constructions.
9. CEBTP: *Centre d'Expertise du Bâtiment et des Travaux Publics*, French Center of Expertise for Building and Public Works.
10. LCPC: *Laboratoire Central des Ponts et Chaussées*, French Central Laboratory for Roads and Bridges.
11. LRMH: *Laboratoire de Recherche sur les Monuments Historiques*, French Historic Monuments Research Laboratory.

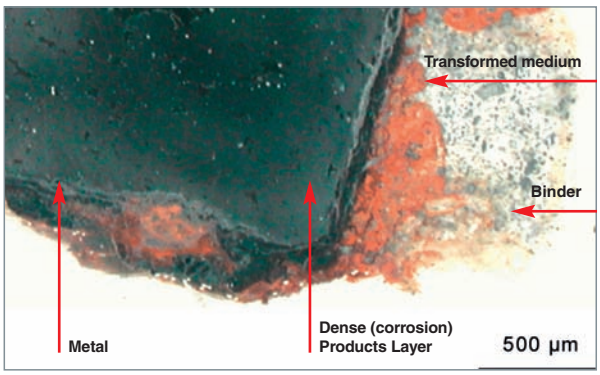

Fig. 150. Macrograph of a sample of ancient iron embedded into a cementitious material (Saint-Gervais Church, Paris, 350 years old) [12].

The thickness of the "dense (corrosion) products layer" varies from a few dozen micrometers for the most recent samples, to several millimeters for, e.g., the *Popes' Palace* in Avignon, which is 650 years old. Similarly, the "transformed medium" thickness increases with the sample age, from a hundred micrometers to several millimeters. The average corrosion rates determined from measured mass losses are lower than 8 µm/year.

Moreover, the evolution of this metal/hydraulic binder interface is very sensitive to the species occurring in the environment [13], and especially to the chemical composition of the interstitial solution, the latter depending on the cementitious material composition. For example, for a same pH value of the solution (equal to 8.3 in this example), in presence or not of silicates (arising from the dissolution, if any, of the cementitious material's hydrate calcium silicates), the average corrosion rates measured using mass losses may vary by a factor 2.

Concrete used as an embedding material around the reinforcement acts as a transport barrier for oxygen, which is the oxidizing agent of the corrosion reaction. Oxygen diffusion through the pores in a liquid or gaseous phase is directly connected with the saturation degree of the cementitious material. A concrete drying / reinforcement corrosion coupled model [14] could thus be proposed, thereby enabling to describe and predict reinforcement corrosion as a function of concrete's saturation degree. The equation governing the corrosion rate (proportional to the oxygen flux consumed) is then as follows:

$$j_{O_2} = \frac{c_{O_2}}{\frac{1}{k\phi S_r} + \frac{e_{CPD}}{D_{O_2,DPL}(t)} + \frac{e_{MT}}{D_{O_2,TM}(t)} + \frac{e_{Concrete}}{D_{O_2,Concrete}(t)}}$$

With k: the kinetic constant of oxygen reduction [m/s], ϕ: the porosity of the dense (corrosion) products layer (DPL), S_r: the DPL's saturation degree, e_{DPL}, e_{TM} and $e_{Concrete}$: the respective thicknessess of DPL, transformed medium and concrete [m], CO_2: the oxygen content of the atmosphere [mol/m3], $D_{O2,DPL}$, $D_{O2,TM}$ and D_{O2},Concrete: the effective diffusion coefficient respectively in DPL, transformed medium and concrete [m²/s].

The oxygen diffusion coefficient in the cementitious material evolves according to [15]:

$$D_{O_2,Concrete}(t) = a(1 - HR(t))^b$$

Where a [m²/s] and b are two parameters obtained from experimental curves, depending on the cementitious material's nature and the concrete's water / cement ratio.

The evolution of relative humidity (RH) over time is determined using a concrete drying model.

It is then possible to assess the thickening of the corrosion products layer as a function of the age of the object.

Effect of reinforcement corrosion: mechanical damage in reinforced concretes

Cracking in the embedding material results from strains imposed by increased volume of corrosion products at the metal/concrete interface. Its modelling requires to describe the kinetics of these strains and their influence on the mechanical behavior of the composite (steel, corroded layer, concrete).

The damage model CORDOBA (an acronym standing for *CORrosion et enDOmmagement du Béton Armé*: corrosion and damaging of reinforced concrete) has been developed using the CEA's finite element software CAST3M, and gives access to cracking pattern of reinforced concrete objects as well as to the corresponding crack initiation kinetics.

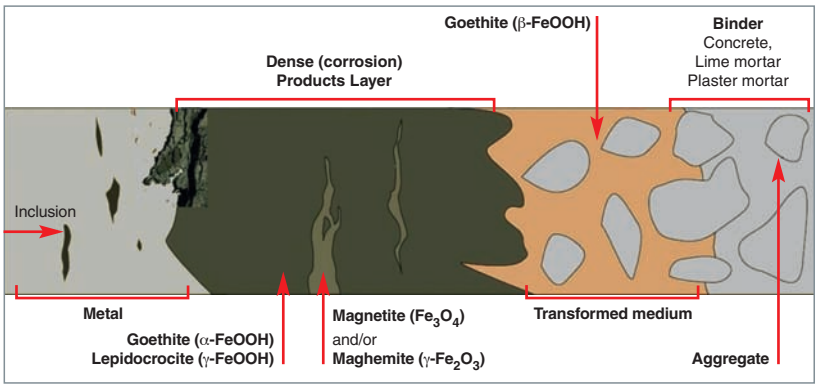

Fig. 151. Schematic representation of the metal / cementitious material interface [12].

The corrosion layer is modelled using interface elements placed between steel and concrete, whose evolution of thickness over time is described referring to its mechanical properties (normal and tangential to the reinforcement) according to the following equations:

$$k_n(t) = \frac{E}{e_{DPL}(t)} \quad \text{and} \quad k_t(t) = \frac{E}{2(1+\upsilon)\times e_{DPL}(t)}$$

where k is the stiffness of the interfacing element, E is the Young's modulus of the Dense (corrosion) Products Layer (DPL) (in GPa), ν is the Poisson coefficient of this layer, and $e_{DPL}(t)$ is DPL thickening over time (cf. previous chapter).

CORDOBA has been recently tested [16] during laboratory tests on beams subjected to accelerated degradations (Fig. 152) as well as by confronting concrete damage predictions with visible cracks on an old building (Perret's water tower at CEA Saclay).

The various alteration processes of reinforced concretes can thus be hierarchized as investigations are proceeding, according to their influence on reinforced concrete works lifetime. For example:

- The evolution of concrete saturation degree has a major impact on corrosion kinetics: a reinforced concrete which undergoes wetting/drying cycles will be damaged faster than the same object put under constant moisture conditions;
- The chemical composition of the cementitious material plays a prevailing role: it is worth mentioning the case of silicates which display an inhibiting effect with respect to corrosion;
- From the mechanical viewpoint, positioning of reinforcement in the work is strategic for its lifetime (spacing between reinforcing bars, bar diameter…).

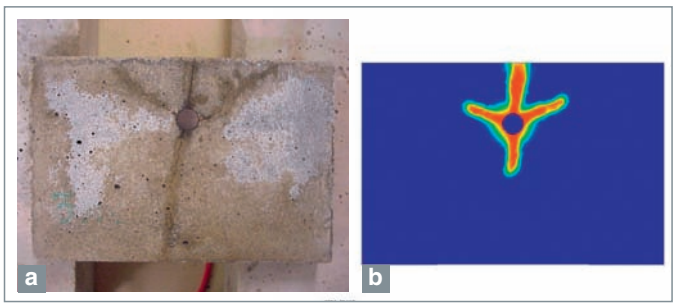

Fig. 152. Comparison of observed and simulated cracking facies:
a) Crack pattern of a reinforced concrete beam that has undergone accelerated corrosion as a result of applying an electric current to the reinforcement.
b) Crack pattern predicted using the CORDOBA model [7].

Concrete behavior in a severe thermal environment

In storage facilities, concretes are likely to be used for galleries, vaults, pits or slabs. These works or structures made out of concrete are designed, first, to attenuate radiation arising from waste and, secondly, to withstand more or less severe thermal loadings different from those usually considered in conventional civil engineering, e.g. for fire resistance (lower amplitude, but longer duration).

There is a need to check that concrete structure integrity and durability will not be affected by these thermal stresses, especially on a timescale of centuries. In a thermal atmosphere, disorders observed in concretes have either a thermo-mechanical origin (effect of temperature gradients), or a thermo-hydric origin (internal vapor pressure). They may occur either on the microscopic scale (cement paste scale), or on the material's scale, or again on the structure's scale. The effects under consideration are thus of the Thermo-Hydro-Mechanical (THM) type with strong coupling of the phenomena involved (drying, vaporization, shrinkage, contraction, dilation, cracking, microstructural evolution...).

In order to possess a tool for predicting the coupled THM behavior of concrete structures / works, there is a requirement:

- To experimentally acquire THM input data values for models, and identify design basis parameters and property evolution with temperature;
- To develop predictive phenomenological models;
- To carry out experimental validations both on the material's scale (in terms of hypotheses) and on the scale of metric structures (tests on mock-ups) representative of works [17].

In terms of thermal environment, a design basis parameter of 80 °C (complying with standards) has been retained, but more extended ranges (60-450 °C) are being explored on the laboratory scale so as to assess non-nominal margins and situations.

Reinforced concrete behavior under temperature on the material's scale

The mechanical properties of concretes vary with temperature: between 20 °C and 200-250 °C, it can be observed a monotonous decreasing evolution of compressive and tensile strength, of the elastic modulus and of the Poisson coefficient. Thermal cycling and heating kinetics (0.1 – 10 °C/min) [20] influence the residual THM properties of concretes only marginally (Fig. 153).

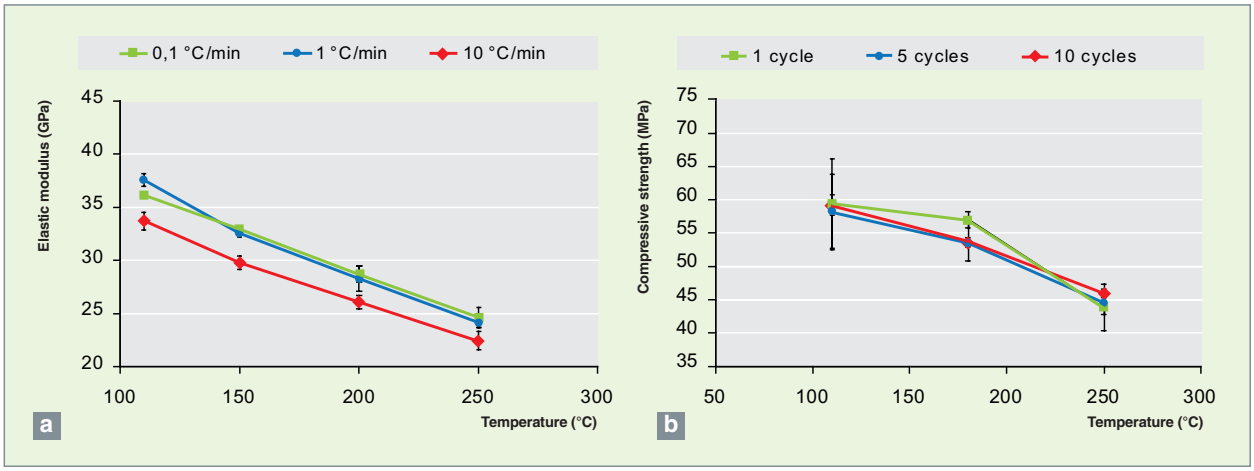

Fig. 153. Evolution of the mechanical residual properties of the standard,"high-performance" concrete after heat treatment at 250 °C, a) Effect of the temperature rise kinetics, b) Effect of cyclic thermal loadings.

The impact of the type of aggregates has also been explored, as well as the effect relating to materials hydric state [17]. Up to 250 °C, a limestone-aggregate-based concrete and a silica-limestone-aggregate-based concrete exhibit very similar damages. In contrast, at 450 °C, the severest overall damage is displayed by the latter.

On the other hand, from 250 °C, the damage undergone by a standard "High-Performance" Concrete (HPC) is quite more significant, showing cracks with an opening of a few dozen µm.

Thermal behavior of reinforced concrete on the structural scale

Various tests on a representative (metric) scale were carried out in order to investigate reinforced concrete behavior under thermal stresses. It is worth mentioning Tests BETHY I and II (dedicated to the study of heating kinetics impact), SESBI tests (dedicated to investigating hydro-mechanical effects) and the tests performed in the MAQBETH Mock-up (devoted to studying the effect of a high temperature gradient) (Fig.154). The latter is an annular structure made out of "High-Performance" reinforced Concrete (HPC) - 66 MPa - of 25 tons, 3 m high, 2.20 m diameter, and 60 cm thick (Fig. 154). It was instrumented with different types of sensors (about 120 sensors on the whole): thermocouples, gas pressure sensors and relative humidity sensors, strain gages and LVDT sensors (Fig. 155) [18].

The MAQBETH test was performed with a high temperature gradient (≈ 230 °C/m) and a heating kinetics of about 0.1 °C/min. It revealed that under such conditions cracking may occur rather early during the thermal transient (< 24 h), and that it strongly conditions water transfers through concrete (hydro-mechanical coupling) under liquid and gaseous form. Yet, this craking does not induce significant effects on the overall mechanics of the structure. Besides, interstitial pore pressures (gas pressure) of about 0.1 MPa could be observed at the frontier of the saturated area at the 200 °C temperature stage. These pressures are sufficiently high to have to be considered in modelling.

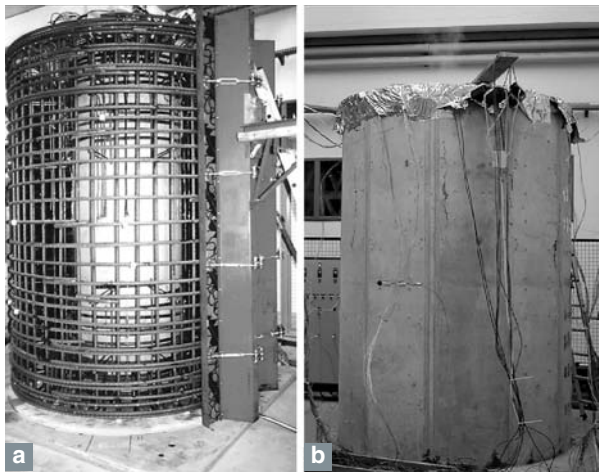

Fig. 154. View of the MAQBETH Mockup dedicated to studying reinforced concrete alteration:
a) Reinforcement of the structure, b) Device under testing.

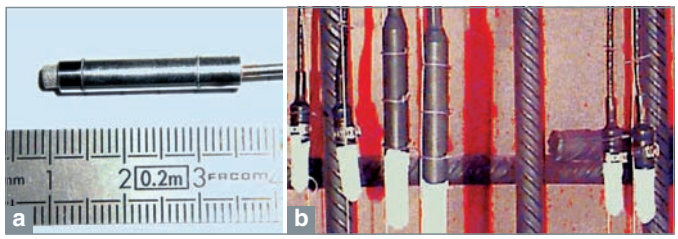

Fig. 155. Instrumentation devices of MAQBETH test:
a) Interstitial pressure sensor,
b) Distribution of the hygrometric probes along the reinforcement.

Simulation and prediction of the thermo-hydro-mechanical behavior of reinforced concretes

Thanks to test case calculations based on these mock-up tests, it was possible to make sure of the reliability of the response level of modelling and simulation tools, to identify and confirm the design basis parameters (effect of temperature gradients, influence of cracking on transport, and of hydric transfers on drying phenomena), and to assess operational margins.

The various works performed - experimental works and development of modelling and simulation tools under the Cast3m code (Thermo-Hydric Model HYDR, Drucker-Prager (DP-II) plasticity thermo-mechanical model, hydro-mechanical approach) have led to a simplified Thermo-Hydro-Mechanical (or simplified THM) model tailored to concrete behavior simulation at temperatures lower than 250 °C [19].

The simplified THM model is based upon a mechanical-type approach of unsaturated porous media, and also relies on reference works dealing with both materials and modelling [20, 21].

This model is simplified in the meaning that, in the assumption it relies on the gaseous phase only consists of water vapor, dry air being disregarded (this is the so-called one "pressure field model"). It is based upon liquid water and vapor mass conservation equations, energy conservation equation (heat equation), and a Bishop-type equation in relation to mechanical behavior. Equations are solved by the finite-element method with Cast3m, using an implicit time integration scheme and an iterative resolution method (save for the mechanical equation related to elastic behavior). This model has been recently improved by introducing concrete cracking through a mechanical approach to damage [19].

The simplified THM model has already undergone validation exercises (without adjustment) based on various heating tests (between 100 and 250 °C, with kinetics ranging from 0.1 to 10 °C/min) performed on concrete and reinforced concrete (instrumented) structures on various scales – e.g. test on a 16 x 32 (cm) cylindrical specimen, or the so-called "pressure test", or tests on the scale of metric structures as in Tests BETHY and MAQBETH – (Fig. 156). Simulations are globally in good agreement with experimental data, which demonstrates the robustness of the simplified THM model integrating damage.

From a scientific viewpoint, a great deal of knowledge and new data has been acquired in relation with concrete behavior under thermal environment, regarding both the evolution of the material and its properties with temperature and the development of simulation tools based on physical models and validated on various scales.

From an operational viewpoint, it has been shown that when a "high-performance" concrete has been subjected to a 80 °C thermal stress on a significant duration, initial care in the material's design and selection can ensure its functions on a one-hundred-year scale.

Ongoing R&D works are especially oriented to taking into account thermal creep mechanism (delayed strains) and acquiring the basic data still lacking (isotherms, cracking impact on transport coefficients...). In addition, as regards full-scale works, a technological demonstration and test tool for models (likely to enable their predictive character to be assessed) is provided by the long time (> 1 year) heating test at 80 °C, on the vault of Marcoule's GALATEE gallery, in which time monitoring is ensured through the instrumentation inserted during construction.

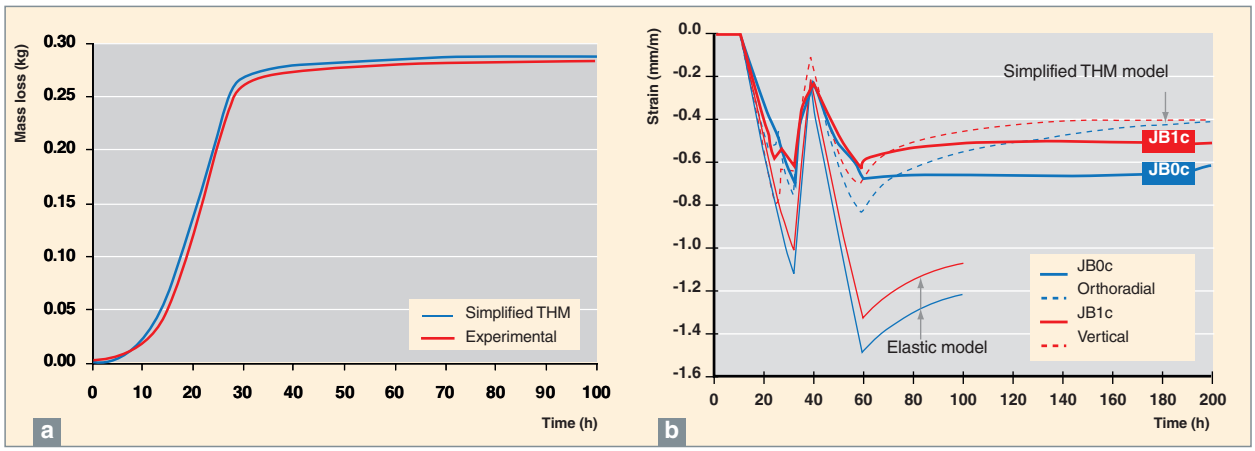

Fig. 156. Examples of validation exercises of the Simplified Thermo-Hydro-Mechanical (or simplified THM) model, in which damage is taken into account:
a) Mass loss of a 16 x 32 cm concrete specimen due to free water outflow and dehydration of solid phases [22];
b) Vertical and orthoradial mechanical strains in the median plane of the MAQBETH mockup. The sharp variations in strains result from temperature growth: it decreases from 150 to 75 °C between 31 and 39 h, and then increases again up to 200 °C after 60 h [23].

It is worth mentioning that these acquired phenomenological knowledge and expertise as well as the models and approach developed in this context may be extended to other issues relating to concrete behavior in temperature (fire resistance of concretes, oil drillings).

References

[1] C. Degranges, N. Bertrand, K. Abbas, D. Monceau and D. Poquillon, *Mat. Sci. Forum*, 461-464 (2004), p. 481.

[2] N. Bertrand, C. Desgranges, D. Gauvain, D. Monceau and D. Poquillon, *Mat. Sci. Forum*, 461-464 (2004), p. 591.

[3] M. Baklouti, N. Midoux, F. Mazaudier and D. Féron, "Estimation of the atmospheric corrosion on metal containers in industrial waste disposal", *Journal of hazardous materials*, 85, 3 (2001), p. 273.

[4] P. Dillmann, F. Mazaudier and S. Hoerlé, "Advances in understanding atmospheric corrosion of iron. I. Rust characterisation of ancient ferrous artefacts exposed to indoor atmospheric corrosion", *Corrosion science*, 46 (2004), pp. 1401-1429.

[5] L. Maréchal, S. Perrin, P. Dillmann and G. Santarini, "Study of the atmospheric corrosion of iron by ageing historical artefacts and contemporary low-alloy steel in a climatic chamber: comparison with mechanistic modelling", in "Corrosion of metallic heritage artefact, Investigation, conservation and prediction for long term behaviour", *EFC Series*, n°48, 2007, pp. 131-151.

[6] S. Camaro, Q. Ragetly, C. Riglet-Martial, "*Composé piégeur de l'hydrogène, procédé de fabrication et utilisation*", Patent 2, 859, p. 202 (2003).

[7] J. Sercombe, B. Gwinner, C. Tiffreau, B. Simondi-Teisseire and F. Adenot, "Modelling of bituminized radioactive waste leaching. Part I: Constitutive equations", *Journal of Nuclear Materials*, 349 (2006), pp. 96-106.

[8] B. Gwinner, J. Sercombe, C. Tiffreau, B. Simondi-Teisseire, I. Felines and F. Adenot, "Modelling of bituminized radioactive waste leaching. Part II: Experimental validation" *Journal of Nuclear Materials*, 349 (2006), pp. 107-118.

[9] X. Lefebvre, J. Sercombe, A. Ledieu, B. Gwinner and F. Adenot, "Bituminized waste leaching in restricted and free swelling conditions: Mechanisms and analytical modelling", *Mat. Res. Soc. Symp. Proc.*, Vol. 932 (2006).

[10] B. Bary and A. Sellier, "Coupled moisture-carbon dioxide-calcium transfer model for carbonation of concrete", *Cement and Concrete Research*, 34 (2004), pp. 1859-1872.

[11] V. L'Hostis (sous la dir. de), "*Benchmark des poutres de la Rance – Diagnostic et modélisation mécanique des poutres en béton armé et précontraint atteintes par la corrosion des aciers*", Numéro spécial de la Revue Européenne de Génie Civil, Vol. 1-2 (janvier 2007).

[12] W.J. Chitty, P. Dillmann, V. L'Hostis and C. Lombard, "Long term corrosion resistance of metallic reinforcements in concretes – A study of corrosion mechanisms based on archaeological artefacts", *Corrosion Science*, 47 (2005), pp. 1555-1581.

[13] B. Huet, V. L'Hostis, F. Miserque and H. Idrissi, "Electrochemical behaviour of mild steel in concrete: influence of pH and carbonate content of concrete pore solution", *Electrochimica Acta*, 51 (2005), pp. 172-180.

[14] B. Huet, V. L'Hostis, G. Santarini, D. Féron and H. Idrissi, "Steel corrosion in concrete: determinist modelling of cathodic reaction as a function of water saturation degree", *Corrosion Science*, Vol. 49, pp. 1918-1932 (2007).

[15] V.G. Papadakis, C.G. Vayenas and M.N. Fardis, "Durability of building materials and components", 1991: Baker, J.M. and Nixon, P.J. and Majumdar, A.J. and Davies, H Eds.

[16] Q.T. Nguyen, S. Care, A. Millard and Y. Berthaud, "*Analyse de la fissuration du béton armé en corrosion accélérée*", Comptes rendus Mécanique, Vol. 335, pp. 99-104 (2007).

[17] C. Gallé and J. Sercombe, "Permeability and pore structure evolution of silico-calcareous and hematite high-strength concretes submitted to high temperatures", *Materials and Structures*, 34 (2001), pp. 619-628.

[18] G. Ranc, "*Comportement des bétons à haute température*", Revue française de Génie Civil, 7 (2003), pp. 397-424.

[19] B. Bary, S. Durand, G. Ranc and O. Carpentier, "A coupled thermo-hydro-mechanical model for concrete subjected to moderate temperatures", *International Journal of Heat and Mass Transfer*, 51 (2008), pp. 2847-2862.

[20] Z.P. Bazant and M. Kaplan, "Concrete at high temperatures. Materials properties and mathematical models", Longman Group limited, Harlow, 1996.

[21] R. Lewis and B. A. Schrefler, "The finite element method in the static and dynamic deformation and consolidation of porous media", John Wiley & sons, New York, 1998.

[22] M.V.G. de Morais, B. Bary, G. Ranc, S. Dal Pont and S. Durand, "Comparative analysis of coupled thermo-hydro-mechanical models for concrete exposed to moderate temperatures, Numerical Heat Transfer", Part A: Applications 55 (7) (2009), pp. 654-682.

[23] M.V.G. de Morais, B. Bary, G. Ranc, S. Durand and A. Courtois, "Simulations of the thermo-hydro-mechanical behavior of an annular reinforced concrete structure heated up to 200 °C", *GeoProc*, 08, Lille, France, 2008.

Bibliography

Monceau (D.) and Poquillion (D.), *Oxydation des matériaux métalliques* (Eds AM Huntz-Aubriot and B Pieraggi), Hermes science publication, Lavoisier, Paris (2003), pp.165-166.

Benoît Bary, Nathalie Bertrand, Clara Desgranges, Christophe Gallé, Valérie L'Hostis, Laurent Maréchal, Stéphane Perrin, Stéphane Poyet, Cécile Richet,
Physico-Chemistry Department

Christophe Joussot-Dubien, Aurélien Ledieu,
Research Department for Waste Treatment and Conditioning

Christophe Tiffreau,
Nuclear Technology Department

and Alain Millard,
Systems and Structures Modelling Department

Corrosion in an Aqueous Saturated Environment

The underground disposal under consideration for long-term management of radioactive waste implements several successive barriers intended to prevent radionuclide release into the biosphere, or at least to delay it sufficiently so that radioactive decay can take place. The outcome of waste packages, and the release of the radionuclides they contain, will deeply depend on the alteration of these various barriers and of their constitutive materials: cement and glass for their containment matrices, metal for their containers and overcontainers, and (possibly) clay for the engineered barrier. The alteration phenomena of these materials have to be investigated, controlled and scheduled in the long run. The disposal facility will be most presumably located far below the groundwater table: waste packages will be placed there in a water-saturated porous environment. This situation will determine their long-term behavior: the alteration phenomena that will take place, are different from the phenomena involved in an unsaturated environment as mentioned in the previous chapter, on account of the specific features of the water-saturated underground environment surrounding packages (an anaerobic and, so, rather reducing environment, water renewed in a very low proportion).

Metal corrosion in a clay environment: the specific case of disposal package containers. What about the liability of occurrence of a gas release?

For more than ten years, dedicated experiments have been conducted to assess the uniform corrosion rate in little or low-alloyed steel under conditions representative of a nuclear waste deep geological repository. Given the anaerobic conditions in the geological layer, the cathodic reaction taking place in the vicinity of metal will be water reduction, with hydrogen generation (see *supra*, pp. 13-14, the chapter titled “Uniform Corrosion”). So the corrosion rate also corresponds with the hydrogen generation rate in this geological layer. This hydrogen release has to be investigated and controlled, for it occurs in a very impervious environment: local hydrogen buildup in the neighbouring of the metal surface may, indeed, lead to increased pore pressure in the rock, the latter being likely to induce the environment’s fracturing.

The originality of corrosion experiments lies in their being instrumented for *in situ* and real-time monitoring of the instantaneous corrosion rate evolution. This monitoring relies on the Electrochemical Impedance Spectrometry method which does not upset the corrosion process. It consists in determining a transfer conductance (the reverse of a resistance), which is directly proportional to the steel’s instantaneous corrosion rate. The proportionality factor is generally determined from an *ex situ* and *a posteriori* assessment of the steel corrosion damage.

On the whole, the experimental program has evolved according to the reference clays considered. Thus, these experiments have been initially carried out in presence of clay pastes consisting of synthetic water with a composition representative of a clay-rich geological site, and FoCa-7 or MX80 clays, for times not exceeding 500 hours. As shown by the results obtained in both cases, the steel’s instantaneous corrosion rate has decreased over time due to formation of a micrometer-thick layer of iron oxide and carbonate corrosion products (Fig. 157).

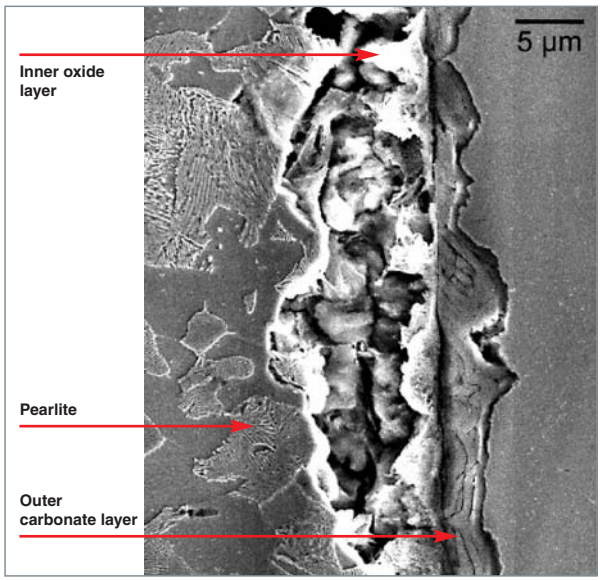

Fig. 157. SEM cross-sectional view of a low-alloy steel corroded in a FoCa-7 clay paste at 90 °C after 550 h under anaerobic conditions.

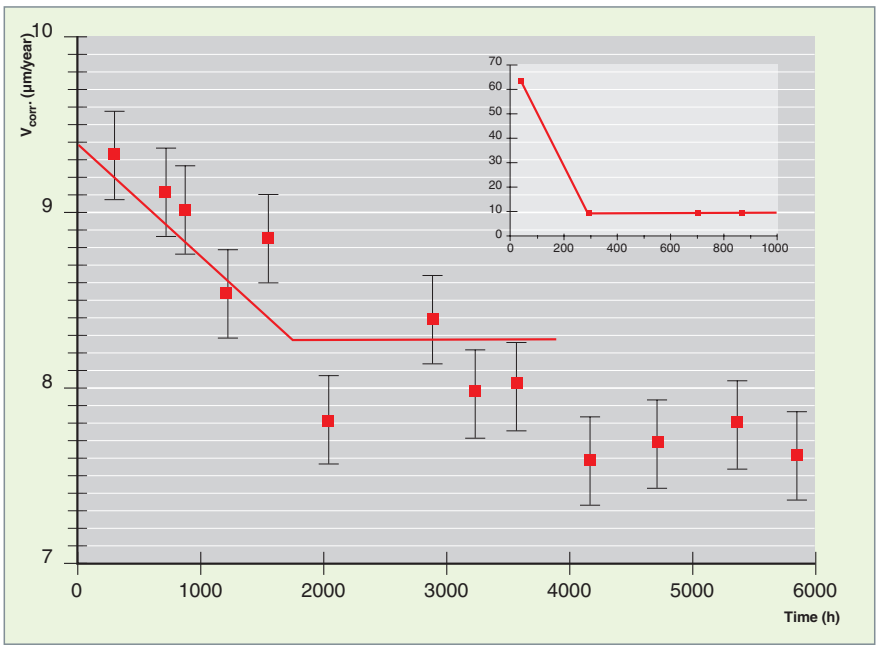

Fig. 158. Evolution of the instantaneous corrosion rate of a steel-1050 in a synthetic clayey water from the Bure site at 90 °C under anaerobic conditions.

For this layer maintains on the steel's surface chemical conditions likely to favor steel fatigue strength, i.e. a high carbonate anion concentration, and a solution pH sufficiently basic for steel to get covered with a spinel-structure iron oxide layer which passivates it.

The evolution observed in the instantaneous corrosion rate of a steel-1050 at 90 °C under anaerobic conditions includes several successive steps (Fig. 158). First of all, for short times, the corrosion rate experiences a very strong decrease, then seems to stabilize at a rate of the order of 10 µm/year (see the insert on Figure 158). As a matter of fact, the corrosion rate goes on decreasing, but much more slowly. It seems to stabilize itself again at a value lower than 8 µm/year for times longer than 3000 hours.

This instantaneous corrosion rate does not jeopardize steel fatigue strength with respect to corrosion. For the predictable corroded thickness over a 1000-year period would be of an approximate 8 mm.

Nethertheless, given this corrosion rate, the hydrogen flux injected into the disposal site would *a priori* remain too much high to be released easily into the geological barrier. So gas pockets might be formed, and induce harmful cracking in the geological environment if ever gas pressure increased too much.

On the other hand, taking into account the high swelling potential of clay MX80 compared with that of a FoCa-7 clay, experiments were conducted on MX80 in pastes with lower clay concentrations, which allowed the beneficial effect of clay-based containment upon steel corrosion resistance to be evidenced (Fig. 159):

ArCorr, the integrated iron-clay experiment

In order to bring about experimental data relevant to the disposal conditions under consideration, further experiments were carried out no longer in clay pastes, but directly in compacted clay. A specific experimental device was developed (the so-called ArCorr device).

This device consists of a water feed autoclave and a containment cell enclosing a compact clay brick. This brick has been machined so as to be able to hold three metal specimens and be inserted into the containment cell body (cf. Figure 160).

Fig. 159. SEM micrographs of siderite layers: (left) sparse deposit on the steel surface, (center) a thick deposit obtained after embedding a steel sample in a clayey paste, and (right) a deposit compacted by MX80-clay swelling.

Machining tolerances are sufficiently accurate to enable clearances to be minimized during containment cell assembling. The water feed autoclave contains a synthetic water representative of that of the Bure site. CO_2 and hydrogen partial pressures are controlled so as to reproduce the pH and redox potential conditions computed by the BRGM[12] under equilibrium conditions.

An overpressure of about 60 bars of helium is added in the autoclave, under which synthetic water is injected into the containment cell. It is aspired into the clay brick under pressure and temperature conditions relevant for the disposal scenario (40 to 50 bars at 90 °C).

Pressure corresponds with the lithostatic pressure in the geological layer, and temperature with that generated by nuclear waste. The ArCorr device makes it possible to simultaneously follow the evolutions of steel's instantaneous corrosion rate, on the one hand, out of containment in the autoclave, and, on the other hand, in containment in compacted clay. The experimenting time has been increased to 6000 hours (compared with the 500-hour previous time), which enables exposure time influence and confinement effect to be evidenced in a clearcut way.

12. BRGM: French *Bureau de Recherches Géologiques et Minières*: Geological and Mining Research Office.

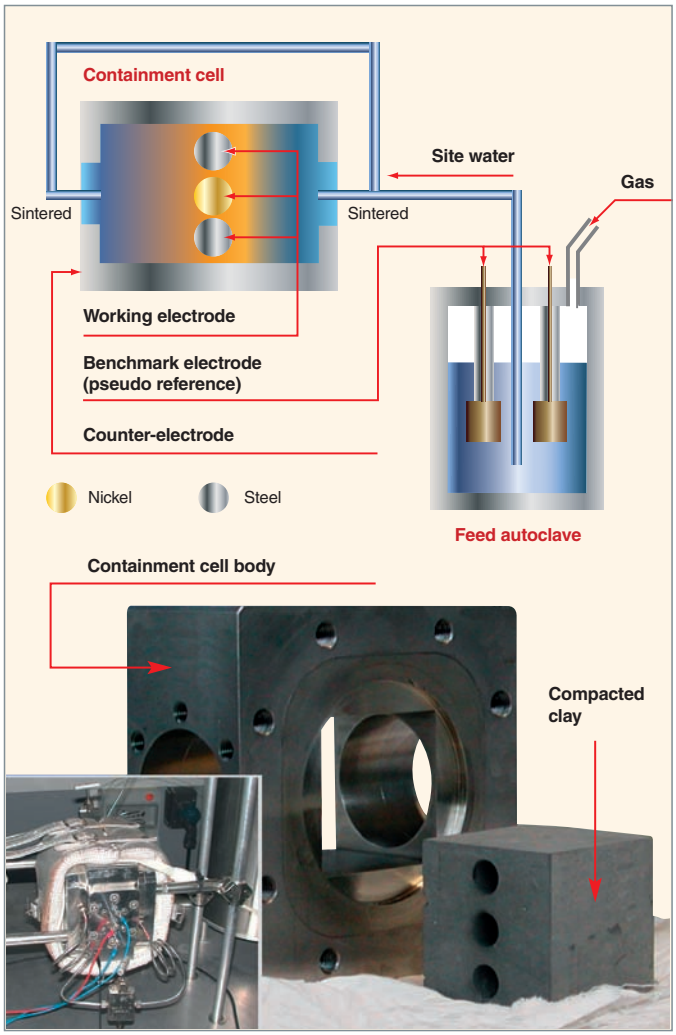

Fig. 160. The ArCorr device implemented at the Physico-Chemistry Department for investigating corrosion in clay environment.

In the case when steel is so confined within a compacted clay MX80 under isostatic conditions at a dry density of 1.8 g.cm^3, the confinement effect upon the corrosion rate can be detected as early as the experiment onset (cf. Fig. 161). The slope of the decrease in corrosion rate between 200 and 3000 hours is definitely faster than under full-bath conditions (in site synthetic water, cf. Fig. 158). However, corrosion rates measured in compacted clay MX80 are, for short times, higher than those measured in full bath (> 10 µm/year in compacted MX80, see Figure 161, and < 10 µm/year in site synthetic water, see Figure 158). Only for an exposure time of about 3000 hours has the situation been reversed. Beyond this time, steel's stationary corrosion rate in compacted clay MX80 is of about 3 µm/year (Fig. 161), while it is about 7 to 8 µm/year in site synthetic water (Fig. 158). This comparison shows that a significant initial corrosion may induce a moderate corrosion in the long term. Hence the need to conduct experiments of sufficient duration so that damage may be predictable on a very long timescale.

As regards steel corrosion strength, the confinement-related gain is not high, for the predictable damage over a 1000-year period would be increased by a 3-mm thickness, which falls within the same order of magnitude than the out-of-containment expected damage (7 mm). In contrast, the hydrogen flux injected into the geological barrier would be divided by at least a 2.5 factor, which would reduce by as much the risks of geological barrier cracking. In order to be able to ensure full durability of the geological barrier with respect to a pos-

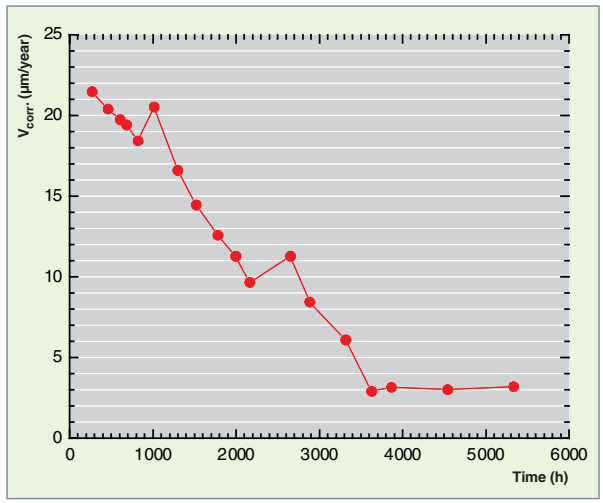

Fig. 161. Evolution of the instantaneous corrosion rate of a low-alloy steel in compacted MX80-clay saturated with synthetic water from the Bure site, at 90 °C, under anaerobic conditions.

sible cracking, ANDRA [1] considers that steel's instantaneous corrosion rate should not exceed 1 µm/year for pluriannual periods of time.

An equivalent experiment conducted in argillite arising from the Bure site (Callovo-Oxfordian argillite) has demonstrated that the evolution of 1050 steel instantaneous corrosion rate is similar to that measured in compacted clay MX80, excepting the fact that in this argillite 1050 steel gets covered with a heterogeneous corrosion products matrix similar to that observed on some archaeological analogues. No doubt that the occurence of this matrix consisting of ferrosilicates and siderite is a beneficial factor for protecting steel against corrosion.

Corrosion-geochemistry coupling: a beneficial effect?

Coupling between low-alloy steel corrosion process and the geochemical evolutions of the near field therefore seems to be fully beneficial. For, despite a relatively high corrosion rate of such steels at the onset, [siderite or ferrosilicate] neoformations lead to a substantial decrease in this corrosion rate on rather short durations.

It can be reasonably assumed that this dynamics will continue in the very long term, and that low-alloy steel corrosion rate will drop to values of about one micron per year. So hydrogen generation rate should be sufficiently low for the near field to be able to release hydrogene without any damage.

The beneficial effect of corrosion-geochemistry coupling will have to be further outlined and enhanced in the future, for example by performing validation experiments in which the aspects of corrosion kinetics and neoformation kinetics will be treated simultaneously, and not sequentially as has been the case until now.

Characterizing complex corrosion interfaces: contribution of multi-technical analyses

Integrated corrosion experiments such as ArCorr (Fig. 162) make it possible to reproduce the thermal and chemical conditions prevailing at the interface between a nuclear waste container and its engineered barrier made of clay material. These corrosion reactions result in the formation of new solid oxidized phases and the transformation of clay materials on contact with metal. Through identifying the crystalline nature of these newly formed phases, it is possible to impose physico-chemical constraints (corrosion reaction stœchiometry, involved reactions and related thermochemical equilibria...) upon the corrosion mechanism in metal. Yet, this identification is made difficult by the fact that the corrosion layers being formed over limited durations induce metal / argillite corrosion interfaces of low thicknesses (a few µm). It is therefore necessary to make use of a wide variety of microscopic techniques likely to help determine the (crystallo)chemical properties of the corrosion layers with a lateral resolution of about 1 µm [2].

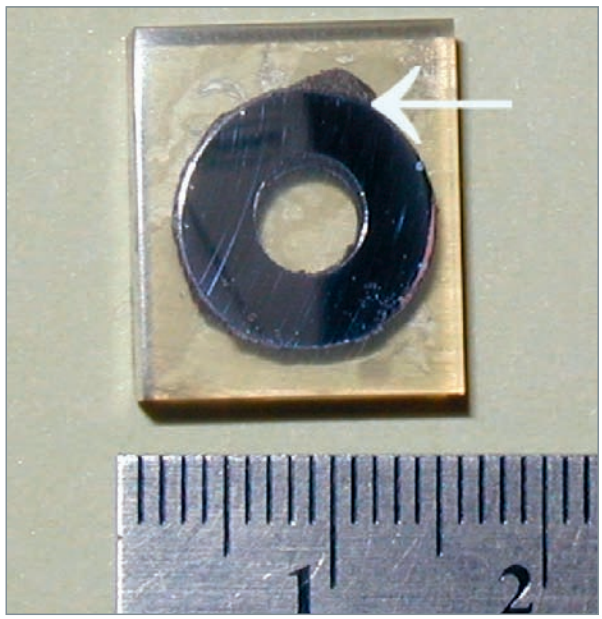

Fig. 162. ArCorr specimens are metallic bars inserted in argillite. A corrosion interface is formed between the bar and argillite (arrow). The bar has been sawn perpendicular to its axis, embedded into a resin, and polished so as to get a cross-section of the iron-argillite interface (see above).

Corrosion interface morphology

As a first optical microscopy examination of corrosion interfaces is carried out, it is possible to find evidence of different distinct layers and determine their thickness (Fig. 163). For example, on contact with the iron corroded during eight months at 90 °C under water saturated conditions, a corrosion layer or Dense corrosion Products Layer (DPL) can be observed. Above this layer can be seen a more external layer, or transformed medium layer (TML), itself in contact with argillite. On the other hand, the surface between iron and DPL can be seen to be scalloped, which indicates that the DPL growth proceeds through direct substitution of corroded metal (this surface would have been plane in the case of DPL formation above the initial surface). Similarly, the DPL contains minerals such as quartz, and clay minerals; so, presumably, it has formed detrimentally to argillite. On the contrary, the surface between the CMT and the DPL is relatively plane. This surface corresponds with the initial metal / argillite contact surface. It can however be noted that this surface may have moved in space relative to a mark in metallic iron. The optical microscope also allows simple assessments of layer thickness. Such assessments will be a guide to selecting the microscopic techniques to be implemented later, taking into account the specific lateral resolution limits of each of these techniques.

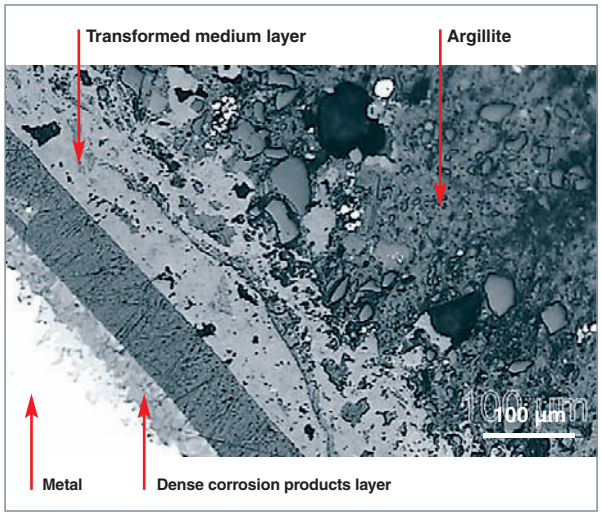

Fig. 163. Optical microscopic view of the thick iron-clay corrosion interface which displays the successive layers of the structure. The resin band which comes across the image, stands for a detachment area formed during the sample preparation.

These simple optical observations may be further improved through Scanning Electron Microscopy (SEM, with a lateral resolution of the order of a few dozen nanometers). Moreover, backscattered electron images give evidence of density contrasts as the lightest zones indicate the areas with the highest electron density (Fig. 164). It can thus be observed that the DPL may in fact be subdivided into two sublayers of distinct average electron densities.

Interface elemental analysis and mapping

An elemental analysis makes it possible to determine which chemical elements are present in the various layers, and at which concentrations. These analyses may be local, or may be performed over more extended areas. Comparing the elemental compositions of the different layers then allows areas enriched or depleted in major elements to be visualized, which helps track some elemental flows that have occurred during corrosion.

This mapping can be carried out, for example, through coupling the scanning of the microscope beam and Energy Dispersive X-ray analysis (EDX). The resulting maps reveal strong heterogeneities in elements distributions among the various layers. For example, this map confirms that the DPL may be subdivided into two sublayers, i.e. an inner DPL only containing Fe and O, and an outer DPL also containing Na and Si (Fig. 164).

These elemental distributions can also be established through micro laser-induced breakdown spectroscopy (µLIBS). This technique consists in measuring the emission spectrum of a plasma induced by a laser impact on a solid surface. Loss in lateral resolution (~ 3 µm) with respect to SEM is compensated by the ability to analyze light elements (H, Li, Be, B…), and to achieve large-sized maps in a very short time (e.g. 300 x 300 µm^2 within 20 minutes). This allows fast characterization of element diffusion fronts over relatively long distances.

Last but not least, a third technique independent from mapping relies on measuring X fluorescence of elements excited by an incident X radiation beam which displays high power and a lateral resolution of only a few µm. These elemental µXRF maps complete those obtained through µLIBS and SEM-EDX analysis. They are also used for pinpointing data obtained through micro X-ray absorption fine structure spectroscopy (µXAFS) [see hereunder].

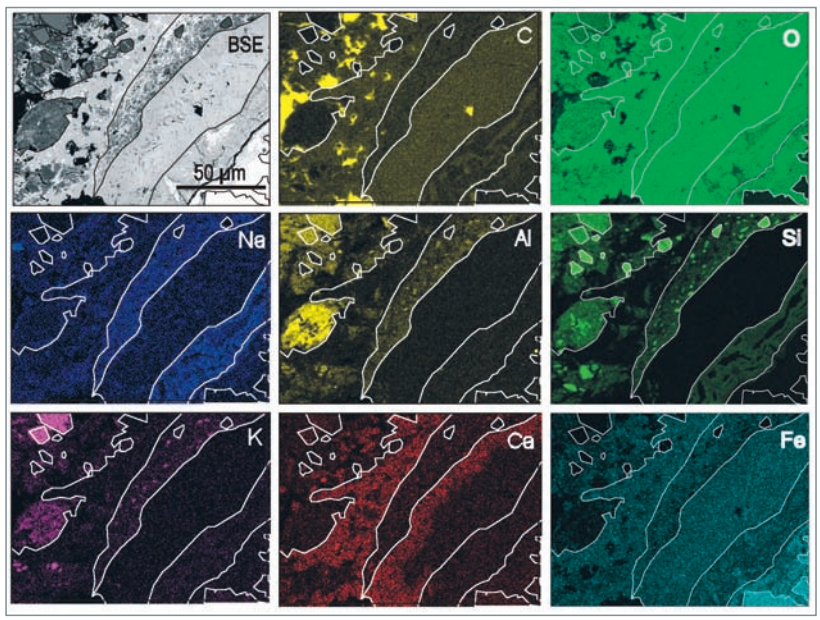

Fig. 164. Backscattered electron (BSE) SEM image (in the top right corner) and Energy-Dispersive X-ray analysis (EDX) elemental distribution maps of the iron / argillite interface. On each image, iron is in the bottom right corner, argillite in the top left corner.

Identifying major minerals and ancillary phases

All the methods presented up to now give a good idea of the chemical composition of the solid phases occurring in the layers at the corrosion interface. Nevertheless, determining the thermochemical properties of these phases also requires to determine their crystallographic nature. Such a determination may partly rely on chemical cartography results, which evidence characteristic basic associations. For example, only detecting Fe and O in the internal Dense corrosion Products Layer (DPL) through EDX analysis reveals that this layer can only consist of iron (hydr)oxides. However, the range of possible phases remains quite broad.

Some major mineral phases can be identified using micro-Raman spectroscopy. The Raman spectra measured on the polished faces enable minerals or minerals classes to be identified (Fig. 165). In the present case, this technique has given evidence of the occurrence of magnetite in internal DPL, and of carbonates in the Transformed Medium Layer (TML). As Fe is known to be prevailing in this TML, the con-

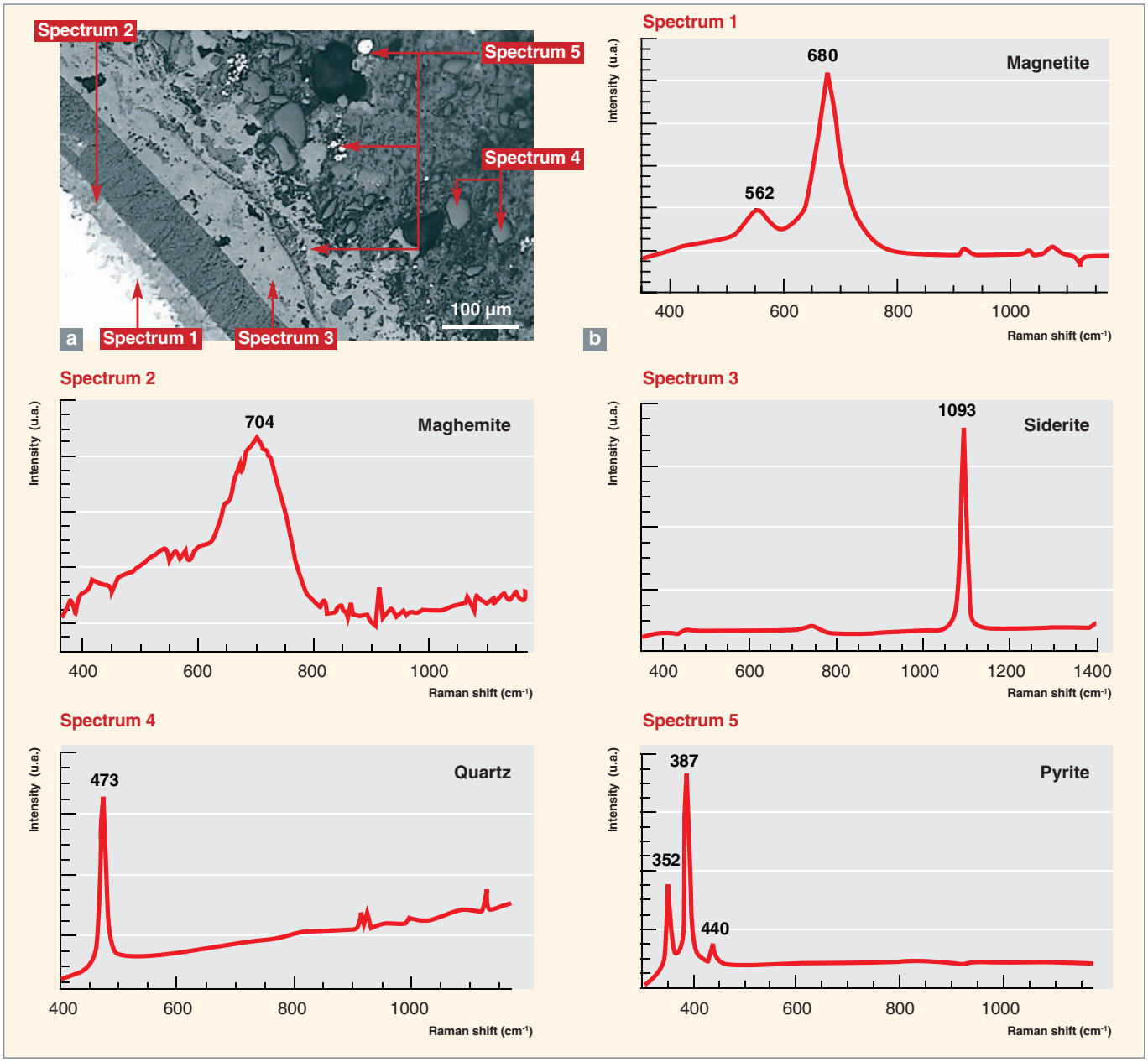

Fig. 165. Examples of Raman spectra recorded (a) for the inner Dense Products Layer (Spectrum 1), the outer Dense Products Layer (Spectrum 2), the Transformed Medium Layer (Spectrum 3), and poorly transformed argillite (Spectra 4 and 5).

clusion to be drawn, indeed, is that these carbonates correspond to siderite ($FeCO_3$).

µRaman spectroscopy is subject to two limits: first, the Raman signals of two similar solid phases may overlap one another, which prevents secondary phase identification; secondly, the Raman signal of some minerals such as illites-smectites is low, which makes it difficult to identify them.

Through comparison with Raman spectroscopy, micro X-ray diffraction (µXRD) can afford a more comprehensive, exhaustive mineral characterization. In particular, it discriminates minerals with close Raman spectral signatures, or reveals secondary solid phases. It also identifies clay minerals, and also gives essential information about clay platelet structure as well as occurring interfolliar ions and the swelling capacities of these minerals. As a counterpart, this technique requires intense and focused X-ray beams. Laboratory sources may be focused up to about 20 x 20 µm^2. The diffractometers using synchrotron radiation feature more reduced beam sizes, but also display lower accessibility.

Molecular environment of major and trace elements

Identifying the minerals present in corrosion interfaces is difficult when these solids do not diffract X rays conveniently and do not emit a significant Raman signal. Such is the case, for example, for gels that may be formed in corrosion layers, with chemical compositions much alike those of crystallized solids, but with distinct thermochemical properties (solubility...). Identifying the molecular environment of trace elements may also contribute to recognize the immobilization mechanism of these elements, which is crucial for determining whether these elements can be remobilized more or less rapidly.

The crystallochemical environment of major elements and traces may be fully characterized with a lateral resolution of about a few micrometers through micro X-ray absorption fine structure (µXAFS) spectroscopy. This technique consists in measuring the X-ray absorption spectrum of a specific element. This absorption spectrum is a true signature of the element's local crystallo-chemical environment, irrespective of whether it is a major element or a trace. For example, by comparing the µXAFS spectrum of Fe in the Transformed Medium Layer (TML) and in siderite (Fig. 165), it can be confirmed that in the TLM Fe is present in a sideritic environment. Moreover, the composition of an intimate minerals mixture may be reproduced through modelling the spectrum of this mixture with a linear combination of reference spectra. Thus, iron spectrum in the Dense Products Layer (DPL) can be modelled with a linear combination of iron contributions to smectitic lamellar ferrosilicates, magnetite, and metallic iron. The occurrence of ferrous phyllosilicates is consistent with the detection of Fe, O, Si, and Na through EDX analysis.

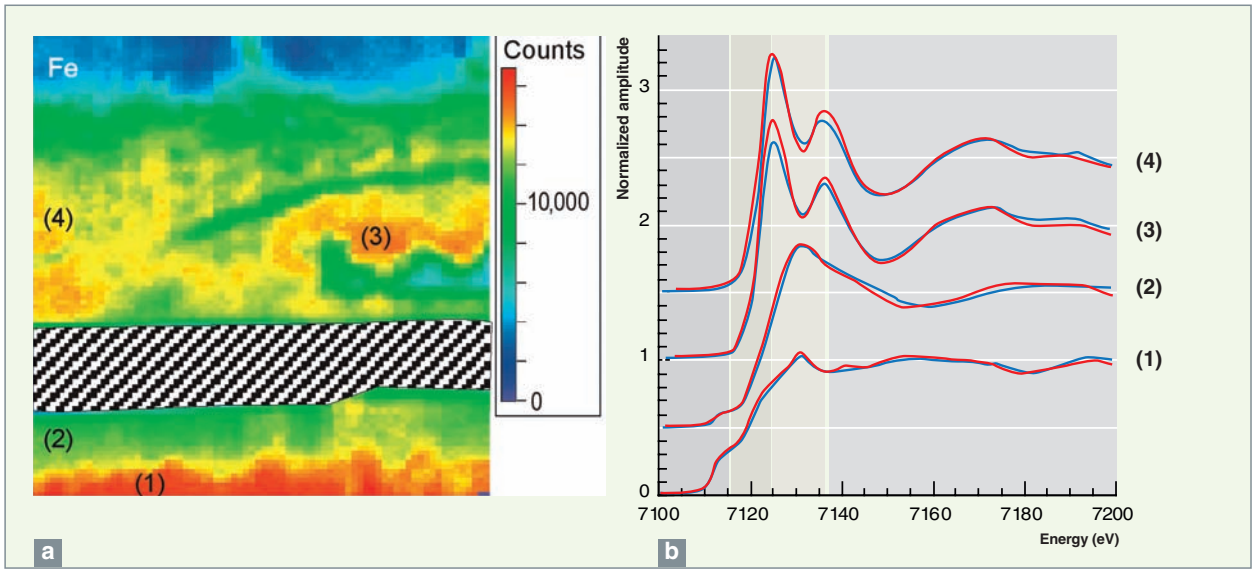

Fig. 166. (a). X-ray fluorescence map displaying iron distribution between metal (bottom) and argillite (top). The figures stand for the points analyzed through X-ray absorption. (b) X-ray absorption spectra after self-absorption correction (full lines) and modelling. (1) 100 % iron metal; (2) Dense Products Layer (DPL): 45% nontronite 28% minnesotaite + 14% iron metal + 12% magnetite (elemental fractions). (3) and (4) Transformed Medium Layer: 100% siderite.

From observations to the interface structural model

Comparing original and post-corrosion element distributions makes it possible to directly determine the concentration gradients between metal and argillite as well as the various element fluxes at the interface. For example, it is clear that high silica amounts observed within the outer DPL can but stand for a dissolved silica input from argillite. Confronting this input with low silica concentration within the TML leads to the assumption that silica-rich claey minerals (illite-smectite) are destabilized within this layer.

These observations enable a synthetic model of the corrosion interface to be built, which reproduces basic and mineralogic data (Fig. 167). In this model, iron corrosion takes place at the metal - internal DPL interface, and results in magnetite formation. This magnetite is destabilized through silica intake, which results in formation of the ferrosilicates (probably phyllosilicates) of the outer DPL. In the TML, clayey minerals and calcium carbonates are dissolved, and then, dissolved carbonate ions react with iron to form siderite ($FeCO_3$).

Characterizations performed using distinct and complementary microscopic and microspectroscopic techniques enable corrosion phenomena and element fluxes between iron and argillite to be described. It is possible to identify the system's layer morphology (optical microscopy and SEM), the solid phase nature (μRaman and μXRD), the element concentration gradients at the iron-clay interfaces (SEM-EDS, μLIBS, and μXRF elemental analyses), and the molecular environment of major elements and traces (μXAFS). These experimental results corroborate the theoretical predictions previously issued [3, 4]. Particularly, they illustrate the silica retention capacity in the Dense corrosion Products Layer and the probable phyllosilicate neo-formation in this DPL, at least over the experiment duration. Last but no least, they show that siderite may be formed at the iron-clay interface under the study conditions. It is worth noting that the presence of siderite has already been reported during archaelogical analogue corrosion, but only in cases of corrosion in a saturated anoxic environment [5].

Identifying the solid phases occuring in the corrosion layers does not go without assessing the reactivity of these layers with respect to the chemical species (especially silica and radionuclides) released by the container corrosion. For the dissolution of the nuclear glass present in the container gets slower due to the increase in dissolved silica concentration. On the other hand, retention of this silica through corrosion products incorporation would limit dissolved silica concentration, thereby favoring further dissolution of nuclear glass. As a matter of fact, as suggested by current results, corrosion products first react with the silica arising from clay minerals minerals, thereby forming phyllosilicates with a high silica content. This suggests that, when nuclear glass is exposed to the altering solution, the corrosion products retention capacity with respect to silica is already reduced. Consequently, glass alteration would not be much disturbed by occurring corrosion products.

It is worth keeping in mind that such characterizations are carried out on a sample otained for a given reaction time. This time is generally short if compared to deep geological disposal timescales. As a consequence, the observations performed may correspond with transient phenomena, which may have a negligible impact in the long term. However, predicting these phenomena enables us, indeed, to gain increased confidence in our ability to depict corrosion phenomena in heterogenous media such as argillites.

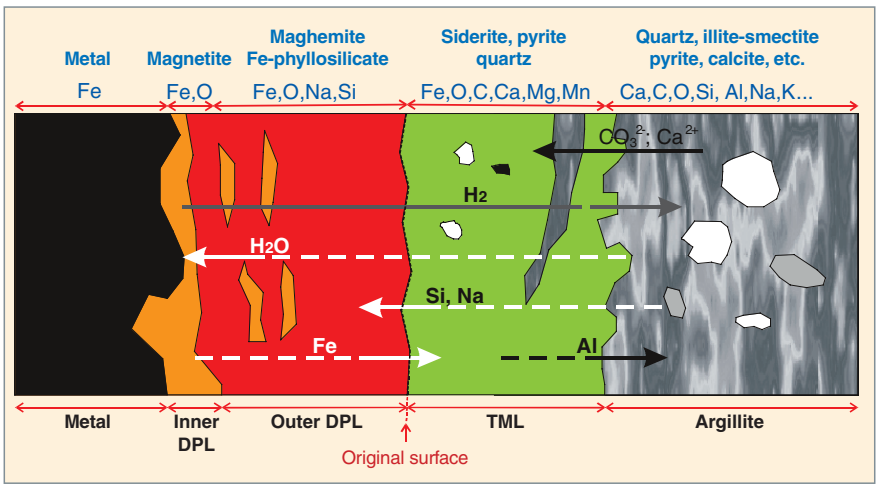

Fig. 167. Schematic model of the iron-argillite corrosion interface after eight months of corrosion at 80 °C and with water saturation.The major elements and the various major mineral phases are mentioned above the figure. Element distribution before/after corrosion gives evidence of the element flows at the interface.

Long-term behavior of glasses and alteration by water: the specific case of nuclear waste disposal

For nearly twenty years France has been treating and recycling spent fuels unloaded from pressurized water reactors, and has been incorporating fission products and minor actinides into glass R7T7 at La Hague Areva NC plant. Glass has been selected for conditioning long-lived high-level waste (**HLW-LL***) owing to its robustness properties with respect to chemical aggressions, its ability to incorporate a wide variety of chemical elements into its structure (Fig. 168), and its easy industrial implementation (see the DEN monograph "Nuclear Waste Conditioning").

A number of theoretical and experimental works have led to the conclusion that glass properties would not be altered in the short, medium and long term by temperature (crystallization being negligible) or irradiation (minor alterations of the macroscopic properties) [6]. In contrast, it has been recognized that after resaturation of the geological site and degradation of the metallic envelopes, water present in the underground environment will be able to alter glass and release part of the radionuclides contained in it. Long-term behavior of these vitrified waste packages on contact with water therefore raises a crucial issue regarding radionuclide source term. The whole issue, indeed, is how fast and according to which mechanisms degradation will take place.

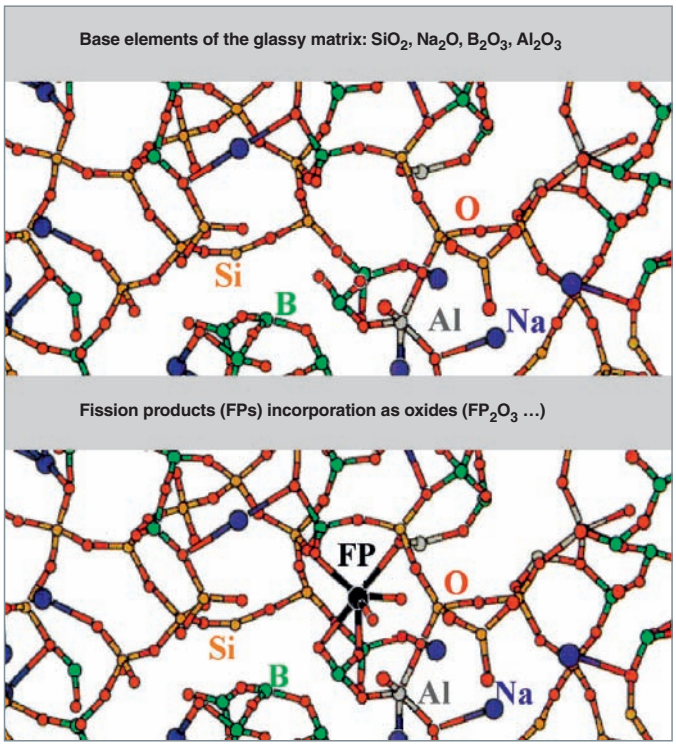

Fig. 168. Principle of element containment in a glassy structure. The amorphous character of glass enables it to host a wide variety of elements arising from spent fuel. Fission products atoms are incorporated into glass where they form covalent and ionic bonds with its main constituents.

Phenomenology of glass alteration by water

A synthesis of the experimental results reached till this date are to be found in Godon *et al.* [6] and Vernaz *et al.* [7]. The main results may be summarized as follows:

- Under static conditions and at 90 °C, glass alteration rate evolves from about 1 µm/d at the onset of the process to under 0.1 nm/d after a few weeks.

- An altered glass layer, amorphous and porous, can be observed systematically through electronic microscopy. It contains water, mostly as structure water around the layer's internal face, and mostly as poral water around its external face. This hydrated layer mainly consists of silicon, aluminium, calcium, zirconium and rare earths, and is often covered by clay crystallized phases.

- The alteration rate is never cancelled, even after the solution saturation with respect to the hydrated layer has been reached. This observation has led to put forth the terminology of "residual rate" to refer to the "long-term" alteration regime.

- As a general rule, the step of reaching this residual regime and the residual rate value depend on parameters that are geometrical (glass surface / solution volume ratio, occurring cracks in glass), chemical (pH, water composition, glass composition), hydraulic (water renewal rate, diffusion), radiological (radiolytic effects), and, of course, on temperature. Most of these effects are coupled and non-linear.

Glass alteration mechanisms in water and reactional kinetics

In presence of water and just as in most borosilicates, reactions take place in glass R7T7, some of them being attributable to the nature of chemical bonds within the glassy network and others, to the properties of dissolved species. Among the main reactions involved, let us quote [6, 7]: first, **ion exchange**, which is particularly related with exchange between alkaline ions loosely bonded with the glass network, and hydrogenated species, and secondly, glass-former **hydrolysis-recondensation** reactions. These two reaction categories govern hydrated layer formation: the first one mainly takes place in the most internal area of the hydrated layer, while the second mostly acts in the latter's outer area. Secondary phase **precipitation** may also be mentioned. At the temperatures of interest (25-90 °C) in the repository, a majority of these phases are phyllosilicates (Fig. 169). Glass

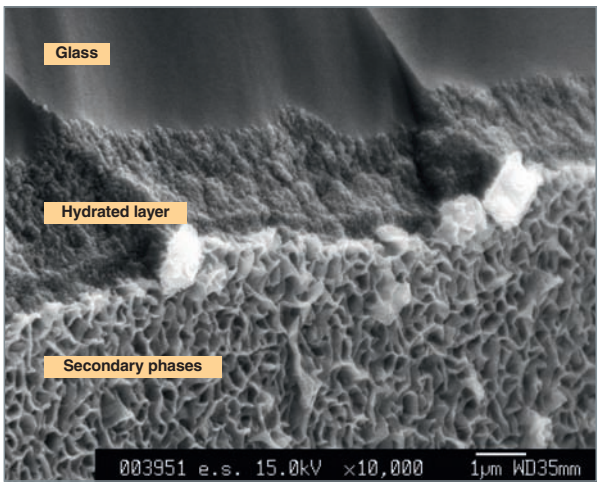

Fig. 169. SEM image of a R7T7 glass specimen altered for 4 months in initially pure water at 150 °C. This cutaway view makes it possible to sucessively pinpoint the outer layer of phyllosilicates precipitated from the solution, the hydrated layer, and the underlying sound glass.

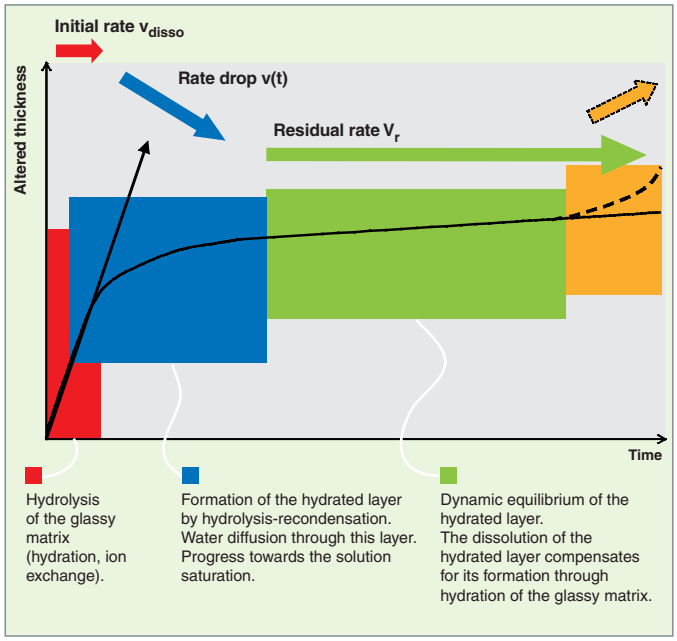

Fig. 170. Schematic representation of the prevailing mechanisms which control glass alteration kinetics. This schematic may apply to any type of glass. However, the various phases will have more or less significant, or even null, developments depending upon the glass composition considered and the alteration conditions (for instance, renewed alteration cannot take place in R7T7 glasses, or only in extreme situations).

major elements such as Si and Al are distributed between the amorphous hydrated layer and the crystallized secondary phases.

Figure 170 shows a simplified representation of the various alteration kinetic regimes of nuclear glasses, which are the following:

- The “initial rate” (or “velocity”), limited by the hydrolysis of the silicate lattice;
- The “rate drop”, associated with the formation of a dense, passivating area within the hydrated layer. This area is formed by ion exchange and hydrolysis reactions and by *in situ* recondensation of a fraction of hydrolyzed silicon. This layer is dissolved on its outer face up to reaching the solution’s saturation. It plays the role of a diffusion barrier with respect to water and glass hydrolyzed species;
- The “residual rate” is due to the dissolution of the hydrated layer, a reaction induced by the solution’s renewal and by the precipitation of the secondary phases which consume the layer forming elements;
- Last but not least, are referred to as “renewed alterations” particular cases in which a sudden rise in the alteration rate can be observed. This regime is associated with a pronounced precipitation of specific secondary phases such as zeolites.

These reactions are split into four simultaneous processes which are likely to be kinetically described (Fig. 171):

- The oxide glass is turned into an amorphous, porous and hydrated “phase” of the oxo-hydroxide type;
- Water transport by diffusion to the reactional interface, through the hydrated layer already formed, limits this glass hydration reaction. So the hydrated layer plays a passivating role;
- This layer is dissolved on its outer face with a kinetics depending upon the solution’s renewal conditions in the vicinity of glass;
- Secondary phases precipitate, thereby consuming the hydroxide layer’s forming elements.

The overview of these processes is sufficient to provide a reliable description of the various alteration rate regimes of glass.

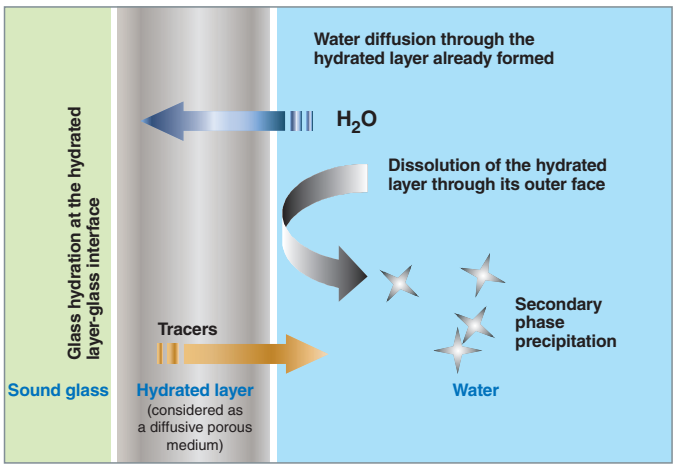

Fig. 171. The four processes involved in glass alteration.

As a general rule the precipitation of secondary phases has to be achieved modelling all the equilibria involved in a geochemistry-transport model which takes into account the precipitation of all the phases likely to be formed. This work is currently under way in Marcoule. In some cases, the precipitation of secondary phases can also be taken into account in a more restrictive manner assuming there is only one phase precipitating according to a first-order kinetics. The work described hereunder was conducted on this very basis of modelling. This assumption enabled the precipitation of secondary phases to be described with only two parameters: Cpsat, solubility limit of the considered phase, and V_{pr}, a kinetic parameter of precipitation.

With these parameters, all accessible by independent, separate-effect experiments, the GRAAL model reasonalby reproduces the alteration kinetics of glass R7T7 as observed through measuring the concentration in silica and tracers (lithium, boron) in solution under all the water renewal conditions (Fig. 172).

A mechanistic model of glass alteration by water: the GRAAL model [8]

In the **GRAAL*** model recently developed at the CEA, the mechanisms hereabove mentioned have been turned into equations using the simplest possible assumptions: it has been assumed that glass hydration reaction is rapidly limited by water transport through the hydrated layer. This transport has been described by a Fick's law assuming this layer homogeneous. First-order kinetic laws have been used for the hydrated layer dissolution and the secondary phase precipitation.

The simultaneous resolution of the model's coupled differential equations enables the altered thicknesses and the silica and tracer concentrations in solution to be calculated at any time. The asymptotic properties of the system reveal a residual regime in which the hydrated layer's alteration rate and thickness become constant.

The main parameters of the model are as follows:

- C_{sat}, solubility limit of the hydrated layer. Its value is fixed by the limit value of silica concentration in the reactor for experiments with non-renewed water;

- V_{disso}, a kinetic parameter for the dissolution rate of the hydrated layer on its outer face, is fixed by measurements of both the in-reactor silica concentration and the release rate of glass tracers for high water renewal experiments (those for which the rate is governed by the layer's dissolution kinetics);

- D, water diffusion constant through the hydrated layer. This value is determined through analysis of the boron profiles.

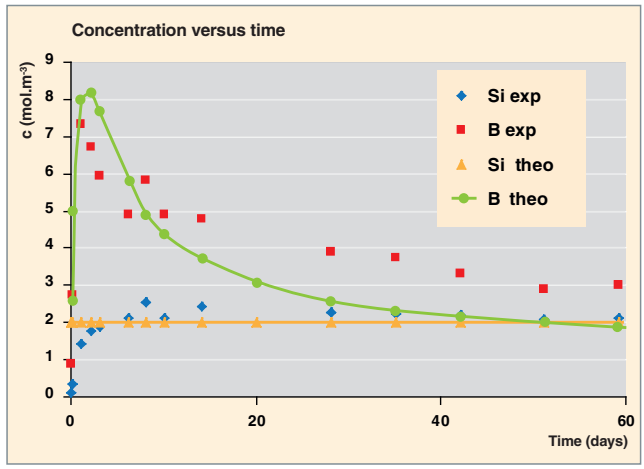

Fig.172. Time evolution of the boron and silicon concentrations released in solution by a R7T7 glass powder that displays a glass surface/reactor volume ratio of 1.2 10^5 m^{-1}, and for water renewal rate of 4.4 10^{-11} $m.s^{-1}$. Uncertainties on expertimental data are on the order of 20%.

The GRAAL model also and mostly reproduces glass alteration for long times, irrespective of the water renewal rate. Data are provided hereafter in relation with silica dissolution (Fig. 173) and the residual rate of tracer release (Fig. 174) for various values of water renewal.

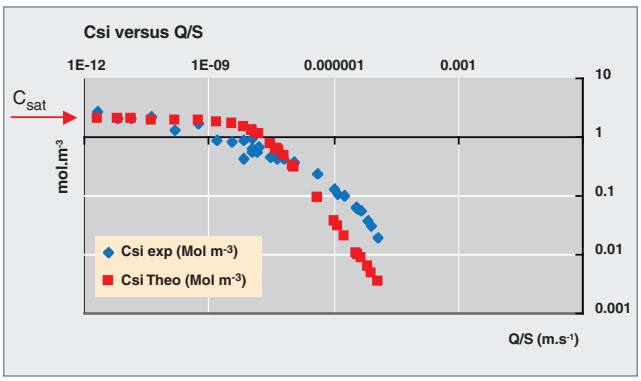

Fig. 173. Concentration in silica dissolved in the reactor water versus the water renewal rate (this parameter Q/S is defined as the water flow rate Q divided by the free surface of glass subject to alteration S). For low Q/S values, there is sufficient time for the reactor water to get saturated in silica; in the opposite case, for high renewal rates, the silica concentration is all the lower as the flow rate is higher, for silica has not sufficient time to saturate the reactor water. Such effect is taken into account in the GRAAL model, which describes it reasonably well.

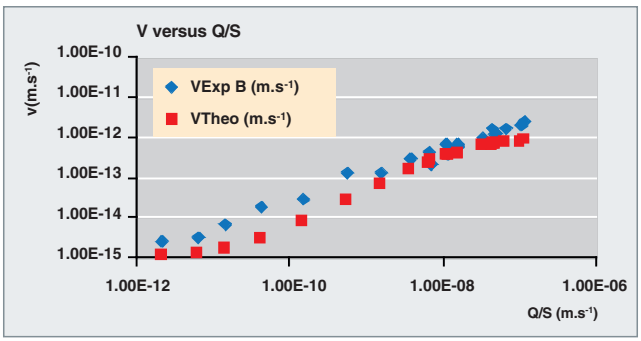

Fig. 174. The residual rate of glass alteration depends on water renewal rate. For high renewal rates, the residual rate (measured from the boron transferred to solution) is limited by the dissolution kinetics of the alteration layer; for low or null renewal rates, the residual rate is governed by the kinetics of secondary phase precipitation.

The agreement between the GRAAL model and experiment with practically no free parameters seems to show that the phenomena involved in glass alteration by water are relatively controlled, including those governing the "residual" regime, i.e. long-term behavior. Although laboratory experiment timescales are much shorter than those of an underground repository, this success gives confidence in the predictions likely to be obtained regarding vitrified waste behavior under disposal conditions.

Atomistic approach of glass hydrolysis

The notion of glass "active sites" likely to react favorably with molecular water, thereby favoring glass lattice hydrolysis, could be be evidenced through *ab initio* calculations [9].

These sites are not associated with the ever existing point defects, but with the structural disorder inherent to glass. This disorder plays a prominent role in chemical processes and the glass lattice looks fairly inhomogeneous in terms of reactivity.

By comparing the stability of different configurations of alumino- and borosilicate glasses, it is possible to classify their anionic sites as a function of their acidity (i.e. the energetic stabilization produced by the ionic exchange phenomenon). For example, the B^{IV}-O-B^{IV} bond is the most basic site: these bonds therefore tend to dissociate themselmes priorately. Then come the -Si-O-, etc. groups. In time, hydrolysis is expressed by a decrease in glass local disorder.

Concerning aluminosilicate glasses, the role of the alkaline (or alkaline earth) component is crucial for diffusion and interdiffusion phenomenology. For example, the charge-compensating Na (or Ca) changes by nature and then becomes a network modifier through chemical concerted reactions (e.g. with creation of H_2O-AlO_3 entities and protonated Al-O-Si).

A modelling built upon these concepts enables experimental trends to be reproduced in relation with water speciation in silicates and aluminosilicates (5). Thus, it is considered that two phenomena take place when a glass (SiO_2, Al_2O_3, Na_2O) is put in contact with water:

- Interdiffusion of H+ (ou H3O+) which are exchanged with the newtwork modifiers Na;
- Molecular water diffusion within glass structure.

Considering that molecular water is not a chemically inert species in glass, its major effect is transforming little by little charge compensators into network modifiers, through two mechanisms at least:

- Direct reaction with Al, which results in the formation of stable H_2O-AlO_3 entities;
- The hydrolysis of glass active sites Si-O-Si, which soon leads to the protonization of a Al-O-Si bond. Two chemical groups Si-OH (silanol) and Al-O(H)-Si (a bridging hydroxyl) are thus generated as well as a non-bridging oxygen (NBO).

These two mechanisms entail the breaking of a bond in the covalent network; that is to say they contribute to its depolymerization. Both of them cause a compensator to be turned into a modifier, which is then available to diffuse and take part in the ion exchange process with the protons.

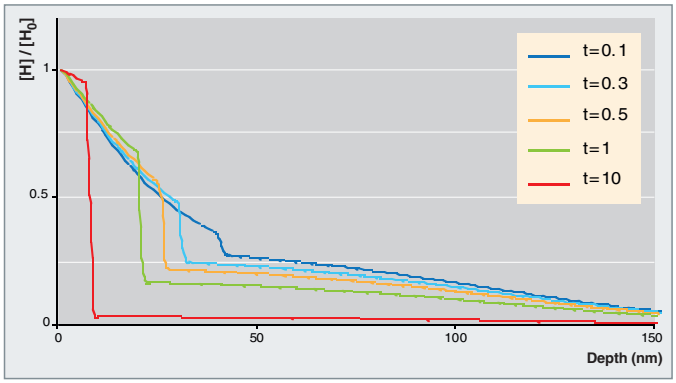

Fig. 175. Modelled profiles of hydrogen concentrations of the altered zone corresponding with various aluminium contents in the glass (t = Al / modifying Na ratio).

Introducing these mechanisms into the simple analytical models of aluminosilicate alteration provides concentrations profiles (Na, H) in which the effects of moolecular water diffusion processes and ionic exchange can be well distinguished; and fairly well reproduce some experimental results (Fig. 175 and 176).

This exercise has shown that the coupling between *ab initio* calculations and analytical modelling - a multiscale methodology - is quite a promising approach. In time, it can be contemplated to conduct similar investigations on the generation of stresses due to hydrolysis or substitution reactions as well as species diffusion in the reaction area.

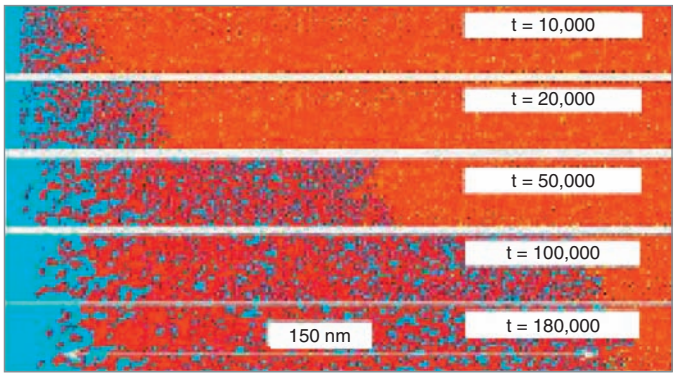

Fig. 176. Simulation of glass alteration through the Monte-Carlo method [10]. The main simulation ingredients are formation and bond rupture probabilities, handled as free parameters. Water is shown in blue, silicon in red, and boron in yellow. Simulation reveals the main phenomena observed, especially the formation of the hydroxide porous layer.

What archaeological analogues teach us about reactive surface contribution to the alteration of a fractured block

Investigating natural and archaeological analogues stands as an important step in assessing long-term behavior of nuclear glasses and in model validation. It contributes to evaluating the ability of these models to account for observations, especially alteration thicknesses, the nature of the mineral phases formed, their role on the glass dissolution kinetics and the long-term prevailing mechanisms.

The analogy here concerned relates with morphology, as the aim is to compare respective behaviors of glass blocks which have been fractured at the end of their making. These archaeological glasses of several kilograms recently discovered far beyond the Embiez Island in the Mediterranean Sea, 56 meters deep, exhibit the following benefit: they have been altered for 18,000 years in seawater under known and constant physicochemical conditions.

Once cracked, nuclear and archaeological glasses therefore expose water a surface aera far broader than their mere geometric surface. Yet, the contribution of these internal surfaces to the overall alteration depends upon the alteration rate regime in these surfaces, which may evolve differently from that in the external surface.

Thus, alteration thicknesses of internal cracks in archaeological glasses (Fig. 177 b) are far less significant (between 5 and 100 µm) than those in peripheral cracks (about 500 µm) (Fig. 177 a), which evidences the key role of parameters such as crack opening and accessibility upon the setting up of chemical conditions favorable to a rate drop regime.

On the other hand, there can be observed a systematic filling of internal cracks by smectitic minerals resulting from the joint precipitation of glass dissolved elements (Ca, Al, Si) and of seawater and sediments (Mg, Al, Fe). In these cracks, the diffusion coefficient of a tracer such as boron is on the order of 10^{-11} m^2/s. It is lower by two orders of magnitude than the coefficients of species diffusion in free water, which suggests a slower transport due to alteration products. This phenomenon therefore contributes to containment and to rate drops in cracks [11].

Confronting these results with those obtained using kinetic and thermodynamic models validates the approach for modelling long-term behavior of nuclear glasses.

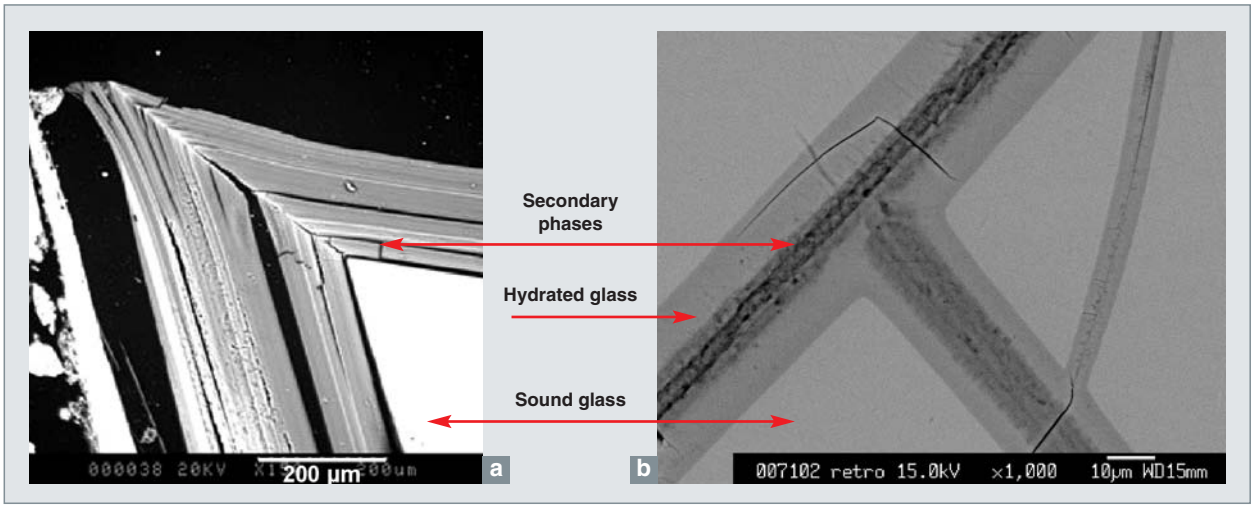

Fig. 177: SEM microphotographs of a peripheral crack of the archaeological glass in direct contact with seawater (a) and of an internal crack (b). Three areas can be pinpointed: the sound glass, the hydrated, dealkalized glass, and the secondary phases.

Influence of repository materials on glass alteration (package / near field interactions)

Some materials of the near field (iron, corrosion products of containers, clays) may lead to a glass alteration especially by delaying protective layer formation. The mechanisms involved are glass silicon sorption on the surfaces of the minerals constituting the near field materials and the neo-formation of secondary phases from the forming elements of the hydroxide layer (Si, Al, Ca…) and the elements arising from iron corrosion or clay minerals dissolution.

The sorption effect is transient, and may be modelled in a simple manner through measuring how much silica can be sorbed by these minerals. In the so-called "$V_0 \rightarrow V_r$" operational model used for the 2005 safety calculations, this very mechanism alone is taken into account. In this model it is considered that as long as corrosion products surfaces in metallic containers can adsorb silicon, glass is being altered at the highest rate "V_0" (which is identical to the rate "V_{disso}" of the more recent GRAAL model); then, once the site saturation has been reached, the conditions for the formation of the hydroxide protective layer are available, so that the rate can rapidly reach its residual value.

The neo-formation of silicon-based secondary phases (arising from glass dissolution and clay destabilization) and of iron (arising from metallic corrosion) plays a key role on the reactivity of the glass / iron / argillite system of the Callovo-Oxfordian [12].

The glass alteration model implemented in the Hytec Geochemical Code enables chemistry / transport couplings to be described at different scales.

Simulations account for the processes experimentally evidenced in a suitable way, thereby validating the choice of the model type. Thus, iron corrosion in the Callovo-Oxfordian argillite features a pronounced destabilization of the main silicates, clay minerals and quartz. Iron is oxided and new minerals are formed: magnetite, siderite, trioctaedric phyllosilicates very rich in iron, serpentines and vermiculite-chlorite, and probably iron-rich, aluminosilicate amorphous gels. Magnetite formation seems to be predominant compared with that of siderite when species diffusion in argillite is limiting.

Glass alteration in this highly reactive environment is relatively rapid, and leads to the formation of a hydrated silicate layer that incorporates Zr, Al, Fe and Ca (Fig. 178).

An operational model, which explicitly or implicitly integrates most of the key phenomena described hereabove, has been developed in order provide the most robust and realistic prediction as possible for the long-term behavior of R7T7 glasses in a repository, while preserving sufficient margins to take into account parametric and conceptual uncertainties [13]. The operational model is based upon the conservative assumption that glass will be altered in its initial rate up to silica saturation of corrosion products in metallic containers. Beyond this initial regime, a passivating hydrated layer will be rapidly formed, and will results in the residual rate regime.

Figure 179 shows the evolution of glass package alteration versus time. The calculation is based upon a normal evolution scenario, for which glass alteration starts at 1000 years (i.e. the leaktightness duration assigned to the metallic over-

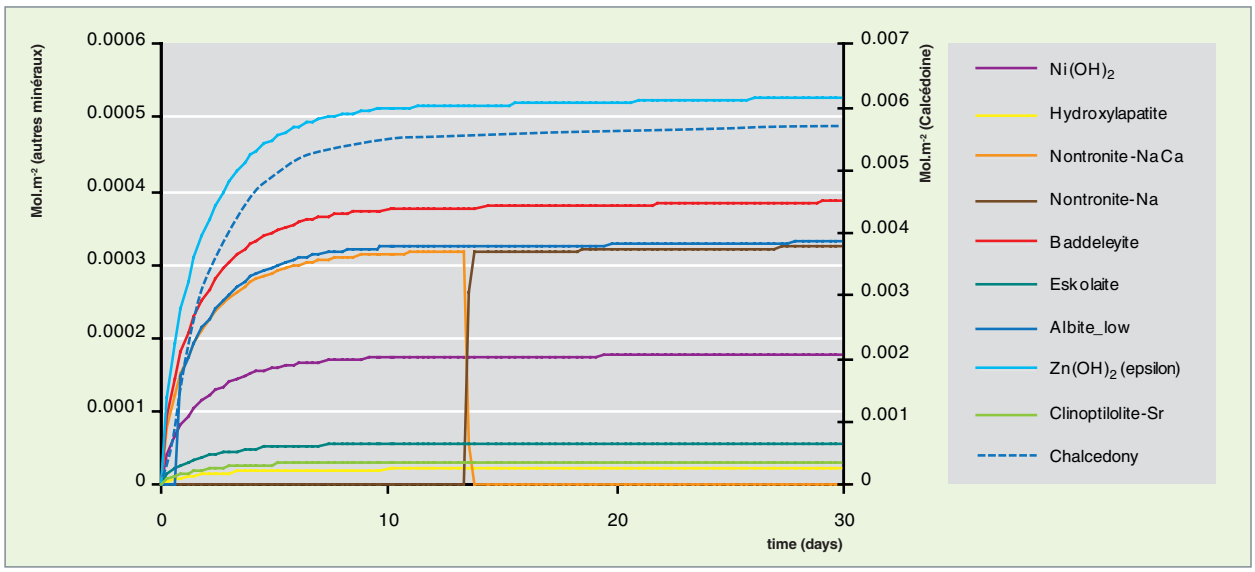

Fig. 178. Evolution of the masses of the minerals formed during the geochemical simulation of glass alteration in initially pure water at S/V = 80 cm^{-1} and 90 °C.

container). Irrespective of the projection time – 10,000 or 100,000 years –, it can be seen that R7T7 glass displays a high containment potential with respect to the radioelements it contains, and that the glass package lifetime is then of several hundreds of thousands of years. In addition, taking into account the retention phenomena of the fission products and actinides in the alteration film could result in an additional gain of about two orders of magnitude in the few thousands of years following the onset of alteration, then in one order of magnitude later on.

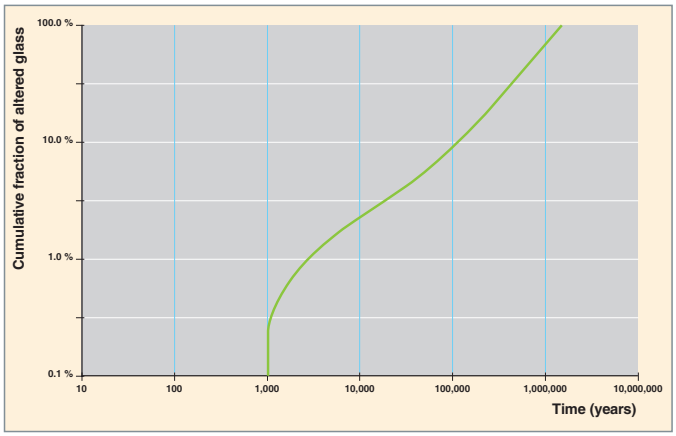

Fig. 179. Cumulative fraction of altered glass as a function of time, for a standard package under disposal conditions. In this case glass alteration is assumed to have started 1000 years after repository closure, when corrosion perforates container and overcontainer metallic walls. According to the assumptions taken here, 100,000 years will be necessary for glass to release 10% of its activity, and over one million years for the package to be altered deep in the core.

A containment matrix tailored to deep disposal

Glass appears as a suitable confining matrix for deep disposal, but with an alteration rate that may depend upon the environment. Ongoing investigations on residual rate, coupling with the environment, and analogies with natural and archaeological glasses are expected to lead to finer predictions of the repository “source term” in the coming years.

All things considered, the GRAAL model now provides a simple description of glass alteration mechanisms. As the latter gives a reasoned and justified figure for the residual rate, it harmoniously fits in the conservative, robust models which **ANDRA*** will have to use to assess containment performance of nuclear glasses under geological disposal conditions.

Ceramic alteration

The French Act of 1991 on long-lived nuclear waste recommended to conduct research on every possible path of waste management, including conditioning modes. As part of this research investigations were carried out on ceramic matrices dedicated to the specific conditioning of various long-lived radionuclides likely to be partitioned [14], such as some fission products (I, Cs) and minor actinides (Am, Cm and Np). Four matrices for actinide confinement have been brought to the technical feasibility stage: (1) britholite ceramic, (2) zirconolite ceramic, (3) TPD (thorium phosphate-diphosphate) ceramic and (4) the monazite/brabantite solid solution. Iodine is inserted into iodoapatite, and caesium into hollandite.

Ceramics for the specific conditioning of radionuclides?

The selection of these matrices relied on several criteria, especially the behavior under corrosion by water. The methodology developed for characterizing containment glass performance was applied to the various materials investigated. A certain number of initially candidate matrices have thus been excluded at the scientific feasibility stage, because they have not displayed sufficient resistance to the Soxhlet alteration test (i.e. the alteration at 100 °C of a monolithic specimen by continuously renewed distilled water). Indeed dissolution rates lower than 10^{-2} g.m^{-2}.d^{-1} could not be obtained under these very aggressive conditions.

Following this first step, the alteration kinetics of each selected matrix was experimentally determined, the main aim being to quantify the effet of pH and temperature (influent parameters under the environmental conditions of geological disposal) upon the initial rate (the material's maximum alteration rate).

In a third step, the evolution of the dissolution rate as a function of reaction progress and time was investigated experimentally in a confined medium (with no renewal of the leaching solution).

The kinetic laws and the alteration mechanisms are deduced at each step from the analysis of the solutions arising from experiments, from post-alteration characterization of specimens through observation techniques such as, e.g., scanning or transmission electron microscopy, and from the thermodynamic modelling of solid-solution equilibria performed using geochemical computer codes.

For each of the materials retained, the status of present knowledge may be summarized as follows.

Iodoapatite

The dissolution rate of iodoapatite of formula $Pb_{10}(VO_4)_{4.8}(PO_4)_{1,2}I_2$ depends upon pH (Fig. 180) and temperature (the apparent activation energy of the dissolution reaction is E_A = 34 kJ.mol^{-1}). The initial rates reached at 90 °C are lower than 10^{-2} g.m^{-2}.d^{-1} within a pH range between 4 and 10.

The dissolution regime is non-stœchiometric and incongruent; the order of release rates of solution elements is as follows: $V_{Iodine} > V_{Phosphorus} > V_{Lead} > V_{Vanadium}$.

Iodine is preferentially released on account of its localization in tunnels of the crystalline network where chemical bonds are the lowest, while V and Pb (and/or P and Pb) precipitate as secondary alteration products.

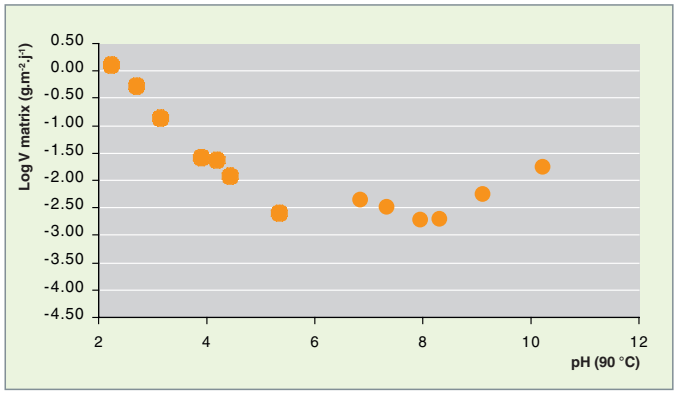

Fig. 180. pH influence at 90 °C upon the initial dissolution rate of apatitic structure materials.

In a highly renewed environment, the iodoapatite surface is turned into a compound of type $Pb_{10}(VO_4)_6(OH)_2$, which expresses the probable exchange $I^- \leftrightarrow OH^-$ under such alteration conditions. Neo-formation of the secondary alteration products observed is in agreement with the thermodynamic equilibria predicted by the geochemical modelling.

In a confined environment and over long experiment times (> 1an), at constant pH and temperature, iodine conversion to a solution can experience a slower rate (V = 10^{-4} g.m^{-2}.j^{-1}), which is attributed to the limitation of the diffusion transfer of reactants and exchange reaction products through residual apatite (or alteration products).

Hollandite

In pure water the dissolution of hollandite $(Ba,Cs)Al_2Ti_6O_{16}$ is non-stoichiometric, as it features an initial preferential release of caesium and barium. The initial alteration rate at 100 °C is on the order of 2.10^{-2} g.m^{-2}.d^{-1}, in relation with caesium release. Dependence of this initial alteration rate on temperature (Fig. 181) between 100 and 300 °C remains low (the related activation energy is Ea = 25 kJ.mol^{-1}). Following a few days, the alteration rate drops quite rapidly over time, including under conditions of very highly renewed solution.

In a confined environment, at 90 °C, the rate gets lower than 10^{-5} g.m^{-2}.d^{-1}, which corresponds with the detection limit of the experimental techniques used.

Britholite

The initial dissolution rate of britholite of formula $Ca_9Nd_1(PO_4)_5(SiO_4)_1F_2$, where Nd simulates a trivalent actinide, is dependent on pH and weakly depends on temperature (Ea = 30 kJ.mol^{-1}). The measured value is lower than 10^{-2} g.m^{-2}.d^{-1} at 90 °C for pH values > 5.

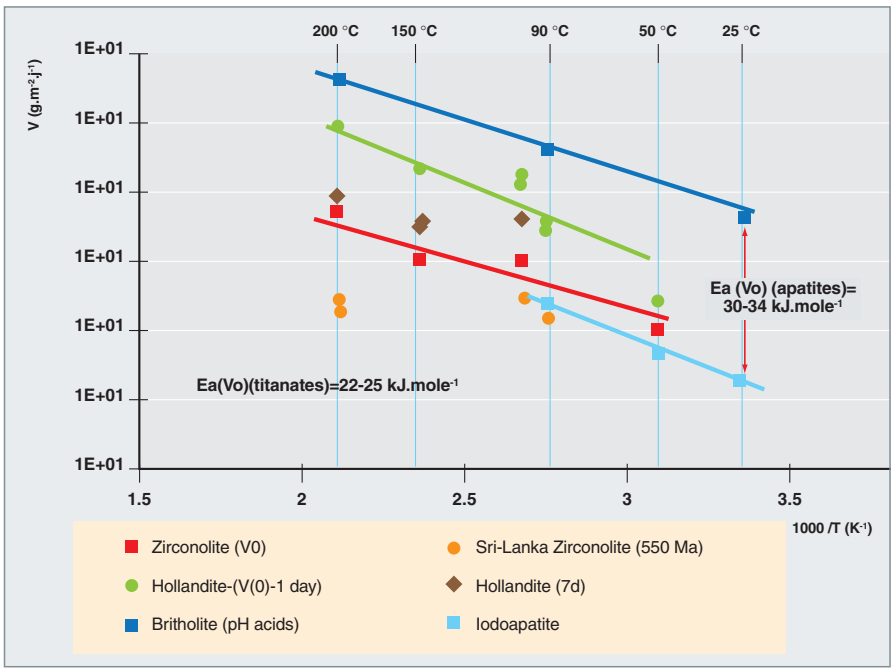

Fig. 181. Temperature dependence of the dissolution rates of titanates (i.e. zirconolite for actinide containment, and hollandite for caesium containment) and of apatitic-structure matrices (iodoapatite for iodine containment, and britholite for actinide containment).

Dependence of this initial alteration rate on temperature (Fig. 181) is also low (Ea ≈ 22 kJ.mol^{-1}). These alteration rates are not considerably modified as a function of the crystallinity degree of zirconolite, as shown by the results obtained on metamict (amorphized) natural analogues, on the one hand, and on synthetic zirconolites bombarded with heavy ions at a dose higher than the amorphization critical dose, on the other hand.

The initial alteration rate little varies between pH 2 and 13 (less than a factor 10). In addition, after a few hours the alteration rates drop to a non-measurable value (< 10^{-6} g.m^{-2}.d^{-1}), whatever the temperature may be (between 50 °C and 200 °C). However, the assumption of reaching a thermodynamic equilibrium between alteration solutions and sound zirconolite may be dropped referring to both calculations and experiments.

The halt in alteration can be explained [17] by the development of a passivating alteration layer (Fig. 182). It consists of decalcified and hydrated zirconolite thereby forming a film of little soluble metal hydroxides (Zr, Ti, Al).

Dissolution is non-stœchiometric and incongruent ($V_{Fluorine} > V_{Silica} > V_{Calcium} > V_{Phosphorus} > V_{Neodymium}$). The causes are the same as for iodoapatite: F is located in the structure tunnel and Nd and P precipitate very rapidly to form a compound of type $NdPO_4.nH_2O$ of very low solubility [15]. Calcium is then considered as the alteration tracer of the matrix.

No other alteration product could be observed though, for some conditions (an alkaline and nearly neutral alkaline environment) whre alteration rates are low (≈10^{-4} g.m^{-2}.d^{-1}), the geochemical diagnostic of solutions shows an oversaturation relative to fluoroapatite and hydroxyapatite minerals.

A mechanism for lowering the dissolution rate in the vicinity of thermodynamic equilibrium is put forth in literature [16] for a natural fluoroapatite which, on the other hand, displays pH-dependent rates and an activation energy practically identical to those obtained on a synthetic matrix. Such a mechanism can be fully considered for britholite, *a priori*, under conditions of very low renewal of alteration solutions.

Zirconolite

The alteration of zirconolite of formula $Ca_{0,8}Nd_{0,2}ZrTi_{1,8}Al_{0,2}O_7$ is incongruent. The initial alteration rates determined from concentrations of calcium (the element with the highest mobility) are very low (typically < 10^{-2} g.m^{-2}.d^{-1} at 100 °C).

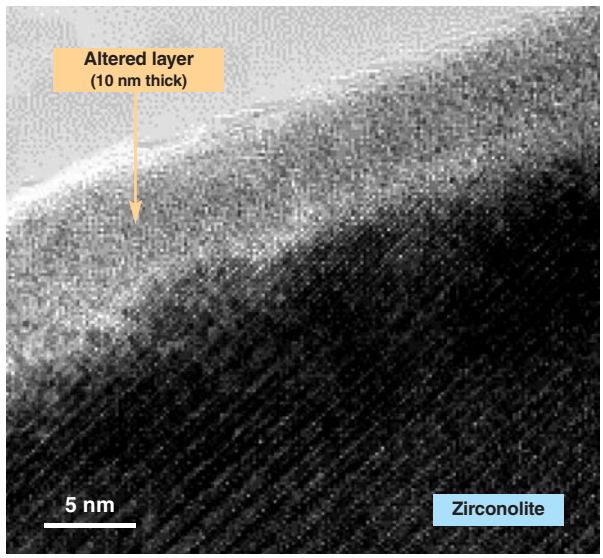

Fig. 182. Altered layer developed at the surface of an altered zirconolite, observed through transmission electron microscopy from Reference [17].

Thorium phosphate-diphosphate (TPD)

A multiparametric study [15] was conducted on TPD of formula $Th_4(PO_4)_4P_2O_7$, in which Th mimicks a tetravalent actinide and related solid solutions (PDT-U, PDT-Np and PDT-Pu). It made it possible to assess the influence on the corrosion rate of several parameters such as, e.g., pH [18] (partial orders: n = 0.31 – 0.40 in an acid medium and m = 0.37 in a basic medium), temperature (E_a = 37 - 49 kJ.mol^{-1} within the range of 4-120 °C), actinide doping ratio (no significant effect for U and Pu), specimen morphology (no significant difference between powder and sintered), presence of solution ions such as phosphates, sulfates, chlorides…

Corrosion rates are always between 10^{-5} and 10^{-8} g.m^{-2}.d^{-1}, including in very aggressive environments such as HNO_3 0.1M. The extrapolation done at pH = 7 and at 90 °C leads to a value between 5 and 8 10^{-6} g.m^{-2}.d^{-1} confirmant which corroborates high resistance of PDT and solid solutions to alteration.

By adopting an approach based on thermodynamic equilibria, secondary phases formed at the back-end of the initial dissolution reaction have been identified for each actinide investigated (Th, U, Pu, Am, Cm). Under conditions of low renewal of the alteration solution, it was demonstrated that the related thermodynamic equilibria could be rapidly reached [19]. All these phases correspond with hydrated phosphate phases with a very low solubility. Thus, under saturation conditions, the migration of the actinides released during the dissolution of the initial matrix would be rapidly and significantly delayed through precipitation within these newly formed phases.

The solid solution monazite/brabantite $Ln_{2-x}(CaAn)_{x/2}(PO4)2$

Most of leaching data is related with monazite ($NdPO_4$), and is issued from a study carried out on a natural mineral aged 500 million years or so [18]. At 70 °C, the dissolution rate depends on pH with a minimum of the order of 4.6 10^{-7} g.m^{-2}.d^{-1} in a medium close to neutrality.

Activation energy is 43 kJ.mol^{-1} (measured at pH 2). An experiment carried out at pH 2 and 25 °C on synthetic $NdPO_4$ resulted in a rate of 1.8 10^{-6} g.m^{-2}.d^{-1} in agreement with data on natural monazites.

Preliminary data on synthetic $LaPO_4$ bear out these values as the La release rate in pure water at 96 °C is lower than 10^{-6} g.m^{-2}.d^{-1}.

Ceramics: a very good resistance to aqueous alteration

All the conditioning matrices investigated exhibit early dissolution rates lower than 10^{-2} g.m^{-2}.d^{-1} (at 90 °C and with a neutral pH) which show their very high resistance to aqueous alteration.

This high performance has also to be corroborated basing upon the study of the alteration of ceramics doped with radioactive elements in order to evaluate the consequences of the self-irradiation effect. In this respect the first results collected on pellets of Pu-238- or Pu-239-bearing zirconolites are encouraging, for they do not display any significant difference if compared with ceramics where inactive neodymium mimicked occurring radioactive actinides. However, the high resistance of these ceramics to aqueous alteration no longer seems to pave the way for their use as confining matrices owing to the high performance of “conventional” matrices such as glass and concrete.

“Underwater” durability of concretes

Given their easy implementation, intrinsic properties and proven physico-chemical durability, hydraulic-binder-based materials (i.e. concretes, generically speaking) stand as a key component of the objects (package, overcontainer) and structures (dedicated civil engineering work, engineered barriers) involved in the long-term management of nuclear waste.

Within the framework of long-term deep geological disposal, underground waters bearing more or less aggressive chemical elements will constitute the major vector of degradation of these cementitious materials.

The overall strategy selected for investigating the long-term behavior of cementitious materials in saturated environment is illustrated on Figure 183 [20]. Models of chemical degradation are aimed at describing the major physico-chemical evolutions of materials (interstitial chemistry, materials flux, transport properties).

Their coupling to radionuclide (RN) retention models and/or mechanical models using the CAST3M Code and/or the ALLIANCES platform is intended to describe and integrate the RN source terms (containment / release) and the mechanical state of the objects and/or structures (mechanical behavior).

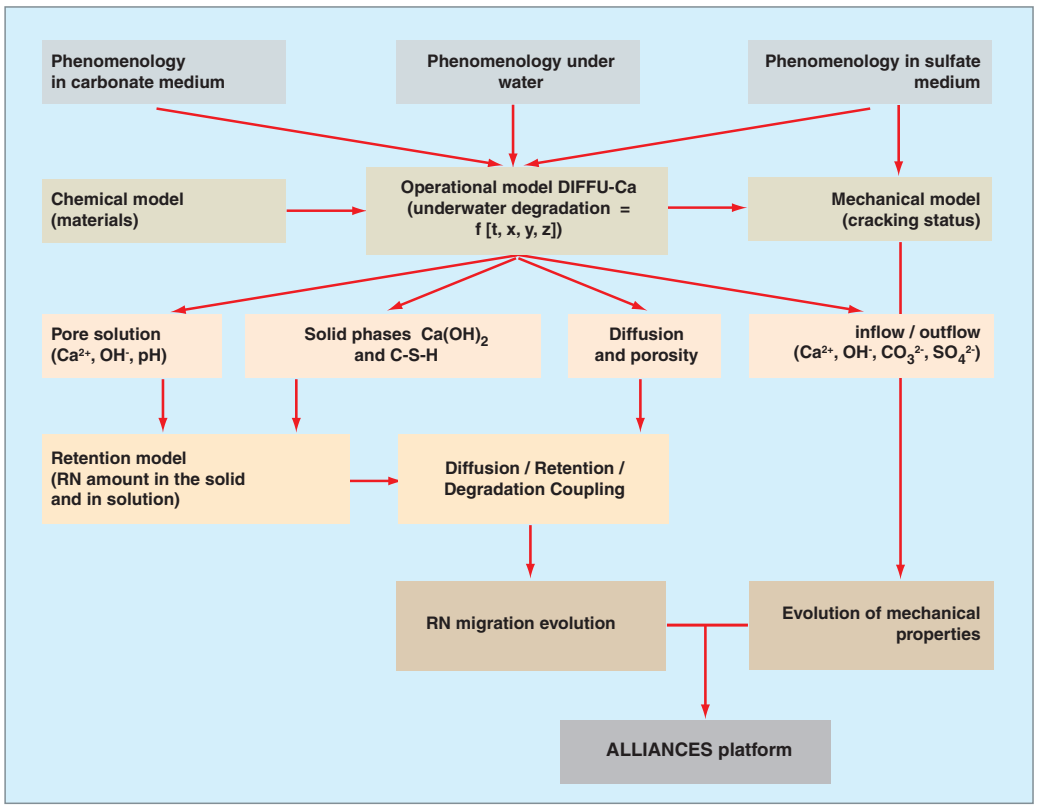

Fig. 183. Schematic representation of the approach for investigating and modelling the long-term behavior of concrete.

Chemical degradation of cementitious materials

Concretes used for management of nuclear waste (packages, structures) have been primarily formulated from Portland cement of type CEM I (100% clinker) or CEM V (a clinker with more or less substantial proportions of blast furnace ash and slag) [see the DEN monograph "Nuclear Waste Conditioning"].

The anhydrous phases which constitute these cements are essentially calcium silicates and aluminates (some of them containing iron). Once hydrated, concrete compounds mainly correspond with hydrated calcium silicates (C-S-H), portlandite [$Ca(OH)_2$], hydrated aluminates (especially ettringite, AFt and monosulfoaluminate, AFm).

A broad range of experimental conditions has been investigated at the CEA that makes it possible to compare the respective influences of the material's various intrinsic or extrinsic parameters upon its resistance to underwater degradation (évolution of its chemical, mineralogical, microstructural, transport, and mechanical properties).

The nature of the cement used influences degradation kinetics owing to its mineralogical composition (low portlandite content in CEM-V cements) and its different diffusional properties (lower diffusivity in CEM-V cements) (Fig. 184a).

On the other hand, as regards concretes (paste + sand + aggregates), the decalcification depth is not influenced by granulates and, so, the degradation process is still fully driven by the hydrated cement paste [21] (Fig. 184b).

The increase in the diffusional process rate under temperature has a direct impact on decalcification kinetics, just as calcite precipitation on the material's surface lowers it through porosity clogging (Fig. 185).

In most cases the evolution of cementitious materials in presence of water may be summarized as the leaching of the phases that prove very rich in calcium. The prevailing phenomena in it are portlandite dissolution and C-S-H decalcification (Fig. 186). Dissolution is controlled by diffusional transport processes, so that the alteration depth is proportional to the square root of time (Fig. 184 and 185).

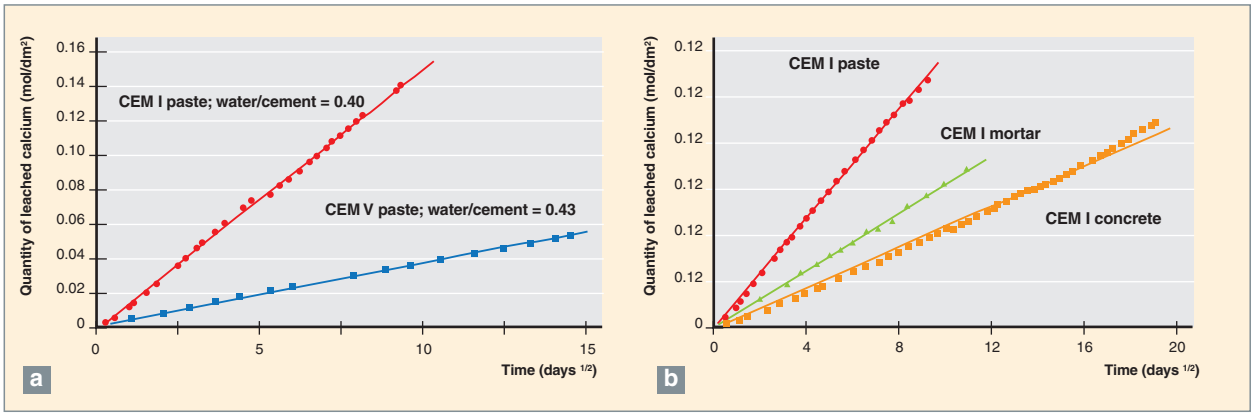

Fig. 184. Comparative evolution of calcium leaching flows as a function of: a) the cement type for CEM I and CEM V pastes, b) the type of material, paste, mortar, or concrete (lines = simulation results, symbols = experimental results).

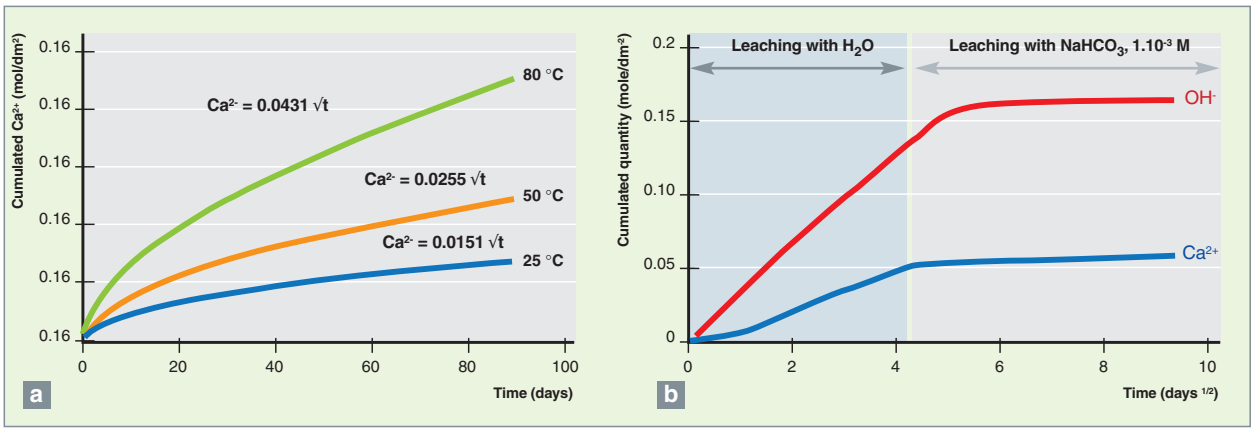

Fig. 185. Comparative evolution of calcium leaching flows versus time: a) as a function of temperature, b) in a carbonate environment.

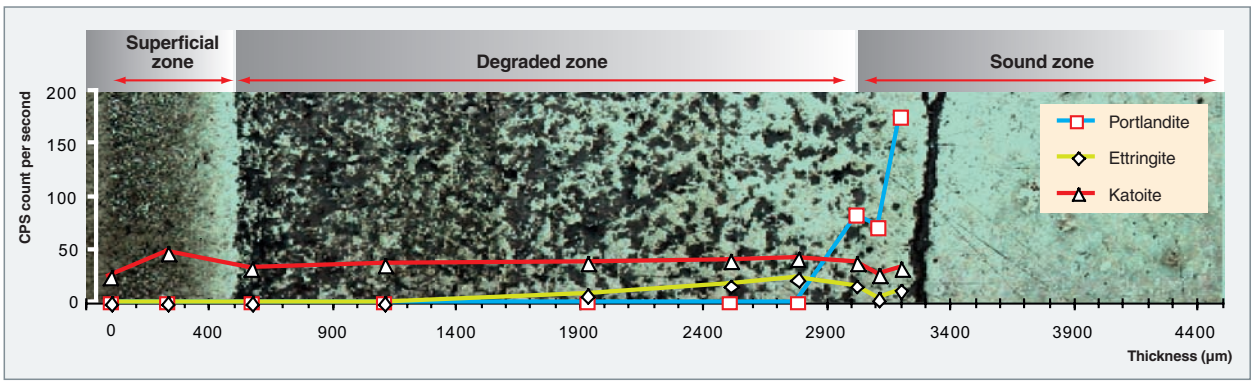

Fig. 186. Micrograph of degraded zones in a CEM I cement paste and projection of mineralogical profiles measured through X-ray diffraction [22].

The DIFFUZON model which allows for the detailed description of the evolution in the cementitious (especially CEM-I-based) system [23], is based on thermodynamic equilibria between mineral phases, and on mass transfer processes. It enables mineralogical evolutions to be finely depicted, and requires to take into account the feedback of dissolution / precipitation phenomena on transport coefficients and, so, on materials microstructure [24] (Fig. 187).

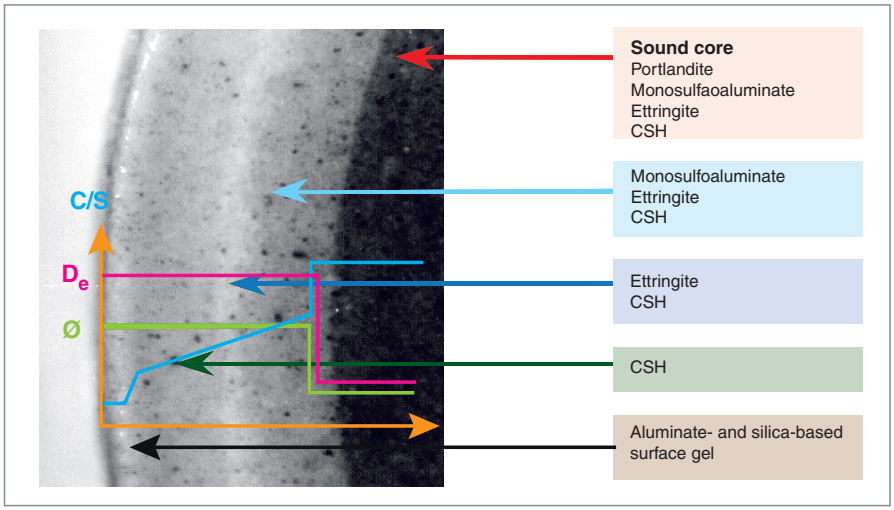

Fig. 187. Phenomenological model of chemical degradation in a cementitious material, and reconstruction of the physico-chemical parameters (C/S, calcium/silica ratio, De calcium effective diffusion coefficient, ϕ porosity).

Chemo-mechanical degradation of cementitious materials

Underground waters may feature substantial SO_4^{2-} sulfate ions concentrations (15 mmol/L on the average). These ions are likely to diffuse through the porous network of cementitious materials and react with aluminate phases, thereby entailing expansive phase precipitation (ettringite and gypsum) [26]. In these newly formed phases grow crystallization pressures which generate stresses, the latter inducing a damage which is likely to reach the environment's cracking and/or fracturing (Fig. 188). Basing on the DIFFU-Ca model, a preliminary phenomenological modelling enables the macroscopic mechanical behavior of cementitious materials to be described in this configuration (Fig. 189).

In order to take into account evolutive boundary conditions and access to better understanding of couplings, especially with mechanics, a simplified model (DIFFU-Ca) was proposed and validated. This model only considers portlandite and C-S-H, and relies on the resolution of only one, but sufficient, mass balance equation for calcium (Eq. 1):

$$\frac{\partial(\phi.C_{Ca})}{\partial t} = Div(D_e.Grad(C_{Ca})) - \frac{\partial S_{Ca}}{\partial t} \quad (1)$$

where t is time, C_{Ca} calcium concentration in solution, S_{Ca} calcium concentration in the solid, ϕ the material's porosity, and D_e calcium effective diffusion coefficient.

The DIFFU-Ca model is the basic brick upon which has been built the "concrete" operational model chiefly dedicated to simulating long-term behavior of concrete engineered barriers. It allows to focus on cementitious materials decalcification by water and coupling with radionuclide migration, taking account or not of a pre-existing microcracking and/or a diffusive barrier related to, e.g., atmospheric carbonation.

These models are set up in the numerical tool CAST3m and are to be integrated more globally in the numerical platform ALLIANCES [25].

Let us take the case of highly conservative and, so, highly enveloping boundary conditions corresponding with leaching in pure water at 25 °C and at pH 7: such a case applied to a CEM-I concrete (cf. Fig. 184b) would result in a degraded thickness of the order of one dozen centimeters over 1000 years.

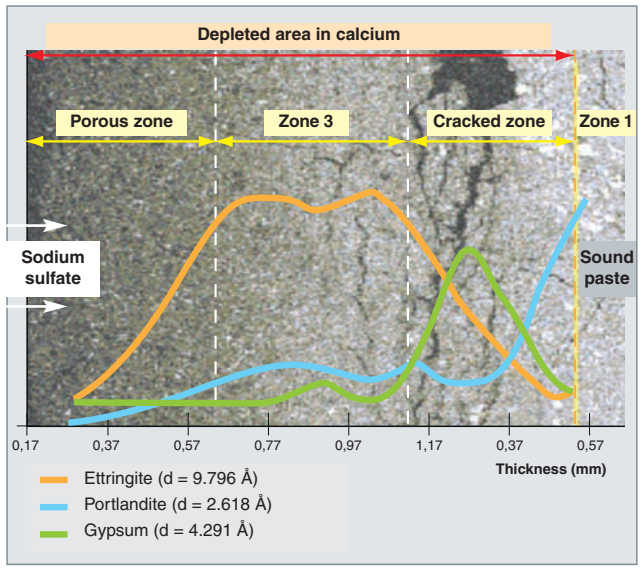

Fig. 188. Microcracking damage of a cementitious matrix due to sulfate ion intrusion, and projection of the areas of localized expansive phases (the latter being identified by X-ray diffraction).

Advances in knowledge, understanding and goals lead to take into account systems increasingly closer to reality, and so increasingly complex, coupled and integrated. As a consequence, outlooks and efforts to be continued are particularly focused on the following items:

- Couplings between physico-chemical evolutions and mechanics (degradation / damaging /cracking). In this field

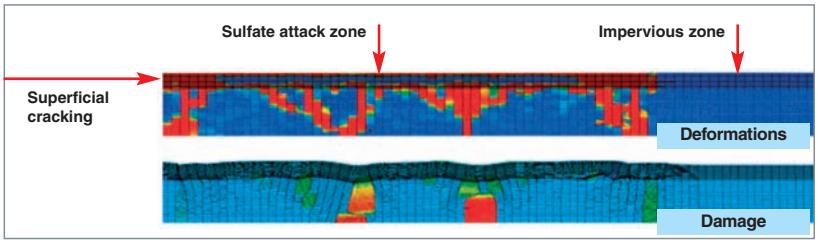

Fig. 189. Maps of damage pattern (top) and deformation areas (bottom) calculated for a cementitious materials platelet after leaching in a sulfate medium.

the latest promising advances have focused on developing a micromechanical approach which relies on homogeneization techniques [27] implemented in the ALLIANCES platform [28] as well as on techniques for 3D-reconstruction of porous media using tools endowed with very high-density mesh systems coupled with optimized multi-physics solvers.

- The multiscale component (homogeneizations, meshing, numerical resolutions). The aim is integrating the effects locally evidenced up to the scale of the structure itself.

Transformation of engineered barrier clays

The barrier function of clays

Within the multibarrier containment system investigated for geological disposal, clay materials play a prominent role in terms of safety, whether they are the host rock of the disposal site (argillite) or the basic material of engineered barrier systems (EBS), if any.

The initial function of the engineerred barrier is limiting the *centripetal flow* of deep waters towards the package and its envelopes. In this case, the swelling properties featured by swelling clays (smectites), and clay material's low porosity and extreme tortuosity are beneficial, as they limit water flow and so the alteration of the near field other materials.

In the event of an early containment failure due to alteration of the first envelopes, the engineerred barrier will also play the role of a *centrifuge* barrier in order to mitigate radionuclide migration from the package to the biosphere. Here are concerned the retention properties of smectites and, more generally, of clay materials (with the related minerals).

In the first hundreds of years of operation of the repository, the near field clay materials will be rehydrated by the site waters and will undergo overheating due to the presence of exothermal packages. Under such conditions metallic corrosion (affecting container, overcontainers…) will be allowed to start, develop, and generate chemical disorders which will affect clay materials during the various phases of the near field evolution, thereby giving rise to substantial pH and redox changes, as well as the release of a high iron amount into the environment. Transformations will occur at the expense of clays at reference temperatures of the order of 80 °C and in saturated and reducing environment, accordingly with commonly retained scenarios.

Metal / clay reactivity raises the issue of long-term stability of clays in terms of durability of the clay material's containment performance and, so, of the impact of alteration in their swelling or retention properties.

Clay reactivity in presence of iron in natural environments

In the environments of marine deposits or along sedimentary sequences, reduced iron-rich pattern often induce the *formation of iron-bearing non-swelling minerals with low retention potential*, of chlorites and serpentines such as, especially, berthierine. However the analogy cannot go further, for metallic iron is not occuring in such natural systems. Reversely, it is present in some meteorites which stand as the only analogue actually known in our system. As a matter of fact, in the early ages of the solar system, silicate dusts, metallic elements and ice accreted. Some of them experienced sufficient growth for radioactive decay mechanisms to generate significant overheating (up to a hundred °C) for a few million years during their interstellar trip. An aqueous alteration can then occur within the matrix of the meteorites on contact with metal (Fig. 190).

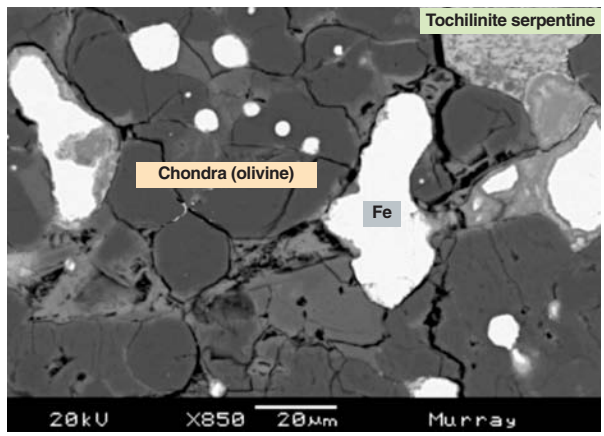

Fig. 190. Metal (white) / silicate (grey) reactive assembly in meteorites.

The hydrated phases resulting from this phenomenon are primarily iron-rich phyllosilicates (Fig. 191): serpentines, chlorites, Fe-smectites. Cronstedtite, an iron-rich phyllosilicate mineral of the serpentine family, can be observed on direct contact with metal. Cronstedtite is described as an early phase which has crystallized in the early steps of metal alteration. The analogic studies carried out on iron-clay natural systems in presence of fluids and at temperatures of 20-150 °C, clearly prove aqueous alteration of metallic iron in an aluminosilicate system at a low temperature induces the formation of iron-bearing phyllosilicates of the serpentine type with a 7 Å mesh parameter, as well as of chlorites at high temperatures. This means that the confining properties of swelling clays and argillites during their reaction with metal-iron are well and truly jeopardized.

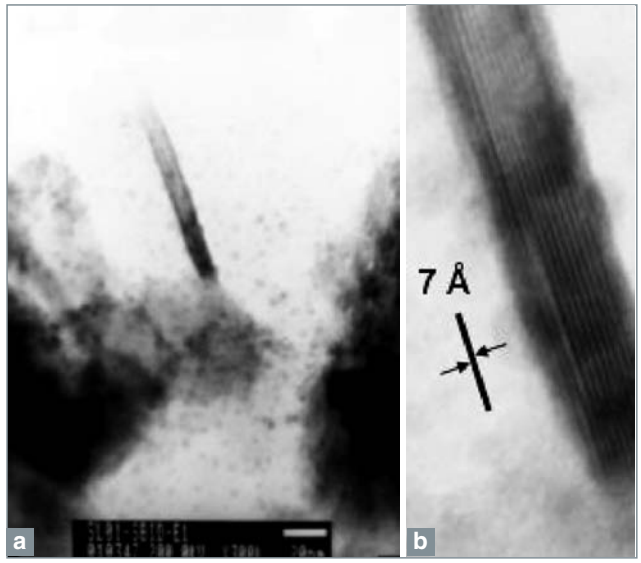

Fig. 192. a) alteration gels of smectite (Texas bedeillite) in presence of metallic iron with crystallization of iron-bearing serpentine rod, b) iron-bearing serpentine (berthierine) crystals issued from Si-Al-Fe gels.

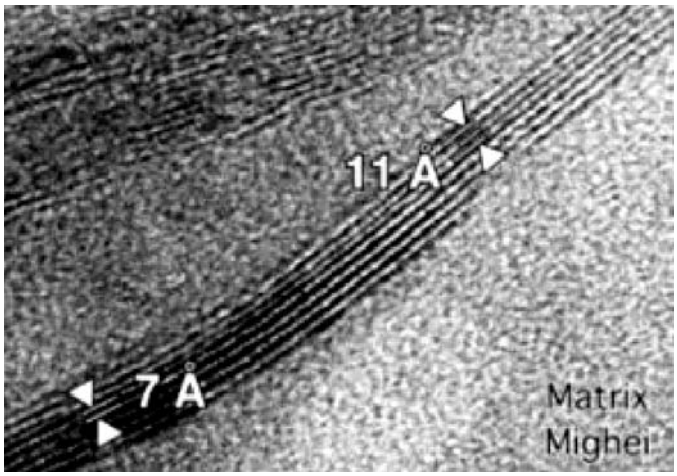

Fig. 191. Iron-bearing serpentine (cronstedtite) with a lattice parameter of 7 Å formed on contact with metal in a meteorite.

Metal / clay reactivity was investigated identifying the geochemical and mineralogical controls which impose constraints on the evolution of the system. A number of clays have been studied in presence of pulverulent metallic iron within a temperature range of 25-200 °C and with a wide variety of experimental solutions going from pure water to site water [29-31].

Irrespective of the type of clay, an attack of clay smectites by metallic iron can be observed as early as 80 °C, which results in smectite conversion into an amorphous gel. Depending on conditions of temperature and iron input to the environment, this gel may grow and form iron-rich serpentines (Fig. 192). In other terms, the alteration of a mineral (clay) promotes the crystallization of another mineral of different crystallographic structure (Fe-serpentines, berthierine).

Dioctahedral smectites display a very high reactivity with respect to trioctahedral species (saponite). Smectites are all the more reactive as the following conditions exist: wide opening of the interfoliar space, high Fe^{3+} content, Fe^{3+} under the form of octaedric clusters, and tetraedric charge deficit (beidellite). The heterogeneity of the side faces of smectites enhances their reactivity by favoring structural protons involvement in metallic corrosion [29].

The reaction between metallic iron and smectite is direct (i.e. results from a physical contact), and takes place within smectite itself [30] through structural water and the related protons. This enables us to define the phenomenon of smectitic corrosion [32] identified in the case of compacted clays.

In any case metal / clay reactivity is accompanied with a significant alteration of smectites which is revealed by a sharp decrease in the related cationic exchange capacity (Fig. 193). Reactional thresholds are thus evidenced, especially regarding metallic iron supply [29], as is clearly shown on Figure 193. Metal / clay reactivity is so maximized when metallic iron is available in high amounts [31] and when the Fe^{2+} flow issued from corrosion is high [32].

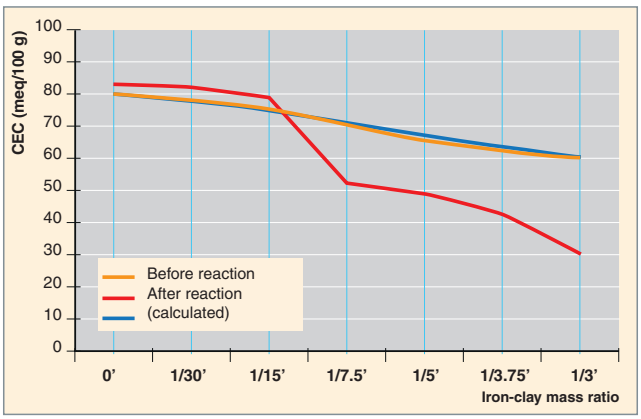

Fig. 193. Evolution of the cation exchange potential of (FoCa-7) clays versus the iron-clay mass ratio of the reactional system.

Clay alteration effects upon waste repository safety

The reactional processes depicted hereabove have been determined in a dispersed environment. In a compacted environment, the experiments Stripa and "Corrosion in argillaceous medium" [32] have shown that the newly formed iron-bearing products (7 Å serpentine) are the same, which suggests that reactional processes in dispersed or compacted environments are identical. However, in a compacted environment more realistic as regards migration and chemistry/transport coupling conditions, and so closer to conditions prevailing in a marl clay site, the potential role of textural heterogeneities on reactivity amplitude and development have to be taken into consideration.

For the kinetics of metal / clay reactivity is not merely thermally activated. Other parameters are likely to be involved, especially reactant availability, which is conditioned, first, by the corrosion processes freeing iron into the system, and, secondly, by water activity which allows smectite to be turned reactive.

In this respect, any heterogeneity in water distribution and availability in the host rock (argillite) as in the whole of the near field, is likely to exert a direct influence upon reactivity. For example, as regards swelling-clay-based engineered barriers, conditions of compaction, emplacement and initial water content will play an important role in reactivity initiation and development. In the case of site argillites, sedimentary heterogeneities, fracturing network and the whole mechanical cohesion are able to locally alter water circulation through the near field and allow iron / clay reactivity to be possibly extended to the host rock argillite.

During the early times of near field operation, water availability is also a function of the environmental perturbations due to digging and to the heat released by packages. This induces an early dehydration which is accompanied with a whole set of changes in the near field that may be chemical (oxidation, mineral phase alteration…) and mechanical (recession, cracking, fracturing…). Such perturbations can generate a set of preferential paths which strengthens the influence of pre-existing heterogeneities, and may enhance reactivity locally. This process may have consequences in relation with safety, since it is likely to locally entail an early rupture of the confining envelopes.

Another of the key issues in safety assessment in relation with near field reactivity will be to know whether this reactivity starting locally may be maintained or coupled with the precipitation of new mineral phases following the dissolution / crystallization process. This precipitation may entail a porosity clogging which will stop water flow and will so induce a drop in reactional rates. Hydrodynamics will then be transferred to a purely diffusive system, which will considerably restrain near field reactivity in space and time, and so strengthen the durability of materials (clays, argillites, steels) involved in containment.

The robustness of the safety assessment will partly rely on determining the impact of each of these processes within the overall reactivity of steels in clay medium.

References

[1] ANDRA, Dossier Argile 2005.

[2] M. Schlegel, C. Bataillon, K. Benhamida, C. Blanc, D. Menut and J.L. Lacour (2008), "Metal corrosion and argillite transformation at the water-saturated, high temperature iron-clay interface: a microscopic-scale study", *Applied Geochemistry*, in press.

[3] J. Wilson, D. Savage, J. Cuadros, M. Shibata and K.V. Ragnarsdottir, "The effect of iron on montmorillonite stability", (I) Background and thermodynamic considerations, *Geochimica et Cosmochimica Acta*, 70, pp. 306-322, 2006.

[4] O. Bildstein, L. Trotignon, M. Perronnet and M. Jullien, "Modelling iron-clay interactions in deep geological disposal conditions", *Physics and Chemistry of the Earth*, 31, pp. 618-625, 2006.

[5] D. Neff. "*Apport des analogues archéologiques à l'estimation des vitesses moyennes et à l'étude des mécanismes de corrosion à très long terme des aciers non alliés dans les sols*", Ph. D. Thèse Université de Technologie, Compiègne, France, 2003.

[6] N. Godon. Dossier de Référence sur le Comportement à Long Terme des Verres Nucléaires. http://www.cea.fr/energie/dossier_gestion_des_dechets/les_dechets_radioactifs. in "*Les déchets scientifiques à haute activité et vie longue*". Rapport scientifique du CEA. Axe 3. Dossier final. Déc 2005. Bibliographie. N. Godon *et al.* 289 p.

[7] E. Vernaz, S. Gin, C. Jégou and I. Ribet, "Present understanding of R7T7 glass alteration kinetics and their impact on long-term behavior modelling", *Journal of Nuclear Materials*, 298 (1, 2), pp. 27-36, 2001.

[8] P. Frugier, S. Gin, Y. Minet, T. Chave, B. Bonin, N. Godon, J-E. Lartigue, P. Jollivet, A. Ayral, L. De Windt and G. Santarini, "SON68 Nuclear Glass Dissolution Kinetics: Current State of Knowledge and Basis of the New GRAAL Model", *Journal of Nuclear Materials*, 380, pp. 8-21, 2008.

[9] F. Bouyer, G. Geneste and S. Gin, "Hydrogen-sodium interdiffusion in borosilicate glasses investigated from first principles", *Journal of Non-Crystalline Solids*, 352 (28-29), pp. 3147-3152, 2006.

[10] C. Cailleteau, F. Angeli, F. Devreux, S. Gin, J. Jestin, P. Jollivet and O. Spalla, "Insight into Silicate Glass Aqueous Alteration Mecanisms", *Nature Materials*, 7, pp. 978-983, 2008.

[11] A. Verney-Carron, S. Gin and G. Libourel, "A fractured Roman glass block altered 1 800 years in seawater: analogy with nuclear waste glass in deep geological repository", *Geochimica et Cosmochimica Acta*, 72, pp. 5372-5385, 2008.

[12] G. de Combarieu, "*Altération du verre de confinement de déchets type R7T7 en condition de stockage géologique*". Thèse de l'université de Paris XI, UFR Scientifique d'Orsay, 249 p., 2007.

[13] I. Ribet *et al.*, "The V0 - Vr operational model for the long-term behavior of vitrified R7T7 waste packages. Advances for future nuclear fuel cycles", Nîmes, Atalante France, 21-6-2004, pp. 1-8.

[14] C. Guy, F. Audubert, J. E. Lartigue, C. Latrille, T. Advocat, and C. Fillet, "New conditionings for separated long-lived radionuclides", *Comptes rendus Physique*, 3 (2002), pp. 827-837.

[15] A.C. Robisson, N. Dacheux, and J. Aupiais, "Influence of the pH on the TPD dissolution", *Journal of Nuclear Material*, 306 (2002), pp. 134-146.

[16] M. W. Guidry and F.T. Mackenzie, "Experimental Study of Ignous and Sedimentary Apatite dissolution: Control of pH, Distance from Equilibrium, and Temperature on Dissolution Rates", *Geochimica et Cosmochimica Acta*, 67 (2003), pp. 2949-2963.

[17] G. Leturcq, P.J. McGlinn, C. Barbe, M.G. Blackford and K.S. Finnie, "Aqueous alteration of nearly pure Nd-doped zirconolite ($Ca_{0.8}Nd_{0.2}ZrTi_{1.8}Al_{0.2}O_7$), a passivating layer control", *Applied Geochemistry*, 20 (2005), pp. 899-906.

[18] E.H. Oelkers and F. Poitrasson, "Experimental study of the dissolution stoichiometry and rates of natural monazite as a function of temperature from 50 to 230 °C and pH from 1.5 to 10", *Chemical Geology*, 191 (2002), pp. 73-87.

[19] N. Dacheux, N. Clavier, A.-C. Robisson, O. Terra, F. Audubert, J.-E. Lartigue and C. Guy, "*Immobilisation of actinides in phosphate matrices*", Comptes rendus Chimie, 7 (2004), pp. 1141-1152.

[20] C. Richet, C. Gallé, P. Le Bescop, H. Peycelon, S. Bejaoui, I. Tovena, I. Pointeau and P. Lovera, "*Synthèse des connaissances sur le comportement à long terme des bétons. Applications aux colis cimentés*", Rapport CEA- R-6050 (2004).

[21] F. Adenot, B. Gérard and J.-M. Torrenti, "*La dégradation des bétons / État de l'art*", in "La dégradation des bétons – Couplage fissuration – dégradation chimique", conducted by J.-M. Torrenti and coll., Hermes Science Publications, Paris, 1999.

[22] H. Peycelon, C. Blanc and C. Mazoin, "Influence of temperature and cement binders on the degradation (decalcification/hydrolysis) in saturated conditions", *Revue Européenne de Génie Civil*, 10, n° 9, pp. 1107-1125 (2006).

[23] F. Adenot, "*Caractérisation et modélisation des processus physiques et chimiques de dégradation du ciment*", Thèse de l'université d'Orléans (1992).

[24] S. Bejaoui, B. Bary, S. Nische, D. Chaudanson and C. Blanc "Experimental and modelling studies of the link between microstructure and effective diffusivity of cement pastes", *Revue Européenne de Génie Civil*, 10, n°9 (2006), pp. 1073-1106.

[25] C. Gallé, H. Peycelon, P. Le Bescop, S. Bejaoui, V. L'Hostis, P. Bouniol and C. Richet "Concrete long term behaviour in the context of nuclear waste management; experimental and modelling research strategy", *Journal de Physique*, IV, 136 (2006), pp. 25-38.

[26] H. Peycelon and C. Solet, "External sulphate attack by ground water. Experimental study on CEM I cement pastes", *Revue Européenne de Génie Civil*, 10, n°9, pp. 1127-1146 (2006).

[27] B. Bary and S. Bejaoui, "Assessment of diffusive and mechanical properties of hardened cement pastes using a multi-coated sphere assemblage model", *Cement and Concrete Research*, 36, pp. 245-258, (2006).

[28] E. Stora, Q.-C. He and B. Bary, "Influence of inclusion shapes on the effective linear elastic properties of hardened cement paste", *Cement and Concrete Research*, 36, pp. 1330-1344, 2006.

[29] M. Perronnet, M. Jullien, F. Villiéras, J. Raynal, D. Bonnin and G. Bruno, "Influence of time and temperature on Fe(0)-bentonite reactivity: Insights for transitory gel formation and maturation", *Applied Clay Science*, 38, pp. 187-202 (2008).

[30] B. Habert, M. Jullien, E. Kohler and D. Bonnin, "Redox of iron in smectites", *Applied Clay Science*, Vol. 12, supplement 2, pp. 149-153, 2006.

[31] S. Lantenois, B. Lanson, F. Muller, A. Bauer, M. Jullien and A. Plançon, "Experimental study of smectite interaction with metallic iron at low temperature", 1, Smectite destabilization, *Clay & Clay Mineral* (2005), Vol. 53, No. 6, pp. 597-612.

[32] F. Papillon, M. Jullien and C. Bataillon, "Carbon steel behaviour in compacted clay: two long term tests for corrosion prediction. Prediction of long term corrosion behaviour in nuclear waste systems", *European Federation of Corrosion Series Number*, 36, Damien Féron and Digby D. Macdonald Editors (2003), pp. 439-454.

Bibliography

"Long-term prediction of corrosion damage in nuclear waste systems", editors D. Féron & D.D. Macdonald, *Journal of Nuclear Materials Special Issue*, Vol. 379 (2008), Nos 1-3.

Bataillon (C.), Martin (F.) and Roy (M.), "Corrosion monitoring of carbon steel in pasty clayey mixture as function of temperature European Corrosion Congress (EUROCORR - 2007)", 09/09/2007 - 13/09/2007, Fribourg , Allemagne.

"Prediction of Long term corrosion behaviour in nuclear waste systems", D. Féron & D. D. Macdonald editors, EFC series N°36, published by Maney Publishing, London, GB (2003), ISBN 1-902653-87-4

Zolensky (M.) and McSween Jr (H.Y.), "Aqueous Alteration. Meteorites and the early solar system", J.F. Kerridge, and M.S. Matthews editors, *University of Arizona Press* (1988), pp. 114-143.

Jullien (M.), Kohler (E.), Raynal (J.) and Bildstein (O.), “Physicochemical Reactivity in Clay-Rich Materials: Tools for Safety Assessment”, *Oil & Gas Science and Technology*, Vol. 60 (2005), No. 1, pp. 107-120.

Latrille (C.), Jullien (M.) and Pozo (C.), “Element transfers in compacted clayey materials under thermal gradient” Water-rock interaction, Sardaigne, Cidu-Rosa editor, Swets & Zeitlinger publisher, 1 (2001), pp. 291-294.

Christian Bataillon, Christophe Gallé,
Patrick Le Bescop, Hugues Peycelon, Cécile Richet,
Michel Schlegel,
Physico-Chemistry Department
Frédéric Angeli, Frédéric Bouyer,
Guillaume de Combarieu, Xavier Deschanels,
Catherine Fillet, Pierre Frugier, Grégory Geneste,
Stéphane Gin, Yves Minet, Nicole Godon,
Jean-Éric Lartigue, Isabelle Ribet,
Aurélie Verney-Carron,
Research Department for Waste Treatment and Conditioning
Michel Jullien,
Nuclear Technology Department
Nicolas Dacheux,
IN2P3, Orsay Institute of Nuclear Physics[13]*,*
(now named Institute of Separative Chemistry in Marcoule[14]*)*
and Bernard Bonin,
Scientific Division

13. IN2P3: *Institut de Physique Nucléaire d’Orsay*, Orsay Institute of Nuclear Physics.
14. ICSM: *Institut de Chimie Séparative de Marcoule,* Institute of Separative Chemistry in Marcoule.

Materials Biodegradation

Microorganisms and nuclear waste

Materials introduced into the nuclear waste repository are likely to evolve (aging, alteration) as a result of not only mechanical, chemical, physical, but also microbiological factors. For microorganisms have been evidenced under extreme conditions and are often presented as a factor prejudicial to radioelement confinement [1].

In this context the aim of the investigations carried out is as follows:

- Better defining the possibility of a bacterial growth within a repository for various types of packages, whether considered in their environment or not;
- Characterizing the influence that microorganisms might have on long-term behavior of occurring materials, whether they are embedding materials (bitumen, hydraulic binders), engineered barrier materials (hydraulic binders) or packaging materials (steel).

As regards this first point, investigations conducted jointly with ANDRA for different types of packages have shown that type C packages (vitrified waste) and SF (spent fuels) do not present any risk of bacterial growth in themselves, whatever their environment may be.

Nevertheless, concerning the baseline repository site, it is assumed that bacterial activity is likely to occur in the hydraulic conditions under consideration (presence of underground waters in the package environment).

Biodegradation of embedding materials: bitumen

Assessing the influence of the microbian parameter in the environment of a bituminized package relies on a (mass and energy balance) thermodynamic study based upon a qualitative and quantitative inventory of present materials (bitumen, salts), and of the composition of the site water likely to be present in the environment of these packages [2].

On acount of its organic nature the bimuminized waste is likely to undergo biodegradation phenomena. Besides, it contains all nutrient (C, H, O, N, P, S) and energetic elements (electron donors and acceptors such as nitrates or sulfates) necessary for bacterial activities. These biodegradation phenomena are thermodynamically possible, yet limited to less than 10% of bitumen mass, the limiting factor being the amount of oxidants present in packages.

As a matter of fact, for a STE3 embedded waste, this phenomenon affects 1 weight percent of bitumen, referring to a diffusional kinetic of biodegradation, and it does not significantly interfere with salt release mechanisms during its degradation in persence of water.

The main direct or indirect consequences of bacterial growth in the environment of STE3 bituminized waste packages are the following:

- Microbial generation of gas (CO_2, N_2 and H_2S under anaerobic conditions). This generation is on the order of 8 L/package/year on the first year, and it is expected to drop to less than 1 L/ package/year after 40 years [3-4];
- Biomass production. The microorganisms generated during bituminized waste biodegradation can fix radionuclides on their outer wall. This microbial fixation is expected to delay radionuclide migration on account of strong interactions between microorganisms and particles in the geological environment.

Biodegradation of embedding materials: hydraulic binders

The chemical composition of hydraulic binders indicates that a direct biodegradability by microorganisms cannot be contemplated (owing to the absence of nitrogen and phosphorus). By contrast, the presence in the concrete package environment of all the elements required for bacterial activities may induce an indirect attack of the material by acids issued from microorganism metabolism.

These microorganisms may belong to one of the following three categories:

- Sulphate-oxidizing bacteria that generate sulfuric acid;
- Nitrifying bacteria that generate nitric acid;
- Mushrooms that generate organic acids.

Biodegradation of cementitious matrices by organic acides issued from microbial metabolism is hardly mentioned in literature. Now, organic acid generation by mushrooms, especially by heterotrophic microorganisms (*Trichoderma viride* and *Aspergillus niger*), is particularly aggressive on cementitious matrices [5] as a result of:

- The complexing effect of organic acids with calcium, a major constituent of the material;
- High generation of biofilm on the material's surface by these microorganisms, which induces a locally high acidity.

These mushrooms have been contacted with cementitious matrices for one year using the experimental device shown on Figure 194, with a continuous circulation of the culture medium containing the microorganisms [6].

A matrix degradation about 5 mm thick can be observed after a 9-month contact with the microorganisms in a solution at pH = 4, as well as very high fragility of the material's surface (Figure 195).

In addition, it is worth noting that these works have made it possible to demonstrate the feasibility of a biodecontamination of hydraulic binders surface-contaminated by radioelements.

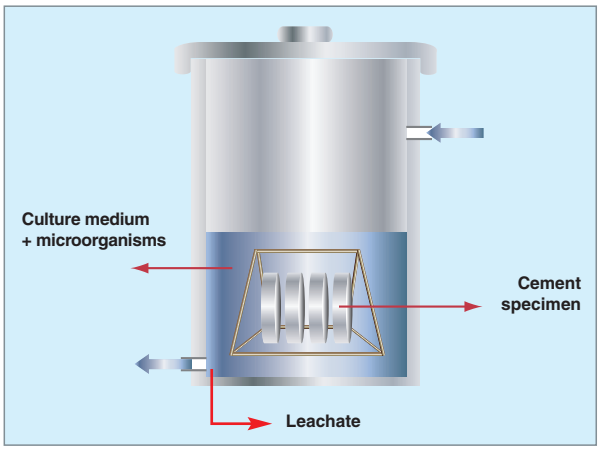

Fig.194. Experimental device for inducing biodegradation in cementitious matrices. Cement sample size: diameter = 110mm, thickness = 30mm.

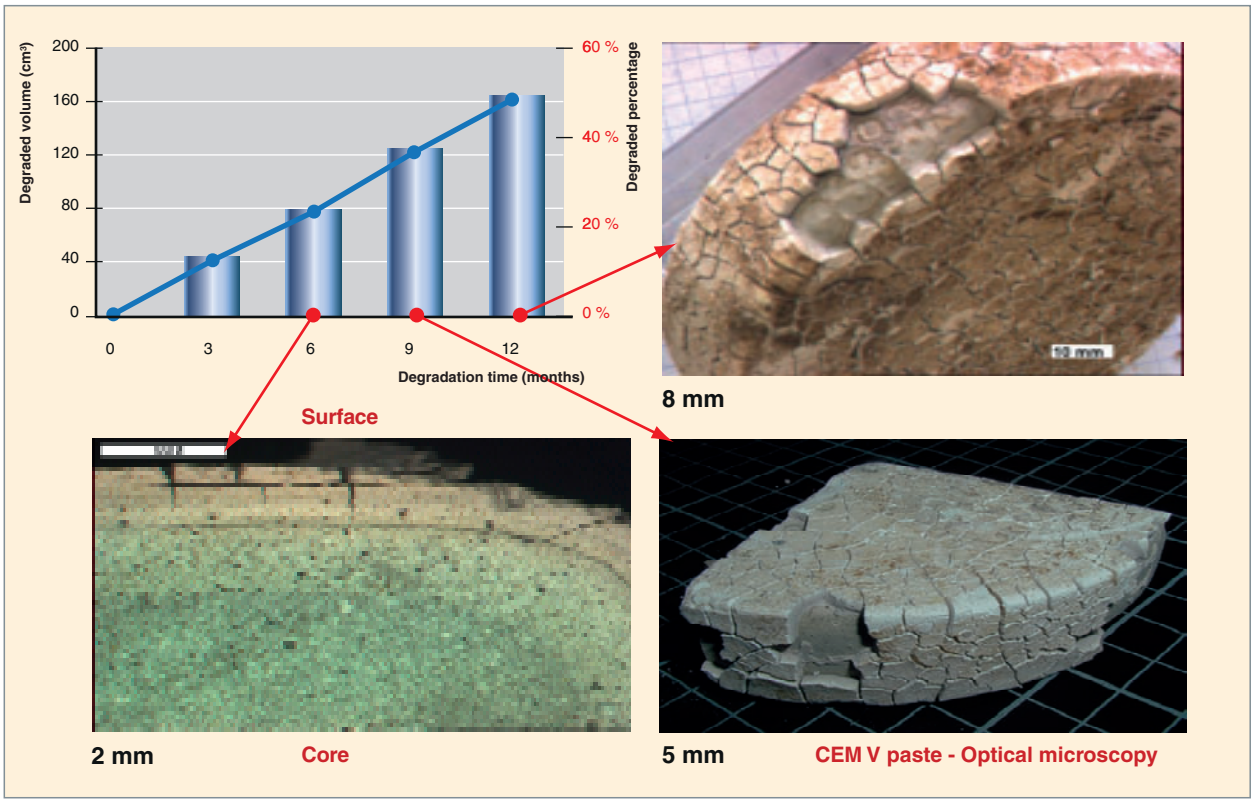

Fig. 195. Degraded volume and volume percentage of the initial CEM V cementitious matrix at the various experimentation times in presence of microorganisms.
Optical microscopy photographs show the corresponding degraded thickness.

Biocorrosion of packaging materials: steels

Even if we use the term “biocorrosion”, Standard ISO 8044 only defines microbial corrosion (i.e. “corrosion associated with the action of microorganisms present in the corrosion system”) and bacterial corrosion (i.e.“microbial corrosion due to the action of bacteria”) to name these interactions between the living world and metallic materials.

Biocorrosion is not a new form of corrosion; in particular, bacteria do not directly attack metals, but metabolisms of microorganisms alter the physico-chemical conditions existing on the metal surface. If it is obvious that biocorrosion cannot exist without microorganisms, in contrast the presence of microorganisms does not necessarily lead to biodegradation phenomena. In order to better understand the role of microorganisms, it is worth keeping in mind that corrosion in aqueous environment is an electrochemical phenomenon by nature.

Microorganisms do not alter this electrochemical nature of corrosion. If the presence of microorganisms ever accelerates the partial (anodic or cathodic) limiting reaction directly or indirectly, then the corrosion phenomenon will be accelerated. Thus, corrosion by microorganisms is well and truly of electrochemical nature and, so, does not constitute a new form of corrosion. The approach adopted consists in taking into consideration three factors which are the environment, the material and microorganisms, together with the specific parameters of each factor, as illustrated on Figure 196. This approach is developed for describing and interpreting microbial corrosion phenomena as well as for implementing preventive or remedial action.

The works conducted deal with microorganism influence on corrosion of unalloyed steels and passivated alloys such as stainless steels. They aim at understanding mechanisms under aerobic or anaerobic conditions.

- In presence of oxygen microorganism influence on the elctrochemical behavior of stainless steels leads to a significant increase in free corrosion potential (E_{cor}). An explanation of this phenomenon based on the enzymatic activity of microorganisms is proposed herein. For within biofilms bacterial cells contain enzymes, such as oxidases which catalyze generation of organic acids and oxygenated water, these products increasing the cathodic reaction [6].

- Under anaerobic conditions, crevice corrosion potential experiences a substantial decrease. This result has been obtained in presence of anaerobic sulphate-reducing bacteria (SRB), but is also reproduced in presence of sulfides alone, the latter being the main products of the metabolism of these bacteria (Table 1).

So the effect of anaerobic sulphate-reducing bacteria, often evidenced in biocorrosion phenomena, is chiefly related to the alterations (pH and sulfide generation) that these bacteria impose to the surrounding medium.

Thus, within the framework of a deep disposal facility where mixed, aerobic and anaerobic conditions will be prevailing, bacterial activity will be likely to lead not only to an increase in free corrosion potential, but also to a (pitting or crevice) localized corrosion.

Reproducing these mixed conditions in laboratory will so be the next goal in order to test the behavior of the packaging materials candidate for deep disposal conditions.

These three examples of investigation of materials biodegradation illustrate the variety of microbial reactions likely to occur within a nuclear waste repository, which are being studied at the Nuclear Energy Division (DEN) as part of programs conducted on nuclear materials corrosion and alteration.

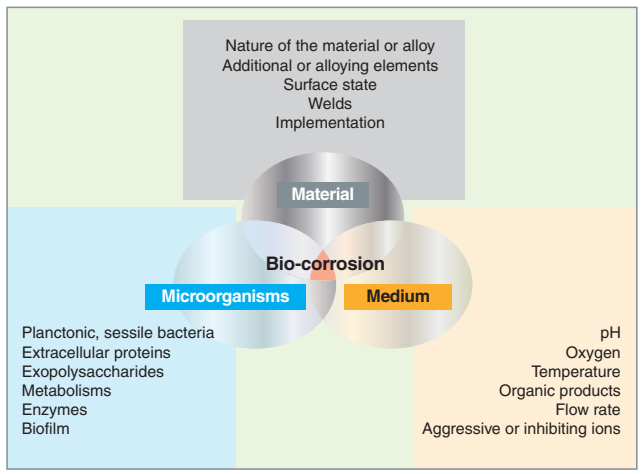

Fig.196. Biocorrosion: material-environment-microorganism interactions.

Table 8.

Compared influence of sulfate-reducing bacteria (SRB) and sulfides on the crevice corrosion potential in various stainless steels

	Seawater		Crevice corrosion potential mV/SCE		
	[S^-] mg.L^{-1}	pH	316L	254 SMO	SAF 2205
SRB	400-450	7.1	-240±15	+40±50	+60±100
Na_2S	400	7.0	-210±15	+20±50	+20±130
Sterile conditions	0.0	8.2	300±100	>300	>300

References

[1] H.A. Grogan, "The significance of microbial activity in a deep repository for L/ILW", *NAGRA Interner bericht*, 1987, NIB. 87-05.

[2] M.F. Libert, F. Jacquot, M.A. Romero and B. Besnainou, "In vitro evaluation of microbial effects on bitumen waste form", in "*Microbial Degradation Processes in Radioactive Waste Repository and in Nuclear Fuel Storage Areas*", Kluwer Academic Publishers, J.H. WOLFRAM (ed), Netherlands, 1997, pp. 275-283.

[3] M.F. Libert, "*Biodétérioration de matériaux utilisés pour l'enrobage de déchets nucléaires: un exemple le bitume*", Bulletin de la Société Française de Microbiologie, 1999, 14-4, pp. 267-271.

[4] M.F. Libert, R. Sellier, G. Jouquet, M. Trescinski and H. Spor, "Effects on microorganisms growth on the long term stability of cement and bitumen", *Scientific Basis for Nuclear Waste Management XVI*, C.G. Interrante, R.T. Palaban (eds.), Boston, Massachussets, (USA), 1992, pp. 267-273.

[5] A. Jestin, M. F. Libert, P. Thouvenot, R. Sellier and J.P. Bournazel, "*Biodégradation de matrices cimentaires*", Revue Française de Génie Civil, 2004, 8-9, pp. 1087-1104.

[6] V. L'Hostis, C. Dagbert and D. Féron, "Electrochemical behaviour of metallic materials used in seawater Interactions between enzymes and passive layers", *Electrochemica Acta*, 2003, 48, pp. 1451-1458.

Bibliography

Electrochemica Acta, Special issue: "Biocorrosion of materials", Guest Editor: D. Féron, Volume 54, Issue 1, December 2008.

Marie Libert, Anne Jestin and Pascal Thouvenot,
Nuclear Technology Department

Conclusion

Corrosion and, more generally, chemical alteration of materials is an important issue for almost all facilities or objects with an expected long lifetime. This is the case, indeed, of nuclear facilities, among other facilities. Reactor safety, fuel cycle plants as well as waste storage and disposal facilities are highly dependent on this issue. Nuclear economic competitiveness is also deeply concerned: the related economic stakes amount to dozens of billions of euros for the world's nuclear industry. Current stakes are particularly high, for today nuclear operators want to extend the lifetime of their reactors. As for third-generation reactors, they are scheduled to last sixty years, that is twice the time initially scheduled for the previous generation's reactors. As the aging of these facilities is known to be strongly governed by corrosion phenomena, it is easy to understand the stakes involved in the efficient control of related phenomena. This justifies the DEN's ongoing research effort initiated long ago, which is aimed at predicting and mitigating corrosion.

A number of factors increase the complexity of chemical alteration phenomena in materials:

- First, phenomena of ion transport through boundary layers or already formed alteration products are *closely coupled* with chemical reactions at the interfaces. These couplings are more or less important depending the systems under investigation, for their hierachization is dependent on a whole set of factors: renewal conditions of the alterating fluid, microstructure of the material under alteration, the material's impurities contents and space distribution, the alterating layer's morphology (thickness, porosity, fracturing degree) and its (electron, ion) transport properties. Depending on their hierarchy, these couplings generate a rich, varied population of alteration phenomena, many examples of which are given in this monograph.

- Secondly, even if the resulting status of corrosion looks global and uniform, corrosion often originates in localized phenomena. The importance of crystal defects (grain boundaries) and surface defects (steps, cracks) is to be emphasized, for physico-chemical conditions in their vicinity may be quite different from those of the surrounding environment seen with a "macroscopic" eye.

- Last but not least, as could be be seen all along this monograph, corrosion's devil takes root in *details*: to quote only a few examples, the material's impurities are important, as they are likely to alter local chemical conditions; the alterating fluid composition deeply impacts on dissolution-precipitation, so that the nature of the precipitated phases may be governed by very minor elements of the solution; even bacteria may play a role, indeed, by locally upsetting pH and redox potential.

To be true, all this may leave the hopeless impression that as regards corrosion, each case is a special case. We can but conclude that, indeed, we have not yet reached a unified approach of corrosion.

A close-up of corrosion science shows it like a patchwork which only displays separate disciplines: thermodynamics, chemical kinetics, chemistry, electrochemistry, metallurgy, mineralogy, up to mechanics and even biology.

However, even if the space scales involved extend over a range of about eight orders of magnitude, some coherence emerges from the approaches implemented to describe the various corrosion phenomena, so that some leading principles can be outlined and phenomena can be somewhat ordered. From now on *ab initio* and molecular dynamics approaches make it possible to model the three major phenomena involved in any corrosion process: redox phenomena at the interfaces, chemical species transport phenomena, and dissolution-precipitation phenomena. In addition, it may be hoped that *ab initio* or molecular dynamics approaches will provide the kinetic parameters required for kinetic models. Similarly it may be hoped that models of type Diffusion-Poisson will enable the limiting steps of the corrosion process to be identified, thus providing stable grounds to the heterogeneous kinetics models under construction. This interconnection of models seems to pave the way for their unification through nesting of the space scales involved.

On the other hand, the tools we make use of for investigating corrosion are improving, indeed: a wide variety of experimental, characterizing and computational tools are now available that are likely to provide better understanding of phenomena, and allow treatment of chemistry / mechanics /transport couplings.

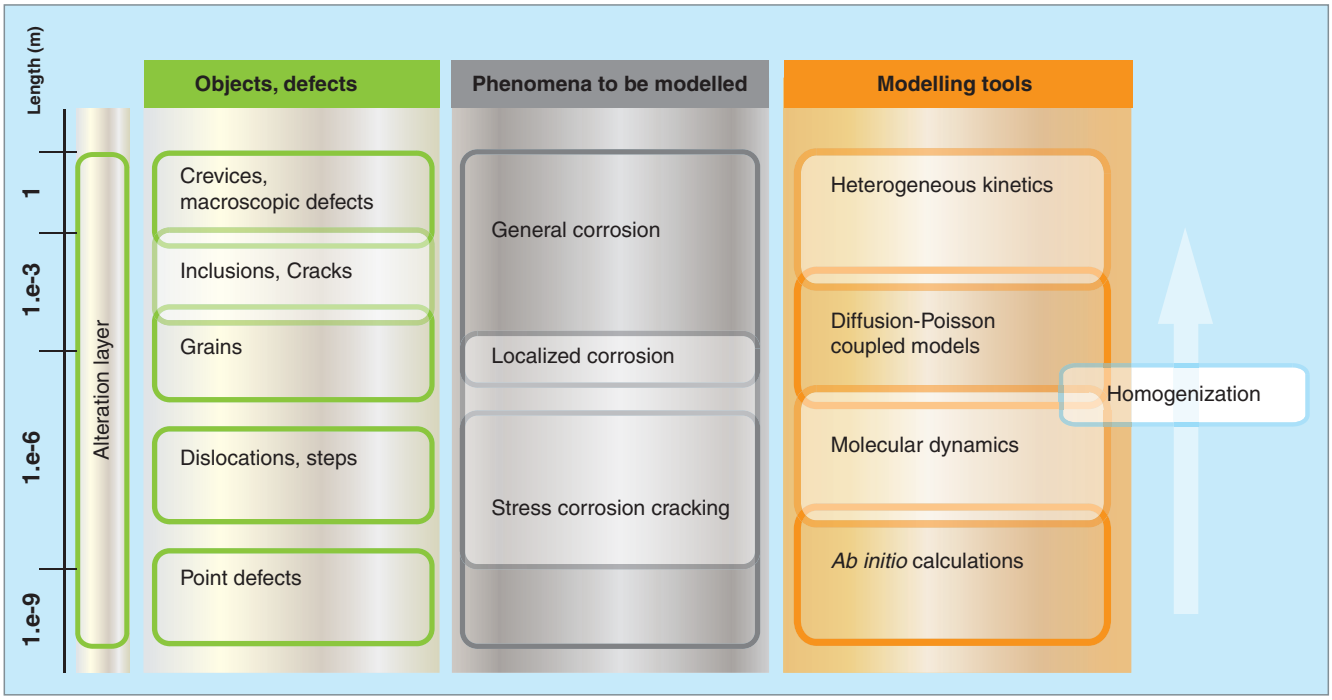

Fig. 197. Metallic corrosion as a multiscale set of phenomena, along with the tools required to describe the latter.

Let us take the challenge that, within a few years, the next edition of this monograph will be structured according to the various phenomena involved in corrosion, instead of the materials and fields of application.

Meeting this challenge will first mean making progress in *unified* understanding of the mechanisms involved in materials corrosion and chemical alteration phenomena. Now, conditions required for this understanding have been brought together and are available today, since experimental and theoretical tools do exist. So, to put it a nutshell, hopes are high, indeed.

Bernard Bonin,
Scientific Division

Glossary – index[15]

ALCYONE: a computer code tailored to model fuel rod thermo-mechanical behavior. 22, 43.

All volatile Treatment: see **AVT***.

ALLIANCES: a numerical platform dedicated to performance modelling and safety calculations in the context of nuclear waste disposal and co-developed by the CEA, ANDRA and EDF (hydro, transport, chemistry, mechanics…), which integrates and couples (CEA's and external) existing codes. 138, 139, 141, 142.

Allotropic: qualifies a solid which displays a crystalline structure thermodynamically stable under certain temperature and pressure conditions. An allotropic transformation consists in turning a solid from one stable crystalline structure into another. 71.

Alloy: a metallurgical product resulting from incorporation of one or several (metallic or nonmetallic) elements into a base metal. 13, 14, 16, 17, 20, 21, 23, 24, 25, 26, 55, 57, 59, 63-68, 82, 87, 89, 92, 93, 95, 96.

Alloys 600 and 690: alloys used, among others, for steam generator tubes in pressurized water reactors. 24-26, 36, 38, 40, 41, 47, 50, 55.

Amorphous: qualifies a solid with a disordered crystalline structure. 129, 130, 134, 143.

Analogue (or **analog**) (**natural**, **archaeological**)**:** natural or ancient materials (glass, metals, cements), the study of which may bring information on their long-term behavior (on the century-to-millenium timescale). 8, 110, 111, 115, 124, 128, 133, 137, 142, 144.

ANDRA: Agence Nationale pour la gestion des Déchets RAdioactifs. The French National Radioactive Waste Management Agency. 5, 9, 115, 124, 135, 144, 147.

Anodic reaction: in corrosion, oxidation of a metallic material which takes place at the anode. It is coupled with a reduction reaction (the so-called **cathodic reaction***), which consumes the electrons generated by the metallic material's oxidation and takes place at the cathode. 13, 16, 23, 24, 36, 40, 98, 99, 103, 110, 149.

Archaeological analogue: see **Analogue (natural, archaeological)*.**

ARCORR: an experimental device developed at the CEA for investigating corrosion in a clay medium. 122, 123.

Assembly: see **Fuel assembly***.

Austenitic structure: a centered-faced cubic crystalline structure that can be found in some metal alloys, especially some steels. 36, 50-54, 77-81, 85, 86, 88, 91, 92, 93, 103.

Autoclave: an airtight experimental device designed for work under given temperature and pressure conditions. 15-18, 20-23, 37, 38, 39, 41, 53, 55, 122, 123.

AVT: All volatile Treatment. An ammoniac- and hydrazine-based chemical treatment of the secondary coolant system in a pressurized water reactor. 46.

Azeotrope: a mixture of liquids that cannot be separated through distillation, because the boiling point temperature of the mixture is not dependent on its composition. 103.

Behavior law US: an empirical or semi-empirical relationship between a property, e.g. of a material, and a parameter of the material, which may be intrinsic (chemical composition, microstructure…), or extrinsic (i.e. related to the environment, testing conditions: T °C, P). 71, 109.

Biocorrosion: a corrosion phenomenon initiated or accelerated by the presence of microorganisms, such as bacteria or mushrooms. 149.

Biofilm: a heterogeneous film consisting of living microorganisms and organic compounds which grows at the interfaces. 148, 149.

Bitumen: an embedding matrix for conditioning long-lived low-and-intermediate-level nuclear waste (LILW-LL). 7, 101, 107, 111-114, 147, 150.

Burnup (or **burn-up**) (also called **burn-up fraction** or **burnup rate**)**:** strictly speaking, it corresponds to the percentage of heavy atoms (uranium and plutonium) that have undergone fission over a given time interval (referred to as the "burnup fraction"). It is commonly used to determine the thermal energy produced in a reactor per unit mass of fissile material, between fuel loading and unloading operations, expressed in megawatt.days per ton (MW?d/t). (See also **Specific burnup***). The discharge burn-up is the value for which a fuel assembly must be effectively unloaded (i.e., after several irradiation cycles). 20, 29, 83-86.

CASA: a thermo-hydrodynamic numerical model. CAST3M a computer simulation code dedicated to mechanics (materials, structures, fluids). 109, 114, 115, 119, 138, 141.

Cathodic reaction: see **Anodic reaction***.

CEM I: a name for Portland type cements in the cement industry which only consist of **clinker***. 139-141.

CEM V: a name for Portland cements including additions of blast furnace slag (a by-product of the steel industry) and fly ash from power stations (or natural or artificial pozzolans). 139, 140, 148.

CIRENE: a loop for studying corrosion of the PWR primary coolant system. 27, 28.

Clad (also called **cladding**)**:** the envelope surrounding the fuel, intended to ensure its containment and mechanical resistance in the reactor core. 9, 11, 14, 15, 17, 19-23, 33, 43, 44, 50, 57-59, 68-70, 79-81, 83-86, 94.

Clinker: a basic constituent of present artificial cements resulting from the baking of a mixture of about 80% limestone and 20% clay at 1,450 °C, which consists of calcium silicates and aluminates (a mixture of lime (CaO) with silica (SiO_2), alumina (Al_2O_3), and iron oxide (Fe_2O_3)). 139.

COCHISE: a corrosion code developed for zirconium and its alloys in PWR primary environment. 21, 22, 33.

15. **Note to readers**.- This set of terms and definitions is strictly intended to be a translation of the French DEN Monograph Glossary and is provided only for convenience purposes. Accordingly, the definitions herein may differ from standard or legally-binding definitions prevailing in English-language countries.

Cold work(ing): an action consisting in pressing (forging…), rolling, or drawing a metal at a temperature lower than its annealing temperature. Cold working generally increases metal resistance to deformation (which is termed work hardening). 24, 44, 48, 51, 52.

COLONBO. 113.

Complexing: the building of a structure consisting of a central metallic ion, to which other ions, atoms or molecules are bonded. The structure stability is governed by the geometry and electric fields of the species involved. 14.

Concrete: a structural material of nuclear reactor containment systems, also used for conditioning low and intermediate level nuclear waste (LILW). 7, 10, 101, 107, 114-120, 138-141, 145, 147.

Conditioning (**of radioactive waste**)**:** all the successive operations to be performed to bring radioactive waste to a stable, safe form suitable for its future management, whatever it may be: **storage***, transmutation, or **disposal***. In particular, these operations may include compaction, embedding, vitrification, and packaging. 10, 101, 111, 112, 114, 120, 129, 135, 138, 139, 146.

Conditioning matrix: see **Embedding matrix***.

Confinement: see **Containment***.

Container: a (metal, concrete…) outer envelope of a waste package. 10, 82, 101, 107, 109, 111, 112, 114, 121, 124, 128, 134, 135, 138, 142.

Containment (also called **confinement**)**:** the physical and/or chemical ability to maintain radioactive and/or toxic elements at a given location or within a given object so as to prevent or limit their dissemination or release. 7, 11, 71, 98, 101, 111, 114, 115, 121-123, 129, 133, 135-138, 142-145, 147.

Contamination (radioactive)**:** see **Radioactive contamination***.

Coolant: a liquid or gas used to transfer heat generated by nuclear fission to a heat exchanger in which steam is produced, the latter being used by a turbine to drive an alternator. The cooled liquid or gas is then sent back to the reactor. 19, 61, 63, 64, 65, 68, 69, 71, 77, 86, 87, 90, 95.

CORAIL: a loop for investigating corrosion in zirconium and its alloys. 15,19.

CORCY: a code that describes corrosion of zirconium alloys. 19-24.

CORDOBA. 116.

CORELE. 27.

Corrosion potential: the potential difference measured between a metallic material (the working electrode) and a reference electrode in contact with the same electrolyte. The free corrosion potential is measured in the absence of net (external) electric current flowing to or from the metal surface. 149.

Creep: the progressive deformation of a solid under a field of stresses applied for long periods of time. Creep may be activated by heat (it is then referred to as "thermal creep"), and/or irradiation. For some materials, such as concretes, creep may be subdivided into drying creep and basic creep. 43, 52-55, 63-65, 78, 119.

CYRANO: an EDF computer code for simulating fuel rod thermomechanics. 21, 22.

DIFFUZON. 140.

Dislocation: a defect affecting atomic arrangement in a crystalline solid. Two types of dislocations can be distinguished, which can be respectively visualized as dislocations caused by insertion of a half-plane of atoms into the crystal (edge dislocations), and as dislocations formed by cutting through the crystal along a half-plane and shifting the crystal's atoms parallel to the edge of the cut half-plane (screw dislocations). 52, 152.

Disposal (**of radioactive waste**)**:** the action of radioactive waste emplacement in a facility specifically laid out to confine it in a potentially permanent way. The disposal facility in which waste is placed without intent to retrieve it is called a repository. Retrieval would still be possible, however, in the case of a reversible disposal (see also **Storage***). Deep geological disposal of radioactive waste is the disposal of such waste in an underground facility (referred to as a deep repository or a geological repository) specifically laid out for this purpose. 7, 10, 101, 112, 129, 147.

Dpa: the number of Displacements Per Atom induced in a material under irradiation. This unit is well-adapted to quantify irradiations in metals. 53. 54. 83. 84.

ECCS: Emergency Core Cooling System. 50.

EKINOX. 108.

Embedding matrix (also called **encapsulation matrix** or **immobilizing matrix** or **conditioning matrix**)**:** an organic or mineral matrix (glass, bitumen, hydraulic binder, ceramic), the function of which is waste immobilization to avoid its dispersion, and/or long-term radionuclide containment. 111.

Encapsulation matrix: see **Embedding matrix***.

Eutectic: The melting temperature of a binary mixture depends upon the mixture proportions. It may be significantly lower than the temperature of the two pure components, and reaches its lowest value with a composition referred to as the "eutectic" composition. 77, 86, 88, 90, 91.

Expansion (**roll**)**:** see **Roll expansion***.

Fast neutron reactor (also called **fast reactor**)**.** 77, 83, 86.

Ferritic: qualifies a metallic phase crystallized in the body-centered cubic system (by analogy with ferrite made out of pure iron). 36, 77-79, 81, 85, 87, 88, 93.

Fission products (**FPs**)**:** nuclides generated either directly through nuclear fission, or indirectly through disintegration of fission fragments. 95.

Fluence: the total number of neutrons received per unit area during an irradiation. 30, 53.

FoCa-7 clay: Calcium smectite clay, also referred to as Fourges-Cahaignes clay, mainly consisting of an interstratified kaolinite-beidellite compound, together with ancillary minerals (quartz, kaolinite, goethite, calcite). This clay is contemplated for use as a material for sealing elements or engineered barriers in radioactive waste disposal facilities. 121, 122.

Fretting: material wear under the conjugate action of friction (as a result of low-amplitude vibratory motion) and corrosion. (This term is applied in particular to the wear affecting a fuel rod clad at the contact point with the spacer grid). 59.

Fuel assembly: in the core of a water-cooled reactor, fuel rods are gathered together in clusters of suitable rigidness which are set in place with a definite position in the reactor core. The so-called "assembly" is the whole of this structure, grouping one hundred to a few hundred rods, which is loaded into the reactor as a single unit. 14, 33, 52, 57, 71, 80, 84, 123, 131, 145.

Fuel cycle: the whole series of stages which nuclear fuel is to follow. The cycle includes ore mining, fissile material concentration, enrichment, fabrication of fuel elements, their use in reactors, **spent fuel treatment***, possible **recycling*** of heavy elements so retrieved, as well as radioactive waste **conditioning*** and **disposal***. 101, 103, 121, 147.

Fuel pellet: see **Pellet** (**fuel**)*.

Fuel rod: see **Rod***.

Galvanic coupling: an electric contact between two different materials. 46, 104.

General corrosion: corrosion that proceeds over all the surface of a material. 9, 11, 13, 23, 26, 28, 33, 35, 77, 79, 80, 82, 83, 97.

Generation IV: the usual name for an international collaboration (Generation IV International Forum) designed to develop fourth-generation nuclear systems. 61, 71.

GFR: Gas-cooled Fast Reactor. 61.

Glass: a confining matrix used for conditioning high-level nuclear waste (HLW). 129.

GRAAL: a model of nuclear glass alteration. 131, 132, 134, 135, 145.

Graphite. 71.

Hard rolling: see **Roll expansion***.

Hastelloy: a series of nickel alloys used at high temperatures. 61, 71.

Helium. 63.

High-performance concrete (**HPC**)**:** a concrete that displays a compressive strength of 60-120 MPa owing to a specific formulation endowing it with high compacity as well as low porosity. 118, 119.

HLW-LL: Long-Lived High-Level Waste. 129.

Illite: a clay mineral of formula $(K,H_3O)(Al,Mg,Fe)_2(Si,Al)_4O_{10}[(OH)_2,(H_2O)]$. 127, 128.

ILW-LL: Long-Lived Intermediate-Level radioactive Waste.

Immobilizing matrix US**:** see **Embedding matrix***.

Impedance measurement: a technique for measuring the electrical characteristics of a system (resistance and capacity - electrical impedance), as well as their variations. 23.

Intergranular corrosion: a corrosion located at the boundary grains of a crystalline material or at their close neighbouring. This is a specific case of **localized corrosion***. 9, 78, 103-105.

Internals (also called **vessel internals**)**:** an abbreviation for the vessel internal equipment in a reactor. 11, 50, 52-54, 133.

Interstitial atom: see **Point defect***.

Irradiation: exposure to radiation of a living organism or substance. 7, 20, 30, 52, 74, 82, 112, 138.

JACOB. 113.

Leaching: the contacting of a solid body with a liquid with the purpose of extracting some elements. By extension, refers to any experiment focusing on the alteration of a solid in a liquid. 112-114, 124, 139-142.

Lepidocrocite: a mineral corresponding to the γ-FeO(OH) polymorph. 110, 116.

LFR: Lead (alloy)-cooled Fast Reactor. 61.

LILW-LL: Long-Lived Low and Intermediate Level radioactive Waste. 111.

Localized corrosion: a corrosion that concentrates preferentially on discrete sites on the surface of a material. It may appear as cracks, pits, or grooves. 11, 30, 34, 83, 149, 152.

Magnetite: a ferrimagnetic mineral of the oxide family. It crystallizes in the cubic system, and is part of the spinella group. Its chemical formula is Fe_3O_4. 30, 88, 89, 108, 109, 116, 126-128, 134.

Martensitic (**structure**)**:** a face-centered cubic (FCC) crystalline structure found in some metallic alloys, especially in some steels.

Matrix (embedding)**:** see **Embedding matrix***.

METEOR: a CEA computer code for modelling fuel rod thermomechanics. 21, 43.

Microstructure: in the case of nuclear fuel or a material, the form, size, and ordering of its components (grains of a polycrystalline material, minerals) and of its voids (porosity, vacancies…). 52.

Minor actinides: heavy nuclei formed in a reactor through successive neutron captures from the fuel nuclei. These isotopes* mainly are neptunium (237), americium (241, 243), and curium (243, 244, 245). 129, 135.

Mixed OXide fuel: see **MOX fuel***.

MOX fuel (also called **Mixed OXide fuel**)**:** a nuclear fuel containing Mixed OXides of (natural or depleted) uranium and plutonium. 29.

MSR: Molten Salt Reactor. 61.

Natural analogue: see **Analogue** (**natural**, **archaeological**)*.

OCR: Oxide-Clad Reaction: a type of internal corrosion observed in the fuel pins of the Sodium-cooled Fast Reactor. 84.

OSCAR: a code based upon a phenomenological description of contamination in a PWR primary coolant system. 29.

Package: a packaging for transport, storage and/or disposal together with its specified radioactive contents. 109, 111, 112-114, 121, 129, 134, 138, 142.

PACTOLE: a code used to describe and predict contamination in a PWR primary coolant system. 26-29.

Passivation: decrease in the corrosion rate of a metal, in a given environment, that results from the formation of a thin corrosion products layer (the so-called passivation layer). Incomplete passivation may lead to localized corrosion. 13, 14, 35, 57, 59, 69, 105, 115.

Passivation layer: a chemical barrier able to passivate a surface, i.e. delay, or even prevent corrosion in the underlying material.

PCI: see **Pellet-clad interaction***.

Pellet (**fuel**)**:** a small cylinder made of a ceramic consisting of uranium, plutonium or other actinides, which is used as nuclear fuel and stacked within a **clad*** to make up a fuel **rod***. 43.

Pellet-Clad interaction (also called **Pellet-Cladding Interaction**) (**PCI**)**.** 43.

PHREEQC: a computer code designed for the coupled description of geochemical equilibria in sorption and dissolution-precipitation. 29.

Pitting corrosion: localized corrosion resulting in cavities extending from the surface into the material. 35.

Point defect: a local defect in a point of a crystal lattice, that results either from a missing atom (**vacancy***), or from an additional atom located between normal atomic sites (**interstitial atom***), or from a foreign atom substituting for one of the lattice atoms. A Frenkel pair is produced by pushing an atom off its site in the crystal, thereby forming a vacancy and an interstitial atom. 152.

Polarization: in corrosion, applying a potential different from free corrosion potential. 23, 31, 32, 33, 98, 99.

Potential (**corrosion**)**:** see **Corrosion potential***.

Primary coolant system (also called **primary coolant circuit**)**:** a closed loop system or set of closed loops which enables fuel rod heat to be extracted through a flowing **coolant*** in direct contact with these **fuel rods***. 50.

PUREX: a hydrometallurgical process for spent fuel treatment which is being implemented on the industrial scale in order to extract from spent fuel the still energetically valuable materials, uranium and plutonium. This process separates these two elements from minor actinides and fission products, considered as waste. 103.

Pyrochemistry: high-temperature chemistry (several hundred Celsius degrees). Pyrochemistry does not involve water or organic molecules, only liquid metals and molten salts. 99.

R7T7: a borosilicate glass type intended for confining waste which arise from spent fuel treatment, and named after the R7 and T7 workshops of La Hague Plant where it is produced. 129.

Radioactive contamination: the undesirable presence of a radioactive substance on a surface or within a medium. 9, 11, 14, 17, 27-29, 77, 79, 80-83, 93, 96, 98, 148.

Radiolysis: the breakdown of molecules by ionizing radiation. 53.

RAMAN spectrometry: the spectrum of light scattered by a substance illuminated with a monochromatic infrared radiation exhibits rays that result from coupling between the emitted radiation and the vibrations and rotations of the molecules which it goes through (Raman effect). Analyzing these rays brings information about the molecules in the substance. 15, 17, 32, 111, 115, 126-128.

RBS: Rutherford Back Scattering. This analytical technique consists in analyzing the backscattering of alpha particles sent onto a sample. It gives access to the local composition of the sample in the neighbouring of its surface. 25, 108.

Reactor vessel (also called **vessel**)**:** a vessel that contains the core of a reactor and its coolant. 27, 45, 47, 52, 95.

Recycling: reuse in a reactor of nuclear materials derived from **spent fuel treatment***. 61, 101.

Repository: see **Disposal** (**of radioactive waste**)*.

RIFF: a French acronym for *"Réaction à l'Interface Fissile-Fertile"*: fissile-fertile interface reaction. 84-85.

RHRS: Residual Heat Removal System. 50.

Rod: a small-diameter tube closed at both ends used as a component of the core in a nuclear reactor and containing fissile, fertile or absorbing material. When containing fissile material, the rod is a fuel element. 14, 20-23, 43, 57.

ROG: a French acronym for *"Réaction Oxyde-Gaine"*: oxide-clad reaction: a type of internal corrosion observed in the fuel pins of a sodium-cooled fast reactor. 84.

Roll expansion (also called **hard rolling**)**:** the pushing back of the metal of a tube part sleeved into a support, so as to increase its outer diameter and couple it to its support. Example: the U-shaped tubes which constitute the PWR steam generator tube bundle, are rolled into a tubesheet. 45.

SCC: see **Stress corrosion cracking***.

SCWR: SuperCritical Water-cooled Reactor. 61.

SEM: Scanning Electron Microscope. 23, 24, 65, 66, 70, 92, 93, 121, 122, 125, 128, 134.

Sensitized (US) (or **sensitised** UK)**:** qualifies a steel or alloy in which chromium carbide precipitates are located at grain boundaries. The material is then **sensitive*** to the intergranular corrosion phenomenon. 48, 103.

Sensitivity (also called **susceptibility**)**:** see **Sensitized***. 36, 43-48, 51, 52, 64, 78.

SFR: Sodium-cooled Fast Reactor. 61.

Siderite: Iron (II) carbonate, of empirical formula $FeCO_3$, which crystallizes in the trigonal crystal system and exhibits rhombohedral crystals. 122, 124, 126-128, 134.

Silica fume: it consists of particles approximately a hundred times smaller than cement grains (about 0.1 µm average diameter), and displays pozzolan properties due to its high amorphous silica content. Besides, it completes cement grain sizes in the ultrafine range.

Simulation: a set of methods which consists in reproducing or predicting complex system operation through calculation, especially in the various nuclear research and development branches. After validation, these methods may be used for designing new systems. 8, 21, 22, 27, 28-30, 69, 70, 80, 83, 89, 90, 101, 114, 119, 120, 123, 134, 135, 140, 141.

Smectite: a mineral consisting of aluminium silicate and hydrated magnesium, of the phyllosilicate family. 127, 128, 133, 142.

Sorbed: see **Sorption***.

Sorption: the light, reversible fixation of an atom or a molecule onto a solid surface. 14, 134.

Specific burnup (also called **specific burn-up** or **burn-up rate** or **burn-up**)**:** the total amount of energy released per unit mass in a nuclear fuel. Generally expressed in megawatt x day per ton (MW•d/t). 20, 29, 83-86.

Spectrometry: the measurement and interpretation of quantity spectra related to the physical or chemical constitution of a body or to the analysis of a wave. For instance, mass spectrometry relies on separating the atoms or molecules of a body as a function of their mass. 25, 28, 29, 115, 121.

Spectrometry (**Raman**)**:** see **Raman spectrometry***.

Spent fuel treatment: see **Treatment** (of **spent fuel**)*.

Stainless steel: iron base alloy containing at least 12% chromium. 31, 32, 36, 42, 43, 55, 57, 58, 78, 79, 103.

Storage (of radioactive materials or waste)**:** the action of placing radioactive materials or waste temporarily in a surface or subsurface specially designed facility, pending their retrieval. The facility in which waste is placed with the intention of further retrieval is referred to as a storage facility (see also **Disposal** [**of radioactive waste**]*). 7, 10, 101, 112, 129, 147.

Stress corrosion cracking (SCC): a cracking that results from a process involving the conjugate action of corrosion and deformation on the material under applied or residual mechanical stresses. 9, 11, 35-37, 39-56, 77, 78, 83, 152.

Stress intensity factor (K): a quantity characterizing the loading at the crack tip in a material subjected to stress. The crack propagates if the stress intensity factor goes beyond a threshold value, characteristic of the material. 35, 39, 44, 46, 48.

Susceptibility (also **called sensitivity***)**:** see **Sensitized***. 36.

Synchrotron radiation: any charged particle submitted to an acceleration emits an electromagnetic radiation. Such a property is used to produce intense X-ray beams in dedicated particle accelerators, e.g. ESRF or Soleil synchrotrons. Synchrotron radiation is used to probe matter structure on the atomic scale. 111, 127.

TEM: Transmission Electron Microscope. 16, 17, 24, 25, 109.

Test loop: an experimental device dedicated to specific studies under dynamic or recirculation conditions (closed loop, purification, desired conditions maintained). 15, 19, 28, 66, 86.

THERMODY: a computer code dedicated to the thermodynamics of aqueous environments at high temperature. 29.

Transpassive range: a potential range where the passive layer of a passivable alloy is no longer stable, and which features a high increase in the corrosion current in the absence of pitting. 103.

Treatment (of spent fuel) (also called **reprocessing** or **spent fuel treatment**)**:** an operation that consists in separating valuable materials in spent fuel from the remainder, which can be then considered as waste and conditioned accordingly. **103.**

Tribocorrosion: wear corrosion. **57.**

Uniform corrosion: a **general corrosion*** that extends at the same rate (uniformously) on all the material surface. **13, 14, 16, 21, 24, 27, 32, 121.**

Vacancy: see **Point defect***.

Vessel: see **Reactor vessel***.

Vessel internals: see **Internals***.

VHTR: Very High Temperature Reactor. **61.**

Work hardening: see **Cold work(ing)***.

XANES: X-ray Absorption Near Edge Structure (see **XAS***).

XAS: X-ray Absorption Spectroscopy used for measuring the modulations in the X-ray absorption coefficient in an energy range of a few hundred electronvolts beyond the ionization threshold of a chemical element. This analysis provides information on the electronic characteristics (oxidation degree) of the element being probed (XANES), as well as its atomic environment: nature, distance, and number ot atoms in the vicinity of the analyzed element (EXAFS). **111.**

XPS: X-ray Photoelectron Spectroscopy. When a material specimen is bombarded by X rays, the energy of the photoelectrons emitted brings information about the chemical species present in the neighbouring on the specimen surface. **24, 70.**

Zircaloy: an alloy of zirconium and one or several other metals (tin, iron, chromium, nickel), which displays outstanding mechanical strength and chemical resistance. It is used for **fuel clads*** in water-cooled reactors. **15-23, 33, 43, 44, 56, 57.**

Table of contents

Contributors to this Monograph:

Frédéric Angeli,
Fabienne Audubert,
Marianne Balat-Pichelin,
Fanny Balbaud,
Benoît Bary,
Christian Bataillon,
Nathalie Bertrand,
Bernard Bonin,
Jean-Philippe Bossis,
Vincent Bouineau,
Frédéric Bouyer,
Céline Cabet,
Jacques Chêne,
Guillaume de Combarieu,
Catherine Corbel,
Jean-Louis Courouau,
Nicolas Dacheux,
Philippe Deloffre,
Xavier Deschanels,
Clara Desgranges,
Philippe Dubuisson,
Stéphanie Fabre,
Damien Féron (Topic Editor),
Catherine Fillet,
Lionel Fournier,
Pierre Frugier,
Christophe Gallé,
Grégory Geneste,
Stéphane Gin,
Joël Godlewski,
Nicole Godon,
Catherine Guerre,
Emmanuel Herms,
Valérie L'Hostis,
Anne Jestin,
Michel Jullien,
Pierre Laghoutaris,
Jean-Éric Lartigue,
Christian Latgé,
Patrick Le Bescop,
Marie Libert,
Alexandre Maître,
Loïc Marchetti,
Laurent Maréchal,
Laure Martinelli,
Yves Minet,
Frédéric Nguyen,
Dominique Pêcheur,
Michel Pelletier,
Stéphane Perrin,
Hugues Peycelon,
Christian Phalippou,
Stéphane Poyet,
Olivier Raquet,
Cécile Richet (Topic Editor),
Jean-Charles Robin,
Fabien Rouillard,
Gérard Santarini,
Michel Schlegel,
Anne Terlain,
Pascal Thouvenot,
Marc Tupin,
Aurélie Verney-Carron,
Dominique You.

… along with, of course, all the members of the DEN Monographs Editorial Board:

Bernard Bonin (Editor in chief), Bernard Bouquin (Communication Division), Martine Dozol (CEA Cadarache Center), Alain Forestier (CEA Saclay Center), Michaël Lecomte (CEA Marcoule Center), Michel Beauvy, Georges Berthoud, Mireille Defranceschi, Gérard Ducros, Damien Féron, Yannick Guérin, Christian Latgé, Yves Limoge, Charles Madic †, Gérard Santarini, Jean-Marie Seiler, Étienne Vernaz.